

**PROPERTIES OF Ni-Mn BASED HEUSLER ALLOYS
WITH MARTENSITIC TRANSITION**

Thesis submitted for the degree of
Doctor of Philosophy (Science)

in

Physics (Experimental)

by

Sandeep Singh

Department of Physics
University of Calcutta
July 2014

To my parents

Acknowledgements

It is my great pleasure to express my gratitude to all the persons for their help and encouragement. First I would like to express my special appreciation and thanks to my supervisor Dr. Chhayabrita Biswas, who has supported me throughout my thesis with her patience and knowledge. In particular, I am very grateful for her continuous assistance, guidance and friendly attitude. She always encouraged me to get to the bottom of every problem and helped to understand it fully. Also, I am very grateful to her for the freedom I was given during my PhD.

I am grateful to Prof. Kalobaran Maiti and his research group of Tata Institute of Fundamental Research, for providing XPS and UPS facilities and help with the data acquisition. In his lab I also learned the techniques of XPS and UPS. Specially, I would like to thank Ganeshda, Deep, Nishina and Bindudi. Without their help I would not have been able to complete photoemission experiments.

The large part of the experimental work presented in this thesis were performed at the UGC-DAE-CSR, Indore. I would especially like to express my appreciation for Dr. Rajeev Rawat, Dr. A. M. Awasthi and Dr. S. R. Barman for allowing me to use the facilities of their laboratory. I should also take this occasion to thank Prof. I. Das of SINP, Kolkata for initial support by providing the chemicals and other facilities for sample preparation. I am grateful to Prof. D. Das of UGC-DAE-CSR, Kolkata, who provided the SQUID for magnetic measurements. I would also like to thank Mr. P. V. Rajesh for performing SQUID measurements for me.

I would like to thank my head of department Prof. P. K. Mukhopadhyay for providing the arc furnace for sample presentation. I also express my thanks to Dr. B. Rajini Kanth, who first showed me the operation of arc furnace. I must also acknowledge the help of many technical staffs in various labs of S N Bose Centre and other centres.

I am thankful to my seniors Abhinav Kumar, Prashant Singh, A P Jena, Debraj Ray, Soumyajit Sarkar, Hirak Kr. Chandra and Kapil Gupta. They always helped and supported me. Abhinav bhaiya and Prashantji are like elder brothers to me. Whenever I have problems related to computer or any software it was always Jenaji who had the right answers for me. In S N Bose campus I enjoyed the company great friends. I am glad to have friends like Rajeev Chauhan, Sandeep Agarwal, Rajib Nath, Abhijit Chakraborty, Tanumay Pramanik, Manotosh Chakraborty, Shahnewaz Mondal and Sudip Garain who shared their precious time with me and provided cheerful environment. I appreciate my juniors Saikat Debnath, Shishir Pandey, Basudeb Mandal, Ruma Das, Ruma Mandal, Wasim Iqbal, Rajshree Das, Tukun, Tanmoy Ghosh, Dilip Sao for spending joyous time with me. I am indebted to all of them for providing a stimulating and fun filled environment. Evening outing with Saikat, Shishir and Basudeb was always refreshing and relaxing. The political discussion between Shishir and others (including me) at lunch and dinner table was always entertaining. I would like to thank my labmate Soumyadipta Pal for his help with thesis corrections

and useful scientific discussions.

Finally, I would never have been able to complete my thesis without the continued support from my family. I am grateful to my mother and father for their love and confidence in me. It inspired me and constantly drove me forward. Although they knew very little of what I was doing in my lab, they always supported and encouraged me, especially when things were not going well. I wish to thank my elder brothers Shiv Nandan, Shashank and sister in law Alka for continuous motivation, support and advice. The constant love and support of my younger brothers Kuldeep and Anudeep is sincerely appreciated.

Sandeep Singh
Kolkata, July, 2014

List of Publications

Thesis work:

1. Sandeep Singh and C. Biswas, "Magnetoresistance origin in martensitic and austenitic phases of $Ni_2Mn_{1+x}Sn_{1-x}$ ", **Appl. Phys. Lett.** 98, 212101 (2011).
2. Sandeep Singh, Illya Glavatsky, and C. Biswas, "The influence of quench atomic disorder on the magnetocaloric properties of Ni-Co-Mn-In alloys", **J. Alloys Compd.** 601, 108-111 (2014).
3. Sandeep Singh, Illya Glavatsky, and C. Biswas, "Field-cooled and zero-field cooled magnetoresistance behavior of $Ni_2Mn_{1+x}In_{1-x}$ alloys", **J. Alloys Compd.** (2014).
DOI: <http://dx.doi.org/10.1016/j.jallcom.2014.07.012>.
4. Sandeep Singh, Soumyadipta Pal, and C. Biswas, "Disorder induced resistivity anomaly in $Ni_2Mn_{1+x}Sn_{1-x}$ ", **J. Alloys Compd.** (2014).
DOI: <http://dx.doi.org/10.1016/j.jallcom.2014.07.072>.
5. Sandeep Singh, Ganesh Adhikary, D. Biswas, Kalobaran Maiti, and C. Biswas, "Electronic structure modification of $Ni_2Mn_{1.4}Sn_{0.6}$ upon martensitic phase transition", **AIP Conf. Proc.** 1349, 849-850 (2011).
6. Sandeep Singh and C. Biswas, "Disorder induced resistivity changes in $Ni_2Mn_{1+x}Sn_{1-x}$ ", **AIP Conf. Proc.** 1349, 1005-1006 (2011).
7. M. Maniraj, S. W. D' Souza, Sandeep Singh, C. Biswas, S. Majumdar, and S. R. Barman, "Electronic structure of nearly stoichiometric Ni-Mn-Sn and Ni-Mn-In", (**J. Electron Spectrosc. Relat. Phenom.**) Submitted.
8. Soumyadipta Pal, Sandeep Singh, P. Mahadevan, K. Maiti, and C. Maji, "Role of coulomb correlation in the electronic structure of Ni-Mn-Sn" **Under preparation.**
9. Soumyadipta Pal, Sandeep Singh, P. Mahadevan, and C. Maji, "Spin-lattice coupling driven magnetic field induced reverse phase transition in $Ni_2Mn_{1+x}Sn_{1-x}$ " **Under preparation.**
10. C. Maji, Sandeep Singh, Soumyadipta Pal, Ganesh Adhikary, P. Mahadevan, and Kalobaran Maiti, "Electronic structure influence on instability of martensitic phase of $Ni_2Mn_{1+x}Sn_{1-x}$ " **Under preparation.**

Contributory work:

1. Sandeep Singh , Anchal Dwivedi, R. Dabrowski, and R. Dhar, “*Electro-optical features of anti ferro electric liquid crystal material (S)-(+)-4-(1-methylheptyloxycarbonyl) phenyl 4’-(6-octanoyloxyhex-1-oxy) biphenyl-4-carboxylate in its ferro and anti ferro electric phases*”, **Physica B** 406, 40-44 (2011).
2. R. Dhar, Sandeep Singh, I. M. L. Das and R. Dabrowski, “*Thermodynamic and dielectric studies of liquid crystalline compound (S)-(+)-4-(1-methylheptyloxycarbonyl) phenyl 4’-(6-octanoyloxyhex-1-oxy) biphenyl-4-carboxylate*”, **Phase Transitions** 82, 251-265 (2009).

Contents

Table of Contents	ix
1 Introduction	1
1.1 Heusler alloys	2
1.2 Martensitic transition in Heusler alloys	4
1.3 Advanced functional properties	10
1.3.1 Magnetic shape memory effect	10
1.3.2 Magnetoresistance	12
1.3.3 Magnetocaloric effect	13
1.4 Applications	14
1.5 Outline of thesis	15
2 Experimental methods	23
2.1 Arc melting process	24
2.2 Scanning electron microscope	24
2.3 Energy dispersive X-ray analysis	25
2.4 Differential scanning calorimetry	27
2.5 X-ray diffraction	28
2.6 Four probe method	29
2.7 Vibrating sample magnetometer	30
2.8 Superconducting quantum interference device (SQUID)	31
2.9 Photoelectron spectroscopy	32
2.9.1 Theory of photoemission	33
2.9.2 Experimental setup	35
3 Heusler alloy preparation and characterization	45
3.1 Sample preparation	46
3.2 Chemical composition	46
3.3 Determination of transition temperatures	47
3.4 Surface micro-structure at room temperature	51
3.5 Crystal structure at room temperature	54
3.6 Conclusion	58

4	Magnetic property	61
4.1	Introduction	62
4.2	Result and Discussion	63
4.2.1	Ni ₂ Mn _{1+x} Sn _{1-x} alloys	63
4.2.2	Ni ₂ Mn _{1+x} In _{1-x} alloys	70
4.2.3	Co doped Ni-Mn-In alloys	76
4.2.4	Inverse magnetocaloric effect	79
4.3	Conclusion	84
5	Electrical-transport property	89
5.1	Introduction	90
5.2	Result and Discussion	91
5.2.1	Ni ₂ Mn _{1+x} Sn _{1-x} alloys	91
5.2.2	Ni ₂ Mn _{1+x} In _{1-x} alloys	102
5.2.3	Co doped Ni-Mn-In alloys	109
5.3	Conclusion	113
6	Magneto-transport property	119
6.1	Introduction	120
6.2	Result and Discussion	121
6.2.1	Ni ₂ Mn _{1+x} Sn _{1-x} alloys	121
6.2.2	Ni ₂ Mn _{1+x} In _{1-x} alloys	125
6.2.3	Co doped Ni-Mn-In alloys	135
6.3	Conclusion	138
7	Electronic structure	143
7.1	Introduction	144
7.2	Clean surface preparation under UHV	145
7.3	Data analysis procedure	146
7.4	Result and Discussion	149
7.4.1	Surface characterization	149
7.4.2	Core level	154
7.4.3	Valence band	160
7.5	Conclusion	167

Chapter 1

Introduction

1.1 Heusler alloys

Heusler alloys are topic of research from hundred of years since its discovery. In 1903 F. Heusler discovered that it is possible to make ferromagnetic alloy with non-magnetic elements [1]. Heusler alloys are ternary, magnetic, intermetallic alloys defined by the generic formula X_2YZ . Cu_2MnSn was the first Heusler alloy discovered by Heusler, which becomes ferromagnetic, even though none of its constituents is ferromagnetic by itself. In 1910 Ross and Gray [2] demonstrated that the magnetic properties of the Cu_2MnSn alloy were affected by heat-treatment and quenching from $580^\circ C$ caused an almost complete loss of magnetization. The Heusler alloys have been repeatedly investigated and in 1928 Persson [3] shows that the structure of near composition Cu_2MnAl ferromagnetic alloy was body-centred cubic but with the Al atoms forming a face-centred superlattice as in the DO_3 (Fe_3Al type) structure [4]. Potter [5] in 1929 came to the same result of Persson, after he investigated the structure of single crystals of Cu_2MnAl . At that time it was very difficult

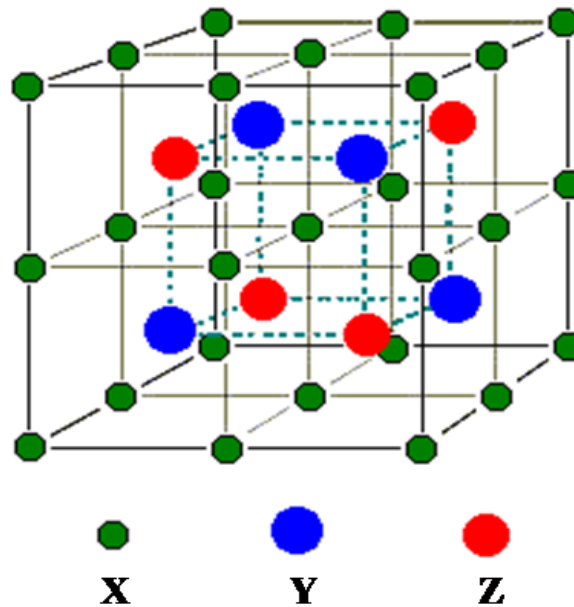


Figure 1.1 The L_{21} crystal structure of Heusler alloys.

to determine whether the Mn atoms were similarly ordered because of the difficulties in distinguishing between Cu and Mn sites using X-rays. The definitive work on the structure of Heusler

alloys was carried out by Bradley and Rodgers (1934) [4,6]. They confirmed that Cu and Mn also forms ordered face-centred cubic (f.c.c.) sublattice [6].

The full Heusler structure with chemical formula X_2YZ consists of four interpenetrating f.c.c. sublattices with atoms at $A(0,0,0)$, $C(1/2,1/2,1/2)$, $B(1/4,1/4,1/4)$, and $D(3/4,3/4,3/4)$ positions which results in $L2_1$ crystal structure as shown in Fig. 1.1 [7]. In Heusler alloys there is always some degree of chemical disorder, heavily influencing many of their physical properties. In the fully ordered Heusler alloy, the four sublattices A, B, C, and D are occupied by X, Y, X, and Z atoms, respectively. In reality, this fully ordered state is hard to attain, and there is varied possibility of disorder [4]. When X atoms remain ordered and full disorder occurs between Y and Z sites only, B2 (CsCl type) structure is obtained. If disorder occurs between one X site and either Y or Z sites, the atomic arrangement may lead to DO_3 (Fe_3Al) structure. An A2 structure occurs if there is random atomic ordering between all X, Y and Z sites.

Heusler alloys are traditionally considered to be local moment systems [8, 9]. The Mn based (X_2MnZ) alloys are the most studied system in Heusler alloys. The magnetic moment is mainly localized on Mn. The localized character of the magnetization results from the exclusion of minority-spin electrons from the Mn $3d$ states. The magnetism arises due to the RKKY type indirect exchange interaction. When the interaction is mediated by the X conduction electrons the alloy is ferromagnetic and if it is mediated by the Z conduction electrons, it can have either sign, depending on the position of the Fermi level (E_F) in the Mn–Z $p-d$ hybrid states [9].

Heusler compounds are promising materials in many fields of contemporary research. The spectrum of their possible applications ranges from magnetic and magneto-mechanical materials over semiconductors and thermoelectrics to superconductors [10]. Heusler alloys also show great potential for spintronic applications [11]. Due to the half-metallicity of some Heusler alloys, they exhibit 100% spin polarization at the Fermi level. The NiMnSb half Heusler [12] alloy and full Heusler alloys such as Co_2MnSi and Co_2MnGe [13] are known to possess full spin polarization.

1.2 Martensitic transition in Heusler alloys

Till the last century, studies on Heusler alloys have been done from structural and magnetism point of view. But recent interest in Heusler alloys is due to the reversible martensitic transformation (MT). The high temperature phase called austenite or parent phase transforms to low temperature and lower symmetry phase called martensite and vice versa as shown in Fig. 1.2. The MT is defined as a lattice deformation involving shearing deformation and resulting cooperative atomic movement. There is a 1-to-1 correspondence called "lattice correspondence" between the lattice points of parent and martensitic phases. The MT is a first order structural transformation which results in large transformation strain. In order to reduce the strain during nucleation and growth two types of lattice invariant shear (LIS) mechanisms could take place; dislocation slip or twinning [14]. These are called LIS because they do not change the structure of martensite [15]. Generally

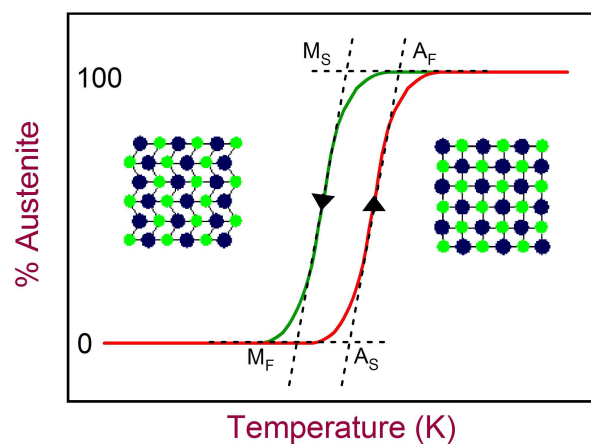


Figure 1.2 Schematic of martensitic transformation.

twinning is the LIS for most of the martensitic crystals. Each martensitic crystal formed can have a different orientation direction, called a variant. The assembly of martensitic variants can exist in two forms: twinned martensite, which is formed by a combination of "self-accommodated" martensitic variants, and detwinned or reoriented martensite in which a specific variant is dominant [16]. Thus, Heusler alloys which exhibit a crystallographically reversible, thermoelastic MT result

in shape memory effect. The MT is shown by some other materials like steel and some ceramics but their transition is irreversible in nature [17]. These transformations are also subject to the constraints of nucleation and growth. Due to first order phase transformation it shows hysteresis during heating and cooling. The characteristic transformation temperatures are called austenitic start (A_S), austenitic finish (A_F) (during heating) and martensitic start (M_S), martensitic finish (M_F) (during cooling).

In recent times martensitic transition in Ni-Mn based Heusler alloys have attracted a lot of attention due to their possible applications. The general formula for the Ni-Mn based Heusler alloys are Ni_2MnZ , where Z can be Al, Ga, Sn, Sb, In etc. In these series of alloys only Ni_2MnGa shows the MT in stoichiometric composition and other shows the MT in off-stoichiometric composition. The Ni_2MnGa is most studied alloy. The MT in these Heusler alloys are reversible in nature. Due to the reversibility of the MT and magneto-structural coupling, these alloys has magnetic shape memory effect [18–20]. Alloys which show the magnetic shape memory effect are also known as magnetic shape memory alloys. In such alloys, application of external magnetic field in martensitic state can induce large strain. In 2004 Sutou et al. [21] reported new type of magnetic shape memory alloy in the Ni-Mn-X (In, Sn, Sb) Heusler alloy system, where magnetic field induced reverse phase transformation can give rise to a large strain. The occurrence of magnetic field induced structural transitions, is an indication of a relationship between structural and magnetic degrees of freedom at the microscopic level. It is necessary to understand this relationship in order to gain an insight into the details of the martensitic transformation.

In the austenite state, Ni-Mn-Z (Sn, In, Sb, Ga) have $L2_1$ structure [space group Fm-3m] which consists of four interpenetrating f.c.c. sublattices, as shown in Fig. 1.1. For the stoichiometric composition, Ni atoms occupy the 8c positions (in Wyckoff notation), while Mn and Z atoms occupy 4a and 4b positions, respectively [4, 22, 23]. When the temperature is decreased, they can undergo a martensitic transformation and acquire a number of structures. In particular, they transform to the $L1_0$ tetragonal structure at low Z concentrations, since this is also the ground-state structure of the parent compound NiMn [24]. The modulated structures related to the tetragonal structure are observed depending upon the Z concentrations. The relationship between the $L2_1$ and

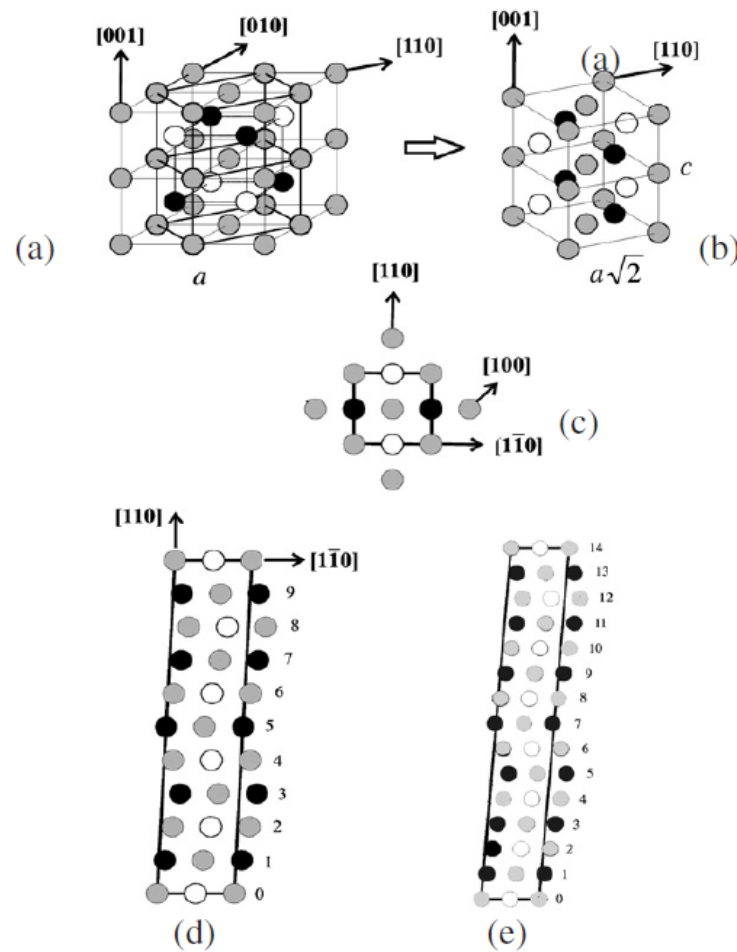


Figure 1.3 Austenite and martensite structures of Heusler alloys shown for the case of Ni_2MnGa . Light grey: Ni, white: Mn, black: Ga. (a) The $L2_1$ Heusler structure showing also the relationship with the tetragonal unit cell, which is also shown in part (b). (c) The tetragonal unit cell viewed from the top and (d) the 5 M (or 10 M) and (e) 7 M (or 14 M) modulated structures obtained by shearing the tetragonal cell [24].

the tetragonal structures is given in Fig. 1.3 (a). The tetragonal structure is also shown separately in Fig. 1.3 (b). The tetragonal structure viewed from the top plane in Fig. 1.3 (b) is shown in Fig. 1.3 (c). In general five fold (5M) and seven fold (7M) modulated structures are found in these alloys. The generated modulations for the 5M and 7M cases are shown in Fig. 1.3 (d) and Fig. 1.3 (e), respectively. The ‘M’ refers to the monoclinicity resulting from the distortion associated with the modulation. The 5M and 7M modulations are sometimes referred to as 10M and 14M.

The structural stability of the martensitic phase of Ni-Mn-Z alloys depends on the composition. Figure 1.4 shows the magnetic and structural phase transition temperatures of Ni-Mn-Z Heusler alloys with Z as Sn, In and Ga plotted as a function of the valence electron concentration per atom e/a [24]. For all the three cases the ground-state structure evolves essentially as cubic \rightarrow 10 M \rightarrow 14 M \rightarrow L1₀ with increasing e/a [24]. The e/a increases with x in Ni₂Mn_{1+x}Z_{1-x} (Sn, In, Sb and Ga) systems and at $x = 1$, $e/a = 8.5$ having L1₀ structure of NiMn.

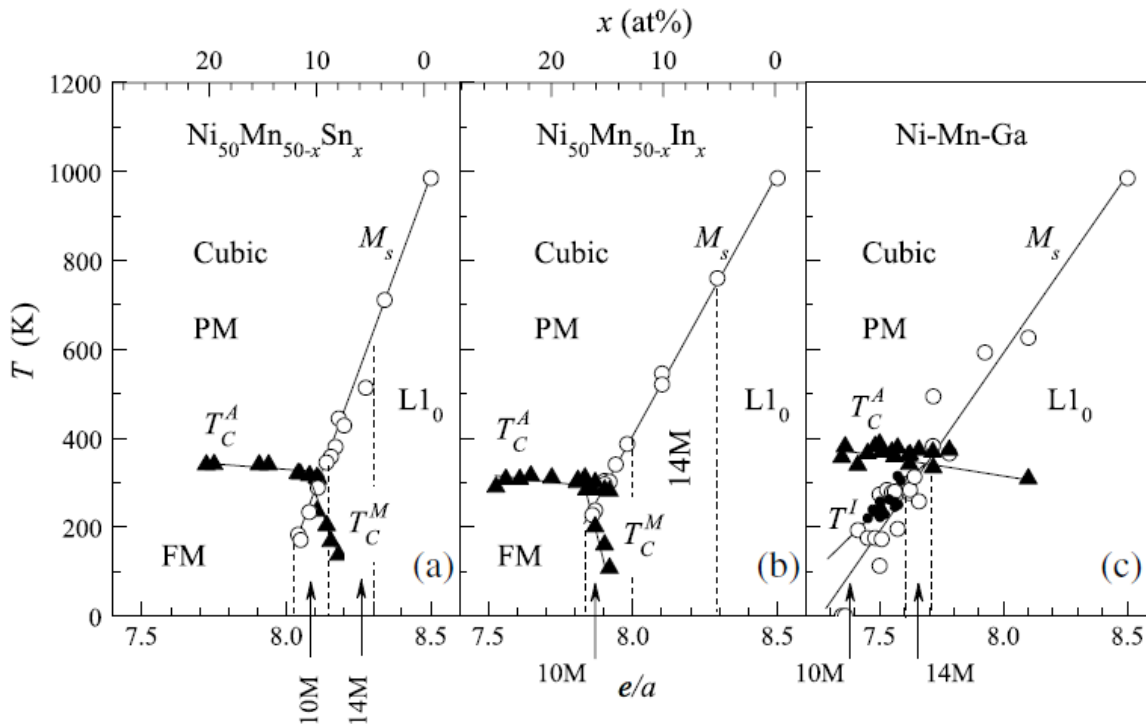


Figure 1.4 The magnetic and structural phase diagram of Ni-Mn-Z Heusler alloys with Z as (a) Sn, (b) In and (c) Ga. The triangles and the circles correspond to the magnetic and martensitic transformation temperatures respectively. The regions corresponding to the different structures are separated by discontinuous lines. Small solid circles in (c) correspond to the premartensitic transition temperature [24].

The Ni-Mn based martensitic Heusler alloys show number of features in the temperature dependence of the magnetization $M(T)$ depending on the measurement conditions. These alloys show different behaviour in the zero field cooled (ZFC), field cooled cooling (FC), and field cooled heating (FH) mode in the presence of applied fields [25]. The Ni-Mn-Z, Z = (Sn, In, Sb) alloys have

similar behaviour. However, Ni-Mn-Ga magnetization behaviour is different. Most of the Ni-Mn-Ga alloys have ferromagnetic ground state in the martensitic phase, while Ni-Mn-Z, Z = (Sn, In, Sb) systems have mixed (ferro/anti-ferro) magnetic state in the martensitic phase [26–28]. A typical magnetization behaviour for Ni-Mn-Z, Z = (Sn, In, Sb) systems are shown in Fig. 1.5 [29]. There is large decrease in the magnetization upon the martensitic transition. The splitting between the ZFC magnetization and the FC/FH magnetization is observed in the martensitic phase. In the

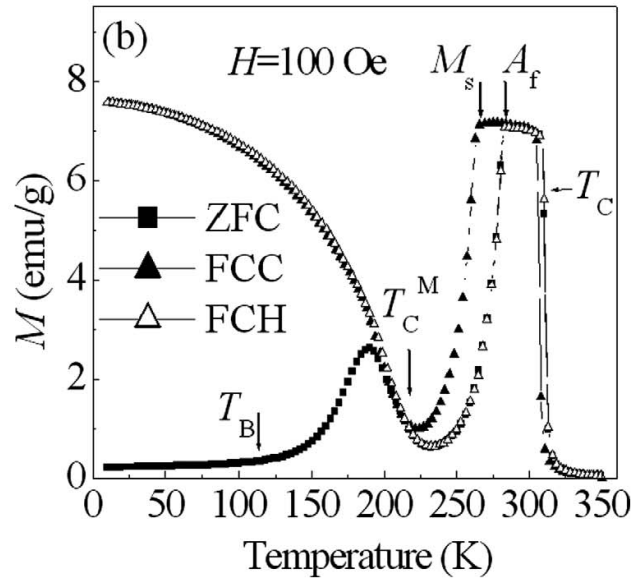


Figure 1.5 ZFC, FCC, and FCH $M(T)$ of the $\text{Ni}_{49.5}\text{Mn}_{34.5}\text{In}_{16}$ sample measured in $H=100$ Oe [29].

off-stoichiometric composition the extra Mn goes to the Z (Sn, In, Sb) site, which is confirmed by the neutron diffraction study [23]. In the martensitic phase presence of anti-ferromagnetic coupling between the Mn atoms at Mn site and Mn atom at Z site have been predicted [23, 28, 30, 31]. Currently the mixed nature of the magnetic interactions in the martensitic state is reported using ferromagnetic resonance (FMR) study on the Ni-Mn based Heusler alloys [32]. The presence of exchange bias [29, 33, 34] and reentrant spin glass [35] like behaviour are reported in the martensitic phase, which also supports the presence of anti-ferromagnetic coupling.

The martensitic Heusler alloys are particularly interesting for fundamental investigations, also, due to interplay between their complex crystal structures and their magnetism. Most of the novel

properties of martensitic Heusler alloys are related to the martensitic transformation. This stimulates the interest to understand the electronic structure. Most of the theoretical explanations concerning the underlying mechanism of martensitic phase transition are phenomenological studies based on the free energy expansion [36, 37]. Few first-principles calculations, especially on Ni-Mn-Ga systems have provided the interpretations on the origin of martensitic phase transition, such as a Jahn-Teller distortion [38] and Fermi surface nesting [39].

From the theoretical calculations of Ni₂MnGa magnetic moment in the austenitic phase is found to be 4.13 $\mu_B/f.u.$ and the individual moments per site for Ni, Mn, and Ga are 0.36, 3.44, and -0.04 μ_B , respectively [40]. The density of state (DOS) is dominated by Ni and Mn 3d states in the bonding region below Fermi energy (E_F). The shape and the total width (6 eV) of the valence band is same for both the phases. The majority spin Ni 3d states extend from -4 eV to above E_F , and from partial density of states calculations the t_{2g} and e_g states are almost uniformly distributed. The minority-spin Ni 3d t_{2g} states are centered around -1.5 eV with a width of 0.6 eV. Ni 3d partial DOS has a sizeable contribution near E_F , which is primarily of e_g character. The minority-spin Mn 3d states dominate the antibonding region above E_F with the peak around 1.5 eV and has small contribution below E_F . Both Mn 3d t_{2g} and e_g states contribute equally to this peak. In contrast, the majority spin Mn 3d states are almost fully occupied and the t_{2g} and e_g states are clearly separated appearing at -3 and -1.3 eV, respectively.

Fujii et al. [38] calculated the density of states of both martensitic and austenitic phases using the Korringa-Kohn-Rostocker method and suggested that the band Jahn-Teller effect stabilizes the martensitic phase. A signature of the band Jahn-Teller effect is splitting of a peak exactly at E_F into two peaks below and above E_F resulting in a lowering of total energy. However, Barman et al. [40] results clearly show that, although splitting occurs, both the split peaks are below E_F . So, the stabilization of the martensitic phase is related to the lowering of the total energy and cannot be described purely in terms of the band Jahn-Teller effect. The experimental ultraviolet photoelectron spectroscopy (UPS) valence band (VB) spectra have been studied by A. Chakraborti [41]. The experimental spectrum exhibits a broad main peak centered at 1.4 eV and a weak feature at 3.5 eV. UPS measurements by Opeil et al. [39], shows the sudden redistributions of the UPS intensity

corresponding to the onset of the pre-martensitic transition and martensitic transition, respectively.

1.3 Advanced functional properties

1.3.1 Magnetic shape memory effect

The shape memory effect occurs when a material is deformed by mechanical stress in the martensitic state and regains its original shape upon heating above martensitic phase transformation temperature. The alloys have memory of their original shape. Upon application of the mechanical stress in the martensitic phase, shape change occurs due to the detwinning of the twin variants. Heating above the martensitic phase transformation temperature, it recovers the original shape by the reverse phase transformation as shown in Fig. 1.6. The alloys which show the shape memory effect are called shape memory alloys (SMA). Shape memory property of SMA can be controlled by stress and temperature.

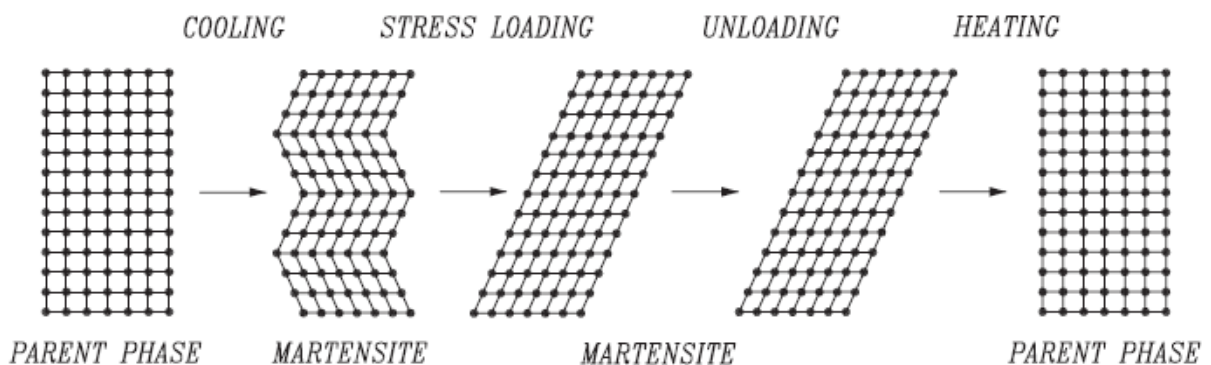


Figure 1.6 Schematic diagram of the Shape memory effect [24].

In the ferromagnetic Heusler alloys with the reversible martensitic transformation, magnetic field is an extra degree of freedom to control the shape memory effect. In 1996 Ullakko shows the possibility of magnetic shape memory effect in Ni_2MnGa [42]. The magnetic field provides the faster control over the stress and temperature controlled shape memory effect. Actuation frequency range for magnetic shape memory alloys (MSMA) is 10Hz - 1000Hz, which is much higher than

SMA 0.1Hz - 20Hz [16]. In recent years, there has been an increasing interest in MSMA due to their unique ability to produce very large strains of up to 10% under a magnetic field [10, 43–45], which is considerably larger than those in piezoceramics and magnetostrictive materials showing strain of about 0.2% on application of electric or magnetic field. The Ni_2MnGa is the most studied Heusler alloy showing martensitic phase transition. The large magnetic field induced strain (MFIS) values ($\sim 1 - 10\%$) are reported for Ni-Mn-Ga single crystals [46, 47]. The shape memory effect is originating from the rearrangement of martensitic variants [43, 44, 48, 49]. In MSMA, magnetic field induced reorientation of twin variants is the main mechanism responsible for the large magnetic field induced strain as shown in Fig. 1.7. Interestingly, recently, new type of magnetic shape memory alloys Ni-Mn-X (In, Sn, Sb) are found where magnetic field induced reverse phase transformation can give rise to a large strain [21]. The magnetic field induced reverse phase transformation is accompanied by the shift in the martensitic transition temperature.

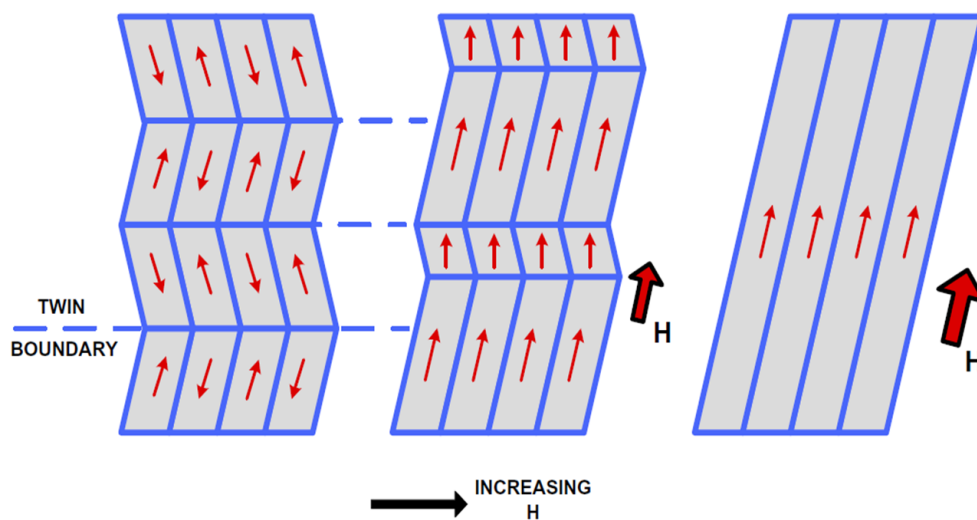


Figure 1.7 Effect of applied magnetic field, H , on the reorientation of the martensite twin variants [27].

Thus the main mechanisms that result in the field induced external strain in MSMA are: i) martensite variant reorientation as a result of magnetic field-induced twin boundary motion and ii) magnetic field-induced reverse phase transformation [26]. There are different class of materials in the Heusler alloy system, where MFIS is governed by these two different mechanisms. In

the former mechanism, if the magnetocrystalline anisotropy energy (MAE) of a magnetic field-favoured martensite variant is larger than the energy required for twin boundary motion then that variant will grow at the expense of others, resulting in a field induced macroscopic shape change. So the alloys, which have higher MAE in the martensitic phase will show large MFIS by the field induced reorientation of twin variants. Few examples are Ni-Mn-Ga, Ni-Co-Al, Ni-Fe-Ga, Ni-Co-Ga etc [45]. The MAE is limited by the saturation magnetic field, above which the MAE does not increase with the field. So actuation stress level is also limited by the field and actuation stress upto 5 MPa is achieved [45]. The MAE is also crystal orientation dependent. Since the MAE provides only a few MPa of stress for twin boundary motion, and both MAE and MFIS are orientation dependent, the field-induced variant reorientation mechanism is limited to single crystals. Thus, the high cost of single crystals and low actuation stress levels restrict the potential applications of these MSMA.

The second mechanism for MFIS involve the Zeeman energy (ZE) difference between the parent and martensitic phase. The ZE is crystal orientation independent. In this case MAE of the martensitic phase is very less or negligible. The ZE difference is not saturated with the field. So we can get the large actuation stress level (upto 200 MPa) with the MFIS in the polycrystals [26]. The MFIS could be maximized by maximizing the ZE difference. The ZE difference is maximized by increasing the difference between the saturation magnetizations of both phases. When a ferromagnetic phase transforms to a paramagnetic or antiferromagnetic phase, or vice versa the ZE difference is increased. Off-stoichiometric Ni-Mn-Sn, Ni-Mn-In, Ni-Mn-Sb and Ni-Co-Mn-In are the promising materials for this mechanism, in which ferromagnetic austenite transform to the non-magnetic (para or anti-ferro) martensitic phase [26].

1.3.2 Magnetoresistance

The magnetoresistance (MR) is the field dependent change in the electrical resistance of a ferromagnetic material. It finds applications in magnetic field sensors and reading heads of hard disk drives. Thus development of new functional materials that exhibit large magnetoresistance (MR) is

important for many technological applications. Near and above the Curie point, T_C , corresponding to the onset of magnetic order, scattering of charge carriers by magnetic fluctuations can substantially increase the electrical resistance [50]. These fluctuations can be suppressed by a magnetic field, leading to a negative MR.

The Ni-Mn based Heusler alloys emerged as a promising candidate for large MR. MR in the ferromagnetic state of $Ni_{2+x}Mn_{1-x}Ga$ is studied for different compositions in the austenitic, pre-martensitic, and martensitic phases and it is found to increase with x [51, 52]. Maximum MR of -7.3% (8 Tesla) is obtained at 300 K in the austenitic phase of $Ni_{2.35}Mn_{0.65}Ga$ [52]. The MR upto -4% (5 Tesla) is obtained across the martensitic transition in $Ni_{1.75}Mn_{1.25}Ga$ [53]. The MR behavior in the austenitic phase is explained on the basis of the $s-d$ scattering model [51, 52]. In the martensitic phase MR shows a cusplike shape. This has been explained by the changes in twin and domain structures in the martensitic phase [51].

1.3.3 Magnetocaloric effect

Caloric effects occur in any macroscopic physical system as a consequence of its thermal response to changes of variables such as volume, strain, magnetization, polarization, etc. When the variable is magnetization it is called magnetocaloric effect (MCE). The total entropy of a magnetic material with localized magnetic moments is the sum of the electronic (S_e), lattice (S_l), and magnetic (S_m) contributions of entropy.

$$S_{\text{Total}} = S_e + S_l + S_m \quad (1.1)$$

where S_e is the electronic entropy, S_l is the lattice entropy and S_m is the magnetic entropy. Usually, S_e and S_l are magnetic field independent while, S_m strongly depends on the magnetic field. In general, an isothermal application of a magnetic field decreases the configurational entropy of the spin structure. The change in magnetic entropy (ΔS_m) is negative. A subsequent adiabatic demagnetization allows the spins to become disordered again, by means of the thermal energy provided by the phonon bath of the isolated sample and the temperature decreases. It is called conventional MCE. It is generally observed near second order magnetic transition T_C . As opposed to cooling

by adiabatic demagnetization, cooling by adiabatic magnetization (inverse MCE) requires an increase of configurational entropy on applying a magnetic field. The ΔS_m is positive. The inverse MCE is observed in systems where first-order magnetic transformations, such as antiferromagnetic/ferromagnetic (AF/FM), AF-collinear/AF-non-collinear or antiferromagnetic /ferrimagnetic (AF/FI), take place.

At the first order martensitic transformation, transformation temperature change (ΔT) induced by magnetic field (H) is approximately given by the Clausius-Clapeyron relation:

$$\left(\frac{dT}{dH}\right) = -\left(\frac{\Delta M}{\Delta S}\right) \quad (1.2)$$

where T is the absolute temperature, and where ΔM and ΔS are the difference of magnetization and entropy of the low and high temperature phases, respectively. Interestingly, when $\Delta M > 0$ ($dT/dH > 0$), the magnetocaloric effect is conventional, while it is inverse when $\Delta M < 0$ ($dT/dH < 0$) [24]. The second condition is satisfied when the magnetization of the low temperature phase is lower than the magnetization of the high-temperature phase. An interesting group of alloys in relation to the MCE is Ni-Mn based ferromagnetic Heusler alloys. Most of the Ni-Mn-Ga alloys show conventional MCE at martensitic transformation while Ni-Mn-Sn, Ni-Mn-In and Ni-Mn-In alloys show the inverse MCE at martensitic transformation [24].

1.4 Applications

Heusler alloys are emerging as promising materials for technical applications. The spectrum of their possible applications range from magnetic and magneto-mechanical materials over semiconductors and thermoelectrics to superconductors [10]. Spintronics, which uses the spin degrees of freedom, is currently attracting great interest due to a high potential for applications in magnetic sensors and other devices based on tunnel magnetoresistive effect [54]. Hence, the materials with a high degree of spin polarization at the E_F are needed to ensure high tunnel magnetoresistance ratio (TMR). The magnetic Heusler alloys with martensitic transition have excellent properties like large magnetic shape memory [43, 44, 46, 55], large magnetoresistance [56–61] and large magne-

totaloric effect [62–65]. They are capable of various applications like magnetic field induced Actuation, magnetomechanical sensing, magnetic refrigeration and energy harvesting [26]. Magnetic shape memory materials have recently been used as actuators to produce mechanical motion and force. Manufacturing automation, microsurgical instruments, micro-sensors [66], micro-actuators such as micro-valves [67], and stepper motors are potential application areas of magnetic shape memory actuators. These alloys also attract attention due to the tunability of their properties by substitution of atoms. The constituent elements are non-toxic and low cost.

1.5 Outline of thesis

The thesis focuses on the properties of Ni-Mn based Heusler alloys having martensitic transition from functional and fundamental point of view. The structural, magnetic, electrical, magneto-transport properties and electronic structure of off-stoichiometric Ni-Mn-Sn, Ni-Mn-In and Co substituted (at Ni site) Ni-Mn-In Heusler alloys are studied.

Chapter 2 describes the technical and theoretical aspects of various instruments and methods used for study of various properties. Starting from the sample preparation by arc melting technique and sample characterization techniques like, energy dispersive X-ray analysis (EDAX) for chemical quantification using scanning electron microscope (SEM), differential scanning calorimetry (DSC) to obtain the transition temperatures and X-ray diffraction (XRD) method for the crystal structure determination, are discussed. The measurements techniques like, four probe method for electrical transport, superconducting quantum interference device (SQUID) and vibrating sample magnetometer (VSM) methods for magnetization measurements are also discussed. The theory of photoelectron spectroscopy and experimental setup of photoelectron spectrometer are briefly discussed.

Chapter 3 presents EDAX, SEM, DSC and XRD results of off-stoichiometric Ni-Mn-Sn, Ni-Mn-In and Ni-Co-Mn-In alloys. The EDAX and SEM result shows that samples are in good quality and homogeneity in different parts of sample is within $\pm 3\%$. The room temperature crystal structure is obtained with the help of powder XRD.

Chapter 4 talks about the magnetic properties in the austenitic and martensitic phases of Ni-Mn-Sn, Ni-Mn-In and Ni-Co-Mn-In alloys. The change in the magnetic property as a function of temperature and Mn concentration is discussed. The effect of high magnetic field (upto 15 Tesla) on the martensitic transformation and magnetic state is studied in $\text{Ni}_2\text{Mn}_{1.6}\text{In}_{0.64}$ and $\text{Ni}_{1.81}\text{Co}_{0.22}\text{Mn}_{1.45}\text{In}_{0.52}$. The magnetocaloric effect is also explored in the Co doped Ni-Mn-In alloys.

Chapter 5 discusses the electrical transport property of Ni-Mn-Sn, Ni-Mn-In and Ni-Co-Mn-In alloys. The electrical resistivity behaviour as a function of temperature at high magnetic field (upto 8 Tesla) is explored. The effect of excess Mn concentration on the electrical resistivity is discussed. The chemical, structural and magnetic disorder effect in the martensitic phase is investigated. The resistivity data is fitted in the martensitic and austenitic phase to find out the contributions from different scattering mechanisms.

In **Chapter 6** longitudinal magnetoresistance (MR) behavior of Ni-Mn-Sn, Ni-Mn-In and Ni-Co-Mn-In alloys are studied as functions of temperature, magnetic field, and composition. Possible origin of large MR in the vicinity of martensitic transformation is discussed. The origin of MR below and above martensitic transition is understood through the experimental data fitting with magnetic field dependence H^n of MR. The analysis presents origin of MR in austenitic phase and martensitic phase. The MR is also explored with respect to field-cooled (FC) and zero-field-cooled (ZFC) state. The possible origin for different FC and ZFC MR is discussed.

Chapter 7 deals with electronic structure of Ni-Mn-Sn and Ni-Mn-In alloys by X-ray photoelectron spectroscopy (XPS) and ultraviolet photoelectron spectroscopy (UPS). The clean surface of Ni-Mn-Sn is prepared by scraping and surface composition is determined by XPS. The valence band and core-levels of Ni-Mn-Sn is studied as functions of temperature and composition by UPS and XPS. The change in the electronic structure upon the martensitic phase transition and within the martensitic phase is discussed. The clean surface of Ni-Mn-In is prepared by Ar ion (1.5 k eV) sputtering and annealing at various temperatures. The surface composition are studied at different annealing temperatures.

Bibliography

- [1] F. Heusler, *Verhandl. Deut. Physik. Ges.* **5**, 219 (1903).
- [2] A. D. Ross, and R. C. Gray, *Proc. Roy. Soc Edinburgh* **31**, 85 (1910).
- [3] E. Persson, *Naturewiss.* **16**, 613 (1928).
- [4] P. J. Webster, *Contemp. Phys.* **10**, 559 (1969).
- [5] H. H. Potter, *Proc. Phys. Soc.* **41**, 135 (1929).
- [6] A. J. Bradley and J. W. Rodgers, *Proc. R. Soc. A.* **144**, 340 (1934).
- [7] J. Dubowik, I. Gościańska, A. Szlaferek, and Y. V. Kudryavtsev, *Mater. Sci. (Poland)* **25**, 583 (2007).
- [8] A. Hamzic, R. Asomoza, and I. A. Campbell, *J. Phys. F: Metal Phys.* **11**, 1441 (1981).
- [9] J. Kübler, A. R. Williams, and C. B. Sommers, *Phys. Rev. B* **28**, 1745 (1983).
- [10] T. Graf, F. Casper, J. Winterlik, B. Balke, G. H. Fecher, and C. Felser, *Z. Anorg. Allg. Chem.* **635**, 976 (2009).
- [11] *Half-metallic Alloys. Fundamentals and Applications*, I. Galanakis, P. H. Dederichs (Eds.), Springer, Berlin, 2005, pp. 1-34.
- [12] R. A. de Groot, F. M. Mueller, P. G. van Engen, and K. H. J. Buschow, *Phys. Rev. Lett.* **50**, 2024 (1983).

- [13] S. Ishida, S. Akazawa, S. Fujii, S. Kashiwagi, and S. Asnjo, *J. Phys. Soc. Jpn.* **64**, 2152 (1995).
- [14] K. Otsuka and C.M. Wayman, *Shape Memory Materials*, Cambridge University Press, Cambridge, 1998, p. 1.
- [15] H. E. Karaca, Ph. D. thesis, "Effects of thermo-mechanical treatment on the shape memory behaviour of NiTi and CoNiAl alloys", 2003
- [16] *Shape Memory Alloys – Modeling and Engineering Applications* by Dimitris C. Lagoudas, Springer, 2008.
- [17] K. Bhattacharya, S. Conti, G. Zanzotto, and J. Zimmer, *Nature* **428**, 55 (2004)
- [18] V. A. Chernenko and V. A. L'vov, *Mat. Sci. Forum* **583**, 1 (2008).
- [19] H. D. Chopra, C. Ji, and V. V. Kokorin, *Phys. Rev. B* **61**, R14913 (2000).
- [20] L. J. Li, C. H. Lei, Y. C. Shu, and J.Y. Li, *Acta Mater.* **59**, 2648 (2011).
- [21] Y. Sutou, Y. Imano, N. Koeda, T. Omori, R. Kainuma, K. Ishida, and K. Oikawa, *Appl. Phys. Lett.* **85**, 4358 (2004).
- [22] P. J. Webster, K. R. A. Ziebeck, S. L. Town, and M. S. Peak, *Philos. Mag. B* **49**, 295 (1984).
- [23] P. J. Brown, A. P. Gandy, K. Ishida, R. Kainuma, T. Kanomata, K.-U. Neumann, K. Oikawa, B. Ouladdiaf, and K. R. A. Ziebeck, *J. Phys.: Condens. Matter* **18**, 2249 (2006).
- [24] A. Planes, L. Mañosa, and M. Acet, *J. Phys.: Condens. Matter* **21**, 233201 (2009).
- [25] V. K. Sharma, M. K. Chattopadhyay, and S. B. Roy, *Phys. Rev. B* **76**, 140401(R) (2007).
- [26] H. E. Karaca, I. Karaman, B. Basaran, Y. Ren, Y. I. Chumlyakov, and H. J. Maier, *Adv. Funct. Mater.* **19**, 983 (2009).

- [27] H. E. Karaca, I. Karaman, B. Basaran, D. C. Lagoudas, Y. I. Chumlyakov, and H. J. Maier, *Acta Mater.* **55**, 4253 (2007).
- [28] V. D. Buchelnikov, P. Entel, S. V. Taskaev, V. V. Sokolovskiy, A. Hucht, M. Ogura, H. Akai, M. E. Gruner, and S. K. Nayak, *Phys. Rev. B* **78**, 184427 (2008).
- [29] B. M. Wang, Y. Liu, L. Wang, S. L. Huang, Y. Zhao, Y. Yang, and H. Zhang, *J. Appl. Phys.* **104**, 043916 (2008).
- [30] T. Krenke, M. Acet, E.F. Wassermann, X. Moya, L. Mañosa, and A. Planes, *Phys. Rev. B* **72**, 014412 (2005).
- [31] T. Krenke, M. Acet, E. F. Wassermann, X. Moya, L. Mañosa, and A. Planes, *Phys. Rev. B* **73**, 174413 (2006).
- [32] S. Aksoy, O. Posth, M. Acet, R. Meckenstock, J. Lindner, M. Farle, and F. E. Wassermann, *J. Phys.: Conf. Ser.* **200**, 092001 (2010).
- [33] Z. Li, C. Jing, J. Chen, S. Yuan, S. Cao, and J. Zhang, *Appl. Phys. Lett.* **91**, 112505 (2007).
- [34] V. V. Khovaylo, T. Kanomata, T. Tanaka, M. Nakashima, Y. Amako, R. Kainuma, R. Y. Umetsu, H. Morito, and H. Miki, *Phys. Rev. B* **80**, 144409 (2009).
- [35] S. Chatterjee, S. Giri, S. K. De, and S. Majumdar, *Phys. Rev. B* **79**, 092410 (2009).
- [36] P. Entel, V. D. Buchelnikov, V. V. Khovailo, A. T. Zayak, W. A. Adeagbo, M. E. Gruner, H. C. Herper, and E. F. Wassermann, *J. Phys. D: Appl. Phys.* **39**, 865 (2006).
- [37] M. Ye, A. Kimura, Y. Miura, M. Shirai, Y. T. Cui, K. Shimada, H. Namatame, M. Taniguchi, S. Ueda, K. Kobayashi, R. Kainuma, T. Shishido, K. Fukushima, and T. Kanomata, *Phys. Rev. Lett.* **104**, 176401 (2010).
- [38] S. Fujii, S. Ishida, and S. Asano, *J. Phys. Soc. Jpn.* **58**, 3657 (1989).

- [39] C. P. Opeil, B. Mihaila, R. K. Schulze, L. Manósa, A. Planes, W. L. Hulst, R. A. Fisher, P. S. Riseborough, P. B. Littlewood, J. L. Smith, and J. C. Lashley, *Phys. Rev. Lett.* **100**, 165703 (2008).
- [40] S. R. Barman, S. Banik, and A. Chakrabarti, *Phys. Rev. B* **72**, 184410 (2005).
- [41] A. Chakrabarti, C. Biswas, S. Banik, R. S. Dhaka, A. K. Shukla, and S. R. Barman, *Phys. Rev. B* **72**, 073103 (2005).
- [42] K. Ullakko, J. K. Huang, V. V. Kokorin, and R. C. O’Handley, *Scripta Mater.* **36**, 1133 (1996).
- [43] A. Sozinov, A. A. Likhachev, N. Lanska, and K. Ullakko, *Appl. Phys. Lett.* **80**, 1746 (2002).
- [44] K. Ullakko, J. K. Huang, C. Kantner, R. C. O’Handley, and V. V. Kokorin, *Appl. Phys. Lett.* **69**, 1966 (1996).
- [45] H. E. Karaca, I. Karaman, B. Basaran, Y. I. Chumlyakov, and H. J. Maier, *Acta Mater.* **54**, 233 (2006).
- [46] V. A. Chernenko, *Adv. Mater. Res.* **52**, 3 (2008).
- [47] G. Kostorz and P. Müllner, *Z. Metallkunde* **96**, 703 (2005).
- [48] D. Y. Cong, P. Zetterström, Y. D. Wang, R. Delaplane, R. L. Peng, X. Zhao, and L. Zuo, *Appl. Phys. Lett.* **87**, 111906 (2005).
- [49] U. Gaitzsch, M. Pötschke, S. Roth, B. Rellinghaus, and L. Schultz, *Acta Mater.* **57**, 365 (2009).
- [50] M. E. Fisher and J. S. Langer, *Phys. Rev. Lett.* **20**, 665 (1968).
- [51] C. Biswas, R. Rawat, and S. R. Barman, *Appl. Phys. Lett.* **86**, 202508 (2005).
- [52] S. Banik, S. Singh, R. Rawat, P. K. Mukhopadhyay, B. L. Ahuja, A. M. Awasthi, S. R. Barman, and E. V. Sampathkumaran, *J. Appl. Phys.* **106**, 103919 (2009).

- [53] S. Banik, R. Rawat, P. K. Mukhopadhyay, B. L. Ahuja, A. Chakrabarti, P. L. Paulose, S. Singh, A. K. Singh, D. Pandey, and S. R. Barman, *Phys. Rev. B* **77**, 224417 (2008).
- [54] S. A. Wolf, D. D. Awschalom, R. A. Buhrman, J. M. Daughton, S. von Molnár, M. L. Roukes, A. Y. Chtchelkanova, and D. M. Treger, *Science* **294**, 1488 (2001).
- [55] R. Kainuma, Y. Imano, W. Ito, Y. Sutou, H. Morito, S. Okamoto, O. Kitakami, K. Oikawa, A. Fujita, T. Kanomata, and K. Ishida, *Nature (London)* **439**, 957 (2006).
- [56] S. Y. Yu, Z. H. Liu, G. D. Liu, J. L. Chen, Z. X. Cao, G. H. Wu, B. Zhang, and X. X. Zhang, *Appl. Phys. Lett.* **89**, 162503 (2006).
- [57] K. Koyama, H. Okada, K. Watanabe, T. Kanomata, R. Kainuma, K. Oikawa, W. Ito, and K. Ishida, *Appl. Phys. Lett.* **89**, 182510 (2006).
- [58] M. Khan, A. K. Pathak, M. R. Paudel, I. Dubenko, S. Stadler, and N. Ali, *J. Magn. Magn. Mater.* **320**, L21-L25 (2008).
- [59] S. Y. Yu, L. Ma, G. D. Liu, Z. H. Liu, J. L. Chen, Z. X. Cao, G. H. Wu, B. Zhang, and X. X. Zhang, *Appl. Phys. Lett.* **90**, 242501 (2007).
- [60] V. K. Sharma, M. K. Chattopadhyay, K. H. B. Shaeb, Anil Chouhan, and S. B. Roy, *Appl. Phys. Lett.* **89**, 222509 (2006).
- [61] A. K. Pathak, B. R. Gautam, I. Dubenko, M. Khan, and S. Stadler, *J. Appl. Phys.* **103**, 07F315 (2008).
- [62] T. Krenke, E. Duman, M. Acet, E. F. Wassermann, X. Moya, L. Mañosa, and A. Planes, *Nat. Mater.* **4**, 450 (2005).
- [63] Z. D. Han, D. H. Wang, C. L. Zhang, H. C. Xuan, B. X. Gu, and Y. W. Du, *Appl. Phys. Lett.* **90**, 042507 (2007).
- [64] V. K. Sharma, M. K. Chattopadhyay, and S. B. Roy, *J. Phys. D: Appl. Phys.* **40**, 1869 (2007).

- [65] B. Gao, F. X. Hu, J. Shen, J. Wang, J. R. Sun, and B. G. Shen, *J. Appl. Phys.* **105**, 083902 (2009).
- [66] V. O. Golub, A. Y. Vovk, L. Malkinski, C. J. O'Connor, Z. Wang, and J. Tang, *J. Appl. Phys.* **96**, 3865 (2004).
- [67] M. Kohl, Y. Liu, B. Krevet, S. Dürr and M. Ohtsuka, *J. Phys. IV (France)* **115**, 333 (2004).

Chapter 2

Experimental methods

2.1 Arc melting process

Polycrystalline samples are prepared by arc-melting technique in a tri-arc furnace. An arc furnace (Fig. 2.1) consists of a water-cooled cylindrical copper hearth that acts as the anode and also functions as a crucible for melting the samples. The water-cooled tungsten tip acts as the cathode. The appropriate amount of constituent elements is kept in the Cu crucible inside a close chamber. The air inside the chamber is evacuated out by a rotary pump followed by flushing of Ar gas through the chamber. This process is repeated 3 - 4 times in order to ensure the O₂ free environment inside the chamber. The arc is struck between the tungsten tip and the copper hearth, by allowing the cathode to touch the anode momentarily in presence of an Ar gas.

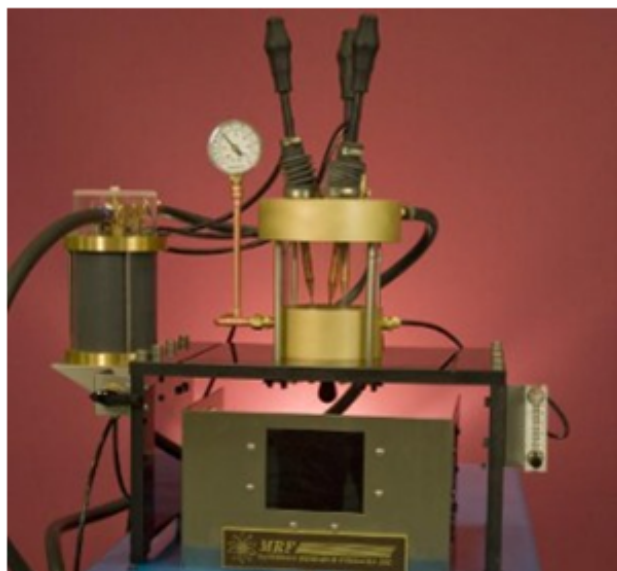


Figure 2.1 Tri-arc furnace setup.

2.2 Scanning electron microscope

The scanning electron microscope (SEM) is one of the important tools to get information about the surface topography of a sample. The schematic diagram of SEM is shown in Fig. 2.2. In SEM a high energy electron beam is focused on the sample surface. Upon the interaction of electron

beam with sample the back-scattered electrons, characteristic X-ray and secondary electrons are produced. The secondary electrons are generated when the incident electron beam, on passing

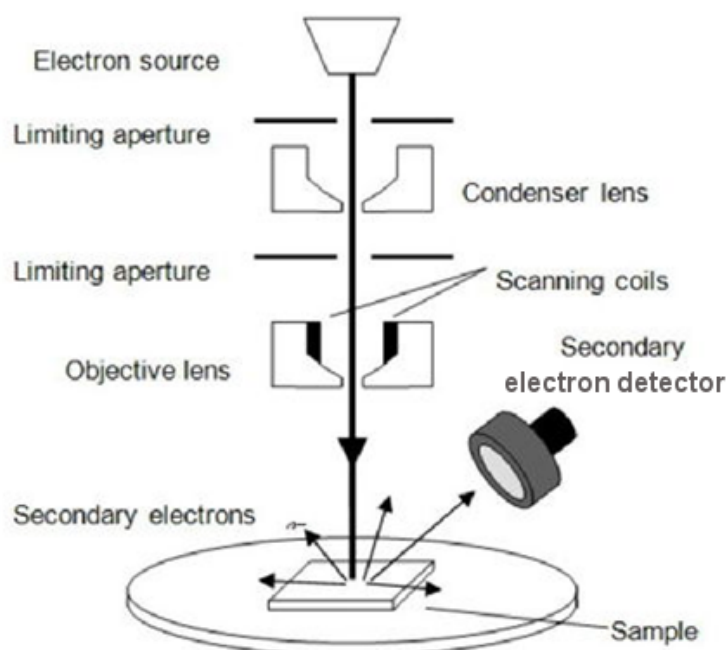


Figure 2.2 Schematic diagram of scanning electron microscope set-up (Source: <http://www2.warwick.ac.uk/fac/sci/physics/>).

through the atom, imparts some of its energy to the loosely bound electrons at the surface. These electrons leave the respective atom with very small kinetic energies and are termed as secondary electrons. Each incident electron can generate a large number of secondary electrons, whose intensity strongly depends on the topography of the sample surface. These secondary electrons are accelerated by a collector by applying a voltage to it, which then guides these electrons into the detector. By detecting the secondary electrons, surface topography is imaged.

2.3 Energy dispersive X-ray analysis

The energy dispersive X-ray analysis (EDAX) is an analytical technique used to probe the chemical composition as well as the degree of chemical homogeneity by detecting characteristic X-ray. The

sample is excited by high energy electron beam (20 - 30 keV) and the emitted characteristic X-rays is detected by an energy-dispersive spectrometer. The electron beam interaction with sample is shown in Fig. 2.3. The probed depth in EDAX analysis is around 1 - 3 μm . The EDAX is not a surface sensitive technique due to the large free mean path of the X-ray. Also the high energy electrons has large penetration depth. The composition obtained from these measurements have the maximum error within $\pm 5\%$.

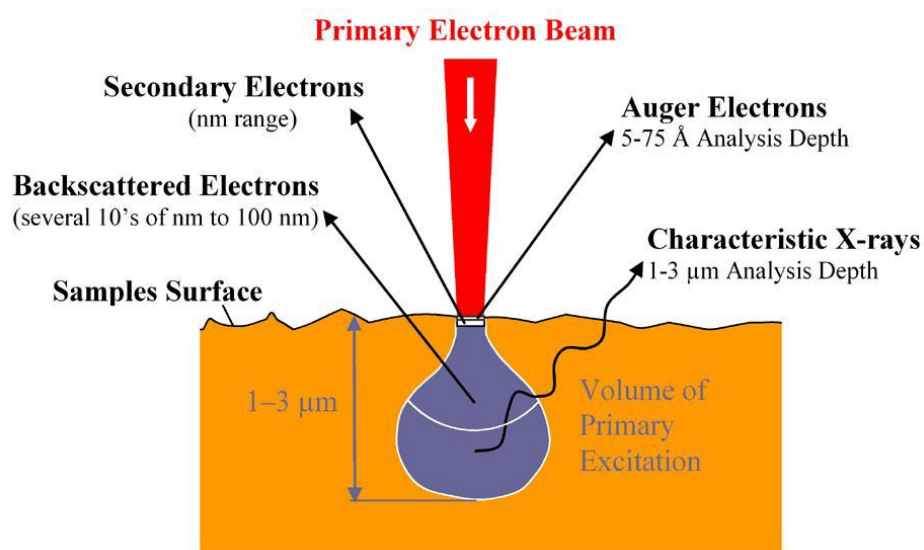


Figure 2.3 Diagram for electron beam interaction with sample (Source: <http://www.surfgroup.be/semedx>).

The SEM, Model No: FEI QUANTA 200 is used for chemical composition quantification in EDAX mode. For all the studied alloys chemical composition is determined both before and after annealing. The EDAX quantification at different parts of sample is performed at 10000x magnification. The actual composition is calculated by averaging the results obtained from different parts of sample.

2.4 Differential scanning calorimetry

After determining the alloy composition, their transition temperatures are determined by differential scanning calorimetry (DSC). It measures the heat flow associated with various transitions in the material as a function of time and temperature in a controlled atmosphere. It provides quantitative and qualitative information about physical and chemical changes in material that involve endothermic or exothermic processes, or change in heat capacity. A differential calorimeter measures a heat of a sample relative to a reference. The simple DSC set up is shown in Fig. 2.4. Inside the oven there are two mountings, the sample pan and reference pan. The sample and reference pans

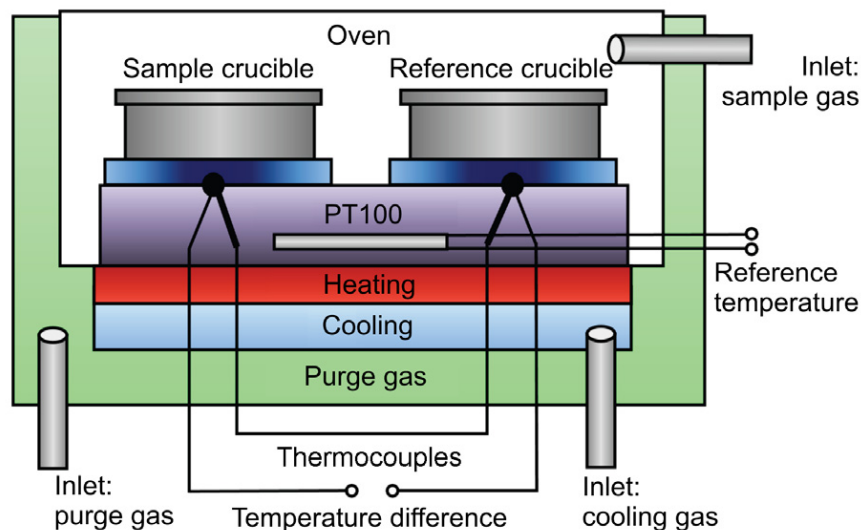


Figure 2.4 Schematic set up of differential scanning calorimeter [1].

are heated by separate heaters. The sample and reference are maintained at the same temperature, and the difference in thermal power required to maintain them at the same temperature is measured and plotted as a function of temperature or time. The difference in the input energy required to match the temperature of the sample to that of the reference would be the amount of excess heat absorbed or released by the molecule in the sample during an endothermic or exothermic process, respectively [2]. Thus by observing the difference in heat required to match the same temperature between the sample and reference, differential scanning calorimeters are able to measure the temperatures of various phase transitions. The differential scanning calorimeter Q 2000 of TA

instruments is used for the measurement of structural and magnetic transitions.

2.5 X-ray diffraction

The X-ray diffraction (XRD) is one of the basic tools to find out the crystal structure of material. To get the crystallographic information the wavelength (λ) should be of the order of atomic spacing. When the material is shined with X-ray, it gives rise to scattering in all directions. Most of these scattered wave cancel each other by destructive interference. They add constructively in a specific direction. The constructive interference occurs whenever the Bragg law, $n\lambda = 2d \sin \theta$, is satisfied [3], where λ is the wavelength of incident radiation, d is the spacing between the atomic planes of the solid, θ is the Bragg angle and n is the order of diffraction. Fig 2.5 shows the schematic of Bragg diffraction condition. The powder method is used for polycrystalline material. The material to be examined is reduced to very fine powder and placed in a beam of monochromatic X-rays. Each particle of the powder is a tiny crystal oriented at random direction with respect to the incident beam. Due to the random orientation of the particles Bragg reflection condition is satisfied for all the lattice planes. Thus every set of lattice reflections obtained with relative intensity. The

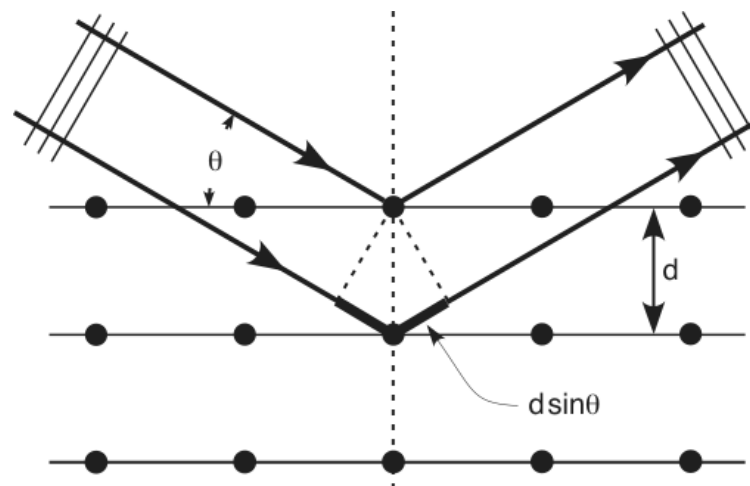


Figure 2.5 Schematic of Bragg diffraction condition (Source: http://en.wikipedia.org/wiki/X-ray_crystallography).

diffractometer is used in $\theta - \theta$ and $\theta - 2\theta$ geometries [4]. In $\theta - \theta$ geometry sample is fixed

and both x-ray source and detector move at the same angular rate ω toward each other. In $\theta - 2\theta$ geometry the source does not move, the sample rotates around its axis at a speed ω , whereas the detector is moving at a speed 2ω along the circle, centered on the sample. The PANalytical XPERT PRO XRD unit is used for measurement. The room temperature XRD pattern is recorded using $\text{CuK}\alpha$ radiation.

2.6 Four probe method

The resistivity and magnetoresistance measurements were performed by the conventional four-probe method in the presence of helium exchange gas. In the four probe method four equidistant contacts (probes) are made in a rectangular slab of sample as shown in the Fig. 2.6. A current

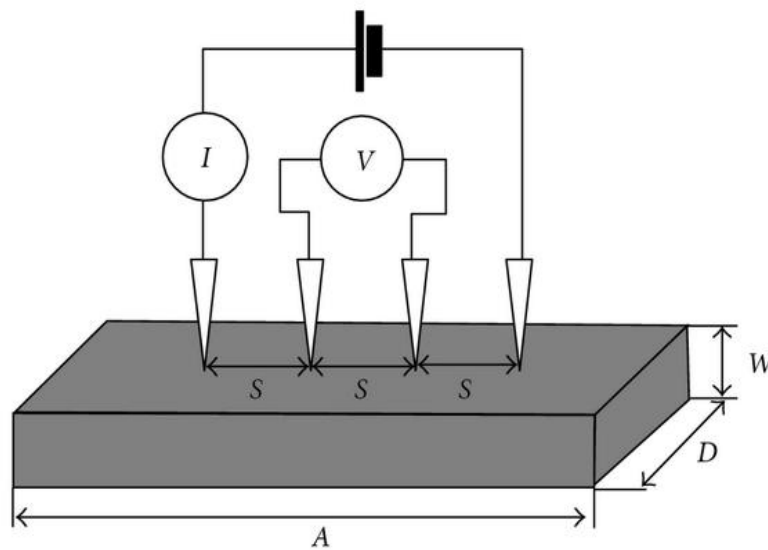


Figure 2.6 Schematic arrangement of four probe on rectangular slab [5].

(I) is passed through the outer probes and induces a voltage (V) in the inner voltage probes. The measured resistance (V/I) is converted to resistivity ($\Omega\cdot\text{cm}$). The use of separate current and voltage probe reduces problem with contact resistance. The resistivity is calculated using equation [6]

$$\rho = (V/I) \cdot W \cdot C(A/D, D/S) \cdot F(W/S) \quad (2.1)$$

where, V is voltage in the inner voltage probes, I is current in the outer voltage probes, W is the thickness of sample, D is the width of the sample, A is the length of the sample, S is the spacing between the voltage probes. $C(A/D, D/S)$ is the finite width correction and $F(W/S)$ is the finite thickness correction. The values of $C(A/D, D/S)$ and $F(W/S)$ were taken as evaluated by Smits [6].

2.7 Vibrating sample magnetometer

A Vibrating sample magnetometer (VSM) operates on Faraday's Law of Induction, which tells us that a changing magnetic flux will induce a voltage in a pickup coil. The direction of the induced current is given by Lenz's law. The time dependent voltage thus induced $V_{induced}$ is given as:

$$V_{induced} = \frac{\Delta\phi}{\Delta t} \quad (2.2)$$

$$= \left(\frac{\Delta\phi}{\Delta z}\right)\left(\frac{\Delta z}{\Delta t}\right) \quad (2.3)$$

where, ϕ represents the magnetic flux; the axis of oscillation of the sample is conventionally chosen to be along the z -axis, the " z " therefore represents the position of the sample along this axis. If the sample is made to oscillate sinusoidally, then the induced voltage in the pickup coil will have the form:

$$V_{induced} = cmA\omega \text{Sin}\omega t \quad (2.4)$$

where, " c " is a coupling constant, " m " is the DC magnetic moment of the sample, " A " is the amplitude of oscillation, and $\omega = 2\pi f$ where, " f " is the frequency of oscillation of the sample. The measurements are most reliable if the oscillations are performed exactly midway between the pickup coil pair. The centering of the sample must be within 0.1 mm to be able to achieve the rated accuracy of 10^{-6} emu. The position of the sample with respect to the detection coils must be known accurately for the accurate determination of the magnetic moment. A schematic diagram of a VSM is shown in Fig. 2.7. The sample (S) is mounted on the tip of a glass rod using Teflon tape, which is then placed in the VSM. The sample is centrally located between, stationary pick-up coils and oscillated vertically in a uniform magnetic field. At the upper end of the glass rod there is a

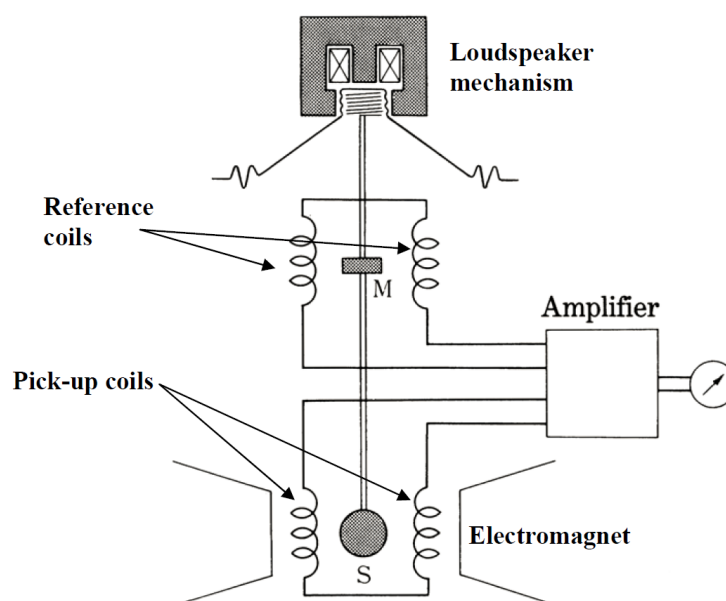


Figure 2.7 Vibrating sample magnetometer [7].

reference in the form of a small permanent magnet (M) situated between a set of reference coils. The AC signal induced in the pick-up coil by the magnetic field of the sample is compared with the signal from a standard magnet M and is converted to a number proportional to the magnetic moment.

Two different commercial VSM is used for the dc magnetization measurements of the present samples. The VSM from Lake Shore upto 1.6 Tesla magnetic field is used in the temperature range 80 - 400 K. The quantum design PPMS in VSM mode upto 14 Tesla magnetic field is used in the temperature range 4 - 400 K.

2.8 Superconducting quantum interference device (SQUID)

The SQUID is a very sensitive magnetometer used to measure extremely low magnetic fields. The SQUID operate on the principle of flux quantization. In its simplest form, a SQUID consists of a superconducting ring interrupted by two Josephson junctions. When two superconductors are separated by a sufficiently thin insulating barrier, it is possible for a current to flow from one to

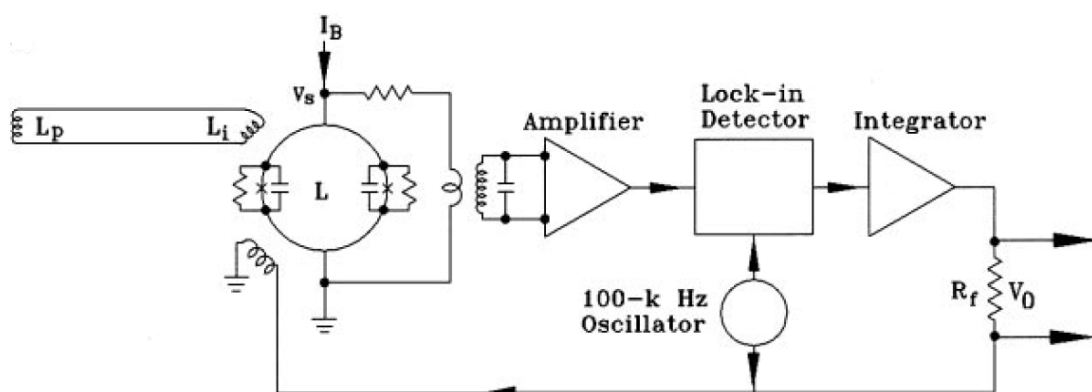


Figure 2.8 A simplified circuit for a dc SQUID magnetometer [8].

the other, even with no voltage applied between them. The maximum zero-voltage current (the critical current) of the dc SQUID varies sinusoidally with the integral of the magnetic field through the area of the SQUID loop owing to interference of the quantum phases of the two junctions. If field is applied so that external flux enters the loop, then the loop must compensate by generating a circulating current to maintain the flux quantization condition. This circulating current will cause one of the Josephson junctions to exceed its critical current, and a voltage, V_S , will develop across the SQUID. The period of modulation is the superconducting flux quantum. With flux modulation, phase-sensitive detection, and flux feedback (Fig. 2.8), this phase can be measured to a few parts per million with a one-second time integration [8]. This makes the SQUID the most sensitive sensor of magnetic fields known. The quantum design SQUID magnetometer is used in the temperature range 5 - 300 K for the magnetization measurement as a function of temperature.

2.9 Photoelectron spectroscopy

The Photoelectron spectroscopy (PES) is a very powerful and well established tool to investigate the electronic structure of solids by probing the occupied electronic states. PES is based on the photoelectric effect. It involves the irradiation of a sample with electromagnetic radiation and the energy analysis of photoelectrons which are generated close to the sample surface. A photon absorbed by the atom or solid excites an electron from the initial electron state to a final electron

state inside the crystal. The photoexcited electron transports through the solid to the surface and is transmitted out of the solid into the vacuum if the kinetic energy of the photoelectron is more than the work function of the solid. The photoelectron distribution curve represents the occupied density of electronic states. When photons in the ultraviolet (UV) spectral range are used, the technique is called ultraviolet photoelectron spectroscopy (UPS), and that with X-ray radiation, it is called X-ray photoelectron spectroscopy (XPS). The ultraviolet photoelectron spectroscopic method is used mainly for the study of valence electron density of states with high resolution. Using XPS, the deeper core-levels could be studied, which can reveal the information on the relative abundance of specific atoms and their chemical environment.

2.9.1 Theory of photoemission

In a PES experiment, the photo-current results from the excitation of an electron by the electromagnetic field from the initial state i (wave function Ψ_i) to the final state f (wave function Ψ_f). The transition probability between the initial $|\Psi_i(N)\rangle$ and the final state $|\Psi_f(N)\rangle$ of an N -electron system is governed by Fermi golden rule and is given by the following formula

$$\begin{aligned} w_{fi} &= \frac{2\pi}{\hbar} |\langle \Psi_f(N) | \Delta | \Psi_i(N) \rangle|^2 \delta[E_f(N) - E_i(N) - h\nu] \\ &= \frac{2\pi}{\hbar} m_{fi} \delta[E_f(N) - E_i(N) - h\nu] \end{aligned} \quad (2.5)$$

where, m_{fi} is the square of the transition matrix element of the perturbation, $E_f(N)$ and $E_i(N)$ denote the energies of the final and initial states, respectively, and $h\nu$ is the photon energy. The delta function ensures the energy conservation during the excitation process. The perturbation Hamiltonian Δ is given by

$$\Delta = \frac{e}{2mc} (A \cdot p + p \cdot A) \quad (2.6)$$

where, e and m refer to the charge and the mass of the electron, c denotes the speed of light, A is the vector potential of the incident radiation and p is the momentum operator ($-i\hbar\nabla$) of the

electron. $\nabla \cdot \mathbf{A}$ is generally taken to be zero because the wavelength of the incident radiation is greater than the lattice constant. Thus, by using Eq. 2.6, the matrix element appearing in Eq. 2.5 is proportional to

$$m_{fi} = A_0 \cdot \langle \Psi^f(N) | \nabla V | \Psi^i(N) \rangle \quad (2.7)$$

where V is the potential felt by the electrons. $\nabla V = 0$ inside a free electron metal. Thus, photoemission from inside a free electron metal is not possible. The only region from where electrons could be photoexcited is at the surface where $\nabla V \neq 0$, and this is known as the surface photoeffect.

The absorption of a photon with energy $h\nu$ causes the excitation of an N -electron system, with above transition probability (Eq. 2.7) into a final state ion characterized by $\Psi_f(N-1, k)$ with the total energy $E_f(N-1, k)$ plus a photoelectron with $\Psi_f(1)$ (one electron orbital) and kinetic energy E_{kin} ; k denotes the initial level from which the electron was removed. It is assumed that the ejected photoelectron is weakly coupled to the $(N-1)$ electron system [9] left behind (the so called sudden approximation) and the photo excitation process can be written as

$$\Psi_i(N), E_i(N) \xrightarrow{h\nu} \Psi_f(N-1, k), E_f(N-1, k) + \Psi_f(1), E_{kin} \quad (2.8)$$

The conservation of energy is described by the following equation

$$E_i(N) + h\nu = E_f(N-1, k) + E_{kin} \quad (2.9)$$

and the binding energy with respect to the vacuum level is expressed as

$$E_B^V(k) = E_f(N-1, k) - E_i(N) = h\nu - E_{kin} \quad (2.10)$$

If it is assumed that the remaining $(N-1)$ electrons have the same spatial distributions and energies in the final state as they had in the initial state before the emission of the electron, then the binding energy equals the negative orbital energy of the emitted electron.

$$E_B^V(k) = -\epsilon_k \quad (2.11)$$

This approximation is the Koopman's Theorem [10]. Since in solid the BE is referred with respect to the Fermi level, the BE is given by

$$E_B^V(k) = h\nu - E_{kin} - \phi \quad (2.12)$$

where, $E_B^V(k)$ is given by Koopman's orbital energy ($-\epsilon_k$) of the k^{th} electron and ϕ is the work function.

2.9.2 Experimental setup

The photoelectron spectrometer consists mainly of three sections, a vacuum system, a source of the primary beam (X-ray, UV) and electron energy analyser with detection system. The typical experimental configuration for photoelectron spectrometer and photoemission curve is depicted in Fig. 2.9.

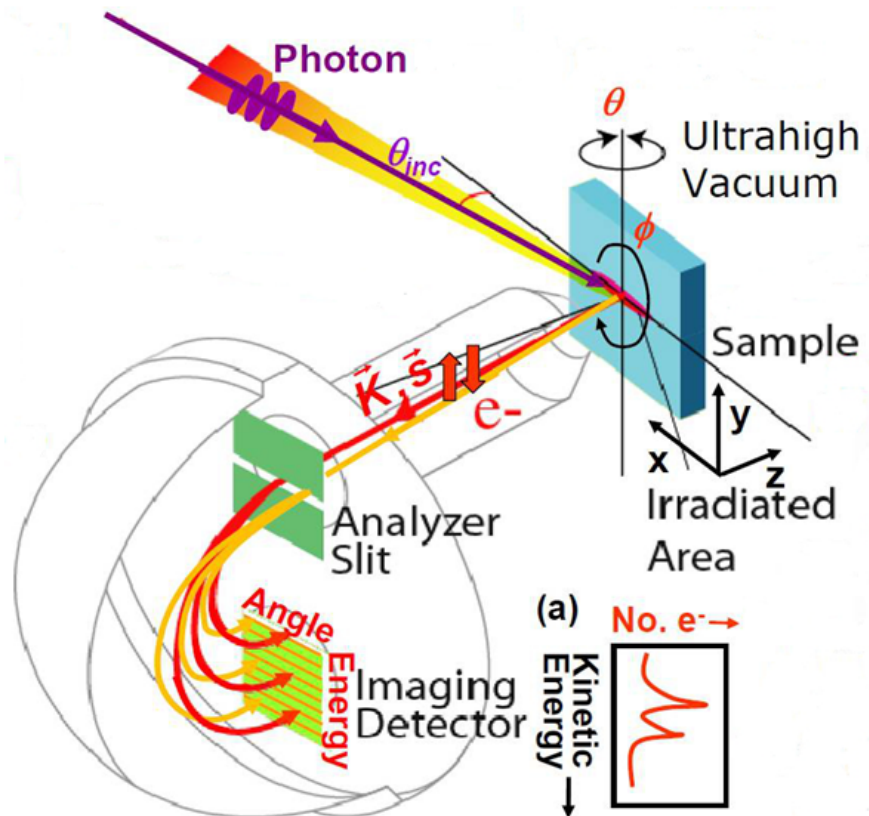


Figure 2.9 Illustration of a typical experimental configuration for photoemission experiments, including (a) simple spectra or energy-distribution curve [11].

In order to get information about the energy of the electron inside the solid, it is necessary that the electron should come out of solid surface without any change in the energy due to inelastic

collisions. The large number of electrons, which undergo inelastic scattering processes, form the secondary electrons background in a photoemission spectrum. Since the escape depth of electron is limited by inelastic scattering the PES is very surface sensitive techniques [12–15]. An important

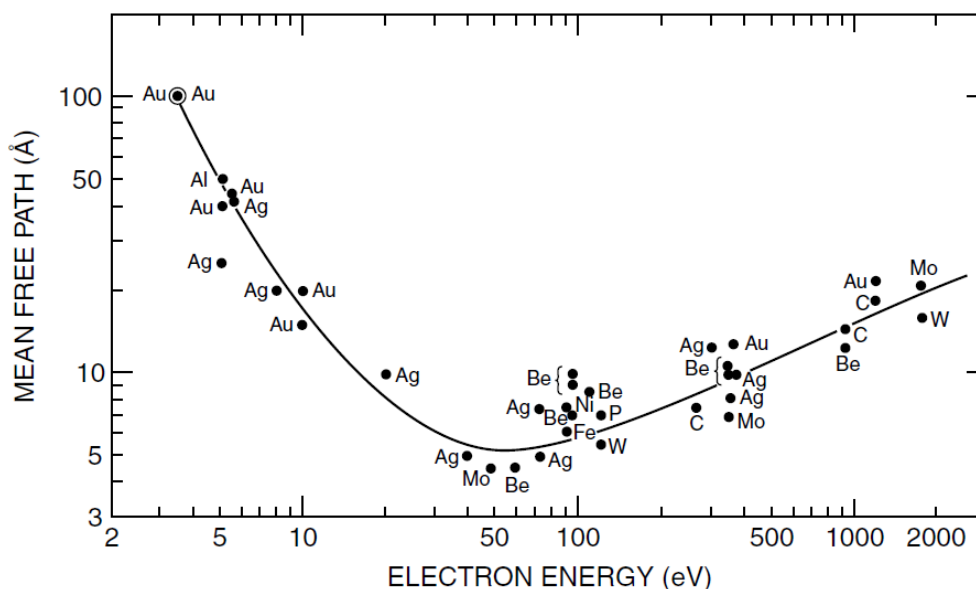


Figure 2.10 Universal curve of escape depth as a function of E_{kin} [15].

parameter to describe the surface sensitivity is the mean escape depth (λ), which is identical to the mean free path of a photoelectron in a solid. The so-called universal curve in Fig. 2.10 shows λ as function of E_{kin} . The electron escape depth is only in the order of few Å. The minimum in mean free path (≈ 5 Å) is around 50 eV and above that the mean free path follows the $E^{1/2}$ behavior. It increases to about 20 Å for electron energies of 10 and 1400 eV. At low energies below 50 eV it deviates from the square root behavior since in this range the probability of inelastic scattering decreases. The electrons have insufficient energy to excite plasmons (the main inelastic scattering mechanism in metals) [16]. Thus, the electron can come out from a depth of ≈ 20 Å without undergoing any further collision.

Ultra-high vacuum

Due to the surface sensitivity of PES technique the experiments are performed under ultra-high vacuum (UHV) [17]. To achieve ultra high vacuum (10^{-9} mbar - 10^{-11} mbar) several types of pumps are used.

(a) Turbomolecular pump backed by rotary pump: The turbomolecular pump exploits the interaction of gas molecules with very fast moving solid surface that add a directed component to their motion and transfer them to an outlet [18]. Most turbomolecular pumps employ multiple

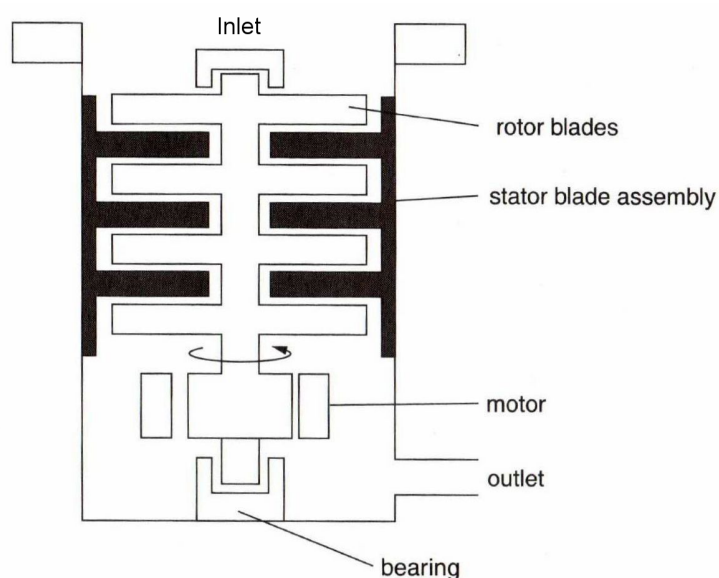


Figure 2.11 Schematic of a turbomolecular pump [18].

stages consisting of rotor and stator pairs each with multiple and angled blades mounted in series (Fig. 2.11). Gas captured by the upper stages is pushed into the lower stages and successively compressed to the level of the fore-vacuum (backing pump) pressure. As the gas molecules enter through the inlet, the rotor, which has a number of angled blades, hits the molecules. Thus the mechanical energy of the blades is transferred to the gas molecules. With this newly acquired momentum, the gas molecules enter into the gas transfer holes in the stator. This leads them to the next stage where they again collide with the rotor surface, and this process is continued, finally leading them outwards through the exhaust. All gases are pumped at roughly the same rate.

Turbomolecular pumps are suitable for generating vacuum in the range of 10^{-2} mbar to 10^{-10} mbar.

(b) Ionization pump: An ionization pump (also referred to as a sputter ion pump) is capable of reaching pressures as low as 10^{-11} mbar under ideal conditions. A sputter-ion pump consists basically of two electrodes, anode and cathode, and a magnet. The anode is usually cylindrical and made of stainless steel [18]. The cathode plates positioned on both sides of the anode tube are made of titanium, which serves as the gettering material. The magnetic field is orientated along the axis of the anode. Electrons are emitted from the cathode due to the action of an electric field. Due to the presence of the magnetic field, they move in long helical trajectories which improves the chances of collision with the gas molecules. These electrons ionize gas within the chamber. The positive ions are accelerated towards cathode by electrical potential, typically 3kV to 7kV, which allows the ions to be captured by a solid electrode. Ionization pump are not suitable for pumping inert gases. The operating pressure range is 10^{-4} mbar to 10^{-11} mbar.

(c) Titanium sublimation pump: It consists of a titanium filament through which a high current (typically around 40 Amps) is passed periodically. This current causes the filament to reach the sublimation temperature of titanium, and hence the surrounding chamber walls become coated with a thin film of clean titanium. Since clean titanium is very reactive, components of the residual gas in the chamber which collide with the chamber wall are likely to react and to form a stable, solid product. Thus the gas pressure in the chamber is reduced. The freshly deposited titanium has highly reactive surface and captures most of gases except He, Ar and other chemically inert gases including methane. The surface onto which titanium is deposited are chilled to improve the capture rate, and they also provide shield to prevent it from reaching inappropriate parts of the system [18]. The suitable operating pressure range is 10^{-5} mbar to 10^{-11} mbar.

Measurement of ultra-high vacuum

The ultra-high vacuum is measured with help of ionization gauge. The hot cathode ionization gauge is most commonly used. Schematic of a hot cathode ionization gauge is shown in Fig. 2.12. A current of electrons released thermionically from a filament is accelerated to ionize the gas

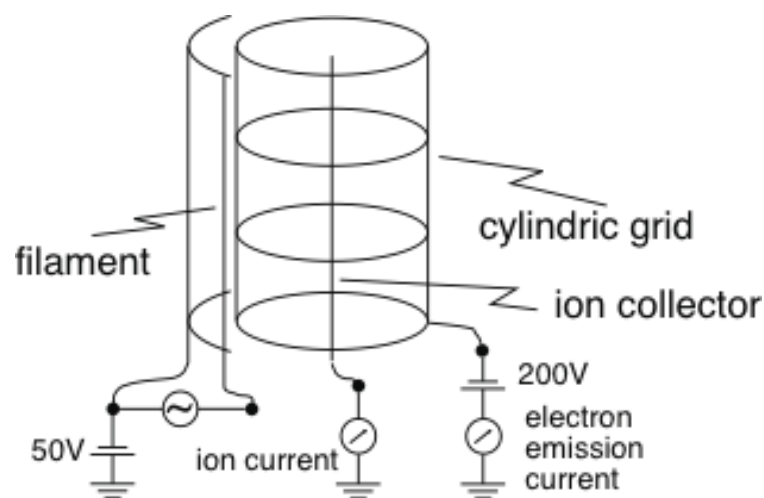


Figure 2.12 Schematic of a hot cathode ionization gauge (Source: <http://philiphofmann.net/>).

molecule inside grid, creating positive ions. The rate of ionization is proportional to the number density of molecules and hence the pressure. The current of ions thus generated is collected by collector. The measured collector current is a parameter for pressure. The ion gauge is used for measuring pressure between 10^{-4} mbar and 10^{-11} mbar.

Photon source

The photon sources used for PES measurements are AlK_{α} (1486.6eV), MgK_{α} (1253.6eV), He I (21.2 eV) and He II (40.8 eV). For core level studies of $\text{Ni}_2\text{Mn}_{1+x}\text{Sn}_{1-x}$ and $\text{Ni}_2\text{Mn}_{1+x}\text{In}_{1-x}$ alloys, AlK_{α} (monochromatic) and MgK_{α} (non-monochromatic) radiations are used, respectively. X-rays are generated by bombarding a target (anode) with high energy electrons from a heated filament. The X-ray source consists of a cathode (filament), which emits thermal electrons through heating (usual emission current of about 30 mA), and an anode to which the electrons are accelerated by applying a high voltage of typically 9 kV to 15 kV. The non-monochromatized X-rays are dominated by very intense $\text{K}_{\alpha 1}$ and $\text{K}_{\alpha 2}$ doublets resulting from X-ray emission from the $2p_{3/2} \rightarrow 1s$ and $2p_{1/2} \rightarrow 1s$ transitions, respectively. There are also weaker characteristic lines (or satellites) resulting from similar transitions within the multiply ionised atom (e.g. $\text{K}_{\alpha 3}$, $\text{K}_{\alpha 4}$) and from valence band $\rightarrow 1s$ transitions (K_{β}). The natural line width of the K_{α} (0.85 eV for

AlK_α and 0.7 eV for MgK_α) limits the spectrometer resolution [19]. The X-ray radiations are monochromatized by means of a quartz crystal monochromator; this results in the elimination of the Bremsstrahlung, satellite and ghost radiation and allows the characteristic X-ray linewidth to be reduced below 0.3 eV.

To study the valence electronic structure (outermost less tightly bound electrons), higher energy resolution and higher photon flux are required. The high intensity photon source based on He plasma, generated with the electron cyclotron resonance (ECR) technique is used as UV source to study the valence band of $\text{Ni}_2\text{Mn}_{1+x}\text{Sn}_{1-x}$. A microwave generator is coupled to a small discharge cavity in a magnetic field tuned to the microwave frequency to meet the ECR condition. The microwave generator is based on a klystron which works by shooting an electron beam through a sequence of resonator cavities. The photon flux is much higher than that from conventional discharge UV sources. The source line width obtained is approximately 1 meV. The He gas discharge lamp is used as UV source to study the valence band of $\text{Ni}_2\text{Mn}_{1+x}\text{In}_{1-x}$. The Helium lamp provides photon energies of 21.2 eV (He I) and 40.8 eV (He II), which corresponds to ($1^1\text{S}2^1\text{P} \rightarrow 1^2\text{S}$) and ($2^1\text{P} \rightarrow 1^1\text{S}$) transitions in para Helium, respectively [20, 21]. The He gas maintained at a pressure of about 1.5×10^{-6} mbar in the UHV chamber. The discharge is produced by applying a high voltage of the order 1.5 kV. The radiation is incident on the sample through a long quartz capillary tube and a spot size of 2-3 mm diameter is obtained. The predominance of the photon energies (i.e. whether 21.2 or 40.8 eV) depends on the pressure of the helium gas. From an arc discharge, that is trapped in a quartz capillary, the radiation is led along a windowless path by differentially pumped pressure stages into an UHV analysis chamber. The source width obtained with this UPS lamp is about 5 - 6 meV.

Electron energy analyser

A hemispherical high-resolution electron energy analyzer (Scienta R4000) of 200 mm radius is used for recording the photoelectron spectra of $\text{Ni}_2\text{Mn}_{1+x}\text{Sn}_{1-x}$. Another hemispherical electron energy analyzer (Phoibos 100 from Specs GmbH, Germany) of 100 mm mean radius is used for recording the photoelectron spectra of $\text{Ni}_2\text{Mn}_{1+x}\text{In}_{1-x}$. The hemispherical analyzer consists of a

multi element electrostatic lens system and a hemispherical deflector with entrance (S_1) and exit (S_2) slits. The role of the electrostatic lenses is to decelerate and focus the photoelectrons since kinetic energy of the electrons ejected from the sample is usually too high for the analyser to produce sufficiently high resolution. The electrons then are focused onto the input slit S_1 of the hemispherical deflector for subsequent energy analysis.

The hemispherical deflector consists of two concentric electrostatic hemispheres of radius R_{out} (outer) and R_{in} (inner). Negative potentials V_{in} and V_{out} are applied to the inner and outer hemispheres, respectively, with V_{out} greater than V_{in} . The median equipotential surface between the hemispheres has radius $R_0 = (R_{out} + R_{in})/2$. The hemispheres are kept at a potential difference ($V_{out} - V_{in}$), such that only the electrons reaching the entrance slit with a particular kinetic energy centered at the pass energy (E_p) will pass through the mean radius of hemisphere and reaches the exit slit and the detector. The nominal pass energy is given as $E_p = -ek\Delta V$, e is charge of electron, ΔV is the potential difference ($V_{out} - V_{in}$) applied to the hemispheres, k is the calibration constant for the analyzer. The analyzer resolution (ΔE_a) is given as

$$\frac{\Delta E_a}{E_p} = \frac{S}{2R_0} + \frac{\alpha^2}{4} \quad (2.13)$$

where $S = (S_1 + S_2)/2$, S_1 and S_2 are width of slits, and α is the angular acceptance of the electron beam at the entrance slit. Thus, radii of the hemisphere and the slit width are important parameters in determining the resolution of an electron energy analyzer.

The peak width defined as the FWHM depends on the overall resolution of spectrometer. The overall resolution (ΔE) of the spectrometer is given as [19]

$$\Delta E = \sqrt{\Delta E_n^2 + \Delta E_p^2 + \Delta E_a^2} \quad (2.14)$$

where ΔE_n is the natural or inherent width of the core level, ΔE_p is the width of the photon source (X-ray line) and ΔE_a is the analyser resolution. The overall resolution of monochromatic AlK_α and He I with Scienta R4000 analyzer is 0.42 eV and 1.5 meV, respectively. The overall resolution of MgK_α and He I with Phoibos 100 analyzer is 0.9 eV and 100 meV, respectively.

The analyzer lens system and the hemisphere should be shielded from the external magnetic field such that the electrons entering the analyzer are not deflected from their path. For this purpose μ -metal (Ni 77%, Fe 18%, Cu 5%, and Cr 2%) shielding is provided since μ -metal has very high magnetic permeability (100,000 - 375,000).

Bibliography

- [1] Applications of Calorimetry in a Wide Context - Differential Scanning Calorimetry, Isothermal Titration Calorimetry and Microcalorimetry (Chapter 12) Edited by Amal Ali Elkordy, InTech (2013).
- [2] P. Gill, T. T. Moghadam, and B. Ranjbar, *J. Biom. Tech.* **21**, 167 (2010).
- [3] Elements of X-ray Diffraction by B D Cullity, Addison-Wesley Publishing Company, Inc. (1978).
- [4] X-ray Diffraction by Polycrystalline Materials by René Guinebretière, ISTE Ltd. (15 March 2007).
- [5] S. Ummartyotin, J. Juntaro, C. Wu, M. Sain, and H. Manuspiya, *J. Nanomater.* **2011**, 606714 (2011).
- [6] F. M. Smits, *The Bell System Technical Journal* **37**, 711 (1958).
- [7] Physics of Ferromagnetism by Soshin Chikazumi, Second Edition, Oxford University Press (2005).
- [8] John R. Kirtley and John P. Wikswo Jr., *Annu. Rev. Mater. Sci.* **29**, 117 (1999).
- [9] G. Borstel, *Applied Physics A* **38**, 204 (1985).
- [10] T. Koopmans, *Physica* **1**, 104 (1933).

-
- [11] C. S. Fadley, *Surf. Interface Anal.* **40**, 1579 (2008).
- [12] *Photoemission in Solids I: General Principles* by M. Cardona and L. Ley, Springer-Verlag Berlin (1978).
- [13] *Practical Surface Analysis Volume I: Auger and X-ray Photoelectron Spectroscopy* by D. Briggs and M. P. Seah, Second edition, John Wiley and Sons Ltd. (1990).
- [14] *Photoelectron Spectroscopy: Principles and Applications* by S. Hufner, Second Edition, Springer-Verlag Berlin (1995).
- [15] *Physics at Surfaces* by A. Zangwill, Cambridge University Press (1992).
- [16] M. P. Seah and W. A. Dench, *Surf. Interface Anal.* **1**, 2 (1979).
- [17] *Introduction Surface Analysis by XPS And AES* by John F. Watts and John Wolstenholme, John Wiley and Sons, Ltd. (2003).
- [18] *Modern Vacuum Physics (Masters Series in Physics and Astronomy)* by A. Chambers, Chapman & Hall/CRC (2005).
- [19] *Surface analysis of polymers by XPS and static SIMS* by D. Briggs, Cambridge University Press (2005).
- [20] *Techniques of Vacuum Ultraviolet Spectroscopy* by J. A. R. Samson, John Wiley and Sons, Inc (1967).
- [21] *Physics of atoms and molecules* by B. H. Bransden and C. J. Joachain, Longman, England (1986).

Chapter 3

Heusler alloy preparation and characterization

3.1 Sample preparation

Off-stoichiometric Heusler alloys of $\text{Ni}_2\text{Mn}_{1+x}\text{Sn}_{1-x}$, $\text{Ni}_2\text{Mn}_{1+x}\text{In}_{1-x}$ and $\text{Ni}_{1.8}\text{Co}_{0.2}\text{Mn}_{1+x}\text{In}_{1-x}$ were prepared from high purity ($\geq 99.99\%$) constituent elements. The appropriate amount of constituent elements were measured by chemical balance within the accuracy of ± 0.1 mg. The polycrystalline ingot of alloys (approximately 3 g) were prepared using arc-melting furnace under argon atmosphere in a water cooled Cu crucible. The melting process was repeated 6 - 8 times to obtain homogeneous compositions. Later samples were wrapped in Mo foil and encapsulated in a vacuum sealed quartz ampoules under $3 - 4 \times 10^{-6}$ mbar vacuum. The sealed ingots were then annealed at 1173 K for 24 hours followed by quenching in ice-water. The alloys are cut afterwards in an appropriate size for various characterization and measurements.

3.2 Chemical composition

The Table 3.1, 3.2 and 3.3 shows the intended and actual composition obtained from energy dispersive X-ray analysis (EDAX) for $\text{Ni}_2\text{Mn}_{1+x}\text{Sn}_{1-x}$, $\text{Ni}_2\text{Mn}_{1+x}\text{In}_{1-x}$ and $\text{Ni}_{1.8}\text{Co}_{0.2}\text{Mn}_{1+x}\text{In}_{1-x}$ alloys, respectively. The actual composition is obtained by averaging the EDAX results from different parts of the alloy. From the tables it is clear that the actual composition is within $\pm 1\%$ of intended composition. The homogeneity in different parts of the sample is within $\pm 3\%$.

Table 3.1 Actual and intended composition of $\text{Ni}_2\text{Mn}_{1+x}\text{Sn}_{1-x}$ deduced from EDAX.

x	Intended composition	Actual composition
0.40	$\text{Ni}_2\text{Mn}_{1.40}\text{Sn}_{0.60}$	$\text{Ni}_{2.02}\text{Mn}_{1.37}\text{Sn}_{0.61}$
0.44	$\text{Ni}_2\text{Mn}_{1.44}\text{Sn}_{0.56}$	$\text{Ni}_{2.01}\text{Mn}_{1.43}\text{Sn}_{0.56}$
0.48	$\text{Ni}_2\text{Mn}_{1.48}\text{Sn}_{0.52}$	$\text{Ni}_{2.01}\text{Mn}_{1.47}\text{Sn}_{0.52}$
0.52	$\text{Ni}_2\text{Mn}_{1.52}\text{Sn}_{0.48}$	$\text{Ni}_{1.99}\text{Mn}_{1.53}\text{Sn}_{0.48}$

The actual composition obtained indicate that the samples are of good chemical quality.

Table 3.2 Actual and intended composition of $\text{Ni}_2\text{Mn}_{1+x}\text{In}_{1-x}$ deduced from EDAX.

x	Intended composition	Actual composition
0.32	$\text{Ni}_2\text{Mn}_{1.32}\text{In}_{0.68}$	$\text{Ni}_{2.02}\text{Mn}_{1.31}\text{In}_{0.67}$
0.36	$\text{Ni}_2\text{Mn}_{1.36}\text{In}_{0.64}$	$\text{Ni}_{2.01}\text{Mn}_{1.36}\text{In}_{0.63}$
0.42	$\text{Ni}_2\text{Mn}_{1.42}\text{In}_{0.58}$	$\text{Ni}_{2.00}\text{Mn}_{1.42}\text{In}_{0.58}$
0.48	$\text{Ni}_2\text{Mn}_{1.48}\text{In}_{0.52}$	$\text{Ni}_{2.0}\text{Mn}_{1.48}\text{In}_{0.52}$

Table 3.3 Actual and intended composition of $\text{Ni}_{1.8}\text{Co}_{0.2}\text{Mn}_{1+x}\text{In}_{1-x}$ deduced from EDAX.

x	Intended composition	Actual composition	Sample name
0.47	$\text{Ni}_{1.8}\text{Co}_{0.2}\text{Mn}_{1.47}\text{In}_{0.53}$	$\text{Ni}_{1.81}\text{Co}_{0.22}\text{Mn}_{1.46}\text{In}_{0.51}$	NCMI1
0.46	$\text{Ni}_{1.8}\text{Co}_{0.2}\text{Mn}_{1.46}\text{In}_{0.54}$	$\text{Ni}_{1.81}\text{Co}_{0.22}\text{Mn}_{1.45}\text{In}_{0.52}$	NCMI2

3.3 Determination of transition temperatures

The structural and magnetic transition temperatures are determined by differential scanning calorimetry (DSC) measurement. The austenite to martensite transformation is exothermic, whereas the reverse transformation is endothermic. The characteristic transition temperatures martensitic start (M_S), martensitic finish (M_F), austenitic start (A_S), austenitic finish (A_F), martensitic magnetic ordering temperature (T_C^M) and austenitic Curie temperature (T_C^A) are marked in Figures. The exothermic, endothermic behavior and phase diagram of $\text{Ni}_2\text{Mn}_{1+x}\text{Sn}_{1-x}$ alloys are shown in Fig 3.1 and Fig. 3.2, respectively. In the phase diagram average transition temperatures obtained from the DSC, magnetization and resistivity measurements are plotted. The structural transition temperature increases with increase in the excess Mn concentration. The increase in Mn concentration increases the valence electron concentration per atom (e/a) which result in high martensitic transition temperature [1]. The T_C^A is almost constant (~ 317 K) with excess Mn concentration. The two compositions $x = 0.40$ and 0.44 have the martensitic transition below room temperature (RT) while

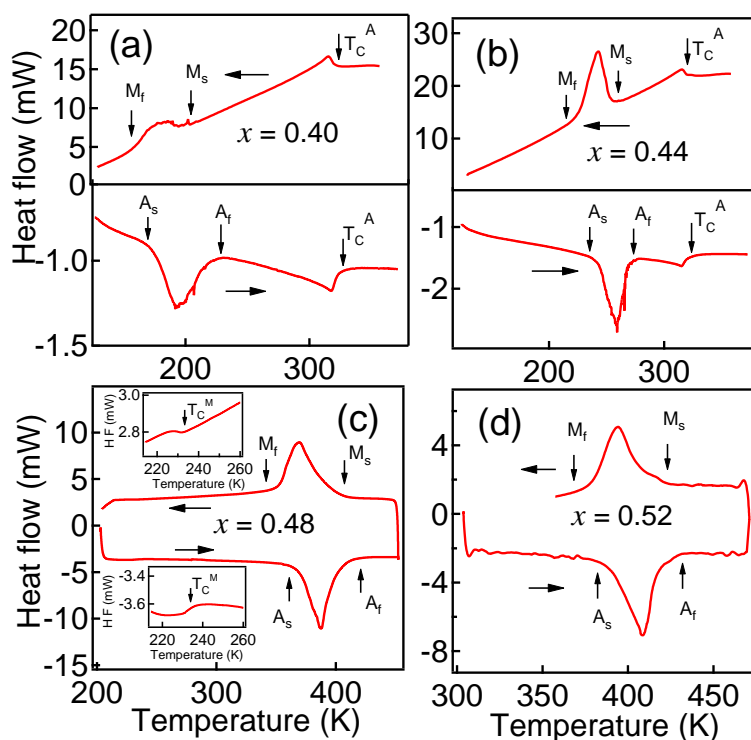


Figure 3.1 DSC during heating and cooling for $\text{Ni}_2\text{Mn}_{1+x}\text{Sn}_{1-x}$ ($0.40 \leq x \leq 0.52$).

for other two compositions martensitic transition is above RT. The $x = 0.48$ composition shows step like behavior at 234 K and 317 K. The step at 317 K matches with the austenitic Curie temperature of other compositions. The martensitic finish temperature of this alloy is 353 K, which is higher than 317 K. This indicates that the some fraction of austenitic phase is still present at 317 K. The 234 K is martensitic magnetic ordering temperature (T_C^M). The results are in good agreement with the earlier reports [1–7].

Figure 3.3 shows endothermic and exothermic behavior of $\text{Ni}_2\text{Mn}_{1+x}\text{In}_{1-x}$ ($0.32 \leq x \leq 0.48$) alloys. The corresponding transition temperatures are given in the Table 3.4. The martensitic transition is present for $x \geq 0.36$ and the transition temperature increases with increase in the excess Mn concentration. This behavior is similar to the $\text{Ni}_2\text{Mn}_{1+x}\text{Sn}_{1-x}$ alloys. The T_C^A is above RT and almost constant (~ 314 K) with excess Mn concentration. The T_C^A of $\text{Ni}_2\text{Mn}_{1+x}\text{In}_{1-x}$ alloys is similar to $\text{Ni}_2\text{Mn}_{1+x}\text{Sn}_{1-x}$ alloys. The $x = 0.32$ composition does not show any martensitic

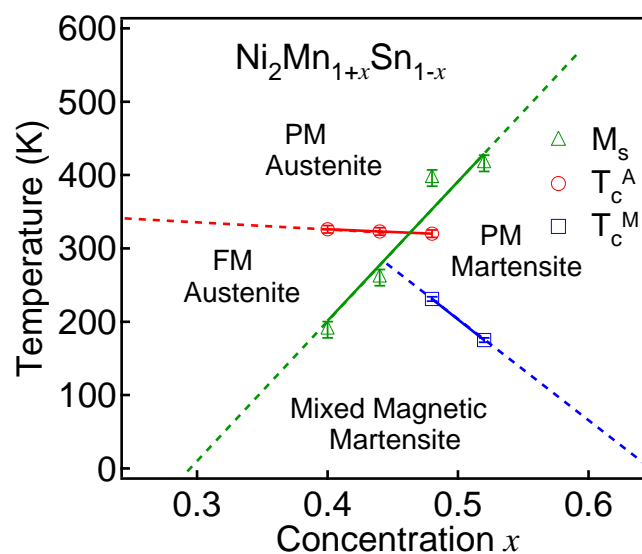


Figure 3.2 Phase diagram of $\text{Ni}_2\text{Mn}_{1+x}\text{Sn}_{1-x}$ alloys obtained from DSC, magnetization and resistivity measurements.

transition upto 5 K. At room temperature $x = 0.32$ and 0.36 are in the austenitic phase while $x = 0.42$ and 0.48 are in the martensitic phase. The results are in good agreement with the earlier reports [8–11].

Table 3.4 The structural and magnetic transition temperatures of $\text{Ni}_2\text{Mn}_{1+x}\text{In}_{1-x}$ obtained from DSC.

x	M_S (K)	M_F (K)	A_S (K)	A_F (K)	T_C^A (K)
0.32					312
0.36	258	201	215	266	314
0.42	391	369	374	394	
0.48	457	437	444	466	

Fig. 3.4 shows the endothermic and exothermic behavior of NCM11 and NCM12 alloys. The corresponding structural and magnetic transition temperatures are shown in Table 3.5. In these alloys structural transition temperatures are highly influenced by excess Mn concentration. Thus,

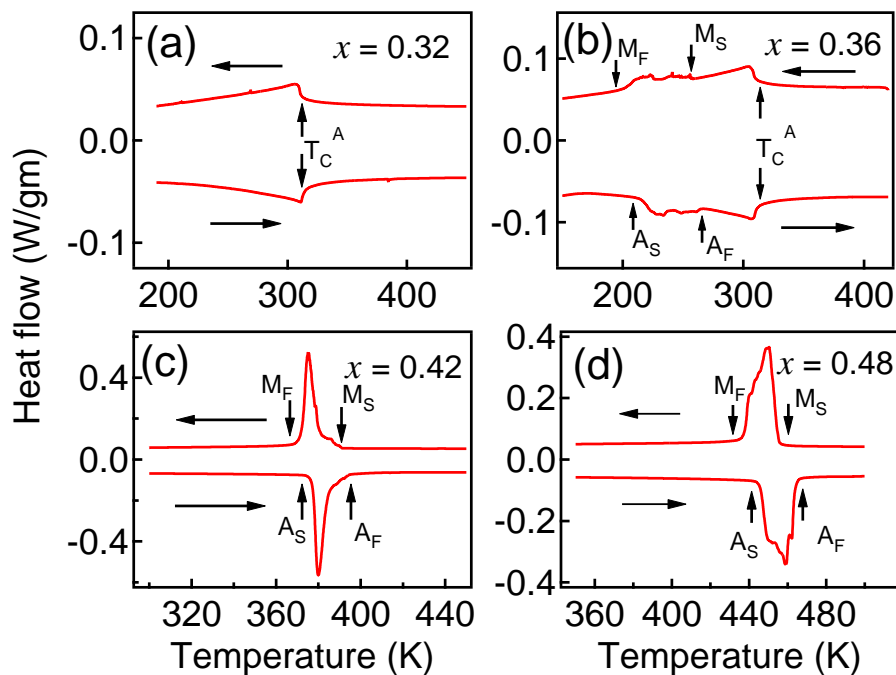


Figure 3.3 DSC during heating and cooling for $\text{Ni}_2\text{Mn}_{1+x}\text{In}_{1-x}$ ($0.32 \leq x \leq 0.48$).

in spite of very small difference in Mn concentration these two alloys have different structural transition temperatures. The structural transition temperatures of these Co substituted (at Ni site)

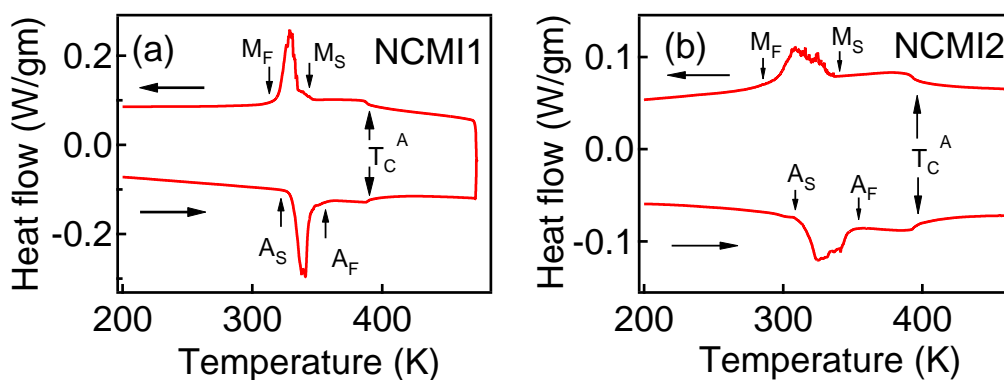


Figure 3.4 DSC during heating and cooling for $\text{Ni}_{1.8}\text{Co}_{0.2}\text{Mn}_{1+x}\text{In}_{1-x}$

$\text{Ni}_2\text{Mn}_{1+x}\text{In}_{1-x}$ alloys are found to be lower than corresponding parent $\text{Ni}_2\text{Mn}_{1+x}\text{In}_{1-x}$ alloys. The Co doping decreases the e/a ratio which results in the decrease in the structural transition

temperature as compared to parent $\text{Ni}_2\text{Mn}_{1+x}\text{In}_{1-x}$ alloy. However, the structural transition temperature increases with excess Mn concentration similar to $\text{Ni}_2\text{Mn}_{1+x}\text{Sn}_{1-x}$ and $\text{Ni}_2\text{Mn}_{1+x}\text{In}_{1-x}$ alloys. The T_C^A is high as compared to $\text{Ni}_2\text{Mn}_{1+x}\text{In}_{1-x}$ as well as $\text{Ni}_2\text{Mn}_{1+x}\text{Sn}_{1-x}$ alloys. Thus,

Table 3.5 The structural and magnetic transition temperatures of Ni-Co-Mn-In obtained from DSC.

Sample	$M_S(\text{K})$	$M_F(\text{K})$	$A_S(\text{K})$	$A_F(\text{K})$	$T_C^A(\text{K})$
NCMI1	346	317	329	359	390
NCMI2	335	292	312	349	397

with Co substitution at Ni site, T_C^A increases. The Co based Heusler alloys are known for higher T_C^A and magnetic moment as compared to Ni based Heusler alloys [12]. In Co-Mn based Heusler alloys [Co-Mn-Z(Al, Ga, Sn, In) [12] and Ni-Co-Mn-Ga [13]] a substantial moment is also associated with the Co sites. The exchange interaction increases and correspondingly higher Curie temperatures [14].

3.4 Surface micro-structure at room temperature

Figure 3.5 shows the room temperature (RT) scanning electron microscope (SEM) images for the all four compositions of $\text{Ni}_2\text{Mn}_{1+x}\text{Sn}_{1-x}$. The formation of twin planes are observed for $x = 0.48$ and 0.52 [Fig. 3.5 (c), (d)], because these alloys are in the martensitic phase at RT. The typical width of twin planes are around $1-3 \mu\text{m}$. The other two compositions ($x = 0.40$ and 0.44) does not show any twin planes since they are in the austenitic phase at the RT. The lines present in the SEM image of $x = 0.40$ and 0.44 are due to sample cutting by diamond saw.

The RT SEM images of $\text{Ni}_2\text{Mn}_{1+x}\text{In}_{1-x}$ alloys are shown in the Figure 3.6. The twin plains are visible for $x = 0.42$ and 0.48 [Fig. 3.6 (c), (d)] compositions since at RT they are in martensitic phase. The width of twin planes are around $2-4 \mu\text{m}$ for $x = 0.42$ and $7-9 \mu\text{m}$ for $x = 0.48$. The other two compositions, $x = 0.32$ and 0.36 , are in the austenitic phase. The SEM images also confirm

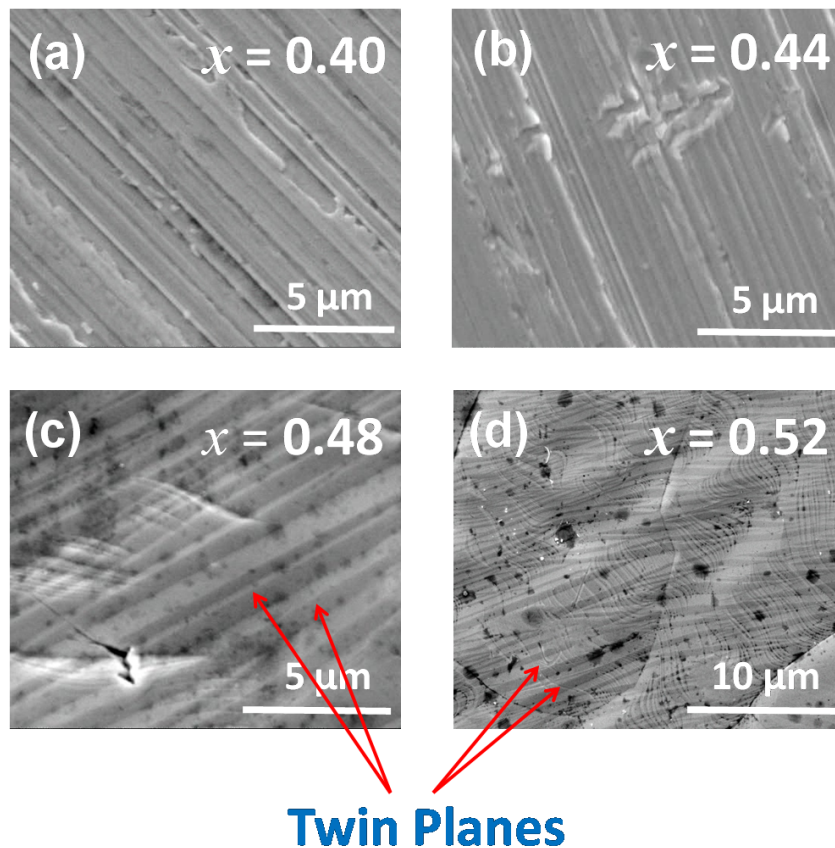


Figure 3.5 SEM image at room temperature for $\text{Ni}_2\text{Mn}_{1+x}\text{Sn}_{1-x}$ ($0.40 \leq x \leq 0.52$).

the absence of any impurity phases.

Figure 3.7 show the RT SEM images of Ni-Co-Mn-In alloys. The SEM image is recorded in piece of sample cut from the diamond saw. The sample with lower Mn concentration NCM12 ($\text{Ni}_{1.81}\text{Co}_{0.22}\text{Mn}_{1.45}\text{In}_{0.52}$) show black spots in the grey matrix. It indicates the presence of two structural phases at room temperature. The DSC results also confirms that the mixture of austenitic and martensitic phase is present at 300 K. The NCM12 is almost in the martensitic phase with small fraction of austenitic phase at room temperature. In the case of NCM11 no black spots are observed due to the presence of complete martensitic phase at room temperature. Thus the black regions are the reminiscence of austenitic phase.

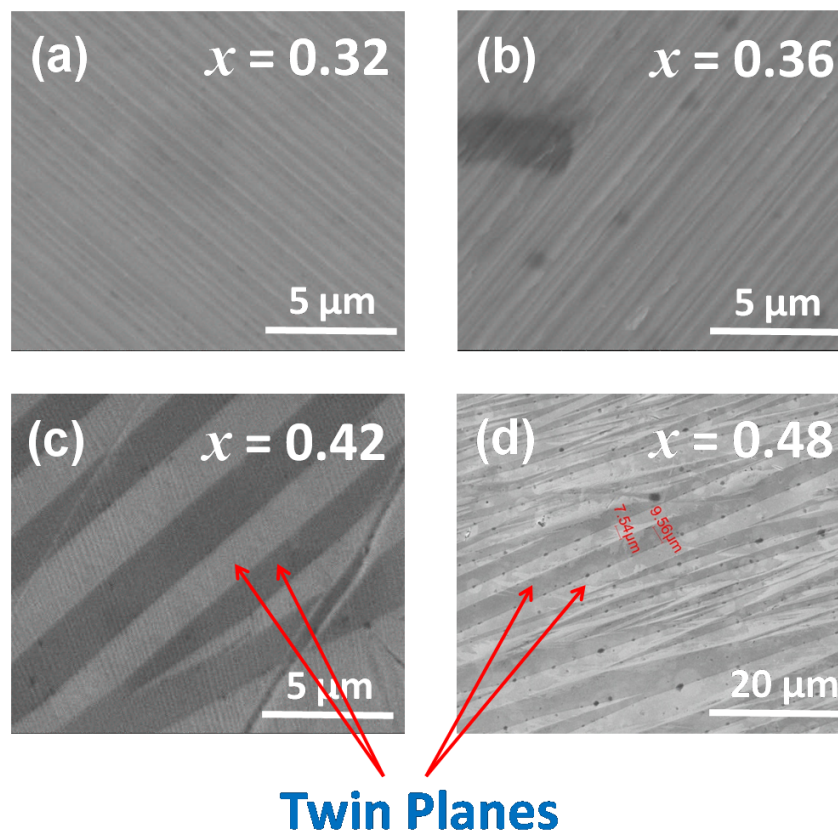


Figure 3.6 Room temperature SEM image of $\text{Ni}_2\text{Mn}_{1+x}\text{In}_{1-x}$ ($0.32 \leq x \leq 0.48$).

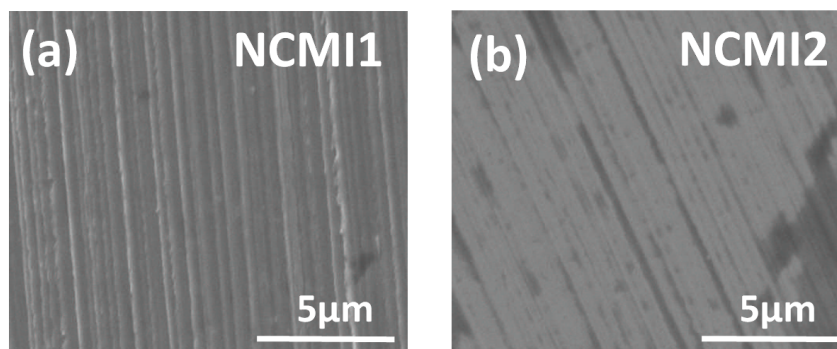


Figure 3.7 Room temperature SEM image of Ni-Co-Mn-In alloys.

3.5 Crystal structure at room temperature

The RT X-ray diffraction pattern (XRD), using $\text{CuK}\alpha$ radiation, of $\text{Ni}_2\text{Mn}_{1+x}\text{Sn}_{1-x}$ ($x = 0.40$ and 0.44) is shown in the Fig. 3.8. The Rietveld refinement is performed to find out the crystal structure and lattice parameter. The XRD pattern is consistent with the single phase cubic Heusler L_{21} (austenite) structure. The lattice constants are reported in Table 3.6. In the austenitic phase

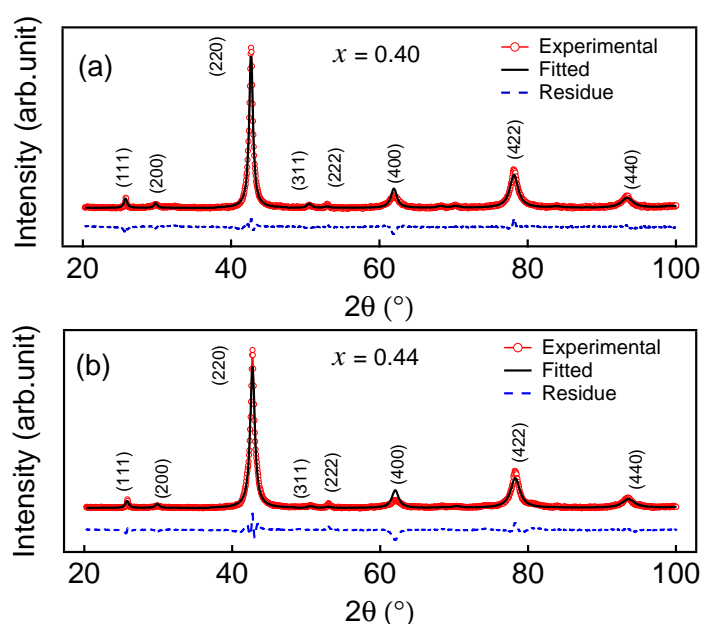


Figure 3.8 Room temperature XRD pattern of $\text{Ni}_2\text{Mn}_{1+x}\text{Sn}_{1-x}$ with fitted pattern, (a) $x = 0.40$ and (b) $x = 0.44$.

lattice constant decreases with excess Mn (x) concentration because Mn has small atomic radii than Sn. The lattice constant very well matches with the previous reports [1, 7]. Figure 3.9 shows the RT powder X-ray diffraction pattern and LeBail fitting of $\text{Ni}_2\text{Mn}_{1+x}\text{Sn}_{1-x}$ for $x = 0.48$ and 0.52 . The XRD pattern gives two phase (14 L and 4 L) orthorhombic structure (space group $\text{Pm}\bar{m}\text{a}$) of martensitic phase. ‘L’ refers to the layers of modulation. The lattice parameters are shown in the Table 3.6. The complex and mixture of various modulated crystal structure is observed in Ni-Mn-Sb [15] and Ni-Mn-In [16, 17] alloys also.

The RT powder XRD of $\text{Ni}_2\text{Mn}_{1+x}\text{In}_{1-x}$ for $x = 0.32$ and 0.36 using $\text{CuK}\alpha$ radiation is shown in

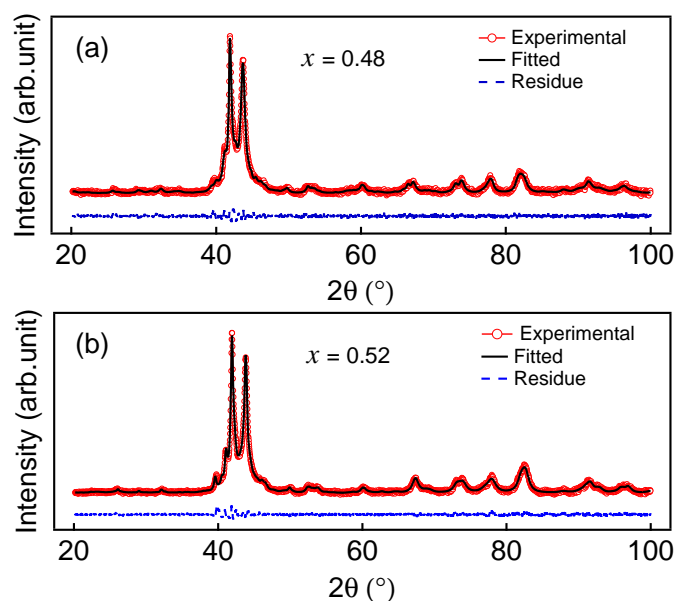


Figure 3.9 Room temperature XRD pattern of $\text{Ni}_2\text{Mn}_{1+x}\text{Sn}_{1-x}$ with LeBail fitting pattern, (a) $x = 0.48$ and (b) $x = 0.52$.

Table 3.6 Room temperature crystal structure and lattice parameter of $\text{Ni}_2\text{Mn}_{1+x}\text{Sn}_{1-x}$.

x	Crystal structure	Lattice parameter (\AA)		
		a	b	c
0.40	$L2_1$	5.99	5.99	5.99
0.44	$L2_1$	5.98	5.98	5.98
0.48	14 L	4.26	28.86	5.54
	4 L	4.32	5.78	8.70
0.52	14 L	4.33	28.51	5.59
	4 L	4.31	5.69	8.59

Fig. 3.10. The Rietveld refinement of the XRD pattern shows cubic $L2_1$ (austenite) structure with lattice parameter (Table 3.7) $a = 6.002 \text{ \AA}$ and $a = 6.001 \text{ \AA}$ for $x = 0.32$ and 0.36 , respectively. The lattice parameter is matching with earlier reports [8]. The small decrease in the lattice parameter with excess Mn is due to the small size of Mn atom compared to In atom. There are few martensitic

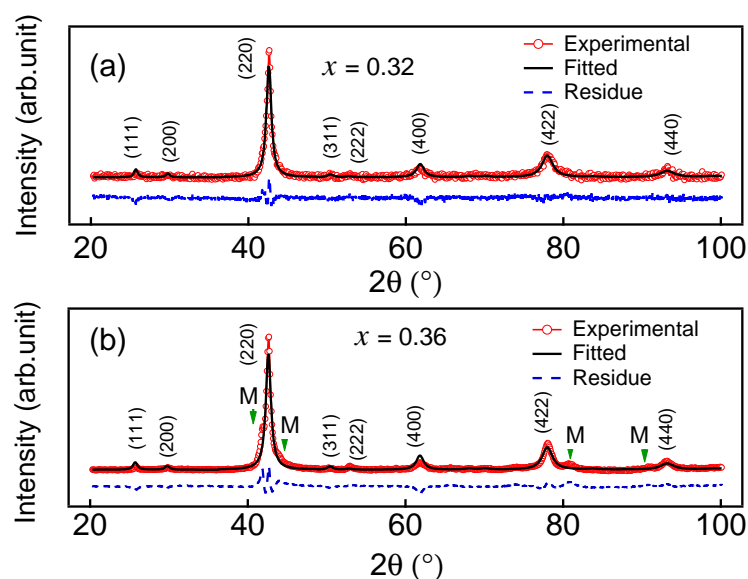


Figure 3.10 Room temperature XRD pattern of $\text{Ni}_2\text{Mn}_{1+x}\text{In}_{1-x}$ with fitted pattern, (a) $x = 0.32$ and (b) $x = 0.36$.

Table 3.7 Room temperature crystal structure and lattice parameter of $\text{Ni}_2\text{Mn}_{1+x}\text{In}_{1-x}$.

x	Crystal structure	Lattice parameter (Å)		
		a	b	c
0.32	$L2_1$	6.002	6.002	6.002
0.36	$L2_1$	6.001	6.001	6.001
0.42	10 M ($\beta = 87.93$)	4.38	5.56	21.98
0.48	10 M ($\beta = 89.06$)	4.42	5.54	22.05

peaks [M in Fig. 3.10 (b)] observed for $x = 0.36$ at RT. The residual stress induced by the grinding process can induce the martensitic phase at temperatures higher than the martensitic transition temperature and is reported earlier for $\text{Ni}_2\text{Mn}_{1.4}\text{In}_{0.6}$ [18].

Figure 3.11 shows the RT powder X-ray diffraction pattern and LeBail fitting of $\text{Ni}_2\text{Mn}_{1+x}\text{In}_{1-x}$ for $x = 0.42$ and 0.48 . The LeBail fitting of XRD pattern gives 10 M modulated monoclinic structure (space group P2/m) of martensitic phase. Where ‘M’ refers to the monoclinicity associated with the modulation. Similar structure for the martensitic phase of $\text{Ni}_2\text{Mn}_{1+x}\text{In}_{1-x}$ is reported in

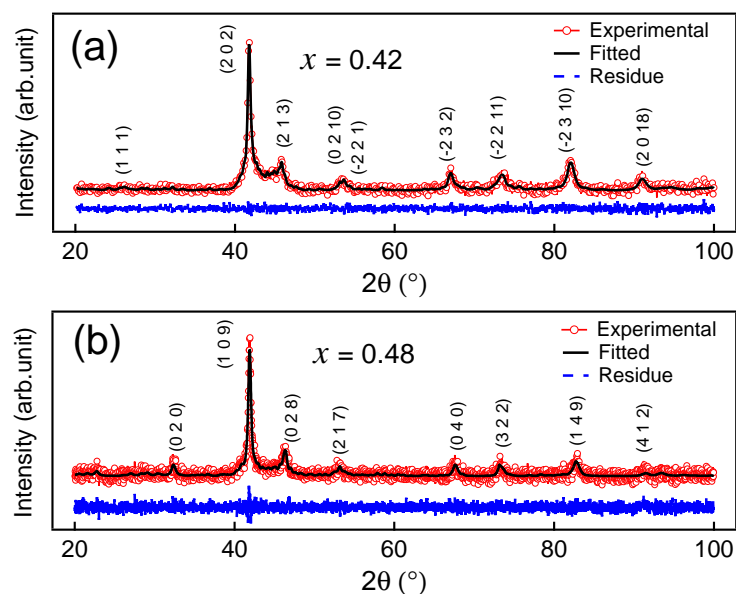


Figure 3.11 Room temperature XRD pattern of $\text{Ni}_2\text{Mn}_{1+x}\text{In}_{1-x}$ with LeBail fitting pattern, (a) $x = 0.42$ and (b) $x = 0.48$.

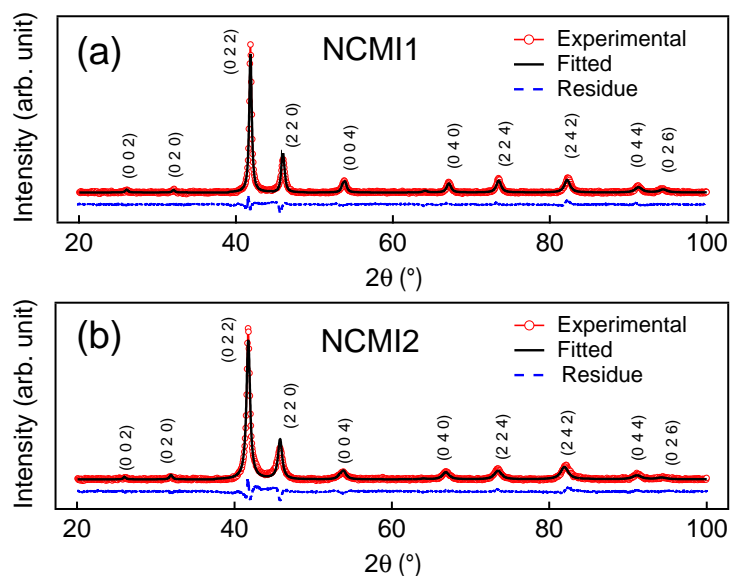


Figure 3.12 Room temperature XRD pattern of Ni-Co-Mn-In alloys with fitted pattern.

Ref. [8, 19]. The corresponding lattice parameters are shown in Table 3.7.

The RT XRD pattern using $\text{CuK}\alpha$ radiation and fitted pattern of NCM11 and NCM12 is shown

in Fig. 3.12. Table 3.5 confirms that both the samples are in the martensitic phase at room temperature. The LeBail fitting gives the tetragonal structure (space group Fmmm) of martensitic phase for both samples. The lattice parameters are $a = b = 5.59 \text{ \AA}$, $c = 6.8 \text{ \AA}$ for NCMI1 and $a = b = 5.6 \text{ \AA}$, $c = 6.8 \text{ \AA}$ for NCMI2. The orthogonal distortion in the structure is checked by freely varying the lattice parameters (a , b and c) in the fitting procedure and no orthogonal distortion is observed. Similar structure is also reported in martensitic phase of Ni-Mn-Ga alloys [20].

3.6 Conclusion

Off-stoichiometric Ni-Mn-Sn, Ni-Mn-In and Ni-Co-Mn-In alloys are characterized for chemical composition, surface micro-structure and transition temperatures. The alloys with good chemical composition, twin structure in the martensitic phase, characteristic transition temperatures, and expected crystal structures are successfully made. The results imply that the samples are of good quality and could be used for further exploration of various properties.

Bibliography

- [1] T. Krenke, M. Acet, E.F. Wassermann, X. Moya, L. Mañosa, and A. Planes, Phys. Rev. B **72**, 014412 (2005).
- [2] T. Krenke, E. Duman, M. Acet, E. F. Wassermann, X. Moya, L. Mañosa, A. Planes, Nat. Mater. **4**, 450 (2005).
- [3] P. A. Bhoje, K. R. Priolkar, and P. R. Sarode, J. Phys.: Condens. Matter **20**, 015219 (2008).
- [4] A. Planes, Physics **3**, 36 (2010).
- [5] Z. Li, C. Jing, J. Chen, S. Yuan, S. Cao, and J. Zhang, Appl. Phys. Lett. **91**, 112505 (2007).
- [6] K. Koyama, K. Watanabe, T. Kanomata, R. Kainuma, K. Oikawa, and K. Ishida, Appl. Phys. Lett. **88**, 132505 (2006).
- [7] P. J. Brown, A. P. Gandy, K. Ishida, R. Kainuma, T. Kanomata, K.-U. Neumann, K. Oikawa, B. Ouladdiaf, and K. R. A. Ziebeck, J. Phys.: Condens. Matter **18**, 2249 (2006).
- [8] T. Krenke, M. Acet, E.F. Wassermann, X. Moya, L. Mañosa, and A. Planes, Phys. Rev. B **73**, 174413 (2006).
- [9] R. Kainuma, K. Oikawa, W. Ito, Y. Sutou, T. Kanomata, and K. Ishida, J. Mater. Chem. **18**, 1837 (2008).
- [10] X. Moya, L. Mañosa, A. Planes, S. Aksoy, M. Acet, E. F. Wassermann, and T. Krenke, Phys. Rev. B **75**, 184412 (2007).

-
- [11] V. K. Sharma, M. K. Chattopadhyay, and S. B. Roy, *Phys. Rev. B* **76**, 140401R (2007).
- [12] P. J. Webster, *J. Phys. Chem. Solids* **32**, 1221 (1971).
- [13] T. Chang-Long, J. Jiu-Xing, T. Xiao-Hua, and C. Wei, *Chinese Phys. B* **19**, 107102 (2010).
- [14] P. J. Webster and K. R. A. Ziebeck, *J. Phys. Chem. Solids* **34**, 1647 (1973).
- [15] S. Aksoy, M. Acet, E. F. Wassermann, T. Krenke, X. Moya, L. Mañosa, A. Planes, and P. P. Deen, *Philos. Mag.* **89**, 2093 (2009).
- [16] K. Oikawa, W. Ito, Y. Imano, Y. Sutou, R. Kainuma, K. Ishida, S. Okamoto, O. Kitakami, and T. Kanomata, *Appl. Phys. Lett.* **88**, 122507 (2006).
- [17] V. V. Khovaylo, T. Kanomata, T. Tanaka, M. Nakashima, Y. Amako, R. Kainuma, R. Y. Umetsu, H. Morito, and H. Miki, *Phys. Rev. B* **80**, 144409 (2009).
- [18] B. L. Ahuja, A. Dashora, N. L. Heda, K. R. Priolkar, L. Vadkhiya, M. Itou, N. Lobo, Y. Sakurai, A. Chakrabarti, S. Singh, and S R Barman, *J. Phys. : Condens. Matter.* **22**, 446001 (2010).
- [19] P. J. Brown, A. P. Gandy, R. Kainuma, T. Kanomata, K. U. Neumann¹, K. Oikawa, B. Oulad-diaf, A. Sheikh, and K. R. A. Ziebeck, *J. Phys.: Condens. Matter* **25**, 456004 (2011).
- [20] Dr. C. Biswas, PhD thesis, "Electronic Structure Studies of Metals and Intermetallics", 2005.

Chapter 4

Magnetic property

4.1 Introduction

Heusler alloys are known to be ideal local moment systems [1]. In Mn based Heusler alloys [Ni-Mn-Sn (In)], the magnetic moment is mainly localized on Mn (Mn1). The RKKY type indirect exchange interaction give rise to the magnetism in these materials. As Mn is substituted for Sn (In), excess Mn (Mn2) atoms occupy Sn (In) sites. The Mn1 atoms have Mn2 atoms as nearest neighbours along the [110] direction [2]. It leads to the anti-ferromagnetic exchange interaction between Mn1-Mn2 in the martensitic phase.

The Ni-Mn-Sn system shows the martensitic transition in off-stoichiometric ($\text{Ni}_2\text{Mn}_{1+x}\text{Sn}_{1-x}$) composition. The martensitic transition is reported for $x \geq 0.36$ [3,4]. The $\text{Ni}_2\text{Mn}_{1+x}\text{Sn}_{1-x}$ system shows large drop in magnetization at martensitic transition. The decrease in magnetization at martensitic transition is explained by the enhanced anti-ferromagnetic coupling between Mn1 and Mn2 atoms [2]. From the neutron diffraction study Brown et al. [5] predicted the antiferromagnetic coupling between Mn2 atoms. The magnetic moment of stoichiometric Ni_2MnSn is $4 \mu_B/f.u.$ at 5 K [6]. The magnetic moment decreases with increasing x concentration in both the austenitic and martensitic phases [6]. The shift in the structural transition is observed under high magnetic field [7]. The magnetic ordering temperature in the austenitic phase (T_C^A) is almost independent of the concentration (x), while that in the martensitic phase T_C^M decreases with increasing x . The T_C^A of Ni-Mn-Sn system is near 320 K [2, 6, 8].

The martensitic transition in $\text{Ni}_2\text{Mn}_{1+x}\text{In}_{1-x}$ system is also observed for $x \geq 0.36$ [9]. Similar to $\text{Ni}_2\text{Mn}_{1+x}\text{Sn}_{1-x}$ system large decrease in magnetization is observed at martensitic transition [10]. The magnetic moment of stoichiometric Ni_2MnIn is $\simeq 4 \mu_B/f.u.$ at 5 K [6]. In the austenitic phase magnetic moment increases with x concentration and it is $\simeq 5.7 \mu_B/f.u.$ for $\text{Ni}_2\text{Mn}_{1.32}\text{In}_{0.68}$ [6]. While in martensitic phase it is $\simeq 1.6 \mu_B/f.u.$ for $\text{Ni}_2\text{Mn}_{1.36}\text{In}_{0.64}$ and rapidly decreases with x concentration [6]. The martensitic transition is highly dependent on concentration (x). The span of the martensite transition is 30 - 40 K. The magnetic ordering temperature in the austenitic phase (T_C^A) is almost independent of the concentration (x). The T_C^A is $\simeq 310$ K [6, 11]. The magnetic ordering temperature of martensitic phase (T_C^M) rapidly decreases with increasing x [8]. The field

induced reverse phase transition is observed in the martensitic phase at high magnetic field [12]. The large shift in martensitic transition temperature [11, 13] and kinetic arrest of martensitic phase transformation [9, 13] under high magnetic field is reported for $\text{Ni}_2\text{Mn}_{1.36}\text{In}_{0.64}$.

The important functional properties are observed across the martensitic transition from high magnetic austenitic phase to low magnetic martensitic phase. Thus, in Ni-Mn-Sn and Ni-Mn-In they are observed below room temperature. The Co based Heusler alloys are known for higher T_C and magnetic moment as compared to Ni based Heusler alloys [14]. Thus, to obtain the improved functional properties above room temperature Co is doped in the Ni-Mn-In alloys. The Co doping in Ni-Mn-In alloys enhances the T_C^A and magnetic moment in the austenitic phase [15, 16]. The martensitic transition temperature decreases with Co doping.

4.2 Result and Discussion

4.2.1 $\text{Ni}_2\text{Mn}_{1+x}\text{Sn}_{1-x}$ alloys

The magnetization as a function of temperature (M-T) and isothermal magnetization for $x = 0.40$ are presented in Fig. 4.1 (a) and (b), respectively. The M-T measurements are done in the zero field cooled (ZFC), field cooling (FC), and field heating (FH) mode. In ZFC mode the sample is cooled from the 300 K to 5 K in zero magnetic field. The magnetization is measured while warming up the sample with 500 Oe applied magnetic field (H). In FC mode, measurement is made while cooling the sample in the presence of 500 Oe applied magnetic field. After reaching 5 K temperature the sample is warmed up again in the same magnetic field for FH measurement. Following the FC curve from high-temperature, magnetization increases with decreasing temperature. It is in the ferromagnetic state because T_C^A is ~ 326 K. As the temperature further decreases, the martensitic transformation begins at M_S , below which large decrease in the magnetization is observed, until it reaches a value of local minimum. This temperature is designated as the martensite finish temperature M_F . Further below the M_F , magnetization slowly increases with decreasing temperature in FC and FH. However, in ZFC magnetization decreases rapidly below T^* temperature and satu-

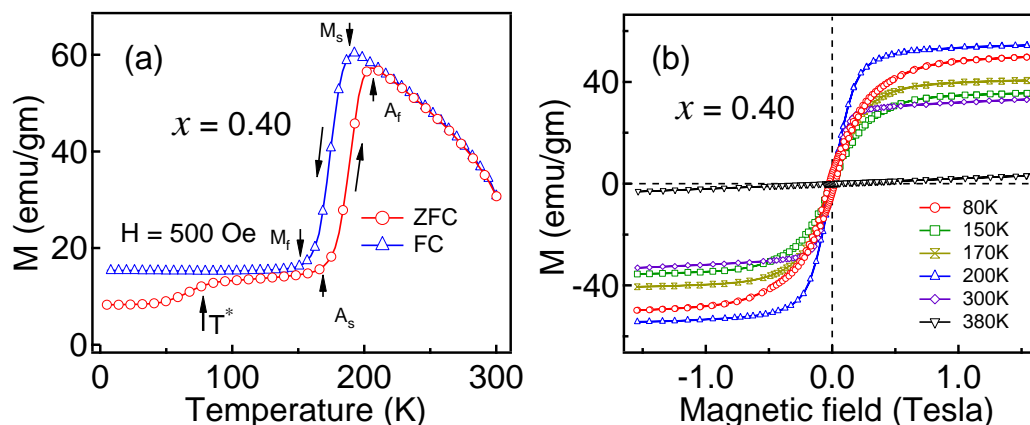


Figure 4.1 (a) Magnetization (ZFC, FC and FH) as a function of temperature of $\text{Ni}_2\text{Mn}_{1.4}\text{Sn}_{0.6}$ at 500 Oe. (b) Isothermal magnetization of $\text{Ni}_2\text{Mn}_{1.4}\text{Sn}_{0.6}$.

rates at low temperature. In a manner similar to the forward austenite-to-martensite transition, the reverse transformation occurs on heating, starts at the austenite start temperature (A_S) and finishes at the austenite finish temperature (A_F). The structural transition temperatures, M_S , M_F , A_S and A_F are 184 K, 161 K, 175 K and 200 K, respectively. The thermal hysteresis ($A_S - M_F$) is ~ 14 K. The temperature corresponding to T^* (marked by an arrow) is 78 K. The structural and magnetic transitions are in accordance with DSC result. The splitting between the ZFC and FC below the structural transition temperature M_F and A_S in Fig. 4.1 (a) indicates the presence of magnetically inhomogeneous phase.

The Mn1-Mn1 interaction is predominantly ferromagnetic [2, 5, 17] but Mn1-Mn2 interaction may have anti-ferromagnetic contributions depending on the distance between the Mn atoms because the Mn-Mn interactions show long-range oscillatory behaviour. The Ni and Sn atoms have small and negligible magnetic moments [5, 17–19]. A weak anti-ferromagnetic coupling ($J_{ij} \simeq -10$ meV) between Mn1-Mn2 is present in the austenitic phase [17]. The extended X-ray absorption fine-structure (EXAFS) measurement by Bhoje et al. [20] gives the Mn1-Mn2 bond length $\simeq 2.93$ Å. The present XRD result (Table 3.6, chapter 3) shows that the Mn1-Mn2 distance in the austenitic phase is 2.99 Å in agreement with EXAFS results. The anti-ferromagnetic exchange interaction gets enhanced by decrease in the Mn1-Mn2 distance upon the martensitic transition due

to change in the lattice parameter. The Mn1-Mn2 distance in martensitic phase of $\text{Ni}_2\text{Mn}_{1.48}\text{Sn}_{0.52}$ is $\simeq 2.77 \text{ \AA}$ and $\simeq 2.89 \text{ \AA}$ for 14L and 4L crystal structure, respectively. The EXAFS result also shows the decrease in Mn1-Mn2 bond length ($\simeq 2.87 \text{ \AA}$) upon the martensitic transition [20]. The anti-ferromagnetic exchange ($J_{ij} \simeq -30 \text{ meV}$) between Mn1-Mn2 is enhanced in the martensitic phase [17]. Thus the magnetic ground state in martensitic phase has coexistence of ferromagnetic (Mn1-Mn1) and anti-ferromagnetic (Mn1-Mn2) spin alignment.

The steplike anomaly in ZFC (marked as T^*) in Fig. 4.1 (a) is due to drop in magnetization arising from the competition between ferromagnetic and anti-ferromagnetic interaction. Such behavior is reported earlier for Ni-Mn-Sn alloys [2, 4, 21, 22]. The exchange bias phenomenon is reported below T^* temperature [4, 23]. The competing magnetic interactions leads to the spin freezing and reentrant spin glass [4] like behaviour at the low temperature martensitic phase.

The isothermal M-H curves upto 1.6 Tesla for $x = 0.40$ is shown in the Fig. 4.1 (b). All M-H curves are measured during cooling cycle under zero field. The M-H curves at 380 K is linear showing the paramagnetic behavior. In the austenitic phase at 300 K and 200 K it shows the ferromagnetic behavior with saturation above 0.5 Tesla. In the martensitic phase at 150 K and 80 K, M-H curve shows ferromagnetic nature but the magnetization saturates at higher magnetic field (1.0 Tesla) compared to austenitic phase. It indicates that magnetocrystalline anisotropy is more in

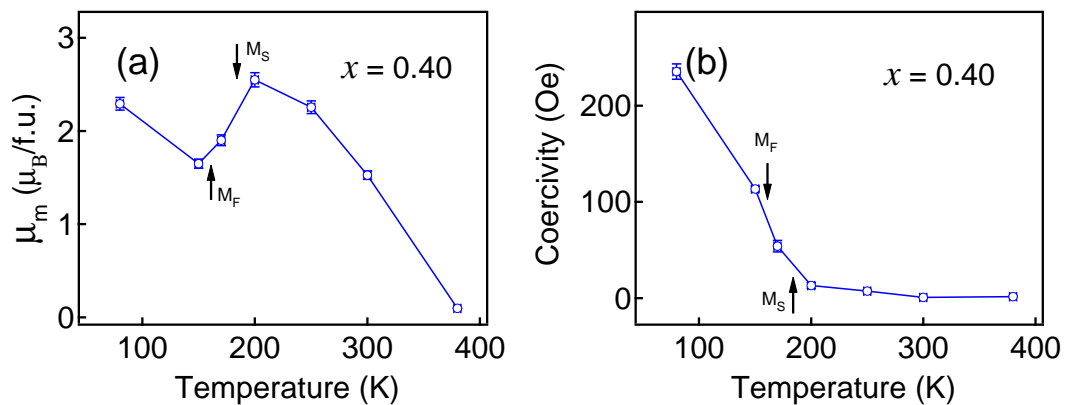


Figure 4.2 (a) Magnetic moment per formula unit (μ_m) as a function of temperature for $\text{Ni}_2\text{Mn}_{1.4}\text{Sn}_{0.6}$. (b) Temperature dependent coercivity of $\text{Ni}_2\text{Mn}_{1.4}\text{Sn}_{0.6}$.

the martensitic phase compared to austenitic phase. The enhanced anti-ferromagnetic coupling in

the martensitic phase is responsible for the larger magnetocrystalline anisotropy.

The total magnetic moment per formula unit (μ_m) and the coercivity as a function of temperature for $\text{Ni}_2\text{Mn}_{1.4}\text{Sn}_{0.6}$ is shown in Fig. 4.2 (a) and (b), respectively. The maximum magnetic moment in the austenitic phase is $\simeq 2.55 \mu_B/f.u.$ at 200 K. Magnetic moment decreases by about $0.9 \mu_B/f.u.$ upon martensitic transition. The austenitic phase has almost zero coercivity. The significant coercivity is observed below M_S , which increases at the low temperature. At 80 K coercivity is ~ 235 Oe. The coercivity in the martensitic phase might be due to spin pinning or domain wall pinning caused by the anti-ferromagnetic spins [2].

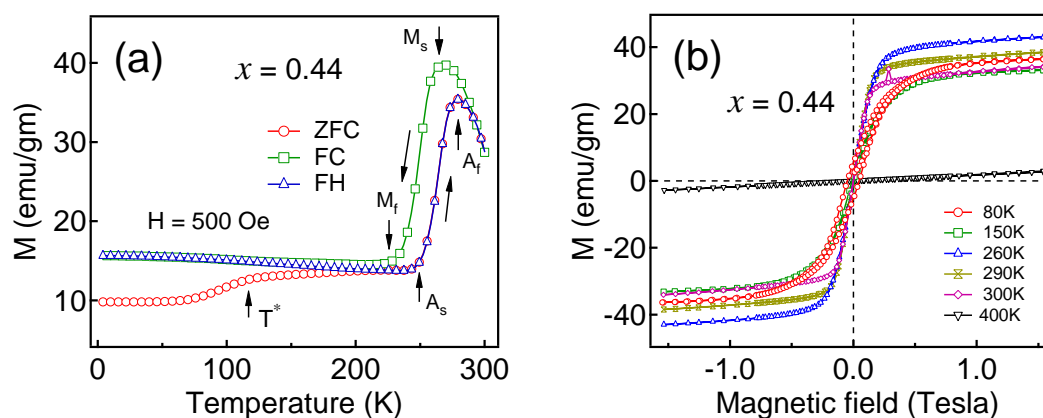


Figure 4.3 (a) Magnetization (ZFC, FC and FH) as a function of temperature of $\text{Ni}_2\text{Mn}_{1.44}\text{Sn}_{0.56}$ at 500 Oe. (b) Isothermal magnetization of $\text{Ni}_2\text{Mn}_{1.44}\text{Sn}_{0.56}$.

The M-T (ZFC, FC and FH), curve for $x = 0.44$ at 500 Oe is shown in the Fig. 4.3 (a). At 300 K sample is in the ferromagnetic austenitic phase as T_C^A is 317 K (from DSC). The M-T shows the similar behaviour as for $x = 0.40$. The transition temperatures, M_S , M_F , A_S , A_F are 263 K, 238 K, 253 K, 278 K, respectively. The thermal hysteresis ($A_S - M_F$) is ~ 15 K. The temperature T^* (marked by an arrow) from where the magnetization rapidly decreases towards low temperature in ZFC is 117 K. The higher T^* temperature as compared to $x = 0.40$ indicate an increased competing interactions in the system, which is due to the increase in Mn2 concentration. The M-H curves for $x = 0.44$ is shown in Fig. 4.3 (b). The M-H curves are measured during cooling cycle under zero field. The M-H curve at 400 K is linear showing the paramagnetic behavior. At 300 K and 260 K

in the austenitic phase M-H curve shows ferromagnetic behavior with saturation in magnetization above 0.5 Tesla. In the martensitic phase at 150 K and 80 K, M-H curve shows ferromagnetic nature but the saturation is achieved above 1.0 Tesla.

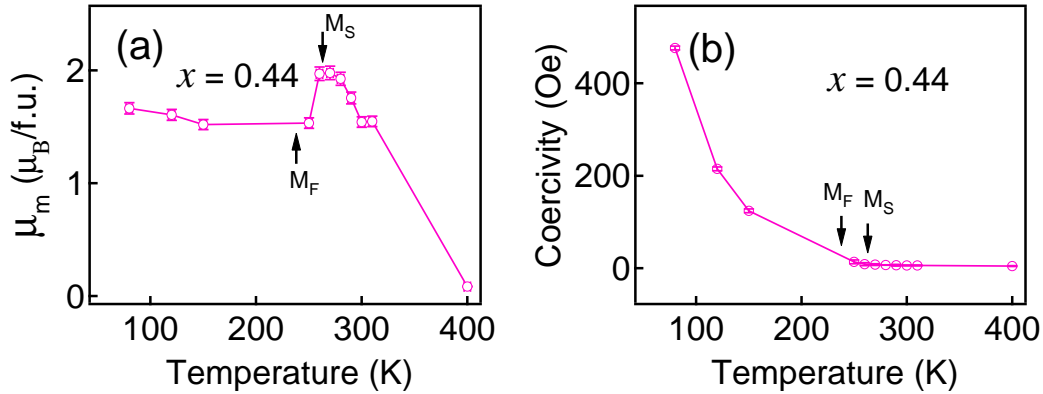


Figure 4.4 (a) Magnetic moment per formula unit (μ_m) as a function of temperature for $\text{Ni}_2\text{Mn}_{1.44}\text{Sn}_{0.56}$. (b) Temperature dependent coercivity of $\text{Ni}_2\text{Mn}_{1.44}\text{Sn}_{0.56}$.

Figure 4.4 (a) and (b) shows the total magnetic moment per formula unit (μ_m) and coercivity as a function of temperature for $\text{Ni}_2\text{Mn}_{1.44}\text{Sn}_{0.56}$, respectively. The maximum magnetic moment in the austenitic phase is $\simeq 2 \mu_B/f.u.$ at 270 K. The significant coercivity is observed below M_F , which increases at the low temperature. At 80 K coercivity is ~ 476 Oe.

The M-T (ZFC, FC and FH), curve for $x = 0.48$ and 0.52 are shown in the Fig. 4.5 (a) and (b), respectively. Both are in the paramagnetic martensitic phase at 300 K. Magnetization is almost constant below 300 K till magnetic ordering temperature T_C^M of martensitic phase. Below T_C^M magnetization increases rapidly with decreasing temperature. The T_C^M is 229 K and 175 K for $x = 0.48$ and 0.52 , respectively. The FC and FH shows similar variation with temperature upto 5 K, while ZFC deviates from FC and FH at low temperature for both the compositions. At the low temperature ZFC shows the decrease in the magnetization with decreasing temperature before saturating at low temperature, a behaviour similar with other compositions ($x = 0.40$ and 0.44). The temperature T^* where the magnetization starts decreasing in ZFC (marked by an arrow in Fig. 4.5) is ~ 130 K and ~ 109 K for $x = 0.48$ and 0.52 , respectively. The Fig. 4.5 (c) and (d) represents the M-H curves for the $x = 0.48$ and 0.52 , respectively. At 300 K M-H curve shows linear variation of

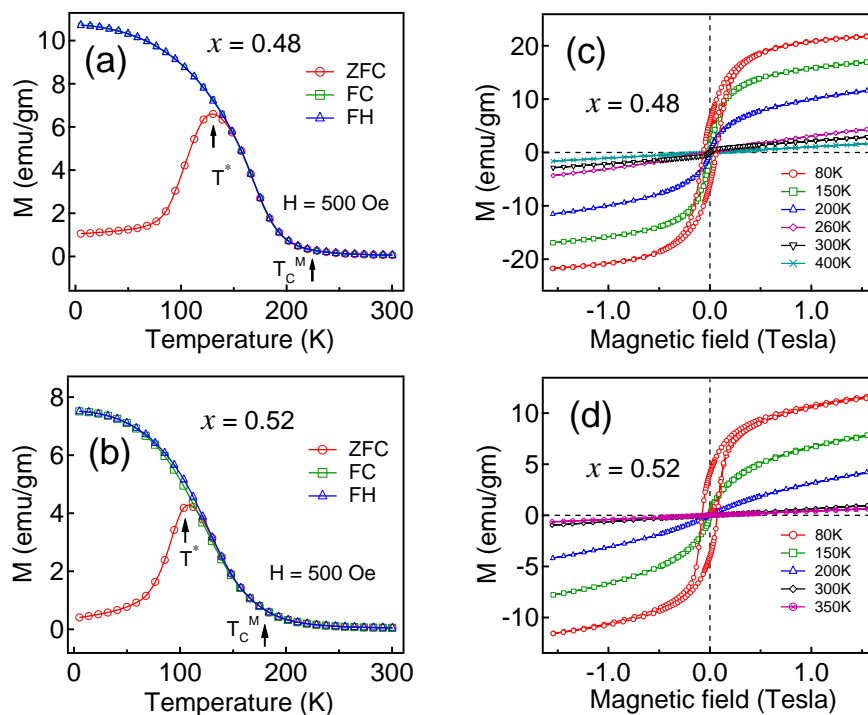


Figure 4.5 Magnetization (ZFC, FC and FH) as a function of temperature of $\text{Ni}_2\text{Mn}_{1+x}\text{Sn}_{1-x}$ at 500 Oe for (a) $x = 0.48$ and (b) $x = 0.52$. Isothermal magnetization for (c) $x = 0.48$ and (d) $x = 0.52$.

paramagnetic phase for both compositions. Below T_C^M , M-H initially rises rapidly but saturation is not reached. The increase of anti-ferromagnetic interactions within the ferromagnetic state due to

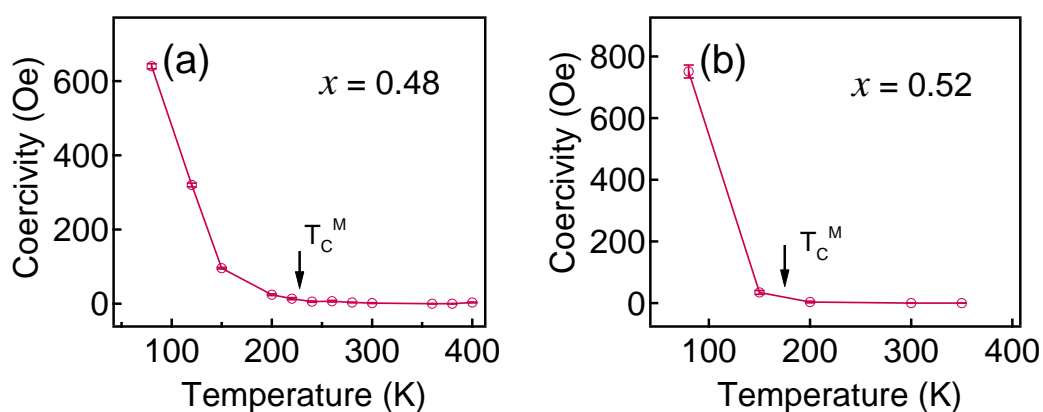


Figure 4.6 Temperature dependent coercivity of (a) $\text{Ni}_2\text{Mn}_{1.48}\text{Sn}_{0.52}$ and (b) $\text{Ni}_2\text{Mn}_{1.52}\text{Sn}_{0.48}$.

the increased Mn2 concentration causes non-saturation.

The coercivity as a function of temperature for $x = 0.48$ and 0.52 is shown in Fig. 4.6 (a) and (b), respectively. Coercivity is observed below T_C^M and it rapidly increases at low temperature. The coercivity is found to be ~ 640 Oe and ~ 751 Oe at 80 K for $x = 0.48$ and 0.52 , respectively.

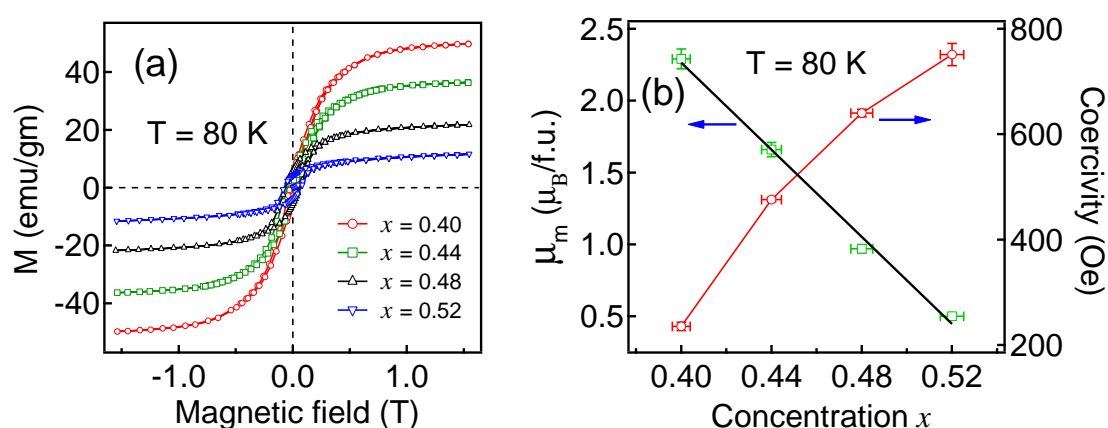


Figure 4.7 (a) M-H curve at 80 K for $\text{Ni}_2\text{Mn}_{1+x}\text{Sn}_{1-x}$. (b) Magnetic moment per formula unit (μ_m) and the coercivity of $\text{Ni}_2\text{Mn}_{1+x}\text{Sn}_{1-x}$ at 80 K as a function of x .

Figure 4.7 (a) shows the isothermal magnetization at 80 K for $0.40 \leq x \leq 0.52$. It clearly reveals that the saturation magnetization decreases with increasing Mn2 (x) concentration. The total magnetic moment per formula unit (μ_m) and the coercivity of $\text{Ni}_2\text{Mn}_{1+x}\text{Sn}_{1-x}$ at 80 K as a function of x is shown in Fig. 4.7 (b). The magnetic moment linearly decreases with increasing x and coercivity increases with increasing x . At 80 K all the compositions are in martensitic phase, thus decrease in the magnetic moment with increasing x confirms the presence of strong anti-ferromagnetic coupling between Mn1 and Mn2 atoms in the martensitic phase. As explained earlier coercivity in the martensitic phase might be due to spin pinning or domain wall pinning caused by the anti-ferromagnetic spins. As the anti-ferromagnetic spins increases with increasing Mn2 (x), pinning also increases, which results in increase of coercivity.

4.2.2 $\text{Ni}_2\text{Mn}_{1+x}\text{In}_{1-x}$ alloys

The magnetization as a function of temperature at 500 Oe for $\text{Ni}_2\text{Mn}_{1+x}\text{In}_{1-x}$ ($0.32 \leq x \leq 0.48$) using VSM is shown in the Fig. 4.8 (a) - (d). Figure 4.8 (a) shows the M-T curve for $x = 0.32$. The T_C^A is 323 K. The ZFC, FC and FH curves overlap each other and no martensitic transition is observed upto 80 K. This may be the critical composition for the martensitic transition. The M-T curve for $x = 0.36$ [Fig. 4.8 (b)] clearly shows the martensitic transition. The T_C^A is 320 K. The martensitic transition temperatures, M_S , M_F , A_S , A_F are 261 K, 195 K, 213 K, 266 K, respectively. The thermal hysteresis ($A_S - M_F$) is ~ 18 K. The structural and magnetic transitions are in accordance with DSC result. Similar to the $\text{Ni}_2\text{Mn}_{1+x}\text{Sn}_{1-x}$ systems the martensitic phase of $x = 0.36$ has bifurcation in ZFC and FC/FH curve due to similar reason [2, 10]. Figure 4.8 (c)

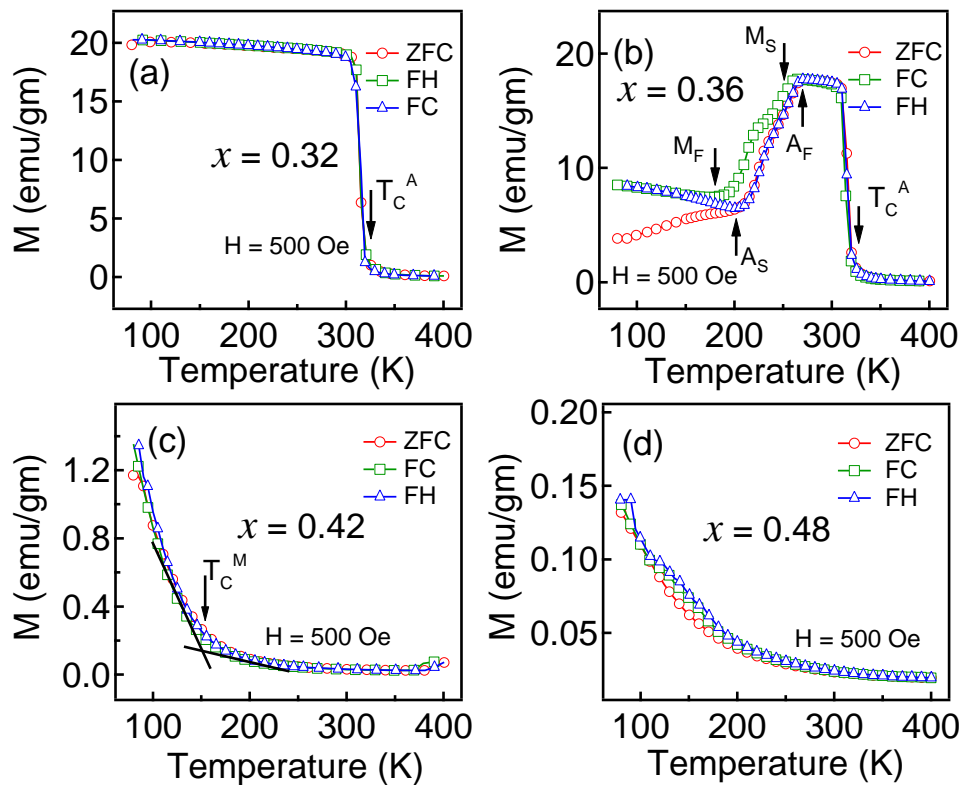


Figure 4.8 Magnetization as a function of temperature for $\text{Ni}_2\text{Mn}_{1+x}\text{In}_{1-x}$ ($0.32 \leq x \leq 0.48$).

shows the M-T curve for the $x = 0.42$. At 300 K it is in paramagnetic martensitic phase with very

small magnetization. The magnetic ordering (T_C^M) occurs around 154 K. The M-T curve of $x = 0.48$ [Fig. 4.8 (d)] shows no magnetic ordering upto 80 K. There is no bifurcation between ZFC and FC/FH till 80 K.

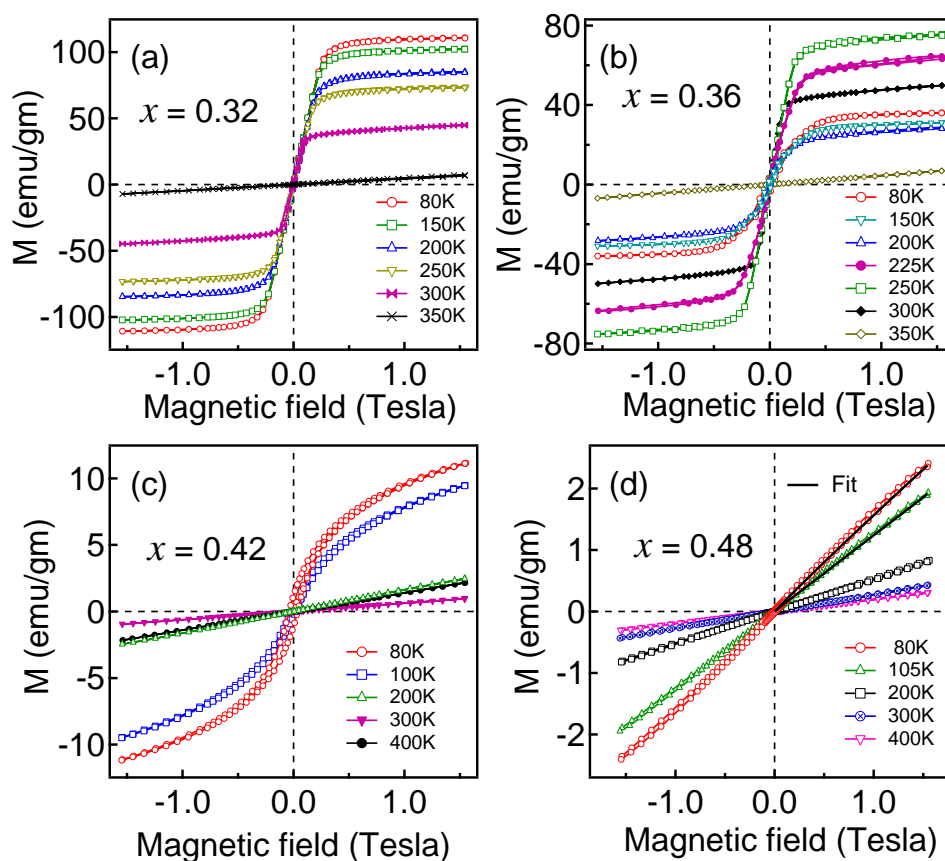


Figure 4.9 Magnetization as a function of magnetic field for $\text{Ni}_2\text{Mn}_{1+x}\text{In}_{1-x}$ ($0.32 \leq x \leq 0.48$).

The isothermal M-H curves of $\text{Ni}_2\text{Mn}_{1+x}\text{In}_{1-x}$ ($0.32 \leq x \leq 0.48$) are shown in Fig. 4.9 (a) - (d). The M-H curve are measured during cooling cycle under zero magnetic field. The M-H curve for $x = 0.32$ and 0.36 [Fig. 4.9 (a) and (b)] shows ferromagnetic behaviour below T_C^A . Linear variation of M-H curve confirms the paramagnetic nature above T_C^A . The M-H curves of $x = 0.42$ [Fig. 4.9 (c)] show weak magnetic behaviour below T_C^M . The M-H curves do not saturate upto 1.6 Tesla. It has significant amount of linear characteristic which might be due to the enhanced anti-ferromagnetism caused by the increased Mn2 (x). The M-H curves of $x = 0.48$ [Fig. 4.9 (d)]

show the linear variation upto 80 K. The linear fitting at 80 K and 150 K is shown in Fig. 4.9 (d). It confirms paramagnetic state upto 80 K for $x = 0.48$.

The total magnetic moment per formula unit (μ_m) as a function of temperature for $x = 0.32$ and 0.36 is shown in Fig. 4.10 (a). The μ_m of $x = 0.36$ is higher than $x = 0.32$ in the austenitic phase (300 K - 250 K). It indicates that Mn2 is ferromagnetically coupled with Mn1 in austenitic phase. The magnetic moment of $x = 0.36$ is $3.5 \mu_B/f.u.$ in the austenitic phase at 250 K. The martensitic phase has $1.4 \mu_B/f.u.$ magnetic moment at 150 K. The large decrease in the magnetic moment ($\Delta M = 2.1 \mu_B/f.u.$) is due to anti-ferromagnetic exchange interaction between Mn1 and Mn2. The anti-ferromagnetic interaction is caused by the decrease in the Mn1 and Mn2 distance due to the structural transition [10]. The coercivity as a function of temperature for $x = 0.32$ and 0.36 is shown in Fig. 4.10 (b). The $x = 0.32$ has negligible coercivity due to the austenitic phase. Similar coercivity is also observed in austenitic phase of $x = 0.36$. Significant coercivity is observed for $x = 0.36$ below M_S and it rapidly increases at low temperature.

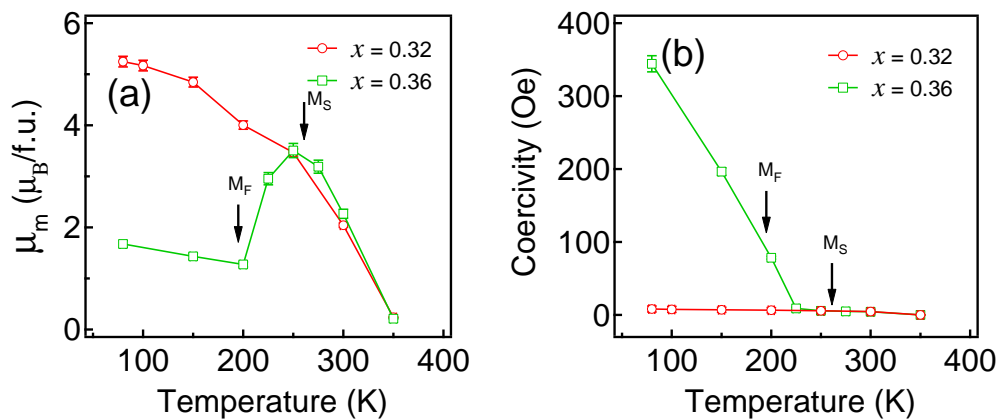


Figure 4.10 (a) Magnetic moment per formula unit (μ_m) as a function of temperature for $Ni_2Mn_{1+x}In_{1-x}$ ($x = 0.32$ and 0.36). (b) Temperature dependent coercivity of $Ni_2Mn_{1+x}In_{1-x}$ ($x = 0.32$ and 0.36).

The $x = 0.36$ composition shows interesting properties [11, 24] and kinetic arrest of martensitic phase transformation [9]. Thus, SQUID measurements are performed at high magnetic field for $x = 0.36$. Figure 4.11 shows the M-T curve at 0.05 Tesla (ZFC, FC and FH) and 14 Tesla (FC). The ZFC, FC and FH magnetization at 0.05 Tesla is very well matching with the VSM result.

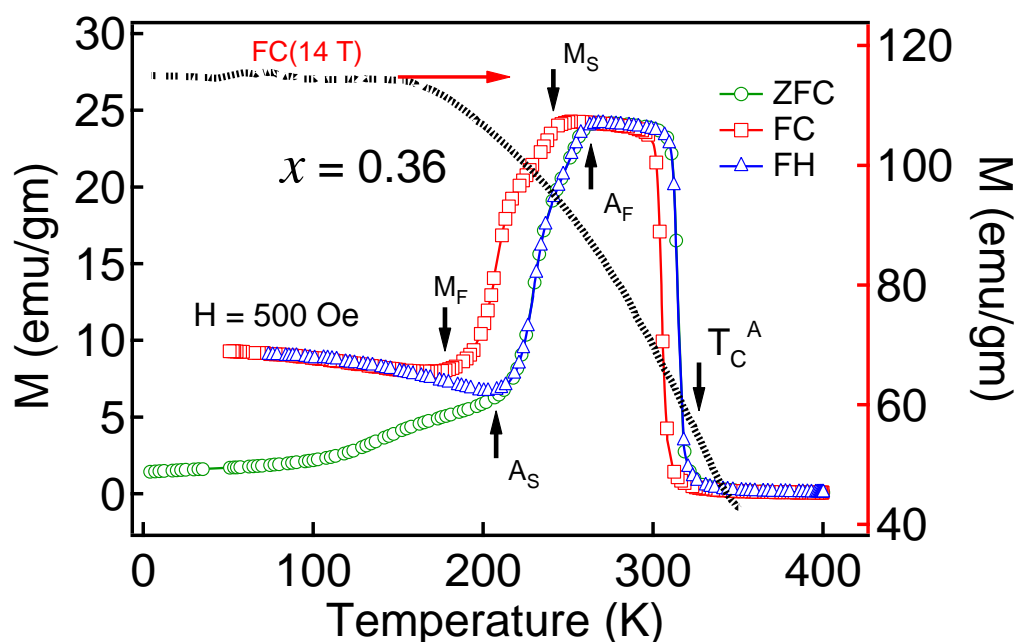


Figure 4.11 Magnetization as a function of temperature for $\text{Ni}_2\text{Mn}_{1.36}\text{In}_{0.64}$.

The small difference in the magnitude is due to the difference in sensitivity and accuracy of two instruments. The magnetization (ZFC, FC and FH) results for $x = 0.36$ [Fig. 4.11] with 0.05 T applied field shows the large drop in magnetization at martensitic transition, whereas with 14 T magnetic field FC magnetization increases with decreasing temperature upto 150 K and saturates below it. This implies that with 14 T FC martensitic transformation is fully blocked. The first order martensitic transformation from ferromagnetic austenite to low magnetization martensite is hindered by the magnetic field [9]. Thus in the presence of magnetic field ferromagnetic austenitic phase can persist upto low temperature. This matches with previous report of kinetic arrest of the first order austenite to martensite phase transition for $x = 0.36$ [13]. Similar phenomenon of kinetic arrest of first-order ferromagnetic to anti-ferromagnetic phase transition has been observed in various intermetallic alloys [25] and in doped manganites [26–29].

The isothermal magnetization upto 14 Tesla is shown the Fig. 4.12 (a) - (f). Measurement is performed during ZFC cycle. At 4 K, M-H curve shows the ferromagnetic behavior and saturation magnetization is ~ 40 emu/gm. At 30 K, M-H curve has similar behavior as 4 K. At 150

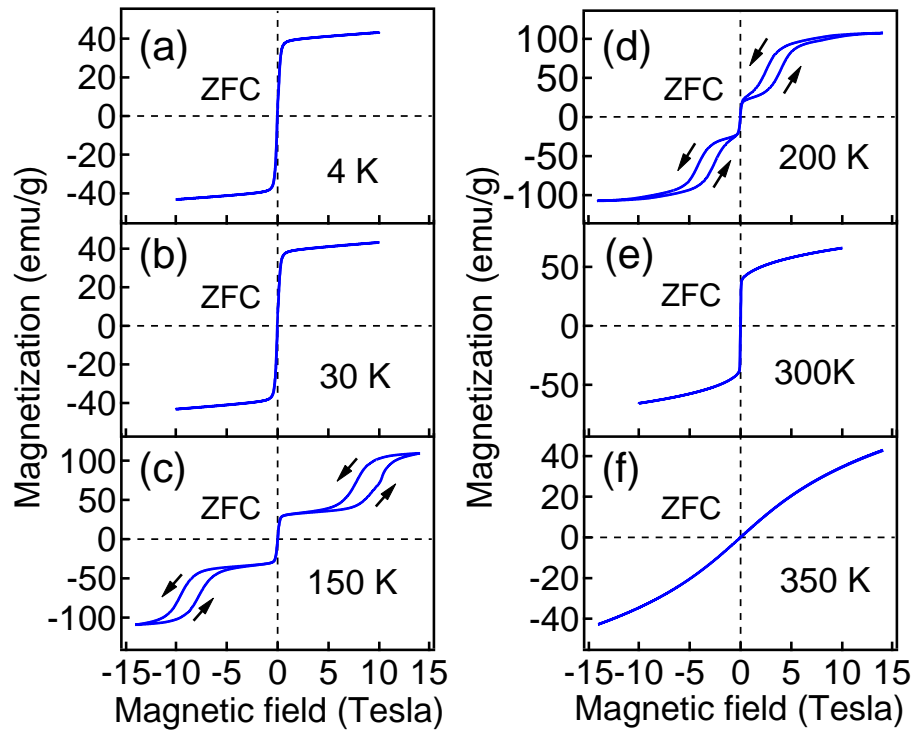


Figure 4.12 Isothermal magnetization as a function of magnetic field for $\text{Ni}_2\text{Mn}_{1.36}\text{In}_{0.64}$ after zero field cooling (ZFC).

K, sample is in complete martensitic phase. At low field below 7 Tesla, predominantly ferromagnetic behaviour is observed. Above 7 Tesla the isothermal magnetization further starts increasing rapidly due to reverse phase transition and above 12 Tesla it saturates. It also shows hysteresis in magnetization around 8 Tesla during increasing and decreasing magnetic field. The hysteresis confirms the magnetic field induced reverse phase transition (MFIRPT). At 200 K during heating it is still in the martensitic phase as austenitic start (A_S) temperature is 213 K. At 200 K the M-H curve has ferromagnetic behaviour upto 2.5 Tesla. Above 2.5 Tesla, the phenomenon of MFIRPT is observed. The transformation is complete above 7 Tesla. The MFIRPT is observed with low magnetic field in the vicinity of martensitic transition. At 300 K, in the austenitic phase it shows the ferromagnetic behavior. At 350 K sample is in paramagnetic phase but the isothermal magnetization deviates from linearity implying that short range ferromagnetic correlations are present in the paramagnetic phase above T_C^A [2].

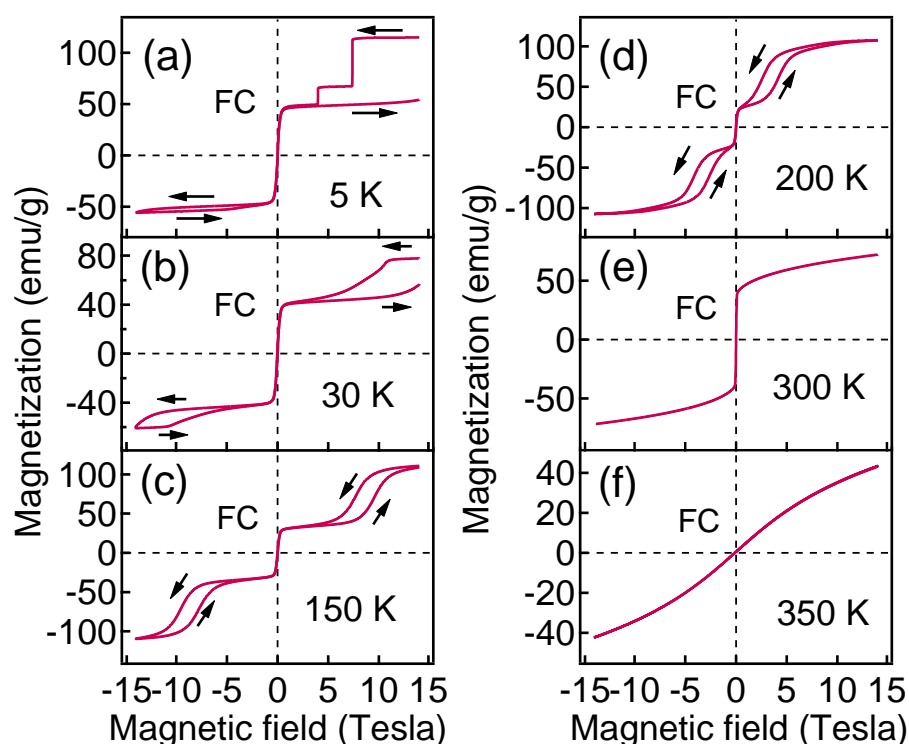


Figure 4.13 Isothermal magnetization as a function of magnetic field for $\text{Ni}_2\text{Mn}_{1.36}\text{In}_{0.64}$ after 14 Tesla field cooling (FC).

Fig. 4.13 (a) - (f) shows the isothermal magnetization after 14 Tesla FC. Measurement is performed during heating cycle with 14 Tesla applied magnetic field. The M-H curves are taken with decreasing magnetic field cycle from 14 Tesla to -14 Tesla and increasing cycle from -14 Tesla to 14 Tesla. The M-H curves at 5 K [Fig. 4.13 (a)] shows the large saturation magnetization (115 emu/gm) at 14 Tesla similar to that obtained with FC M-T at 5 K. This implies that martensitic transformation is completely arrested and only austenitic phase is present at 14 Tesla field. On decreasing magnetic field the magnetization remains constant upto 7.5 Tesla. At 7.5 Tesla a discontinuous and sudden decrease in the magnetization is observed [13]. Again similar drop in magnetization is observed at 4 Tesla magnetic field. The large drop in the magnetization at 7.5 Tesla and 4 Tesla field suggests that some of the arrested austenite phase transform back to martensitic phase. Below 4 Tesla some of the austenite phase is still present. It has the mixed

phase of martensite and austenite because magnetization (~ 49 emu/gm) is still higher than the saturation magnetization (~ 40 emu/gm) recorded at 4 K after cooling the sample in zero field (ZFC). Further, during 0 to -14 Tesla and 0 to 14 Tesla [Fig. 4.13 (a)] no significant change in the phase fraction is observed. It is worth noting that after removing field, further application of 14 Tesla field do not induce MFIRPT. Thus isothermal transition from austenite to martensite phase is irreversible under 14 Tesla field. The 5 K temperature is much below the M_F (195 K) thus very high magnetic field is required for the MFIRPT. Recent study on $\text{Ni}_2\text{Mn}_{1.38}\text{In}_{0.62}$ alloys shows that ~ 17 Tesla field is required for MFIRPT at 4.2 K [12]. At 30 K some fraction of austenitic phase is induced by 14 Tesla field and M-H shows hysteresis in magnetization above 5 Tesla due to MFIRPT. While the ZFC M-H at 30 K shows no hysteresis in magnetization upto 10 Tesla. This implies that with 14 Tesla FC, some arrested austenite phase fraction transforms to martensite phase at low magnetic field. At high magnetic field (14 Tesla) some martensite phase fraction again transforms to austenitic phase. Although complete recovery of initial phase fractions of martensite and austenite is not achieved. At high temperatures, 150 K and 200 K, 14 Tesla FC M-H curves are very identical to ZFC M-H curves, because near the transition temperature 14 Tesla field is sufficient for the complete MFIRPT. In the austenitic phase at 300 K and 350 K M-H curves has similar behavior as ZFC M-H curves.

4.2.3 Co doped Ni-Mn-In alloys

The magnetization as a function of temperature for NCM11 ($\text{Ni}_{1.81}\text{Co}_{0.22}\text{Mn}_{1.46}\text{In}_{0.51}$) at 500 Oe is shown in Fig. 4.14 (a). The magnetization increases below 400 K due to T_C^A (390 K). Below T_C^A magnetization is almost flat till M_S temperature. The martensitic transition temperatures, M_S , M_F , A_S and A_F are 344 K, 327 K, 338 K and 355 K, respectively. Upon martensitic phase transition magnetization drops. The martensitic phase is nonmagnetic and has very small magnetization (less than 0.5 emu/gm). The magnetization in the martensitic phase is almost constant with temperature and no bifurcation between ZFC and FC/FH is observed upto 80 K. The isothermal M-H curves upto 1.6 Tesla is shown in Figs. 4.14 (b) and (c). At 400 K it deviates from linearity implying that

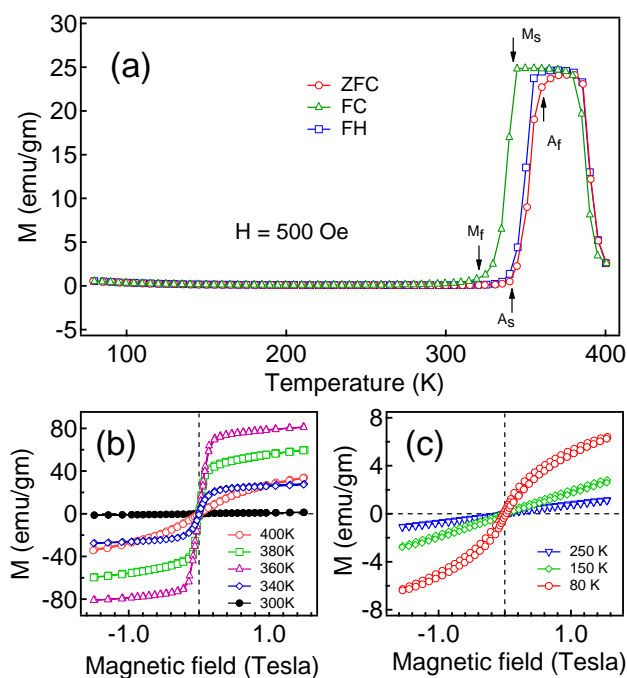


Figure 4.14 (a) Magnetization (ZFC, FC and FH) as a function of temperature for $\text{Ni}_{1.81}\text{Co}_{0.22}\text{Mn}_{1.46}\text{In}_{0.51}$ at 500 Oe. (b) and (c) Isothermal M-H curves at different temperatures.

short range ferromagnetic correlations are present in the paramagnetic phase above T_C^A [2]. The austenitic phase is ferromagnetic and magnetization saturates above 0.5 Tesla. At 250 K and 150 K [Fig. 4.14 (c)] M-H curve is almost linear with small hysteresis. At 80 K, magnetization has parabolic nature. The coercivity is ~ 222 Oe. The magnetic state in the martensitic phase of these alloys is still unclear. It may be paramagnetic or anti-ferromagnetic [30, 31].

Figure 4.15 (a) shows the ZFC, FC and FH behavior of NCMI2 ($\text{Ni}_{1.81}\text{Co}_{0.22}\text{Mn}_{1.45}\text{In}_{0.52}$). The M-T (ZFC, FC and FH) behavior with 500 Oe field shows the large increase in the magnetization just below 400 K, which is due to the onset of T_C^A (397 K). The martensitic transition temperatures, M_S , M_F , A_S and A_F are 334 K, 293 K, 314 K and 348 K, respectively. Below the martensitic finish temperature magnetization still decreases very slowly till 150 K, below which magnetization again slowly increase with decreasing temperature. The bifurcation in the ZFC and FC/FH is observed at 50 K. With 8 Tesla FH, 44 K shift in the structural transition temperature is observed. The NCMI2 has broad martensitic transition as compared to NCMI1. The width of

martensitic transition ($A_F - M_F$) of NCMI2 is 55 K while it is 28 K for NCMI1. The isothermal magnetization behavior for $\text{Ni}_{1.81}\text{Co}_{0.22}\text{Mn}_{1.45}\text{In}_{0.52}$ is shown in Fig. 4.15 (b). It is recorded during ZFC cycle. The magnetization at 400 K has parabolic nature. It is unsaturated upto 14 Tesla. It

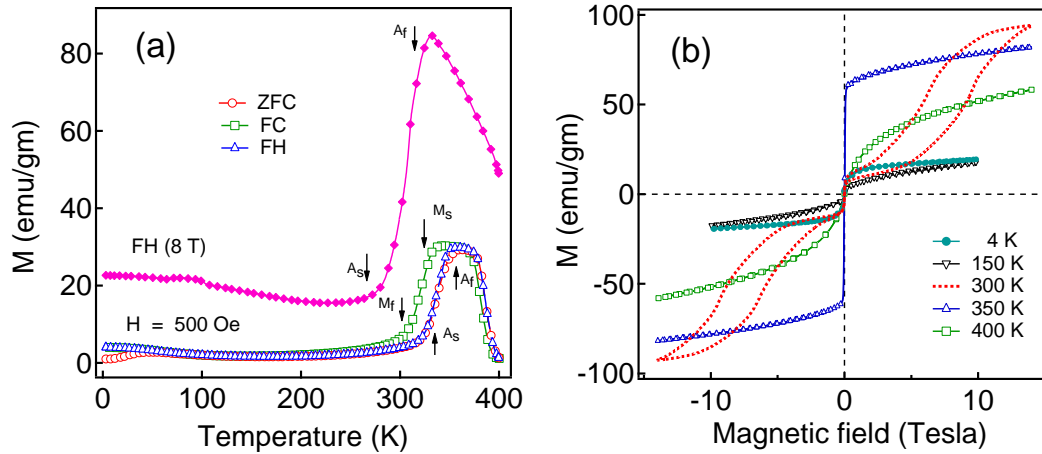


Figure 4.15 (a) Magnetization (ZFC, FC and FH) as a function of temperature for $\text{Ni}_{1.81}\text{Co}_{0.22}\text{Mn}_{1.45}\text{In}_{0.52}$. (b) Isothermal M-H curves for $\text{Ni}_{1.81}\text{Co}_{0.22}\text{Mn}_{1.45}\text{In}_{0.52}$.

indicates the presence of ferromagnetic short-range correlations in the paramagnetic state near the T_C^A . At 350 K, magnetization shows complete ferromagnetic behaviour and it saturates above 0.3 Tesla. The saturation magnetization is 61 emu/gm. At 300 K, during heating it is in the martensitic phase as the austenitic start (A_S) temperature is 314 K. Thus at 300 K magnetization shows the phenomenon of MFIRPT. Similar phenomenon is also observed in $\text{Ni}_2\text{Mn}_{1.36}\text{In}_{0.64}$ alloys. Much below the A_S temperature at 150 K magnetization shows dominant paramagnetic nature with small ferromagnetic characteristic. At 4 K, weak ferromagnetic behaviour with low saturation magnetization of 15 emu/gm above 2.5 Tesla is observed. The magnetic state in the martensitic phase of these alloys is still unclear. It may be paramagnetic or anti-ferromagnetic [30,31], which gradually transform to weak ferromagnetic state at low temperature.

The large change in the magnetization (ΔM) across the martensitic transformation is observed in NCMI1 (~ 24 emu/gm at 500 Oe) and NCMI2 (~ 25 emu/gm at 500 Oe) as compared to $\text{Ni}_2\text{Mn}_{1.36}\text{In}_{0.64}$ (~ 16 emu/gm at 500 Oe). Thus, magnetic field induced functional properties are expected to enhance for Ni-Co-Mn-In alloys.

4.2.4 Inverse magnetocaloric effect

As discussed in the introduction, inverse MCE is observed in systems which undergoes the first-order magnetic transformations. The large inverse MCE is expected in the Co doped Ni-Mn-In alloys due to the large change in the magnetization across martensitic transition. The magnetocaloric properties of NCM11 ($\text{Ni}_{1.81}\text{Co}_{0.22}\text{Mn}_{1.46}\text{In}_{0.51}$) and NCM12 ($\text{Ni}_{1.81}\text{Co}_{0.22}\text{Mn}_{1.45}\text{In}_{0.52}$) is studied in the low magnetic field upto 1.5 Tesla. The change in entropy ΔS_m as function of temperature in different external fields are obtained from magnetization by using Maxwell relation [8, 32–34]

$$\Delta S_m(P, T, H)_{P,T,\Delta H} = \int_0^H \left(\frac{\partial M(P, T, H)}{\partial T} \right)_{P,H} dH \quad (4.1)$$

The corresponding refrigeration capacity (RC) is defined as [32, 35]

$$RC = \int_{T_1}^{T_2} [\Delta S(T)]_{\Delta H} dT \quad (4.2)$$

where T_1 and T_2 correspond, respectively, to the cold and hot temperatures during the cycle. The RC values are calculated using numerical integration of the ΔS_m temperature dependence. The integration limits are the temperatures at half maximum of the ΔS_m peak [inset of Fig. 4.17 (a)].

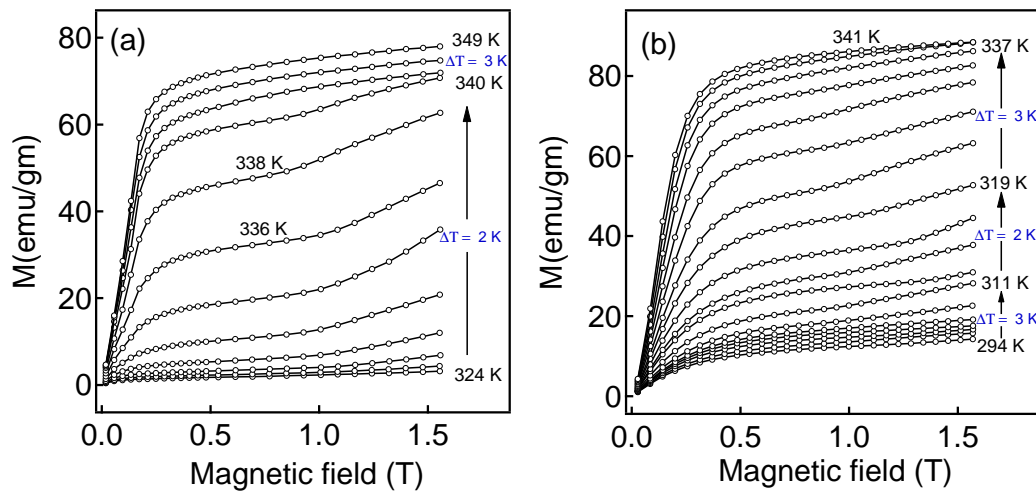


Figure 4.16 Isothermal M-H curves in the martensitic transition region for (a) $\text{Ni}_{1.81}\text{Co}_{0.22}\text{Mn}_{1.46}\text{In}_{0.51}$, (b) $\text{Ni}_{1.81}\text{Co}_{0.22}\text{Mn}_{1.45}\text{In}_{0.52}$.

The magnetization isotherms in the transition region are shown in 4.16 (a) and Fig. 4.16 (b) for NCM11 and NCM12, respectively. The magnetization isotherms are recorded during heating

cycle. The temperature dependence of ΔS_m [calculated by using Eq. 4.1] for NCM11 is shown in Fig. 4.17 (a) and (b) upto 1.5 Tesla during cooling and heating, respectively. The large positive peak is obtained across the martensitic transition. The ΔS_m is negative for conventional MCE, while it is positive for inverse MCE [36]. Thus NCM11 exhibit inverse MCE at the martensitic transition. A clear shift in the peak position during heating and cooling due to the first order nature

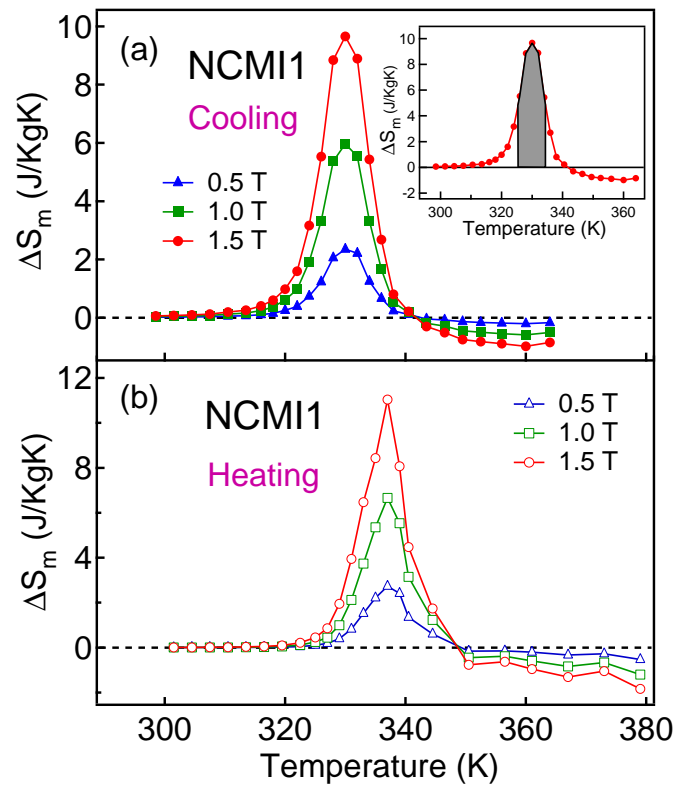


Figure 4.17 Entropy change ΔS_m for $\text{Ni}_{1.81}\text{Co}_{0.22}\text{Mn}_{1.46}\text{In}_{0.51}$ during (a) cooling, (b) heating.

of martensitic transition is also observed. The peak value of ΔS_m is 9.7 J/Kg K (1.5 Tesla) at 330 K during cooling. During heating it is 11 J/Kg K (1.5 Tesla) at 337 K. This value of ΔS_m is higher than single crystal of $\text{Ni}_{1.8}\text{Co}_{0.2}\text{Mn}_{1.5}\text{In}_{0.5}$ [32]. In comparison to other MCE materials like colossal magnetoresistive manganites, Fe-based intermetallic material ($\text{LaFe}_{11.47}\text{Co}_{0.23}\text{Al}_{1.3}$) and Gd, these alloys have much higher ΔS_m value [33]. Maximum ΔS_m is obtained near M_F during cooling cycle while it is obtained near A_S during heating cycle because at low magnetic field maximum change

in the magnetization (ΔM) is obtained near M_F and A_S . In the austenitic phase ΔS_m is negative (conventional MCE) and maximum is below -2 J/Kg K (1.5 Tesla).

The RC value calculated from Eq. 4.2 is 71.2 J/Kg and 43.3 J/Kg for 1.5 Tesla and 1.0 Tesla, respectively, during cooling. During heating it is 65.4 J/Kg and 41.2 J/Kg for 1.5 Tesla and 1.0 Tesla, respectively. The temperature difference ($\Delta T_{RC} = T_2 - T_1$) at half maximum of the ΔS_m peak is ~ 8 K. The ΔT_{RC} represents the suitable temperature interval over which sample could be utilized for magnetic cooling.

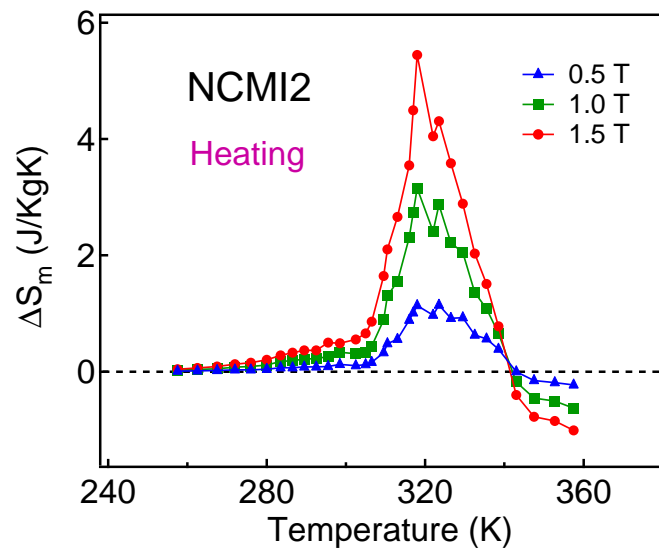


Figure 4.18 Entropy change ΔS_m for $\text{Ni}_{1.81}\text{Co}_{0.22}\text{Mn}_{1.45}\text{In}_{0.52}$ during heating.

Figure 4.18 represent the temperature dependence of ΔS_m during heating for NCM12. As it is clear from the DSC and magnetization results, the martensitic transition hysteresis is wider for NCM12, the ΔS_m also shows wide peak around martensitic transition. The maximum ΔS_m is 5.4 J/Kg K (1.5 Tesla) at 318 K, which is lower than NCM11. On the contrary, RC value [66.1 J/Kg at 1.5 Tesla and 43.9 J/Kg at 1.0 Tesla] is similar to the NCM11 sample. Interestingly the ΔT_{RC} value for NCM12 is ~ 17 K that is higher than NCM11.

Recent studies on Ni-Co-Mn-In alloys show that the ordered alloy has broad martensitic transformation temperature range, higher magnetization and higher T_C^A than disordered alloy [37–39]. Disorder can be induced in the quenched samples if the quenching temperature is higher than order-

disorder transition temperature. Although both NCMI1 and NCMI2 are quenched from higher temperature (1173 K) than order-disorder transition temperature (896 K) [30], NCMI2 is more ordered than NCMI1. The atomic ordering is directly manifested as superlattice line in XRD pattern for ordered alloys. In fully disordered alloy superlattice line is absent. For intermediate ordering

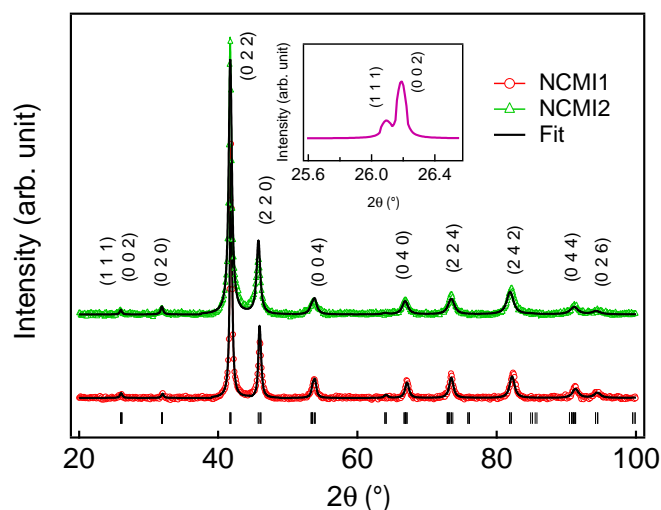


Figure 4.19 Room temperature XRD pattern of NCMI1 and NCMI2 with fitted pattern. The inset shows the calculated pattern of fully ordered NCMI1 alloys around superlattice (111) line.

the superlattice line becomes weaker. For ordered NCMI1 and NCMI2 in the martensitic phase, the superlattice line is expected at $2\theta = 26.09^\circ$ with $hkl = (111)$ as shown in inset of Fig. 4.19. The calculated relative intensity of (111) reflection is only 4%. Moreover, the (002) reflection also appears in the vicinity at $2\theta = 26.19^\circ$ with 14% relative intensity. The experimental XRD pattern (Fig. 4.19) shows a peak at $2\theta = 26.13^\circ$ as a superposition of both (111) and (002) reflection. Thus, given the limited resolution and flux of the laboratory room temperature XRD setup it is difficult to observe and quantify the ordering from XRD. Hence, the disorder effect is clearly studied from resistivity at low temperature as shown in Fig. 4.20. At the low temperature disorder effect dominates and the resistivity is almost constant with temperature in both samples. The residual resistivity (0 Tesla) of NCMI1 is almost 24% higher than NCMI2. Under 1 Tesla magnetic field there is a significant decrease in resistivity for NCMI2 while the decrease is negligible for NCMI1.

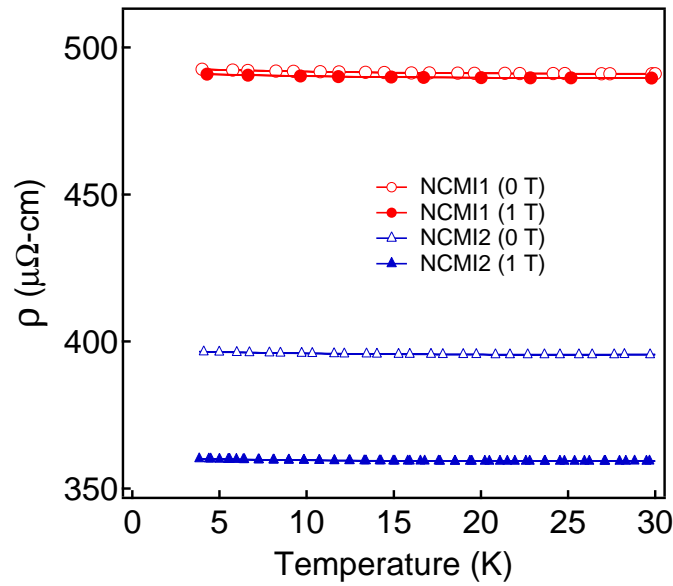


Figure 4.20 Electrical resistivity as a function of temperature for NCM1 and NCM2 with 0 Tesla and 1 Tesla magnetic field.

This shows that the disorder in NCM1 is structure and magnetic related. Application of 1 Tesla magnetic field is not enough to bring magnetic ordering through spin-lattice coupling. Whereas NCM2 has structural ordering. Hence application of 1 Tesla magnetic field brings spin ordering through spin-lattice coupling. Thus the low temperature resistivity confirms that NCM1 is more disordered than NCM2. The excess Mn at In site brings the magnetic disorder. This might be the controlling factor for the quench disorder in these alloys. Thus ordered sample has lower peak value of ΔS_m due to the broad nature of martensitic transition while RC is almost same as compared to disordered sample. This shows that, almost equal cooling capacity lies in a narrow range of temperature for disordered system while it is distributed over wide range of temperature for ordered system. Thus the higher ΔT_{RC} value for ordered sample provides the scope for utilization of sample over wider temperature range.

4.3 Conclusion

The magnetic properties of Ni-Mn-Sn, Ni-Mn-In and Ni-Co-Mn-In alloys are investigated. Austenitic phase has, predominately, ferromagnetic ground state while martensitic phase has mix magnetic (ferro and anti-ferro) ground state. The anti-ferromagnetic coupling occurs between Mn at Mn site (Mn1) and Mn at Sn (In) site (Mn2). The anti-ferromagnetic fraction increases with the increase in Mn concentration. The competition between the ferromagnetic and anti-ferromagnetic spins leads to the ZFC-FC bifurcation at low temperature. The Ni-Mn-Sn alloys has less magnetic moment compared to Ni-Mn-In alloys in the austenitic phase. The coercivity increases in martensitic phase as well as with increasing Mn concentration. In the austenitic phase of Ni-Mn-Sn alloys Mn1 and Mn2 atoms have weak anti-ferromagnetic coupling while in the case of Ni-Mn-In alloys Mn1 and Mn2 atoms have ferromagnetic coupling. This difference might be related with the larger atomic size of In than Sn and higher lattice parameter of Ni-Mn-In alloys compared to Ni-Mn-Sn alloys. Along with MFIRPT, blocking of martensitic transformation is observed for Ni-Mn-In, whereas, Ni-Mn-Sn do not show this property. The blocking of martensitic transformation occurs only under FC. The Co doping in Ni-Mn-In alloys further increases the magnetic moment and T_C^A which results in the martensitic transition above room temperature. The huge change in the magnetization at the martensitic transition in Ni-Co-Mn-In alloys gives the large inverse MCE in low magnetic field. Large inverse MCE ($\Delta S_m = 11 \text{ J/Kg K}$) has been observed in $\text{Ni}_{1.81}\text{Co}_{0.22}\text{Mn}_{1.46}\text{In}_{0.51}$ at 337 K in 1.5 Tesla field. The atomic disorder significantly increases the peak value of ΔS_m and decreases the peak width. The refrigeration capacity (RC) is almost unchanged with atomic disorder.

Bibliography

- [1] J. Kubler, A. R. Williams, and C. B. Sommers, *Phys. Rev. B* **28**, 1745 (1983).
- [2] T. Krenke, M. Acet, E. F. Wassermann, X. Moya, L. Mañosa, and A. Planes, *Phys. Rev. B* **72**, 014412 (2005).
- [3] M. Ye, A. Kimura, Y. Miura, M. Shirai, Y. T. Cui, K. Shimada, H. Namatame, M. Taniguchi, S. Ueda, K. Kobayashi, R. Kainuma, T. Shishido, K. Fukushima, and T. Kanomata, *Phys. Rev. Lett.* **104**, 176401 (2010).
- [4] S. Chatterjee, S. Giri, S. K. De, and S. Majumdar, *Phys. Rev. B* **79**, 092410 (2009).
- [5] P. J. Brown, A. P. Gandy, K. Ishida, R. Kainuma, T. Kanomata, K.-U. Neumann, K. Oikawa, B. Ouladdiaf, and K. R. A. Ziebeck, *J. Phys.: Condens. Matter* **18**, 2249 (2006).
- [6] R. Kainuma, K. Ito, W. Ito, R. Y. Umetsu, T. Kanomata, and K. Ishida, *Mater. Sci. Forum* **635**, 23 (2010).
- [7] S. Chatterjee, S. Giri, S. Majumdar, and S. K. De, *Phys. Rev. B* **77**, 012404 (2008).
- [8] A. Planes, L. Manosa, and M Acet, *J. Phys.: Condens. Matter* **21**, 233201 (2009).
- [9] V. K. Sharma, M. K. Chattopadhyay, and S. B. Roy, *Phys. Rev. B* **76**, 140401R (2007).
- [10] T. Krenke, M. Acet, E.F. Wassermann, X. Moya, L. Mañosa, and A. Planes, *Phys. Rev. B* **73**, 174413 (2006).

- [11] V. K. Sharma, M. K. Chattopadhyay, K. H. B. Shaeb, A. Chouhan, and S. B. Roy, *Appl. Phys. Lett.* **89**, 222509 (2006).
- [12] R. Y. Umetsu, Y. Kusakari, T. Kanomata, K. Suga, Y. Sawai, K. Kindo, K. Oikawa, R. Kainuma, and K. Ishida, *J. Phys. D: Appl. Phys.* **42**, 075003 (2009).
- [13] R. Y. Umetsu, W. Ito, K. Ito, K. Koyama, A. Fujita, K. Oikawa, T. Kanomata, R. Kainumaa, and K. Ishida, *Scripta Mater.* **60**, 25 (2009).
- [14] P. J. Webster, *J. Phys. Chem. Solids* **32**, 1221 (1971).
- [15] R. Kainuma, Y. Imano, W. Ito, Y. Sutou, H. Morito, S. Okamoto, O. Kitakami, K. Oikawa, A. Fujita, T. Kanomata, and K. Ishida, *Nature* **439**, 957 (2006).
- [16] H. E. Karaca, I. Karaman, B. Basaran, Y. Ren, Y. I. Chumlyakov, and H. J. Maier, *Adv. Funct. Mater.* **19**, 983 (2009).
- [17] V. V. Sokolovskiy, V. D. Buchelnikov, M. A. Zagrebin, P. Entel, S. Sahoo, and M. Ogura, *Phys. Rev. B* **86**, 134418 (2012).
- [18] P. J. Webster, K. R. A. Ziebeck, S. L. Town, and M. S. Peak, *Philos. Mag. B.* **49**, 295 (1984).
- [19] A. Ayuela, J. Enkovaara, K. Ullakko, and R. M. Nieminen, *J. Phys.: Condens. Matter* **11**, 2017 (1999).
- [20] P. A. Bhohe, K. R. Priolkar, and P. R. Sarode, *J. Phys.: Condens. Matter* **20**, 015219 (2008).
- [21] S. Aksoy, M. Acet, P. P. Deen, L. Mañosa, and A. Planes, *Phys. Rev. B* **79**, 212401 (2009).
- [22] R. Y. Umetsu, A. Fujita, W. Ito, T. Kanomata, and R. Kainuma, *J. Phys.: Condens. Matter* **23**, 326001 (2011).
- [23] Z. Li, C. Jing, J. Chen, S. Yuan, S. Cao, and J. Zhang, *Appl. Phys. Lett.* **91**, 112505 (2007).
- [24] T. Krenke, E. Duman, M. Acet, E. Eberhard, F. Wassermann, X. Moya, L. Mañosa, and A. Planes, *Phys. Rev. B* **75**, 104414 (2007).

- [25] M. K. Chattopadhyay, S. B. Roy, and P. Chaddah, *Phys. Rev. B* **72**, 180401(R) (2005).
- [26] W. Wu, C. Israel, N. Hur, S. Park, S-W. Cheong, and A. D. Lozanne, *Nature Mater.* **5**, 881 (2006).
- [27] A. Banerjee, K. Mukherjee, K. Kumar, and P. Chaddah, *Phys. Rev. B* **74**, 224445 (2006).
- [28] P. Chaddah, K. Kumar, and A. Banerjee, *Phys. Rev. B* **77**, 100402(R) (2008).
- [29] Y. J. Choi, C. L. Zhang, N. Lee, and S-W. Cheong, *Phys. Rev. Lett.* **105**, 097201 (2010).
- [30] W. Ito, M. Nagasako, R. Y. Umetsu, R. Kainuma, T. Kanomata, and K. Ishida, *Appl. Phys. Lett.* **93**, 232503 (2008).
- [31] A. N. Vasiliev, O. Heczko, O. S. Volkova, T. N. Vasilchikova, T. N. Voloshok, K. V. Klimov, W. Ito, R. Kainuma, K. Ishida, K. Oikawa, and S. Fähler, *J. Phys. D: Appl. Phys.* **43**, 055004 (2010).
- [32] D. Bourgault, J. Tillier, P. Courtois, D. Maillard, and X. Chaud, *Appl. Phys. Lett.* **96**, 132501 (2010).
- [33] V. K. Pecharsky and K. A. Gschneidner, Jr., *J. Appl. Phys.* **90**, 4614 (2001).
- [34] L. Chen, F. X. Hu, J. Wang, J. Shen, J. Zhang, J. R. Sun, B. G. Shen, J. H. Yin, and L. Q. Pan, *J. Appl. Phys.* **107**, 09A940 (2010).
- [35] K. A. Gschneidner, Jr., V. K. Pecharsky, A. O. Pecharsky, and C. B. Zimm, *Mater. Sci. Forum* **315**, 69 (1999).
- [36] T. Krenke, E. Duman, M. Acet, E. F. Wassermann, X. Moya, L. Mañosa, and A. Planes, *Nat. Mater.* **4**, 450 (2005).
- [37] V. Recarte, J. I. Pérez-Landazábal, V. Sánchez-Alarcos, and J. A. Rodríguez-Velamazán, *Acta Mater.* **60**, 1937 (2012).

- [38] J. I. Pérez-Landazábal, V. Recarte, V. Sánchez-Alarcos, C. Gómez-Polo, and E. Cesari, *Appl. Phys. Lett.* **102**, 101908 (2013).
- [39] S. Kustov, M. L. Corró, J. Pons, and E. Cesari, *Appl. Phys. Lett.* **94**, 191901 (2009).

Chapter 5

Electrical-transport property

5.1 Introduction

Earlier the electrical transport in Mn based [Ni₂MnSn, Pd₂MnSn, Cu₂MnAl, Pd₂MnIn, Cu₂NiSn] Heusler alloys is studied in stoichiometric composition (X₂YZ) [1–4]. The transport properties of these compounds are consistent with what would be expected for a local moment ferromagnet [1]. The electrical resistivity in ideal Heusler alloys (X₂YZ) comes from two main sources, scattering of electrons by lattice vibrations and scattering from the interaction with the spin system [1]. The very basic property of electrical resistivity in metals is modified by the presence of disorder in the crystalline system. In the off-stoichiometric Heusler alloys martensitic transformation and disorder effects (site and magnetic) significantly modifies the electrical resistivity [5,6]. The martensitic transition also enhances the structural and magnetic disorder in the system. The understanding of electrical resistivity behavior of Mn-based ferromagnetic Heusler alloys with martensitic transition is very vague and have been attempted earlier by very few [6–11]. The transport property of Ni₂MnGa is dominated by electron-magnon and electron-phonon scattering [7]. The present chapter deals with the disorder induced effects in resistivity of the Heusler alloy with martensitic transition. The electrical resistivity of Ni₂Mn_{1+x}Sn_{1-x}, Ni₂Mn_{1+x}In_{1-x} and Ni_{1.8}Co_{0.2}Mn_{1+x}In_{1-x} have been studied as a function of excess Mn (Mn₂) concentration (*x*) in the martensite and austenite phases. Here the qualitative and quantitative interpretation of electrical resistivity is presented as a function of temperature and magnetic field. The change in the electrical resistivity with the Mn concentration is discussed in term of site and magnetic disorder. The understanding of various scattering processes involved in the total resistivity behaviour with the increase in disorder is presented. At the end, the contribution from different scattering mechanisms which are responsible for anomalous resistivity behaviour at low temperature in the martensitic phase has been estimated through experimental data fitting. The effect of magnetic field on the different scattering mechanisms in austenitic and martensitic phases are also discussed. The analysis of experimental data by least square fit method assuming a model provides an insight of various magnetic and structural interplay in these systems.

5.2 Result and Discussion

5.2.1 $\text{Ni}_2\text{Mn}_{1+x}\text{Sn}_{1-x}$ alloys

The electrical resistivity (ρ) as a function of temperature (T) for $\text{Ni}_2\text{Mn}_{1+x}\text{Sn}_{1-x}$ alloys is shown in the Fig. 5.1. The thermal hysteresis in the ρ -T curve represents the first order structural (martensitic) transition. In the austenitic phase resistivity decreases with decreasing temperature. The martensitic phase transition is accompanied by the large jump in the resistivity. The martensitic phase always has larger resistivity than austenitic phase. At the martensitic transition the resistivity increases by $\approx 78\%$ and $\approx 63\%$ for $x = 0.40$ and 0.44 , respectively. With the increase in the Mn2 concentration ρ of the martensitic phase increases while in the austenitic phase ρ is almost similar.

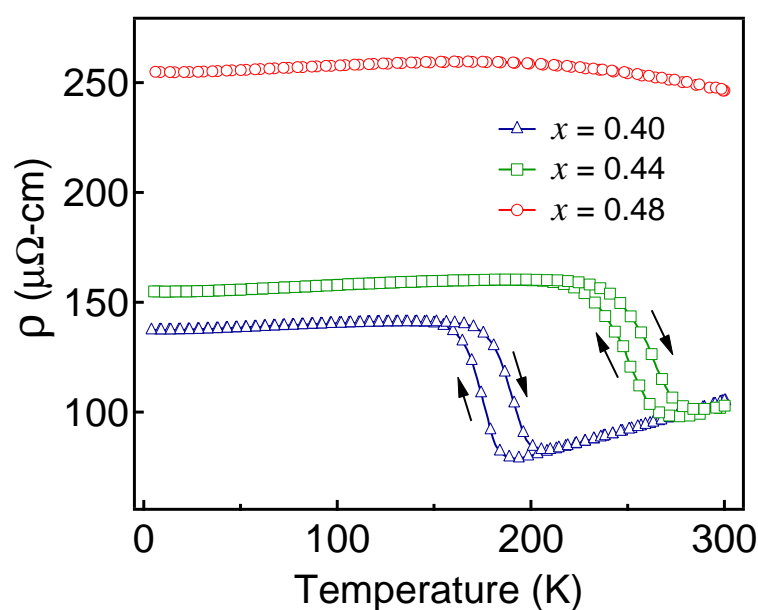


Figure 5.1 Resistivity (ρ) as a function of temperature for $\text{Ni}_2\text{Mn}_{1+x}\text{Sn}_{1-x}$.

The martensitic transition induces the structural and magnetic complexity in the martensitic phase. The structural transformation from austenitic phase to martensitic phase is accompanied by the formation of twin variants. The twin variants are oriented in several directions. The conduction electrons are scattered by these twin variants [11]. Also, the structure of martensitic phase is

modulated [12, 13]. These twins and modulated structures contribute largely to the static disorder in the martensitic phase. Thus the low symmetry martensitic phase have higher residual resistivity than the high symmetry austenitic phase [5].

The alloy properties in the martensitic phase is heavily affected by Mn2 disorder. The change in Mn2 concentration has very little effect on resistivity in the austenitic phase. With the increase in the Mn2 concentration, structure of martensitic phase changes from tetragonal ($L1_0$) to orthorhombic to layered structure (5M or 7M) [12, 13]. The increase in the degree of modulation results in the increase in the static disorder with Mn2 concentration. These structural changes also affects the twin structure [14]. Thus small increase in the Mn2 concentration results in the large increase in the static disorder of martensitic phase. This induces the large increase in the resistivity of martensitic phase with increasing Mn2 concentration.

The effect of magnetic field on the martensitic transformation and electrical resistivity is shown in the Fig. 5.2. With applied magnetic field (7 Tesla) the transition temperatures shift to lower temperature. The thermal hysteresis with 0 Tesla and 7 Tesla magnetic field and transition temperature shift with 7 Tesla magnetic field is shown in Table 5.1. This shift causes the magnetic field induced reverse phase transformation in the vicinity of the transformation. For example, if magnetic field (7 Tesla) is applied at 170 K [shown by dotted line in Fig. 5.2 (a)] then the mixed phase of martensite and austenite will change to almost full austenite.

Table 5.1 Martensite transition temperature shift (ΔT_M) with 7 Tesla magnetic field and thermal hysteresis with 0 Tesla and 7 Tesla magnetic field. The error in temperatures are within ± 1 K.

x	ΔT_M (K)	Hysteresis at 0 Tesla (K)	Hysteresis at 7 Tesla (K)
0.40	13	15	18
0.44	12	13	15

A close observation of resistivity behavior at low temperature reveals the resistivity minimum (ρ_{min}) in the range of 10 - 16 K as a function of composition. The Fig. 5.3 shows the ρ/ρ_{min}

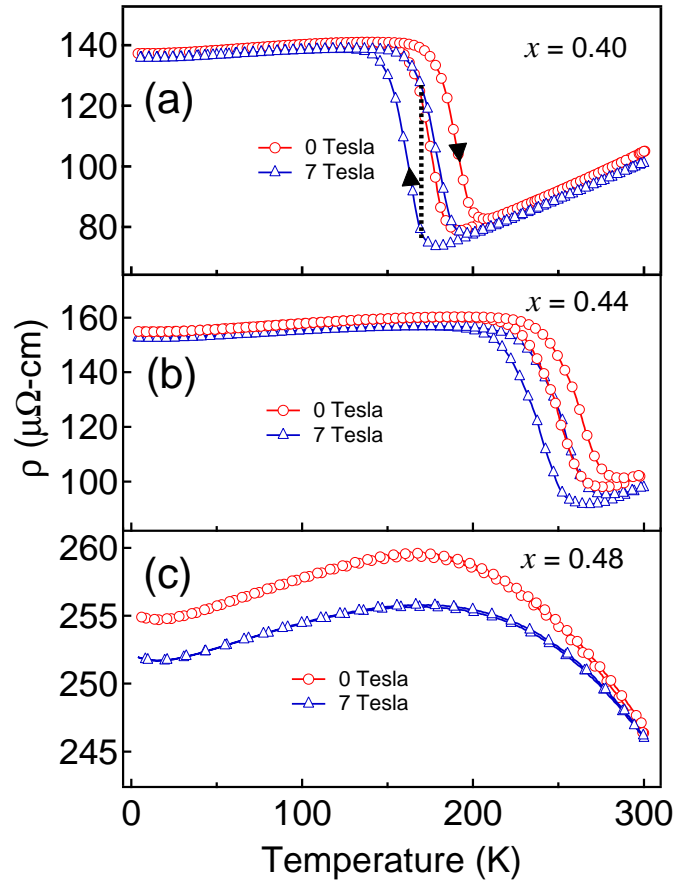


Figure 5.2 Resistivity as a function of temperature for $\text{Ni}_2\text{Mn}_{1+x}\text{Sn}_{1-x}$ with 0 Tesla and 7 Tesla field.

as a function of temperature for all the four compositions without and with applied 7 Tesla magnetic field. The temperature at resistivity minimum [$T(\rho_{min})$], shown by upward arrow in Fig. 5.3, increases with the increase in Mn concentration and is summarized in Table 5.2. Such resistivity upturn have been found in disordered alloy systems [15–17]. The disordered $\text{Ni}_{1-x}\text{Mn}_x$ also shows the resistivity minima at low temperature, which increases with increasing Mn concentration. It is associated with onset of mixed (spin glass and ferromagnetic) or the frustrated state [18]. The $\text{Ni}_2\text{Mn}_{1+x}\text{Sn}_{1-x}$ are disordered system where Mn2 creates the site disorder and perturbation in uniform potential. The magnetization data shows the presence of ferromagnetic and anti-ferromagnetic interactions in the martensitic phase, which can lead to the spin glass like state at

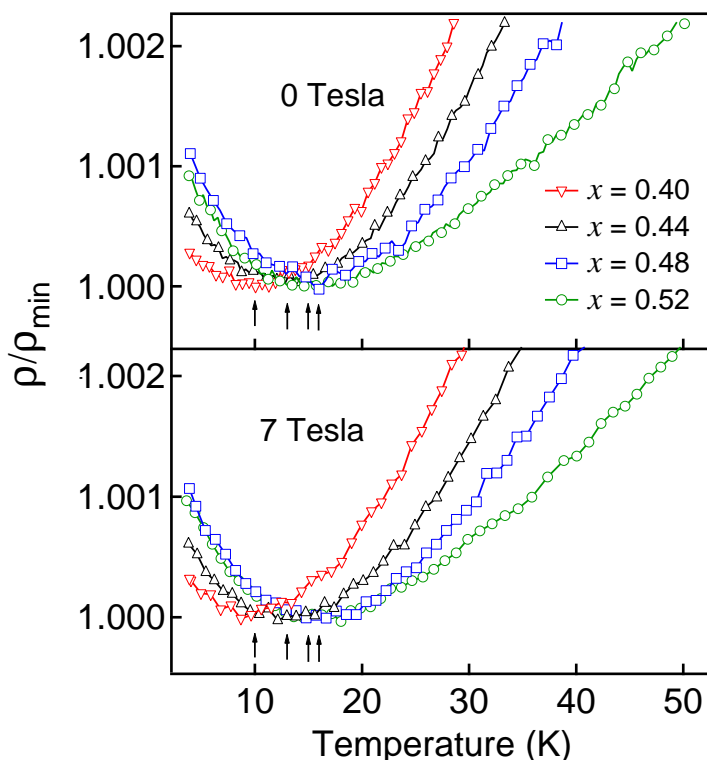


Figure 5.3 Resistivity (ρ) divided by resistivity minimum (ρ_{min}) as a function of temperature under 0 Tesla and 7 Tesla for $\text{Ni}_2\text{Mn}_{1+x}\text{Sn}_{1-x}$.

low temperature. The neutron-polarization-analysis also shows that Mn2 is anti-ferromagnetically coupled to Mn1 in martensitic phase [19]. The magnetic disorder can also result in resistivity upturn at low temperature similar to classical spin-glass systems. For the composition $x = 0.48$, which is in the martensitic phase below 300 K, the resistivity shows the broad maxima around 167 K. Under application of 7 Tesla magnetic field the curvature of maxima becomes more flat. This behaviour of resistivity is very similar to the classical spin glass systems like Au-Cr, Au-Mn, Cu-Mn etc [20]. For the $x < 0.48$ this effect is not so pronounced because of the martensitic transition temperature is very close to resistivity maximum temperature.

The interplay of site and magnetic disorder with structural modification is estimated through different scattering mechanisms that are responsible for anomalous resistivity at low temperature. The experimental data is fitted in the temperature range of $4 \text{ K} \leq T \leq 40 \text{ K}$ and $200 \text{ K} \leq T \leq 300$

Table 5.2 $T(\rho_{min})$ and depth of ρ_{min} of $Ni_2Mn_{1+x}Sn_{1-x}$ under 0 Tesla and 7 Tesla magnetic field. The error in temperature is within ± 1 K.

x	$T(\rho_{min})$ (K)		Depth of ρ_{min} (%)	
	0 Tesla	7 Tesla	0 Tesla	7 Tesla
0.40	10	10	0.03	0.03
0.44	13	13	0.06	0.06
0.48	16	16	0.10	0.10
0.52	15	15	0.09	0.09

K for martensitic and austenitic phase, respectively. Assuming Matthiessen's rule, the measured resistivity is sum of the all contributions given by

$$\rho_{total}(T) = \rho_0 + \rho_{phonon}(T) + \rho_{magnetic}(T) + \rho_{disorder}(T) \quad (5.1)$$

Where, ρ_0 is residual resistivity due to temperature independent scattering of electrons from the lattice defects and impurities. The ρ_{phonon} is the resistivity contribution from scattering of conduction electrons by phonons. For magnetic metals and alloys with d-band density of states, the ρ_{phonon} is expressed by Bloch-Wilson equation [21, 22]. This temperature dependence is true for both martensitic and austenitic phase. The $\rho_{disorder}$ is not valid at high temperature. Also, the effect of disorder in austenitic phase is modified by the martensitic transition. Thus, $\rho_{disorder}$ term is applicable in martensite phase only. The temperature dependence of $\rho_{magnetic}$ in Eq. 5.1 is different in martensitic and austenitic phase and that are discussed below.

Martensitic phase

These alloys have mixed ferromagnetic and anti-ferromagnetic state in martensitic phase as discussed earlier. The frequency dependent ac-susceptibility analysis concludes that reentrant-spin-glass like phase develops from spin frustration arising from the short-range anti-ferromagnetic interaction [23–27]. The resistivity of spin glasses due to the disorder of the spin system has $BT^2 - CT^{5/2}$ variation for the spin diffusive modes below spin freezing temperature (T_f) with

positive coefficients B and C [28, 29]. Thus, $\rho_{magnetic}$ is considered as $BT^2 - CT^{5/2}$ in the low temperature martensitic phase.

The $\rho_{disorder}$ is due to the site-disorder induced localization of the electronic wave function, which has $-\sqrt{T}$ dependence of temperature [30]. The $-\sqrt{T}$ dependence is also valid for the electron-electron interaction effect [30–32]. With the increase in site-disorder the depth of ρ_{min} is increasing (Table 5.2). However, the depth of ρ_{min} is not destroyed by magnetic field (Table 5.2). The $T(\rho_{min})$ is also not effected by the magnetic field (Table 5.2). These imply interplay of both disorder induced localized states and electron-electron interaction at low temperature. Hence the Eq. 5.2 for the martensitic phase is expressed as

$$\rho_{total}(T) = \rho_0 + A\left(\frac{T}{\theta_D}\right)^3 \int_0^{\frac{\theta_D}{T}} \frac{x^3}{(e^x - 1)(1 - e^{-x})} dx + (BT^2 - CT^{5/2}) - D\sqrt{T} \quad (5.2)$$

where A is the strength of conduction electron scattering by phonon's, B and C are represents the strength of diffusive spin excitation and D is the measure of localized states and electron-electron interaction. From the least square fitting by Eq. 5.2, the individual contributions to the total resistivity are plotted in Fig. 5.4. The corresponding coefficients are summarized in Table 5.3 (ZFC) and Table 5.4 (FC).

Table 5.3 The parameters obtained from least square fitting of ZFC experimental data by Eq. 5.2 for $\text{Ni}_2\text{Mn}_{1+x}\text{Sn}_{1-x}$.

x	ρ_0 ($\mu\Omega$ -cm)	A ($\mu\Omega$ -cm)	B $\times 10^{-4}$ ($\mu\Omega$ -cm/ K^2)	C $\times 10^{-5}$ ($\mu\Omega$ -cm/ $K^{5/2}$)	θ_D (K)	D $\times 10^{-2}$ ($\mu\Omega$ -cm/ $K^{1/2}$)
0.40	137	26.44 \pm 1.28	11.6 \pm 0.7	14.9 \pm 3.2	251 \pm 4	9.1 \pm 0.5
0.44	155	19.62 \pm 0.79	11.1 \pm 0.3	12.4 \pm 0.4	253 \pm 4	12.7 \pm 0.2
0.48	256	28.53 \pm 3.11	21.3 \pm 1.1	24.5 \pm 1.4	260 \pm 10	29.0 \pm 0.9
0.52	251	15.57 \pm 2.98	23.7 \pm 0.7	25.6 \pm 0.9	284 \pm 19	26.5 \pm 0.5

The strength of conduction electron-phonon scattering (A in Table 5.3) is randomly varying with the Mn2 concentration. The room temperature XRD pattern for $x = 0.48$ and 0.52 (Table 3.6)

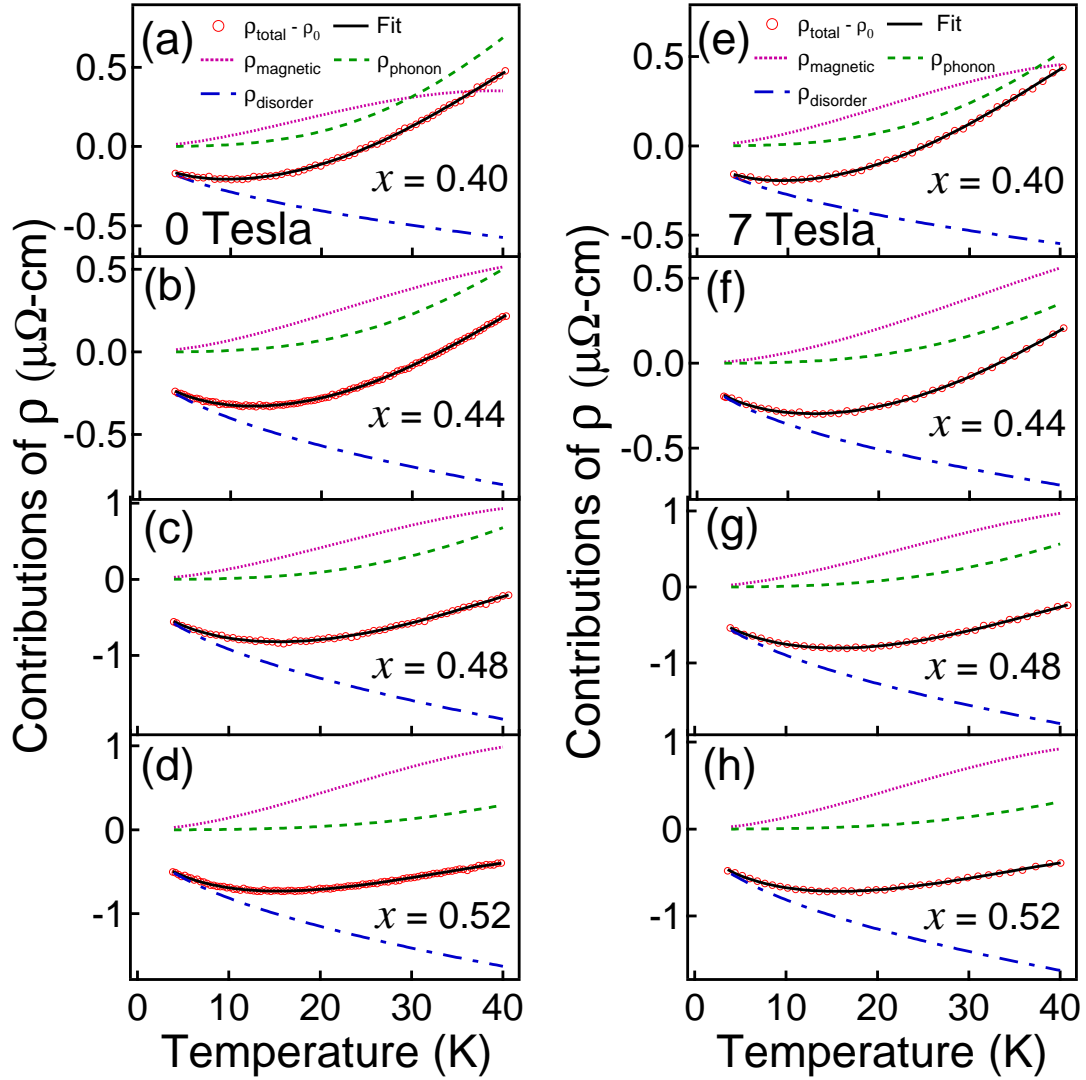


Figure 5.4 Different contributions to resistivity (ρ_{phonon} , ρ_{magnetic} and ρ_{disorder}) deduced by fitting the experimental data with Eq. 5.2 for $\text{Ni}_2\text{Mn}_{1+x}\text{Sn}_{1-x}$ under ZFC (0 Tesla) [(a) - (d)] and FC (7 Tesla) [(e) - (h)].

shows that martensitic phase has two modulated orthorhombic structures 4L and 14L, where L is the layer of modulation. Previous report on Ni-Mn-Sn alloys also show two crystal structures in the martensitic phase [33]. Further the phase fraction of 4L (31% - 44%) and 14L (56% - 69%) is found to be randomly varying with concentration x . Thus the random change in the phase fraction of two structures in the martensitic phase might be responsible for the random variation of A .

Table 5.4 The parameters obtained from least square fitting of FC experimental data by Eq. 5.2 for $\text{Ni}_2\text{Mn}_{1+x}\text{Sn}_{1-x}$.

x	$\rho_0(\mu\Omega$ $-cm)$	$A(\mu\Omega$ $-cm)$	$B \times 10^{-4}(\mu\Omega$ $-cm/K^2)$	$C \times 10^{-5}(\mu\Omega$ $-cm/K^{5/2})$	θ_D (K)	$D \times 10^{-2}(\mu\Omega$ $-cm/K^{1/2})$
0.40	136	20.4 ± 0.4	11.4 ± 1.2	13.5 ± 1.2	253 ± 2	8.6 ± 0.4
0.44	153	13.7 ± 0.2	8.9 ± 0.7	8.7 ± 1.2	253 ± 2	11.3 ± 0.2
0.48	253	23.8 ± 0.5	20.8 ± 1.7	23.3 ± 1.2	260 ± 3	28.4 ± 0.8
0.52	248	16.5 ± 0.1	21.0 ± 0.5	24.0 ± 1.2	283 ± 2	25.7 ± 0.5

However the morphology of martensitic twin variants can also play the important role. Thus, the electron-phonon scattering strength is not a systematic function of impurity. The application of magnetic field (7 Tesla) also gives the random variation of A (Table 5.4).

The strength of conduction electron scattering by magnetic disorder (B and C in Table 5.3) varies randomly for $x = 0.40 - 0.48$ compositions. The application of magnetic field decreases the magnitude of B and C (Table 5.4). However, this variation of B and C remains random for $x = 0.40 - 0.48$. The fitted temperature range is below the spin freezing temperature with random spin orientation. With the application of magnetic field the spin alignment is more ordered. This is also evident from the field cooled thermo-magnetic behavior [Fig. 4.1 and Fig. 4.3]. Thus, B and C parameter decreases with applied magnetic field. However, The magnetic disorder scattering contribution dominates in the fitting temperature range and it increases with the Mn2 concentration. The Debye temperature (θ_D in Table 5.3 and 5.4) for $x = 0.40 - 0.48$ increases with increasing Mn2 concentration.

The coefficient D (Table 5.3 and 5.4) in the disorder induced resistivity, which is a measure of magnitude of localization and electron-electron interaction, increases with increasing Mn concentration. The substitution of Mn at Sn site creates a perturbation in the uniform potential. The random variation of B and C, also, indicate that the Mn are randomly substituting Sn site. Hence, the uniform potential of the system becomes random. Here the electrons do not move in classical paths but rather they diffuse from site to site. Due to the phase coherence between the counter-

propagating partial waves the electrons get localized. In the weak disorder limit the electronic wave function remains extended throughout the system. If the disorder is very strong the wave function may become localized leading to Anderson localization [30]. According to the scaling theory of localization [30] for intermediate disordered electronic systems in the metallic limit, the impurity d band should form localized states that are non-hybridized with the conduction electron states. The host conduction band has the best chance of remaining extended. In $\text{Ni}_2\text{Mn}_{1+x}\text{Sn}_{1-x}$ ($0.4 \leq x \leq 0.52$) the localized states of impurity d band is formed by the Mn2 d bands. The co-existence of localized and extended states in disordered transition metal alloy gives rise to pseudogap near the Fermi edge [34]. The pseudogap formation give rise to the resistivity upturn at low temperature. Due to the increased localised states, e-e interaction (coulomb repulsion) is enhanced with Mn2 (x) concentration. Further the magnitude of D decreases in the FC condition because magnetic field reduces the phase coherence.

The $x = 0.52$ crosses the 50% substitution of Mn at Sn site. It is equivalent to substitution of Sn at Mn site in ordered NiMn alloy. The maximum magnetic and site disorder is expected for $x = 0.50$ alloy. Thus, for $x = 0.52$ the ρ_0 and D decreases. This decrease is also observed with of applied magnetic field. Due to same reason, the $T(\rho_{min})$ and depth of ρ_{min} for $x = 0.48$ and 0.52 are not significantly different.

Austenitic phase

The austenitic phase has ferromagnetic coupling between Mn1 atoms. The neutron diffraction and neutron-polarization-analysis experiments suggest ferromagnetic coupling above martensitic transition between Mn1 and Mn2 atoms. In ferromagnetic metals and alloys there is a distinct contribution to the electrical resistivity arising from the exchange interaction between the conduction electrons and the localized magnetic electrons. The theoretical calculation for ferromagnetic metals and alloys based on spin-wave disorder description gives $\rho_{magnetic}$ the T^2 dependence [22, 35–37]. However, the first principle density functional calculation of $\text{Ni}_2\text{Mn}_{1+x}\text{Sn}_{1-x}$ alloys predict anti-parallel magnetic moment alignment between Mn2 and Mn1 [38]. The Mn2 atoms in $\text{Ni}_2\text{Mn}_{1+x}\text{Ga}_{1-x}$ alloys also have anti-ferromagnetic coupling with Mn1 in the austenitic

phase [39]. In both the configurations if the spin disorder is less, the $\rho_{magnetic}$ will have T^2 dependence. Thus, austenitic phase is given as

$$\rho_{total}(T) = \rho_0 + A\left(\frac{T}{\theta_D}\right)^3 \int_0^{\frac{\theta_D}{T}} \frac{x^3}{(e^x - 1)(1 - e^{-x})} dx + BT^2 \quad (5.3)$$

where, B is the strength of conduction electron scattering by spin-wave disorder. According to

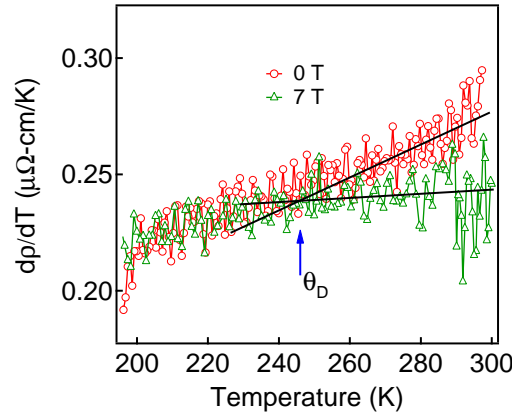


Figure 5.5 The dp/dT as a function of temperature in the austenitic phase of $x = 0.40$ with 0 Tesla and 7 Tesla magnetic field. Solid lines are slope of linear region. The intersection point of solid lines is taken as Θ_D .

thermodynamics of ferromagnet within theory of Landau phase transition of the second order, the θ_D will vary with an applied magnetic field [40]. However, the earlier reports [12, 41] show

Table 5.5 The parameters derived from least square fitting of experimental data to the Eq. 5.3 for $x = 0.40$ in austenitic phase under different magnetic fields.

Magnetic field (T)	$\rho_0(\mu\Omega$ $-cm)$	$A(\mu\Omega$ $-cm)$	$B \times 10^{-4}(\mu\Omega$ $-cm/K^2)$	Θ_D (K)
0	45	69.85 ± 0.09	2.00 ± 0.01	246
4	45	67.78 ± 0.06	1.94 ± 0.01	246
7	45	66.41 ± 0.01	1.91 ± 0.01	246

that austenitic phase of Ni-Mn-Sn also has co-existence of ferromagnetic and anti-ferromagnetic

coupling like martensitic phase. Thus, above theory for ferromagnet is not applicable. In the mixed magnetic martensitic phase the θ_D with 0 Tesla and 7 Tesla magnetic field remains constant within the error for $x = 0.40$ (Table 5.3 and 5.4). Thus θ_D is kept constant during fitting of austenitic phase resistivity with 0 Tesla, 4 Tesla and 7 Tesla. The reported value of θ_D is 255 K for austenitic phase of stoichiometric Ni_2MnSn alloy [42]. This value is within the fitting range ($200 \text{ K} \leq T \leq 300 \text{ K}$) of $x = 0.40$ austenitic phase. Thus, θ_D is estimated from experiment. Above θ_D the total resistivity (ρ) varies as $AT + BT^2$ where, AT is phonon contribution and BT^2 is magnon contribution. The first derivative of ρ makes phonon contribution constant and magnon contribution varies linearly as $A + 2BT$. The first derivative of 0 Tesla and 7 Tesla ρ will have different slope since spin disorder reduces with 7 Tesla. The intersection of $d\rho/dT|_{0T}$ and $d\rho/dT|_{7T}$ will give estimation

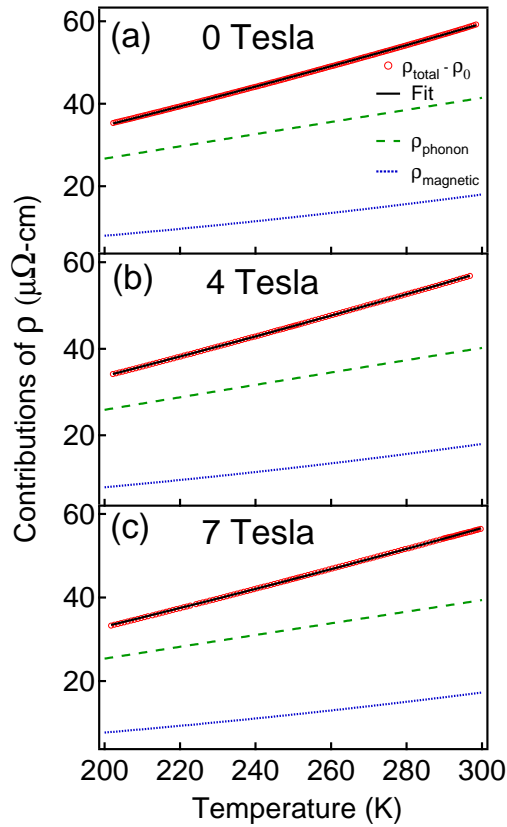


Figure 5.6 The ρ_{phonon} and $\rho_{magnetic}$ contributions to resistivity for $x = 0.40$ in the austenitic phase along with raw data ($\rho_{total} - \rho_0$) and fit with Eq. 5.3. (a) ZFC (b) FC (4 Tesla) (c) FC (7 Tesla).

of θ_D as shown in Fig. 5.5 since θ_D is assumed to be constant. The estimated value of θ_D is 246 K similar to Ref. [42]. The parameters obtained from the fitting of the experimental data (Fig. 5.6) is summarized in the Table 5.5.

The residual resistivity in the high symmetric austenitic phase is very less compared to the low symmetric phase. The strength of electron-phonon scattering magnitude is higher than that in the martensitic phase and it dominates over the whole temperature range (Fig. 5.6). With the application of magnetic field the B parameter decreases due to reduction of spin fluctuation. The electron-phonon scattering strength (A in Table 5.5) also decreases in the presence of magnetic field. The decrease in A and B with magnetic field implies magneto-elastic coupling in austenitic phase.

5.2.2 $\text{Ni}_2\text{Mn}_{1+x}\text{In}_{1-x}$ alloys

The electrical resistivity behavior of $\text{Ni}_2\text{Mn}_{1+x}\text{In}_{1-x}$ ($0.32 \leq x \leq 0.48$) alloys is shown in the Fig. 5.7. No martensitic transition is observed for $x = 0.32$ composition. Only $x = 0.36$ shows the

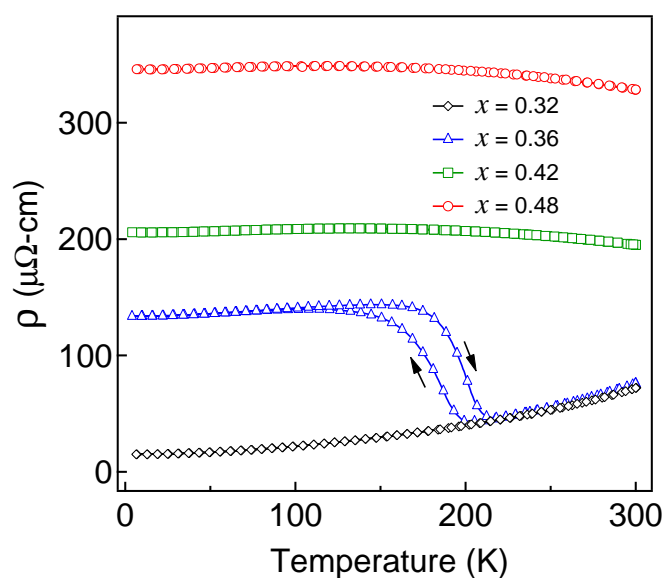


Figure 5.7 Resistivity as a function of temperature for $\text{Ni}_2\text{Mn}_{1+x}\text{In}_{1-x}$.

martensitic transition below room temperature. It is interesting to note that the small decrease in

the Mn concentration ($x = 0.32$) completely suppress the martensitic transition. For $x = 0.32$, ρ follows normal metallic behaviour. The overall nature of ρ vs T behavior for $x = 0.36 - 0.48$ is very much similar to $\text{Ni}_2\text{Mn}_{1+x}\text{Sn}_{1-x}$ alloys. The major difference is the change in the resistivity at the martensitic transition. The resistivity increases more than 200% at the martensitic transition for $\text{Ni}_2\text{Mn}_{1.36}\text{In}_{0.64}$, while it was only about 78% (maximum) for $\text{Ni}_2\text{Mn}_{1+x}\text{Sn}_{1-x}$ alloys.

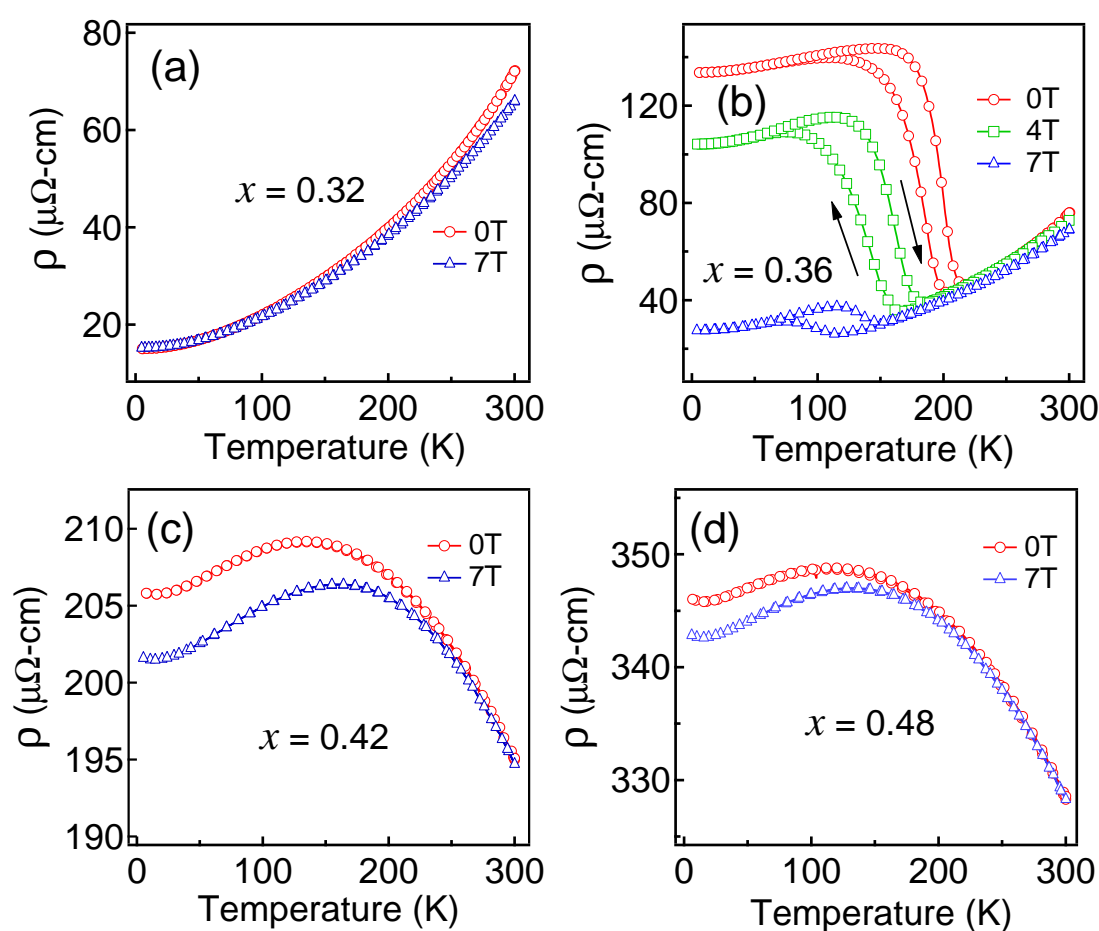


Figure 5.8 Resistivity as a function of temperature for $\text{Ni}_2\text{Mn}_{1+x}\text{In}_{1-x}$ with 0 Tesla and 7 Tesla magnetic field.

The effect of magnetic field on martensitic transformation is shown in the Fig. 5.8 (b). For $x = 0.36$, large decrease in the resistivity below the martensitic transition under FC and FH is observed. With FC and FH martensitic transition temperature shifts to lower temperature. The resistivity

change upon martensitic transition also decreases with field and only $\sim 20\%$ increase is observed at 7 Tesla. At higher magnetic fields the resistivity behaviour tends to be similar to that for $x = 0.32$. As discussed in chapter 4, martensitic transformation is hindered by the magnetic field. With 7 Tesla FC only few % of austenitic phase transforms to martensitic phase and rest phase is arrested in austenitic state. The martensitic percentage is calculated using equation $[(\rho_{(H)} - \rho_{(A)}) / (\rho_{(M)} - \rho_{(A)})] \times 100$ where, $\rho_{(H)}$ is resistivity with magnetic field (H) at 5 K, $\rho_{(M)}$ is resistivity under zero magnetic field at 5 K (Full martensite phase), $\rho_{(A)}$ is resistivity of austenitic phase at 5 K considered from $x = 0.32$ because it is in full austenitic phase at 5 K and there is negligible difference in the resistivity of austenitic phase of $x = 0.32$ and $x = 0.36$ at 5 K. Accordingly, with 7 Tesla FC 90% austenite phase and 10% martensite phase is present at 5 K. For $x = 0.32$ [Fig. 5.8 (a)], at 7 Tesla magnetic field, there is small decrease in the resistivity near 300 K. Close to T_C^A (317 K) magnetic spin fluctuation is high. Under magnetic field the spin fluctuations are reduced thus the scattering of conduction electron is reduced. It results in the decrease of electrical resistivity near T_C^A . The composition $x = 0.42$ and 0.48 are in the paramagnetic martensitic phase at room temperature. There is no significant effect of magnetic field on resistivity at 300 K [Fig. 5.8 (c) and (d)]. With decreasing temperature the resistivity shows a broad maxima around 130 K and 118 K for $x = 0.42$ and 0.48 , respectively. The significant decrease in resistivity with magnetic field is observed around resistivity maximum temperature and further lower temperature. This behaviour of resistivity is similar with the classical spin glass systems like Au-Cr, Au-Mn, Cu-Mn etc [20]. In the classical spin glass systems the resistance maximum roughly corresponds to the temperature where local spin correlations exceeds the thermal disorder and impurity clusters begins to form.

Similar to Ni-Mn-Sn alloys, the Ni-Mn-In alloys also show the resistivity minima at low temperature. It is shown in the Fig. 5.9 (a) and (b) for 0 Tesla and 7 Tesla, respectively. The resistivity minima is not observed for composition $x = 0.32$. It has ferromagnetic cubic ($L2_1$) ground state. The resistivity minima is observed in martensitic phase which has twinned and modulated structure and mixed magnetic state ($x = 0.36, 0.42$ and 0.48). Thus, it confirms that the minima in the resistivity is due to the structural and magnetic disorder. Table 5.6 shows the resistivity minimum temperature [$T(\rho_{min})$] and the depth of minima for $Ni_2Mn_{1+x}In_{1-x}$. The $T(\rho_{min})$ and the depth of

minima increases with Mn concentration. Under 7 Tesla magnetic field resistivity upturn disappears

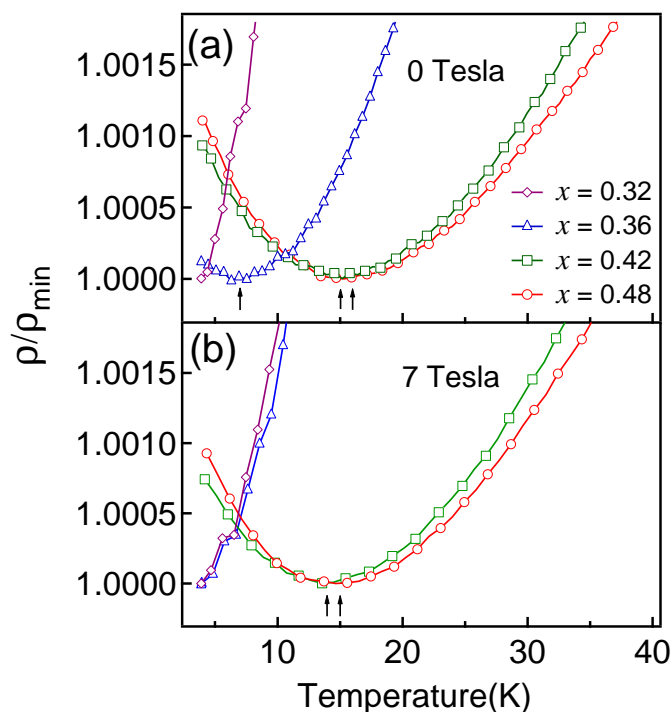


Figure 5.9 Resistivity (ρ) divided by resistivity minimum (ρ_{min}) as a function of temperature under 0 Tesla and 7 Tesla for $\text{Ni}_2\text{Mn}_{1+x}\text{In}_{1-x}$.

peared for the composition $x = 0.36$ and resistivity behavior is almost similar to the composition $x = 0.32$. This is due to the fact that under 7 Tesla magnetic field at 5 K only a small fraction (10%)

Table 5.6 $T(\rho_{min})$ and depth of ρ_{min} of $\text{Ni}_2\text{Mn}_{1+x}\text{In}_{1-x}$ under 0 Tesla and 7 Tesla magnetic field. The error in temperature is within ± 1 K.

x	$T(\rho_{min})$ (K)		Depth of ρ_{min} (%)	
	0 Tesla	7 Tesla	0 Tesla	7 Tesla
0.32	–	–	–	–
0.36	7	–	0.01	–
0.42	15	14	0.09	0.08
0.48	16	15	0.11	0.10

of martensitic phase is present. The presence of large austenitic phase fraction (90%) enhances the structural and magnetic order. The other compositions $x = 0.42$ and 0.48 has negligible decrease in the $T(\rho_{min})$ and depth of minima under 7 Tesla magnetic field.

Martensitic phase

The low temperature resistivity data is fitted in the range of 4 - 40 K using Eq. 5.2 in the martensitic phase ($x = 0.36, 0.42$ and 0.48). The least square fitting of ZFC (0 Tesla) and FC (7 Tesla)

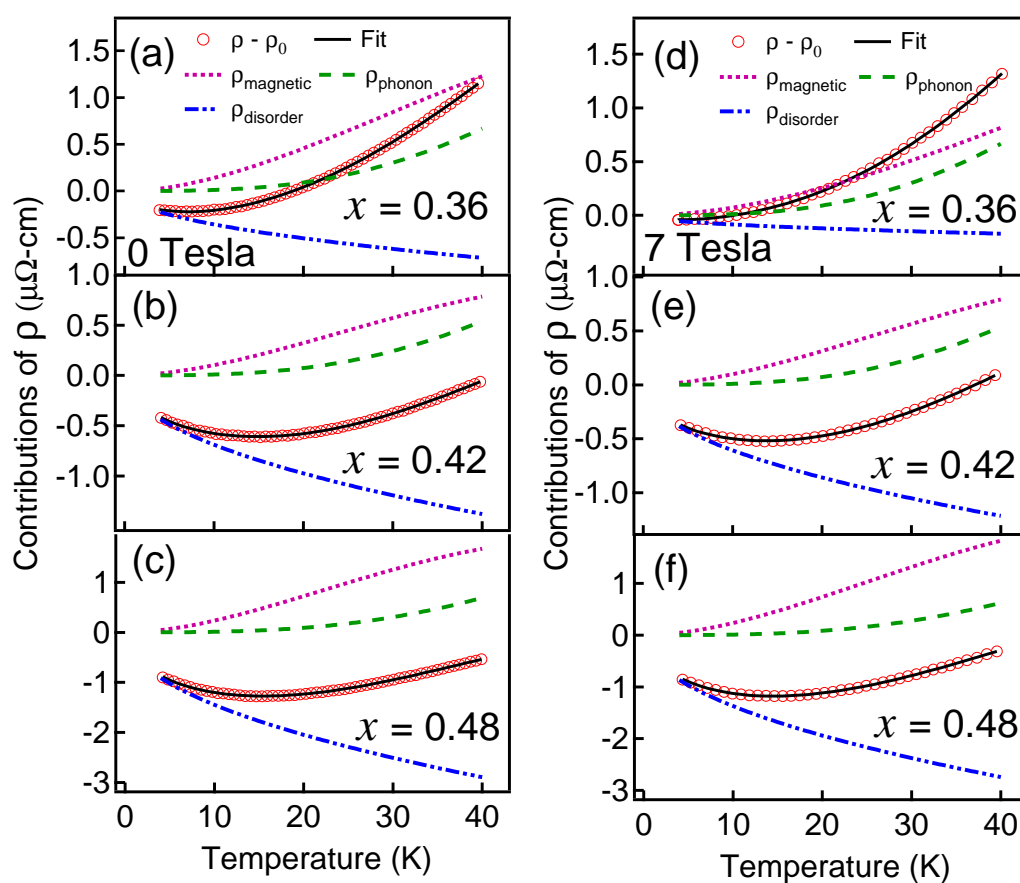


Figure 5.10 Different contributions to resistivity (ρ_{phonon} , $\rho_{magnetic}$ and $\rho_{disorder}$) deduced by fitting the experimental data with Eq. 5.2 for $\text{Ni}_2\text{Mn}_{1+x}\text{In}_{1-x}$ ($x = 0.36, 0.42$ and 0.48) under ZFC (0 Tesla) [(a) - (c)] and FC (7 Tesla) [(d) - (f)].

behavior along with the individual contributions to the total resistivity are plotted in Fig. 5.10. The

corresponding fitting coefficients are summarized in Table 5.7 and Table 5.8 for ZFC (0 Tesla) and FC (7 Tesla), respectively.

From the Fig. 5.10 it is clear that the magnetic contribution to resistivity is dominant in the low temperature. The residual resistivity increases with Mn concentration (ρ_0 in Table 5.7 and 5.8). As discussed earlier martensitic phase is highly disordered due to the presence of modulated and twinned structure that enhances the phonon scattering. Similar to Ni-Mn-Sn alloys the strength of conduction electron-phonon scattering (A in Table 5.7) is randomly varying with the Mn2 concentration. The application of magnetic field (7 Tesla) also gives the random variation of A (Table 5.8). The strength of conduction electron scattering by magnetic disorder (B and C in Table 5.7) varies randomly for $x = 0.36 - 0.48$ compositions under ZFC. The application of magnetic field decreases the magnitude of B and C (Table 5.8) because with the magnetic field spin alignment is more ordered. However, the variation of B and C is not random. The blocking of martensitic transition with 7 Tesla FC sets the spin ordering of austenitic phase (90% austenite) at low temperature. Thus, for $x = 0.36$ the coefficients B and C decreases significantly. Similar to

Table 5.7 The parameters obtained from least square fitting of ZFC experimental data by Eq. 5.2 for $\text{Ni}_2\text{Mn}_{1+x}\text{In}_{1-x}$ ($0.36 \leq x \leq 0.48$).

x	ρ_0 ($\mu\Omega$ -cm)	A ($\mu\Omega$ -cm)	B $\times 10^{-4}$ ($\mu\Omega$ -cm/ K^2)	C $\times 10^{-5}$ ($\mu\Omega$ -cm/ $K^{5/2}$)	θ_D (K)	D $\times 10^{-2}$ ($\mu\Omega$ -cm/ $K^{1/2}$)
0.36	134	29.3 ± 1.0	20.4 ± 0.4	20.2 ± 0.4	264 ± 3	11.3 ± 0.3
0.42	206	25.3 ± 1.2	15.7 ± 0.3	17.1 ± 0.4	271 ± 4	21.8 ± 0.3
0.48	347	38.6 ± 0.4	36.4 ± 0.5	41.1 ± 0.6	290 ± 4	45.7 ± 0.4

Ni-Mn-Sn alloys, coefficient D (Table 5.7 and 5.8) induced by disorder increases with the Mn2 concentration. The increase in Mn2 enhances the site and magnetic disorder, which increases the coefficient D.

The θ_D increases with Mn2 concentration. The θ_D in $\text{Ni}_2\text{Mn}_{1+x}\text{In}_{1-x}$ alloys is reported between 250 K - 290 K [42–44]. The value obtained from fitting (Table 5.7) match well with the reported values. For Ni-Mn-Sn alloys it has been seen that the mixed magnetic martensitic phase

there is no change in θ_D under magnetic field within error range. Thus, for fitting of $x = 0.36 - 0.48$ under 7 Tesla θ_D is kept constant as obtained from ZFC (0 Tesla).

Table 5.8 The parameters obtained from least square fitting of FC (7 Tesla) experimental data by Eq. 5.2 for $\text{Ni}_2\text{Mn}_{1+x}\text{In}_{1-x}$ ($0.36 \leq x \leq 0.48$).

x	ρ_0 ($\mu\Omega$ -cm)	A ($\mu\Omega$ -cm)	$B \times 10^{-4}$ ($\mu\Omega$ -cm/ K^2)	$C \times 10^{-5}$ ($\mu\Omega$ -cm/ $K^{5/2}$)	θ_D (K)	$D \times 10^{-2}$ ($\mu\Omega$ -cm/ $K^{1/2}$)
0.36	28	29.2 ± 1.2	9.5 ± 0.4	6.9 ± 0.5	264	2.7 ± 0.3
0.42	202	25.1 ± 1.1	14.8 ± 0.5	15.5 ± 0.2	271	19.2 ± 0.4
0.48	344	35.0 ± 1.4	35.4 ± 0.9	38.0 ± 0.2	290	43.4 ± 0.5

As discussed for Fig. 5.9 (b), the ρ_{min} disappears for $x = 0.36$ with 7 Tesla FC. The resistivity behavior is still fitted with Eq. 5.2. The coefficient A remains unchanged under FC. It is interesting to note that the coefficient D becomes negligible as compared to that for ZFC (Table 5.7). Further, the magnetic contribution coefficients (B and C) reduce significantly as compared to that for ZFC. This is because 90% austenitic phase is present. The coefficient C is still present because 10% martensitic phase coexists with austenitic phase. Although the resistivity behavior of FC $x = 0.36$ is similar to $x = 0.32$, the origin is not explained completely by Eq. 5.3 for austenitic phase.

Austenitic phase

The austenitic phase ($x = 0.32$) has ferromagnetic ground state as discussed in the chapter 4. In ferromagnetic metals and alloys there is a distinct contribution to the electrical resistivity arising from the exchange interaction between the conduction electrons and the localized magnetic electrons. The theoretical calculation for ferromagnetic metals and alloys based on spin-wave disorder description gives $\rho_{magnetic}$ the T^2 dependence [22, 35–37]. No resistivity minima (Fig. 5.9) for $x = 0.32$ is observed in the austenitic phase thus $\rho_{disorder}$ contribution is nil. Thus, Eq. 5.3 is used for $x = 0.32$ in austenitic phase. The fitting is done over temperature range of 4 K - 120 K.

The least square fitting of ZFC (0 Tesla) and FC (7 Tesla) behavior along with the individual contributions to the total resistivity are plotted in Fig. 5.11. The corresponding coefficients are

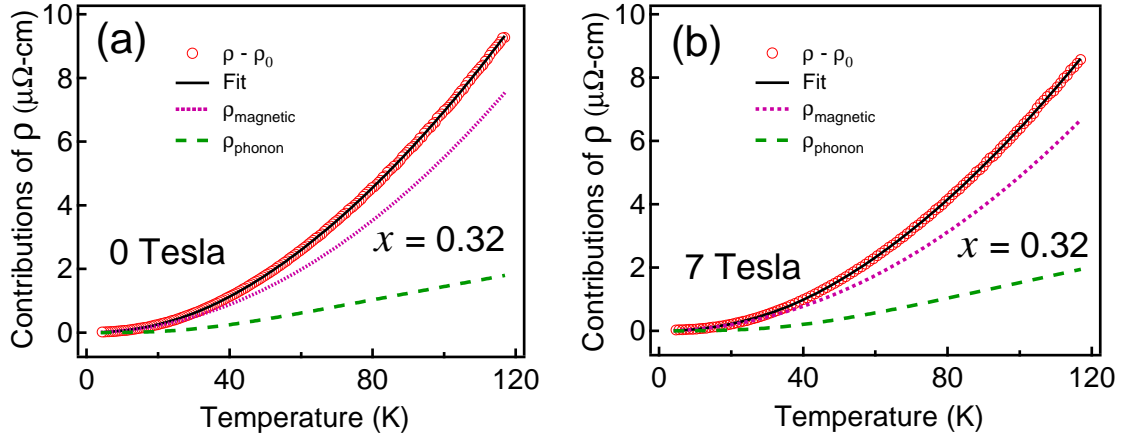


Figure 5.11 Different contributions to resistivity (ρ_{phonon} , ρ_{magnetic} and ρ_{disorder}) deduced by fitting the experimental data with Eq. 5.3 for $\text{Ni}_2\text{Mn}_{1+x}\text{In}_{1-x}$ ($x = 0.32$).

given in Table 5.9. The magnetic contribution B decreases with magnetic field because of increased magnetic ordering. The phonon contribution coefficient A increases along with θ_D . The reported θ_D for stoichiometric composition Ni_2MnIn is 253 K [43]. According to thermodynamics of fer-

Table 5.9 The parameters obtained from least square fitting of experimental data by Eq. 5.3 for $\text{Ni}_2\text{Mn}_{1+x}\text{In}_{1-x}$ ($x = 0.32$).

Magnetic field (T)	$\rho_0(\mu\Omega$ $-cm)$	$A(\mu\Omega$ $-cm)$	$B \times 10^{-4}(\mu\Omega$ $-cm/K^2)$	Θ_D (K)
0	15	8.9 ± 0.4	5.5 ± 0.03	245 ± 3
7	15	13.4 ± 0.08	4.9 ± 0.07	305 ± 4

romagnet within theory of Landau phase transition of the second order, the θ_D will increase with an applied magnetic field [40]. For $x = 0.32$, which is in the austenitic phase with ferromagnetic ordering, θ_D increases with magnetic field in agreement with theory.

5.2.3 Co doped Ni-Mn-In alloys

The previous chapters showed that Co substitution at Ni site decreases the martensitic transition temperature as compared to Ni-Mn-In parent alloy. The magnetic moment and curie temperature

in the austenitic phase also increases. The electrical resistivity as a function of temperature in Ni-Co-Mn-In alloys are shown in Fig. 5.12 (a) and (b). The $\text{Ni}_{1.81}\text{Co}_{0.22}\text{Mn}_{1.46}\text{In}_{0.51}$ (NCMI1) and

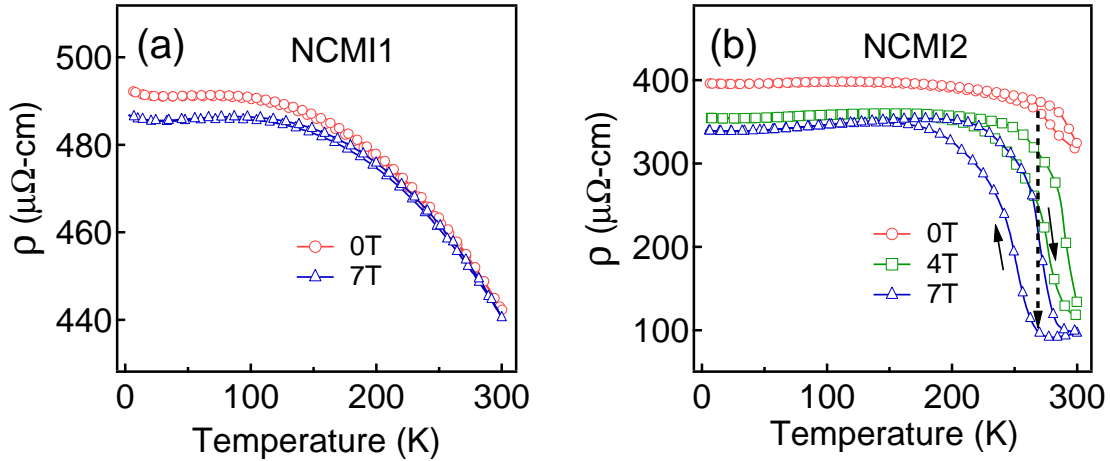


Figure 5.12 Resistivity as a function of temperature at different magnetic fields for (a) $\text{Ni}_{1.81}\text{Co}_{0.22}\text{Mn}_{1.46}\text{In}_{0.51}$ (NCMI1) and (b) $\text{Ni}_{1.81}\text{Co}_{0.22}\text{Mn}_{1.45}\text{In}_{0.52}$ (NCMI2).

$\text{Ni}_{1.81}\text{Co}_{0.22}\text{Mn}_{1.45}\text{In}_{0.52}$ (NCMI2) alloys have higher resistivity as compared to $\text{Ni}_2\text{Mn}_{1.48}\text{In}_{0.52}$. Thus, Co doping also increases the electrical resistivity. The NCMI1 has $\simeq 25\%$ higher resistivity than NCMI2 at 5 K under zero magnetic field even with minute change in their composition.

The magnetic field has similar effect on the electrical resistivity like Ni-Mn-Sn and Ni-Mn-In alloys. The NCMI1 is in the complete martensitic phase below 300 K. Thus field cooling (7 Tesla) from 300 K has no significant effect of electrical resistivity of NCMI1 [Fig. 5.12 (a)]. The NCMI2 has small austenitic phase at 300 K because the martensitic finish temperature is 292 K. Thus the field cooling from 300 K shifts the martensitic transition temperature below 300 K [Fig. 5.12 (a)]. Due to this shift under 4 Tesla magnetic field, there is large decrease in the resistivity at 300 K. Under 7 Tesla FC martensitic transition temperature further shifts (ΔT_M with 4 Tesla and 7 Tesla is 25 K and 64 K, respectively) below 300 K. The significant decrease in resistivity below martensitic transition temperature under FC is because of the presence of austenitic phase fraction due to kinetic arrest of martensitic phase transformation.

Similar to Ni-Mn-Sn and Ni-Mn-In alloys, the Ni-Co-Mn-In alloys also shows the resistivity

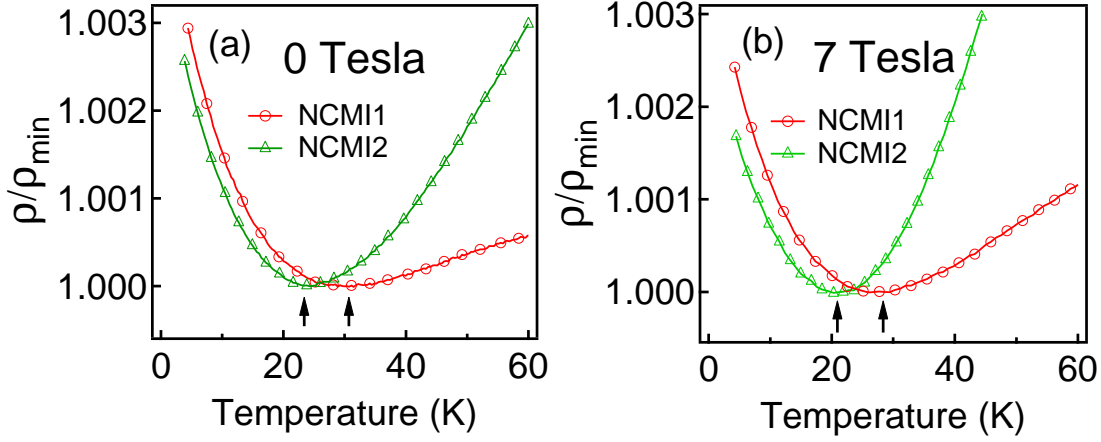


Figure 5.13 Resistivity (ρ) divided by resistivity minimum (ρ_{min}) as a function of temperature for NCM11 and NCM12 under (a) 0 Tesla, (b) 7 Tesla.

minima (ρ_{min}) at the low temperature. It is shown in the Fig. 5.13 (a) and (b) for 0 Tesla and 7 Tesla, respectively. Table 5.10 shows the resistivity minimum temperature [$T(\rho_{min})$] and the depth

Table 5.10 $T(\rho_{min})$ and depth of ρ_{min} of Ni-Co-Mn-In alloys under 0 Tesla and 7 Tesla magnetic field. The error in temperature is within ± 1 K.

Sample	$T(\rho_{min})$ (K)		Depth of ρ_{min} (%)	
	0 Tesla	7 Tesla	0 Tesla	7 Tesla
NCMI1	31	28	0.29	0.24
NCMI2	24	21	0.26	0.17

of minima. The resistivity minima is observed at 31 K (NCMI1) and 24 K (NCMI2), which is quite higher than Ni-Mn-Sn and Ni-Mn-In alloys. The higher $T(\rho_{min})$ of NCM11 than that for NCM12 further confirms that it has more disorder than NCM12. There is significant decrease in the $T(\rho_{min})$ and depth of minima under 7 Tesla magnetic field, while it is negligible in Ni-Mn-Sn and Ni-Mn-In alloys.

The low temperature resistivity data is fitted in the range of 4 - 40 K using Eq. 5.2. The least square fitting by Eq. 5.2 along with the individual contributions to the total resistivity are plotted in Fig. 5.14. The corresponding fitting coefficients are summarized in Table 5.11 and Table 5.12

for ZFC (0 Tesla) and FC (7 Tesla), respectively.

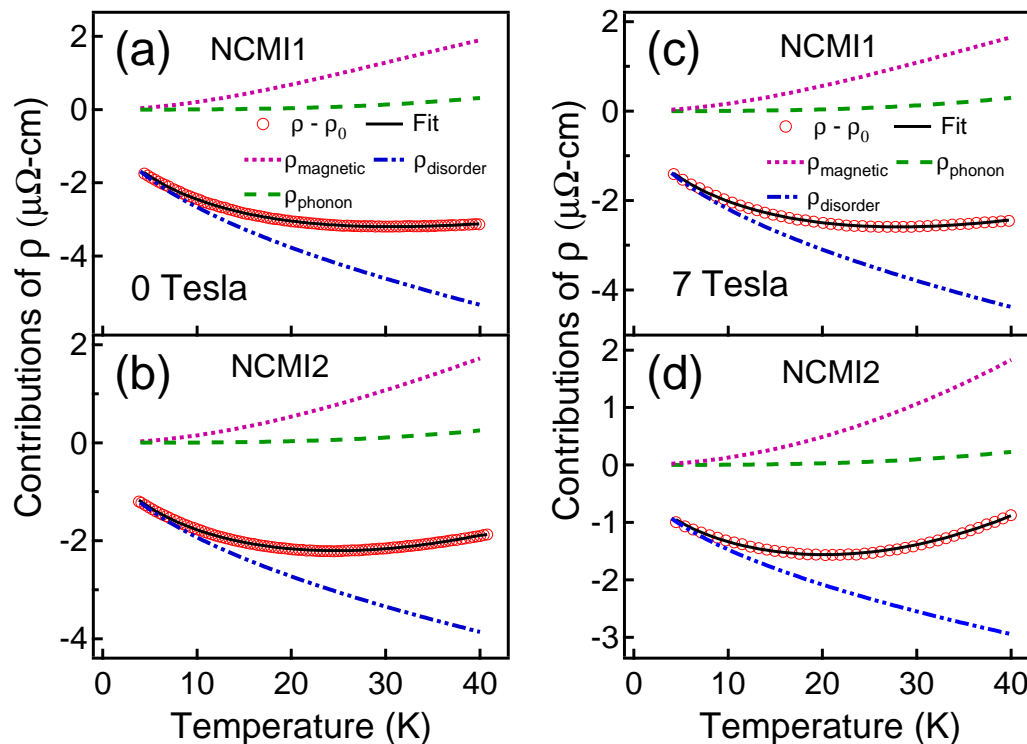


Figure 5.14 Different contributions to resistivity (ρ_{phonon} , ρ_{magnetic} and ρ_{disorder}) deduced by fitting the experimental data with Eq. 5.2 for Ni-Co-Mn-In alloys under ZFC [(a) and (b)] and FC [(c) and (d)].

Table 5.11 The parameters obtained from least square fitting of ZFC experimental data by Eq. 5.2 for Ni-Co-Mn-In.

Sample	ρ_0 ($\mu\Omega$ -cm)	A ($\mu\Omega$ -cm)	B $\times 10^{-4}$ ($\mu\Omega$ -cm/K ²)	C $\times 10^{-5}$ ($\mu\Omega$ -cm/K ^{5/2})	θ_D (K)	D $\times 10^{-2}$ ($\mu\Omega$ -cm/K ^{1/2})
NCMI1	494	39.4 \pm 0.4	29.9 \pm 0.7	28.5 \pm 0.9	384 \pm 2	84.2 \pm 0.6
NCMI2	398	30.0 \pm 0.5	19.5 \pm 0.3	13.8 \pm 0.5	380 \pm 2	60.9 \pm 0.3

From Fig. 5.14 it is clear that magnetic contribution increases with temperature. Since NCM12 is less disordered alloys than NCM1, the A, B, C and D coefficients are less than that for NCM1. With FC all the coefficients for both the alloys decrease indicating decrease in disorder. It is

Table 5.12 The parameters obtained from least square fitting of of FC (7 Tesla) experimental data by Eq. 5.2 for Ni-Co-Mn-In.

Sample	ρ_0 ($\mu\Omega$ $-cm$)	A ($\mu\Omega$ $-cm$)	$B \times 10^{-4}$ ($\mu\Omega$ $-cm/K^2$)	$C \times 10^{-5}$ ($\mu\Omega$ $-cm/K^{5/2}$)	θ_D (K)	$D \times 10^{-2}$ ($\mu\Omega$ $-cm/K^{1/2}$)
NCMI1	488	36.9 ± 0.7	23.1 ± 1.0	20.2 ± 1.4	384	69.3 ± 0.9
NCMI2	340	27.3 ± 0.6	14.2 ± 0.1	4.3 ± 0.1	380	46.6 ± 0.6

interesting to note that the parameter C for NCMI2 under FC becomes almost insignificant. This value is even less than for $Ni_2Mn_{1.36}In_{0.64}$ (Table 5.8). This implies that with FC the spin alignment is almost becoming ferromagnetic and hence behavior has more T^2 dependence. The θ_D in Ni-Co-Mn-In alloy, reported from specific heat measurement is 388 K [45]. In the fitting the initial value of θ_D is used as 388 K and it is varied to find above values that almost match with reported value. The θ_D is almost similar for NCMI1 and NCMI2 within error. The large value of D as compared to that for Ni-Mn-Sn and Ni-Mn-In alloys implies that these alloys have higher structural and magnetic disorder. This might be the influence of quenched atomic disorder.

5.3 Conclusion

The electrical resistivity behaviour of Ni-Mn-Sn, Ni-Mn-In and Ni-Co-Mn-In alloys have been studied in the ZFC and FC conditions. The martensitic transformation enhances the electrical resistivity of martensitic phase due to disordered, modulated and twinned structure. The shift in the martensitic transition temperature is observed under 7 Tesla FC. The phenomenon of kinetic arrest (blocking) of the martensitic phase transformation under 7 Tesla FC is only observed in Ni-Mn-In and Ni-Co-Mn-In alloys. The disordered martensitic phase shows the resistivity minima at the low temperature. The model Eq. 5.2 and Eq. 5.3 assumed to understand the resistivity in martensitic and austenitic phase and anomaly at low temperature. The models could very well describe the resistivity behavior. The $BT^2 - CT^{5/2}$ behavior confirms the spin-freezing state in the martensitic phase where impurity spins (Mn²⁺) are short-range anti-ferromagnetically coupled to Mn atoms at

Mn site. Whereas the T^2 dependence in austenitic phase confirms the long-range ferromagnetic coupling. The resistivity behavior with applied magnetic field implies strong interplay of structural and magnetic states in both austenite and martensite phase. Also, the electron-electron interaction persists with localized states. The $-\sqrt{T}$ variation of the low temperature resistivity anomaly predicts the co-existence of extended and localized states, which could give rise to pseudogap in electronic structure.

Bibliography

- [1] S. P. McAlister, I. Shiozaki, C. M. Hurd, and C. V. Stager, *J. Phys. F: Metal Phys.* **11**, 2129 (1981).
- [2] C. M. Hurd, I. Shiozaki, and S. P. McAlister, *Phys. Rev. B* **26**, 701 (1982).
- [3] A. Hamzić, R. Asomoza, and I. A. Campbell, *J. Phys. F: Metal Phys.* **11**, 1441 (1981).
- [4] J. V. Kunzler, T. A. Grandi, W. H. Schreiner, P. Pureur, and D. E. Brandao, *J. Phys. Chem. Solids* **41**, 1023 (1980).
- [5] J. M. Barandiarán, V. A. Chernenko, P. Lázpita, J. Gutiérrez, and J. Feuchtwanger, *Phys. Rev. B* **80**, 104404 (2009).
- [6] S. Chatterjee, S. Giri, S. Majumdar, and S. K. De, *Phys. Rev. B* **77**, 224440 (2008).
- [7] Y. Zhou, X. Jin, H. Xu, Y.V. Kudryavtsev, Y. P. Lee, and J. Y. Rhee, *J. Appl. Phys.* **91**, 9894 (2002).
- [8] Y. K. Kuo, K. M. Sivakumar, H. C. Chen, J. H. Su, and C. S. Lue, *Phys. Rev. B* **72**, 054116 (2005).
- [9] G. Li, Y. Liu, B.K.A. Ngoi, *J. Magn. Magn. Mater.* **303**, 261 (2006).
- [10] S. Chatterjee, S. Giri, S. Majumdar, and S. K. De, *Phys. Rev. B* **77**, 012404 (2008).
- [11] V. K. Srivastava, R. Chatterjee and R. C. O’Handley, *Appl. Phys. Lett.* **89**, 222107 (2006).

- [12] T. Krenke, M. Acet, E.F. Wassermann, X. Moya, L. Mañosa, A. Planes, *Phys. Rev. B* **72**, 014412 (2005).
- [13] P. J. Brown, A.P. Gandy, K. Ishida, R. Kainuma, T. Kanomata, K.-U. Neumann, K. Oikawa, B. Ouladdiaf, K. R. A. Ziebeck, *J. Phys.: Condens. Matter* **18**, 2249 (2006).
- [14] K. Otsuka and C.M. Wayman, *Shape Memory Materials*, Cambridge University Press, Cambridge, 1998.
- [15] P. R. Stone, K. Alberi, S. K. Z. Tardif, J.W. Beeman, K. M. Yu, W. Walukiewicz, and O. D. Dubon, *Phys. Rev. Lett.* **101**, 087203 (2008).
- [16] S. Chakraborty and A. K. Majumdar, *Phys. Rev. B* **53**, 6235 (1996).
- [17] S. Banerjee and A. K. Raichaudhuri, *Phys. Rev. B* **50**, 8195 (1994).
- [18] S. Senoussi and Y. Öner, *Phys. Rev. B* **88**, 455(R) (1983).
- [19] S. Aksoy, M. Acet, P. P. Deen, L. Mañosa and A. Planes, *Phys. Rev. B* **79**, 212401 (2009).
- [20] P. J. Ford and J. A. Mydosh, *Phys. Rev. B* **14**, 2057 (1976).
- [21] A. H. Wilson, *Proc. R. Soc. Lond. A* **167**, 580 (1938).
- [22] R. S. Patel, A. K. Majumdar, A. F. Hebard, D. Temple, *J. Appl. Phys.* **93**, 10 (2003).
- [23] S. Chatterjee, S. Giri, S. K. De, and S. Majumdar, *Phys. Rev. B* **79**, 092410 (2009).
- [24] D. Y. Cong, S. Roth, J. Liu, Q. Luo, M. Pötschke, C. Hürrieh, and L. Schultz, *Appl. Phys. Lett.* **96**, 112504 (2010).
- [25] L. Ma, W. H. Wang, J. B. Lu, J. Q. Li, C. M. Zhen, D. L. Hou, and G. H. Wu, *Appl. Phys. Lett.* **99**, 182507 (2011)
- [26] A. K. Nayak, K. G. Suresh, and A K Nigam, *J. Phys.: Condens. Matter* **23**, 416004 (2011).

- [27] P. Entel, M. E. Gruner, D. Comtesse, V. V. Sokolovskiy, and V. D. Buchelnikov, *Phys. Status Solidi B*, 1 - 14 (2014).
- [28] K. H. Fischer, *Z. Physik B* **34**, 45 (1979).
- [29] A. Banerjee and A. K. Majumdar, *Phys. Rev. B* **46**, 8958 (1992).
- [30] P. A. Lee and T. V. Ramkrishnan, *Rev. Mod. Phys.* **57**, 287 (1985).
- [31] A. K. Majumdar, *J. Magn. Magn. Mater.* **263**, 26 (2003).
- [32] B. L. Altshuler and A. G. Aronov, *Solid State Commun.* **30**, 115 (1979).
- [33] H. Zheng, W. Wang, S. Xue, Q. Zhai, J. Frenzel, Z. Luo, *Acta. Mater.*, **61**, 4648 (2013).
- [34] M. I. Katsnelson and A. S. Shcherbakov, *J. Phys. C: Solid State Phys.* **19**, 5173 (1986).
- [35] D. A. Goodings, *Phys. Rev.* **132**, 542 (1963).
- [36] I. Mannari, *Prog. Theor.Phys.* **22**, 335 (1959).
- [37] T. Kasuya, *Prog. Theor.Phys.* **16**, 58 (1956).
- [38] M. Ye, A. Kimura, Y. Miura, M. Shirai, Y. T. Cui, K. Shimada, H. Namatame, M. Taniguchi, S. Ueda, K. Kobayashi, R. Kainuma, T. Shishido, K. Fukushima, and T. Kanomata, *Phys. Rev. Lett.* **104**, 176401 (2010).
- [39] J. Enkovaara, O. Heczko, A. Ayuela, and R. M. Nieminen, *Phys. Rev. B* **67**, 212405 (2003).
- [40] V. Yu. Bodryakov, A. A. Povzner, and O. G. Zelyukova, *Phys. Solid State* **41** 1138 (1999).
- [41] V. V. Sokolovskiy, V. D. Buchelnikov, M. A. Zagrebin, P. Entel, S. Sahoo, and M. Ogura, *Phys. Rev. B* **86** 134418 (2012).
- [42] S. M. Podgornykh, S. V. Streltsov, V. A. Kazantsev, and E.I. Shreder, *J. Magn. Magn. Mater.* **311**, 530 (2007).

- [43] G. L. F. Fraga, D. E. Brandão, and J. G. Sereni, *J. Magn. Magn. Mater.* **102**, 199 (1991).
- [44] B. Li, W. J. Ren, Q. Zhang, X. K. Lv, X. G. Liu, H. Meng, J. Li, D. Li, and Z. D. Zhang, *Appl. Phys. Lett.* **95**, 172506 (2009).
- [45] A. N. Vasiliev, O. Heczko, O. S. Volkova, T. N. Vasilchikova, T. N. Voloshok, K. V. Klimov, W. Ito, R. Kainuma, K. Ishida, K. Oikawa, and S. Fähler, *J. Phys. D: Appl. Phys.* **43**, 055004 (2010).

Chapter 6

Magneto-transport property

6.1 Introduction

The magnetoresistance (MR) in the Ni-Mn based Heusler alloys have attracted attention of researchers in 2005, after Biswas et al. [1] reported -5% MR at room temperature in ferromagnetic shape memory alloy $\text{Ni}_{2+x}\text{Mn}_{1-x}\text{Ga}$. The MR is mainly observed in the austenitic phase near T_C and martensitic phase has very low MR. After the discovery of new type of magnetic shape memory alloys in off-stoichiometric Heusler alloys Ni-Mn-Sn, Ni-Mn-In and Ni-Mn-Sb [2], negative MR is explored in these alloys. These alloys exhibit magnetic field induced reverse phase transformation (MFIRPT) [3–5]. The large negative MR is reported in Ni-Mn-Sn [6–9], Ni-Mn-In [10–14] and Ni-Co-Mn-In [15–18] alloys across the martensitic transition. The large difference in the resistivity above and below the martensitic phase transition (MPT) provides the large MR in these materials. Maximum upto -80% MR is obtained at 8 Tesla (T) magnetic field [10]. In the Ni-Mn-Sn system the maximum -50% MR at 18 T have been observed for $\text{Ni}_{50}\text{Mn}_{36}\text{Sn}_{14}$ [6]. The giant magneto-resistance (GMR) of about -93% has been observed in $\text{Ni}_{45}\text{Co}_5\text{Mn}_{37.7}\text{In}_{13.3}$ [15]. The reason for such large MR is solely attributed to MFIRPT and kinetic arrest of martensitic phase transformation. Also, the thermal and the magnetic history is reported to play important role in these systems. The thermal history dependent MR has been studied in $\text{Ni}_{1.98}\text{Mn}_{1.38}\text{In}_{0.64}$ in the metastable region across martensitic transition (MT) [12]. Irreversibility in isothermal MR is observed in reverse martensitic transformation temperature range, while an intriguing “overshooting” phenomenon is observed in forward martensitic transformation temperature range [12]. However, previous reports lack in the full understanding of why the large MR is observed in the vicinity of martensitic transition only and basic discussion on the origin of MR with field-cooled (FC) and zero-field-cooled (ZFC) state. In this chapter origin of MR is discussed in both the structural phases (austenitic and martensitic) and within the structural transition region. It also provides insight into the behavior and origin of MR during FC and ZFC, particularly at low temperature in the martensitic phase. The MR is calculated from the resistivity as $= (\rho_H - \rho_0)/\rho_0$, where ρ_H is resistivity in the magnetic field H and ρ_0 is resistivity at zero magnetic field.

6.2 Result and Discussion

6.2.1 $\text{Ni}_2\text{Mn}_{1+x}\text{Sn}_{1-x}$ alloys

The Fig. 6.1 shows MR as a function of temperature at 7 T applied magnetic field. It has hysteresis during heating and cooling across the martensitic transformation temperature. The -36% ($x = 0.40$) and -22% ($x = 0.44$) MR at 170 K and 248 K, respectively, is obtained during martensitic transformation while cooling. Upon MT the FC (7 T) resistivity increases by 81% ($x = 0.4$, Fig. 5.2) due to disorder related residual resistivity and scattering from various orientation of twin variants. Also, with magnetic field the martensitic transformation temperature shifts to lower temperature giving rise to magnetic field induced reverse phase transition (MFIRPT). Further, the structural transition to lower symmetry is accompanied by the modulation, which increases the scattering of conduction electrons. The combination of all these effects are giving rise to the large negative

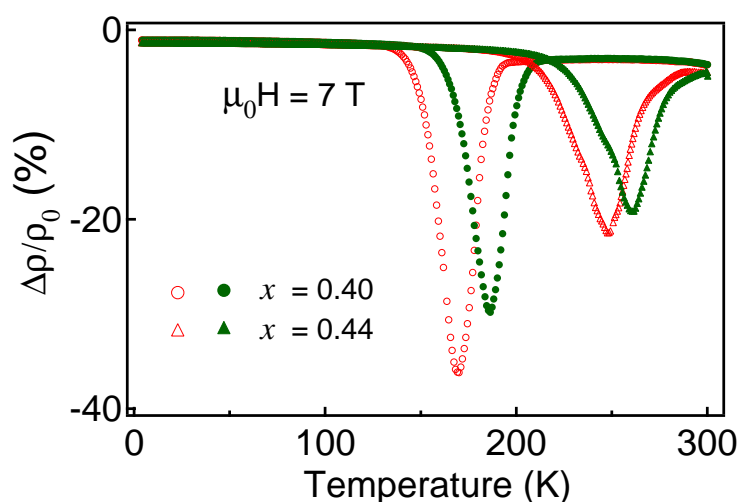


Figure 6.1 MR as a function of temperature at 7 T for $x = 0.40$ and 0.44 during cooling (open symbol) and heating (filled symbol).

MR. For $x = 0.44$ the FC (7 T) resistivity jump decreases to 66% (Fig. 5.2), which is responsible for decrease in MR. While heating the transition is from a less ordered state to more ordered state. The disorder related residual resistivity decreases. The resistivity jump is 74% ($x = 0.4$) and 59% ($x = 0.44$). Thus, the maximum MR obtained is less than that in cooling. The MR is very less

below and above martensitic transformation. Fig. 6.2 shows the MR as a function of temperature at 7 T for $x = 0.48$. The martensitic transformation for $x = 0.48$ is above room temperature. Thus below 300 K it is in complete martensitic phase. At 300 K it shows only -0.2% of MR with 7 T applied magnetic field. The MR shows linear increase upto 190 K with decreasing temperature, where the T_C^M (231 K, average from DSC and Magnetization results) is almost in the middle. The MR maximum (-1.44%) is at 160 K. Below 160 K it slowly decreases upto 5 K. At 5 K MR is -1.19%.

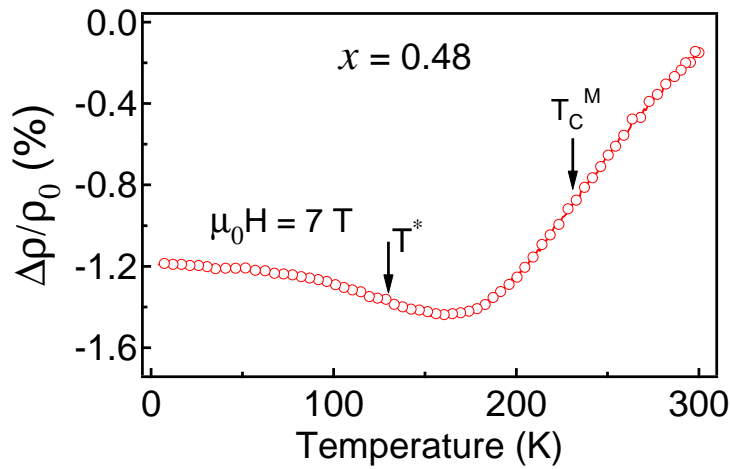


Figure 6.2 MR as a function of temperature at 7 T for $x = 0.48$ during cooling.

To understand the origin of less MR below and above martensitic transformation, isothermal MR is measured at 300, 150, and 5 K during ZFC. The magnetic field dependence of MR is fitted with the equation

$$\frac{\Delta\rho}{\rho_0} = -\alpha(\mu_0 H)^n \quad (6.1)$$

where, α is the strength of MR [19]. The values of α and n , obtained from fitting, are summarized in Table 6.1.

Figures 6.3 (a) and (b) show the MR at 300 K for $x = 0.40 - 0.52$. The MR is negative for all the compositions. For $x = 0.40$ and 0.44 , at 300 K the MR is -4.2% and -4.6% at 8 T, respectively [Fig. 6.3 (a)]. The n is 0.87 ($x = 0.40$) and 0.85 ($x = 0.44$). Similar behaviour is observed in ferromagnetic (FM) austenitic phase of Ni-Mn-Ga and is explained on the basis of $s-d$ scattering

model where s conduction electrons are scattered by localized d spins [1, 20, 21]. The $x = 0.48$

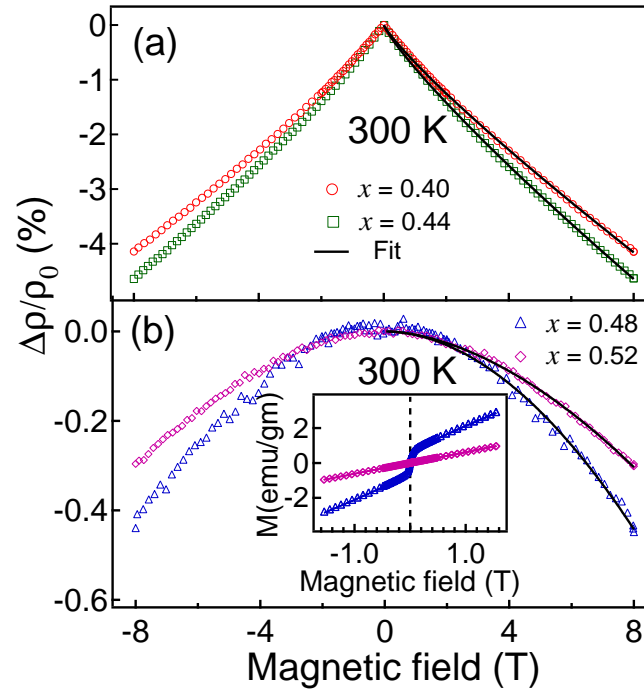


Figure 6.3 Isothermal MR in (a) FM austenitic phase (b) PM martensitic phase. Inset: M-H for $x = 0.48$ and 0.52 at 300 K. Solid lines are fit to the data with Eq. 6.1.

Table 6.1 The parameter obtained from the fitting of experimental data to Eq. 6.1. The error is of the order of 10^{-3} . * n and α for low field ($\mu_0 H \leq 2.5$ T). Unit of α is Tesla^{-n} .

x	300 K		150 K		5 K	
	α	n	α	n	α	n
0.40	0.69 ± 5	0.87 ± 2	0.22 ± 1	1.11 ± 3	0.16 ± 1	1.00 ± 7
0.44	0.79 ± 5	0.85 ± 1	0.21 ± 3	0.99 ± 3	0.15 ± 1	1.00 ± 5
0.48	0.008 ± 0.65	1.92 ± 16	0.33 ± 4	0.79 ± 3	$0.16 \pm 3^*$	$1.15 \pm 24^*$
0.52	0.007 ± 0.2	1.77 ± 16	0.25 ± 2	0.83 ± 3	$0.12 \pm 5^*$	$1.49 \pm 46^*$

and 0.52 has -0.4% and -0.3% MR at 8 T [Fig. 6.3 (b)] and n is 1.9 and 1.77, respectively. So the slight change in the composition gives the huge decrease ($\geq 90\%$) in the MR at 300 K. The $x =$

0.48 and 0.52 are in predominantly paramagnetic (PM) martensitic phase. The deviation from $n = 2$ (ideal PM) suggests presence of anti-ferromagnetic (AFM) phase with short range coupling. The AFM phase arises due to exchange interaction between Mn at Mn site (Mn1) and Mn at Sn site (Mn2). Also for $x = 0.48$ a small fraction of austenite exists at 300 K [M-H in Fig. 3(b) and T_C^A in Fig. 3.2].

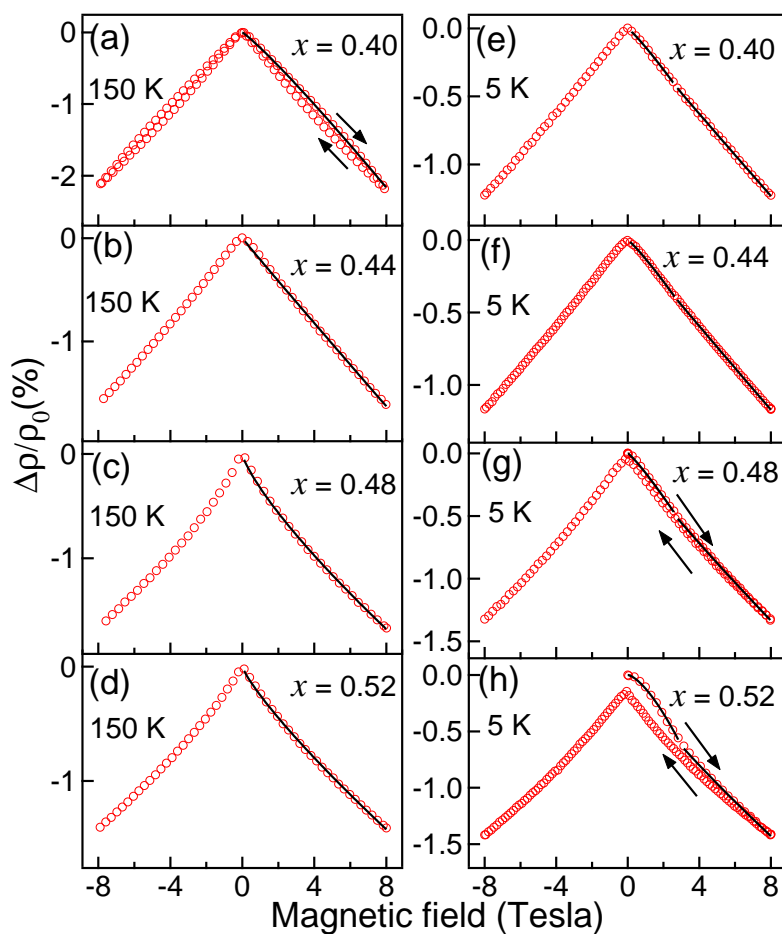


Figure 6.4 Isothermal MR (a) - (d) at 150 K and (e) - (h) at 5 K. Solid lines are fit to the data with Eq.6.1.

The MR at 150 K for all compositions is shown in Figs. 6.4 (a) - (d). The MR lies between -2.2 % to -1.4% at 8 T. All the alloys are in mixed FM-AFM martensitic phase. Thus, MR is less than that in austenitic phase. The effect of magnetic field is to rotate the magnetization within the

unfavorably oriented twins since Zeeman energy is very high than magnetocrystalline anisotropy. Also, the magnetization decreases with increasing Mn due to increase in AFM domains within the FM domain of a twin. Thus, the MR reduces with more Mn2 and n also decreases.

At 5 K [Figs. 6.4 (e) - (h)] MR varies between 1.0% - 1.4 % at 8 T. The *s-d* scattering will die out at this temperature and can not be responsible for the negative MR. The site and magnetic disorder induced weak localization and electron-electron interaction effects are dominant at this temperature [22]. This is also evident from different MR behavior at low ($\mu_0 H \leq 2.5$ T) and high ($\mu_0 H \geq 2.5$ T) magnetic field. The value of n between 1 and 2 at low field suggests the scattering of conduction electron is mainly from the Mn2 *d*-band localized states. The localization increases with Mn2 increase. The localized spins of Mn2 are randomly oriented with short range ordering. The spins become more ordered with $\mu_0 H \geq 2.5$ T. The n also decreases to 0.89 ($x = 0.48$) and 0.84 ($x = 0.52$).

6.2.2 $\text{Ni}_2\text{Mn}_{1+x}\text{In}_{1-x}$ alloys

The FC MR as a function of temperature at 1 T, 4 T and 7 T for $x = 0.32$ is shown in Fig. 6.5 (a). The $x = 0.32$ do not show martensitic transition upto 5 K [2, 23, 24]. It is a ferromagnetic Heusler alloy with cubic austenitic phase only. At 300 K and 7 T magnetic field MR of -8.6% is obtained. It is higher than the Ni-Mn-Ga and Ni-Mn-Sn alloys in the austenitic phase at 300 K. The magnitude of negative MR decreases with temperature. In ferromagnetic Heusler alloys, resistivity in cubic austenitic phase has contributions from residual resistivity, electron-phonon scattering and scattering of conduction electrons by localised spins. With application of magnetic field the scattering of conduction electron by localized spin reduces [1, 25]. The *s-d* scattering model [26] explained the behavior, where *s* conduction electrons are scattered by localized *d* spins. The maximum MR is observed near T_C^A (317 K) and it rapidly decreases towards low temperature. Thus it is the *s-d* scattering mechanism that gives rise to negative MR at high temperature in austenitic phase of 0.32 alloy. The magnitude of negative MR decreases with temperature and below a critical temperature [marked by arrow in the Fig. 6.5 (a)] MR becomes positive. The

critical temperature, where MR switches from negative to positive value, decreases with increasing field [144 K, 65 K and 43 K at 1 T, 4 T and 7 T, respectively]. At 5 K MR is +1.5% at 1 T and it decreases with increasing magnetic field and is +1.2% at 7 T. The positive MR at low temperature is observed in various disordered systems [22]. The positive MR at low temperature might be due to the disorder induced effects which is also observed in the ZFC isothermal MR and is discussed later.

The Fig. 6.5 (b) shows the MR (FC and FH) for $x = 0.36$ at 4 T and 7 T magnetic field. In austenitic phase, at 300 K, the MR is -9% (-4%) at 7 T (4 T). The MR decreases with decreasing temperature. At 215 K MR is only -4.2% for 7 T. The austenitic phase MR behavior could be understood from the $x = 0.32$ composition FC MR. It is the $s-d$ scattering mechanism that gives rise to negative MR at high temperature in austenitic phase of $x = 0.36$ alloy. Further decreasing the

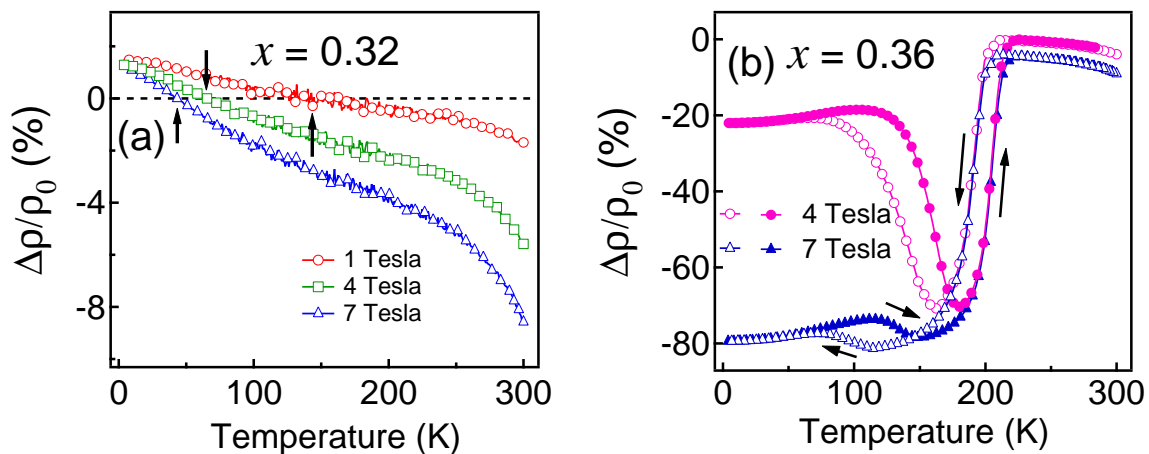


Figure 6.5 (a) FC MR as a function of temperature for $x = 0.32$. (b) FC (open symbol) and FH (filled symbol) MR as a function of temperature for $x = 0.36$.

temperature with applied magnetic field, the MR increases drastically [Fig. 6.5 (b)]. This happens within the martensitic transition temperature range. For 7 T (4 T) magnetic field maximum MR of -81% (-71%) is obtained at 115 K (160 K). Thus MR maximum shifts to lower temperature with increasing magnetic field. The large negative MR is, in general, explained by the kinetic arrest of the first order austenite to martensite phase transformation and shift in martensitic transition temperature. The Fig. 6.6 shows decrease in structural transition temperatures with magnetic field for x

$= 0.36$. The decrease in M_S (ΔT_m) with 4 T is 35 K while with 7 T it is 83 K. Thus MR maximum shifts to lower temperature at higher magnetic field. It is reported [27–29] that the martensitic transformation is hindered by the magnetic field. The kinetic arrest of first-order ferromagnetic phase transition is also observed in various doped manganites [30, 31]. The magnetization (ZFC, FC and FH) results for $x = 0.36$ [Fig. 4.11] with 0.05 T applied field shows the large drop in magnetization at martensitic transition, whereas with 14 T magnetic field FC magnetization increases with decreasing temperature upto 150 K and saturates below it. This implies that with 14 T FC martensitic transformation is fully blocked. The freezing of structural degree of freedom occurs in the presence of magnetic field. The net effect of magnetic field is to align the spin in ferromagnetic state. This spin alignment favors the $L2_1$ lattice through spin-lattice coupling. Thus, martensitic transformation is blocked. With 7 T magnetic field only few % of austenitic phase transforms to martensitic phase and rest phase is arrested in austenitic phase. Thus it is the resistance provided by spin alignment of austenitic phase in ferromagnetic state that give rise to large negative MR.

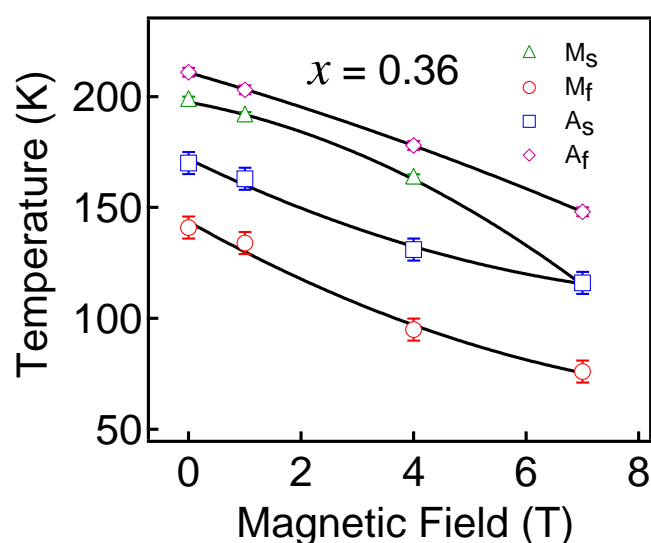


Figure 6.6 Shift in martensitic transition temperatures of $Ni_2Mn_{1.36}In_{0.64}$ as a function of magnetic field.

Further, below the M_F temperature the FC MR is still high to the lowest temperature. At 5 K MR of -79% and -22% are obtained at 7 T and 4 T, respectively [Fig. 6.5 (b)]. This behavior is

very different from that in Ni-Mn-Sn alloys. In Ni-Mn-Sn alloys, at 5 K the MR is similar to that for austenitic phase [25]. As discussed earlier, for $\text{Ni}_2\text{Mn}_{1.36}\text{In}_{0.64}$ the austenitic phase is prevalent at low temperature with FC. However, The magnitude of MR is not same as austenitic phase. At 5 K, $s-d$ scattering is not dominant. The disorder effects mainly contribute to total resistivity. Fig. 5.8 (b) shows that the resistivity of austenitic phase is very less with application of 7 T magnetic field. Also, for $x = 0.32$ the same is observed [Fig. 5.8 (a)]. Thus the effect of magnetic field is to decrease the structural and spin disorder in the system giving rise to large negative MR. With 4 T applied magnetic field the martensitic phase fraction increases. The structure and spin states are mixed austenitic and martensitic phase. Thus the structural and spin disorder increases, which in turn decreases the MR magnitude.

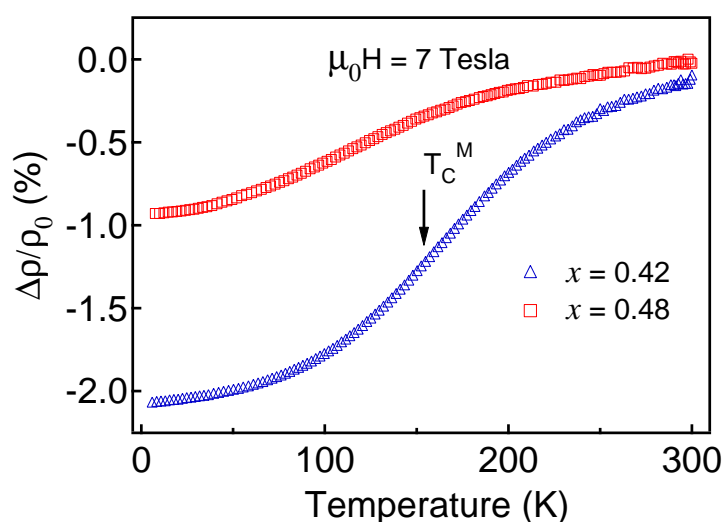


Figure 6.7 The FC MR as a function of temperature of $\text{Ni}_2\text{Mn}_{1+x}\text{In}_{1-x}$ at 7 T (a) $x = 0.42$, (b) $x = 0.48$.

The $x = 0.42$ and 0.48 alloys are in the martensitic phase below room temperature. The FC MR at 7T for $x = 0.42$ and 0.48 is shown in the Fig. 6.7. The MR behavior is totally different from $x = 0.32$ and 0.36 samples. At 300 K, MR is very less and is -0.15% (7 T) and -0.05% (7 T) for $x = 0.42$ and 0.48 , respectively. The magnetization results confirms the paramagnetic martensitic phase for $x = 0.42$ and 0.48 at 300 K. The magnetic ordering temperature is 154 K for $x = 0.42$. The

$x = 0.48$ does not show any magnetic ordering upto 80 K. Thus, very less MR at 300 K is due to the paramagnetic martensitic phase. The magnitude of MR increases with decreasing temperature for both the compositions. There is a sharp increase in the MR between 200 K to 100 K for $x = 0.42$ and it tends to saturate at below 50 K. The mid point (150 K) of this sharp decrease in MR is matching with the magnetic ordering temperature, marked by an arrow in Fig. 6.7. Thus the sharp MR change can be related with the scattering from the magnetic spins.

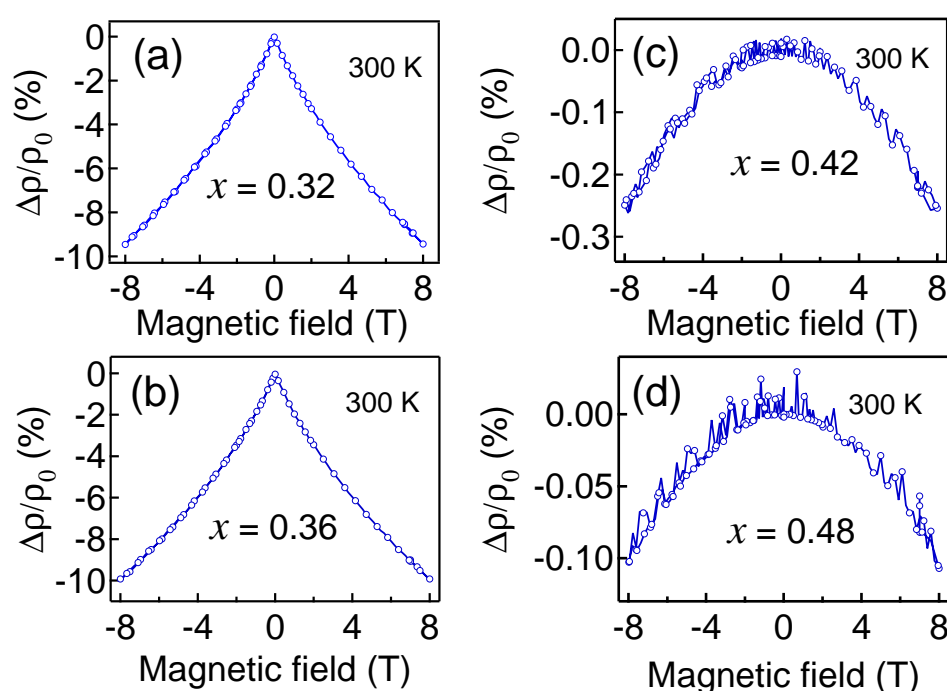


Figure 6.8 ZFC isothermal MR at 300 K of $\text{Ni}_2\text{Mn}_{1+x}\text{In}_{1-x}$ ($0.32 \leq x \leq 0.48$).

The ZFC isothermal MR behavior at 300 K is shown in Figs. 6.8 (a) - (d). For $x = 0.32$ and 0.36 [Figs. 6.8 (a) and (b)], ZFC MR is -9.5% (8 T) and -10% (8 T) at 300 K, respectively. These values of MR are similar to the FC MR. At 300 K, $x = 0.32$ and 0.36 are in the austenitic phase with ferromagnetic spin alignment as evident from the isothermal magnetization. In the ferromagnetic austenitic phase of $\text{Ni}_2\text{Mn}_{1+x}\text{In}_{1-x}$, negative MR is due to the reduction in the scattering of conduction electron by the localised spins. The similar MR behavior in the ferromagnetic austenitic phase of $\text{Ni}_2\text{Mn}_{1+x}\text{Sn}_{1-x}$ [25] and $\text{Ni}_{2+x}\text{Mn}_{1-x}\text{Ga}$ [1, 20, 21] is observed and explained on the ba-

sis of the s - d scattering model, where s conduction electrons are scattered by localized d spins. The MR in austenitic phase of Ni-Mn-In is much larger than that for Ni-Mn-Sn and Ni-Mn-Ga systems. For $x = 0.42$ and 0.48 [Figs. 6.8 (c) and (d)], MR is only -0.25% and -0.1% at 8T , respectively. The parabolic nature of magnetic field dependence confirms the paramagnetic state. The structural and magnetic transition temperatures also show the paramagnetic martensitic phase at 300 K for $x = 0.42$ and 0.48 .

The ZFC isothermal MR at 150 K is shown in the Figs. 6.9 (a) - (d). The composition with no martensitic transition ($x = 0.32$) shows the positive MR below 0.7 T [Fig. 6.9 (a)] and above 0.7 T MR is negative, -3.4% at 8T . The $x = 0.36$ [Fig. 6.9 (b)] gives large isothermal MR of -78% (8 T).

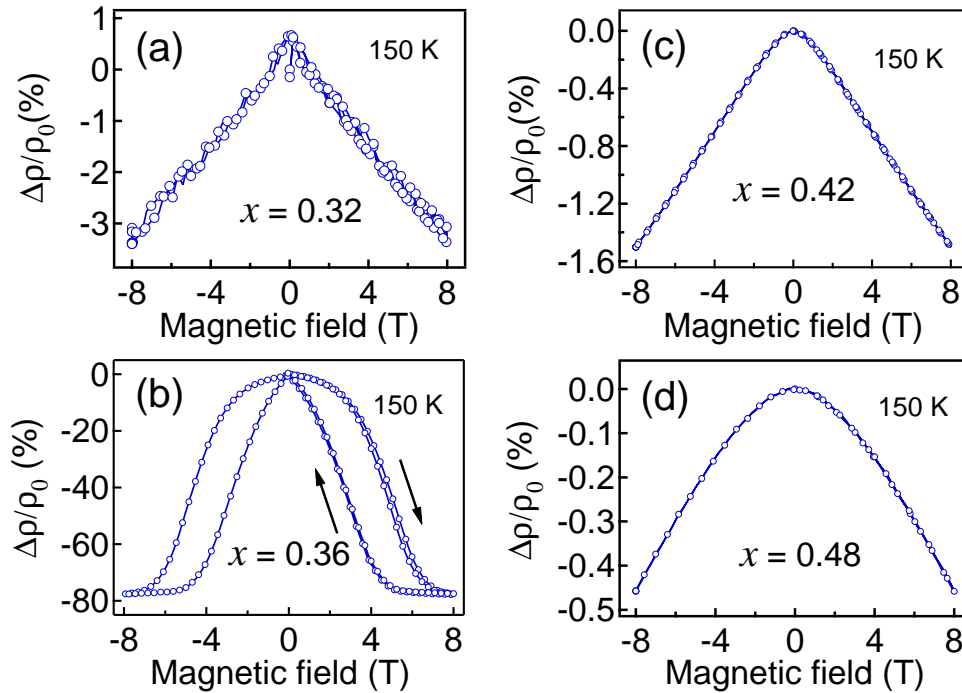


Figure 6.9 ZFC isothermal MR at 150 K of $\text{Ni}_2\text{Mn}_{1+x}\text{In}_{1-x}$ ($0.32 \leq x \leq 0.48$).

At 150 K , $x = 0.36$ alloy is completely in the martensitic phase during cooling since the martensitic finish (M_F) is 168 K . The phenomenon of kinetic arrest of martensitic phase transformation is not observed during ZFC from 300 K . The huge MR is mainly due to the magnetic field induced reverse phase transformation (MFIRPT) [10]. The increase of field from 0 to 8 T induces more and

more reverse phase transition of martensitic phase to austenitic phase. The austenitic phase has less resistivity than martensitic phase. Thus MR increases drastically. The lowering of H reverses back the austenitic phase fraction to martensitic phase. In the equilibrium state of martensitic phase, the isothermal application of magnetic field does not show kinetic arrest of austenitic phase after removing the magnetic field and austenitic phase fraction transforms back to martensitic phase. The effect of MFIRPT is also observable in the isothermal magnetization behavior of $x = 0.36$ at 150 K and 200 K [Figs. 4.12 (c) and (d)] where $M(H)$ behavior shows large hysteresis loop. For $x = 0.42$ and 0.48 MR is -1.5% and -0.5% at 8 T, respectively. The T_C^M of $x = 0.42$ is 154 K. Thus, the MR obtained is due to coexistence of ferromagnetic and anti-ferromagnetic phase. The small MR of $x = 0.48$ is due to paramagnetic phase, which is also evident from the parabolic variation MR.

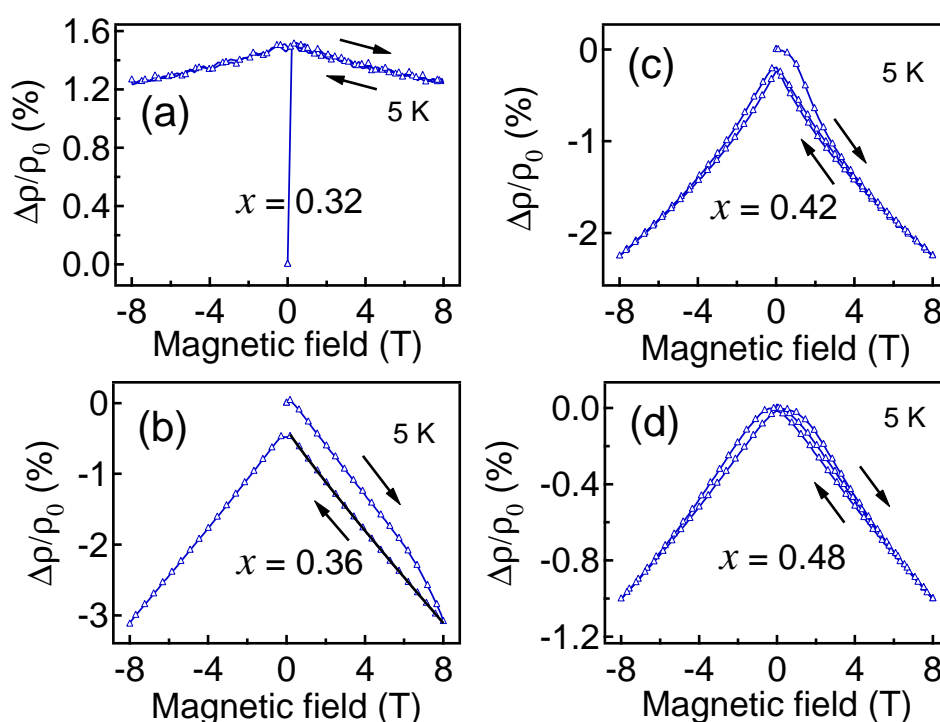


Figure 6.10 ZFC isothermal MR at 5 K of $\text{Ni}_2\text{Mn}_{1+x}\text{In}_{1-x}$ ($0.32 \leq x \leq 0.48$). Solid line is fit to the data with Eq. 6.1.

The ZFC isothermal MR behavior at 5 K is shown in Figs. 6.10 (a) - (d). It is noteworthy that

the MR with FC at 5 K for $x = 0.32$ is positive and that for $x = 0.36$ is negative. At 5 K MR is +1.5% at 1 T and it decreases with increasing magnetic field and is +1.2% at 7 T. At 5 K, the site and magnetic disorder induced e-e interaction and weak localization are dominant. The e-e interaction gives positive MR while weak localization is responsible for negative MR [22]. The positive MR at low temperature is reported in various disordered systems [22]. Thus positive MR for $x = 0.32$ at low temperature might be due to e-e interaction.

The Fig. 6.10 (b) shows the ZFC MR at 5 K for $x = 0.36$. The substantial and interesting difference between FC and ZFC MR behavior is distinctly noticeable at 5 K for $x = 0.36$. The ZFC MR at 5 K is only -3.1% (8 T), whereas FC MR at 5 K is -79% (7 T). This difference in MR with

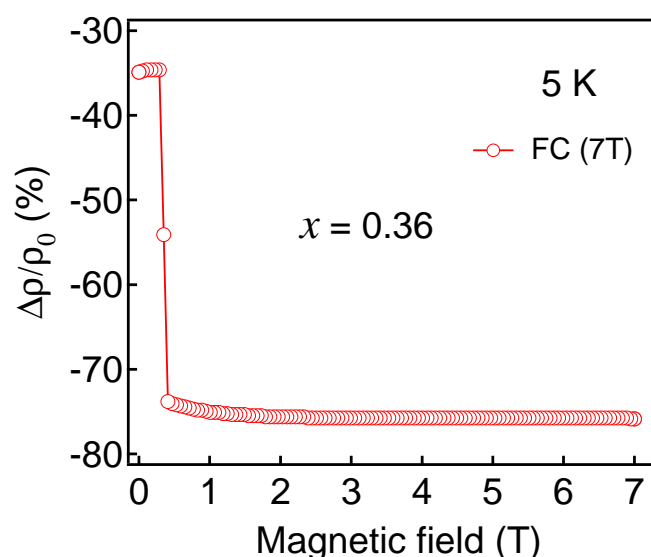


Figure 6.11 Isothermal MR at 5 K for $x = 0.36$ after 7 T FC from 300 K.

FC and ZFC is not observed in Ni-Mn-Sn alloys [25]. This is further verified by isothermal MR measurement at 5 K after field cooling from 300 K to 5 K with 7 T applied magnetic field and is shown in Fig 6.11. The MR at 5 K after 7 T FC is $\simeq -76\%$. Upon reducing the magnetic field isothermally at 5 K the sudden (partial) transformation to martensitic phase is observed around 0.5 T. The MR at zero field is $\simeq -35\%$, which is higher than that observed for ZFC. As discussed in previous chapter, with 7 T FC 90% austenite phase and 10% martensite phase is present at 5 K. Since the austenitic phase has very low resistivity as compared to martensitic phase at 5 K, large

MR is observed with 7 T FC. Below 0.5 T (Fig. 6.11) the fraction of martensitic phase increases ($\simeq 46\%$ martensite), which increases the structural and magnetic disorder. Thus, MR magnitude decreases. In order to understand the origin of MR behavior under ZFC the MR is fitted with the Eq. 6.1. It describes the magnetic field dependence of MR, which will explain the nature of magnetic state. For $x = 0.36$ ZFC MR is almost linear with $n \simeq 1$. To further understand the origin of MR, the ZFC MR at 5 K is also fitted with the simple phenomenological model [32, 33]. The temperature (and field) dependence of resistivity of a ferromagnet can be regarded as governed by its magnetic part $\propto [1 - m(H, T)^2]$, where $m(H, T) = M(H, T)/M_{S_0}$. Here H is magnetic field and T is temperature. M_{S_0} is the saturation magnetization at $T = 0$. Accordingly, the MR of a ferromagnet can be expressed as [32]

$$MR \propto \frac{m(H, T)^2 - m(0, T)^2}{1 - m(0, T)^2} \propto m(H, T)^2 - m(0, T)^2 \quad (6.2)$$

Similarly, magnetic part of resistivity for anti-ferromagnets is proportional to $1 - m_Q(H, T)^2/[1 - \Gamma m(H, T)]$, where $m_Q(H, T)$ is normalized staggered magnetization with anti-ferromagnetic wave-vector Q [34]. The coefficient Γ represents the effect of super-zone boundary, which causes a rapid increase of resistivity just below Neel temperature. Similarly to Eq. 6.2, the MR due to AFM correlations can be expressed as

$$MR \propto \frac{m_Q(H, T)^2 - m_Q(0, T)^2}{1 - \Gamma m_Q(0, T)^2} \propto m_Q(H, T)^2 - m_Q(0, T)^2 \quad (6.3)$$

Hence, both Eqs. 6.2 and 6.3 give $MR \propto m(H, T)^2 - m(0, T)^2$.

The MR at 5 K fitted with the above phenomenological model is shown in Fig. 6.12. The MR is found to vary linearly (decreasing M^2 cycle) as a function of $M(H, T)^2 - M_S^2$ at 5 K similar to that reported for martensitic phase of Ni-Mn-Sn thin films [32]. Also, the ZFC M vs H behavior at 5 K [inset of Fig. 6.12] do not show the phenomenon of magnetic field induced reverse phase transition and kinetic arrest upto 10 T magnetic field. Thus, with ZFC the kinetic arrest do not occur. With ZFC the martensitic phase is present at 5 K. The martensitic phase has complex magnetic and structural ground state. In the off-stoichiometric $\text{Ni}_2\text{Mn}_{1+x}\text{In}_{1-x}$ the extra Mn atoms occupy the In site. The large difference of the atomic number and size between Mn and In create the site

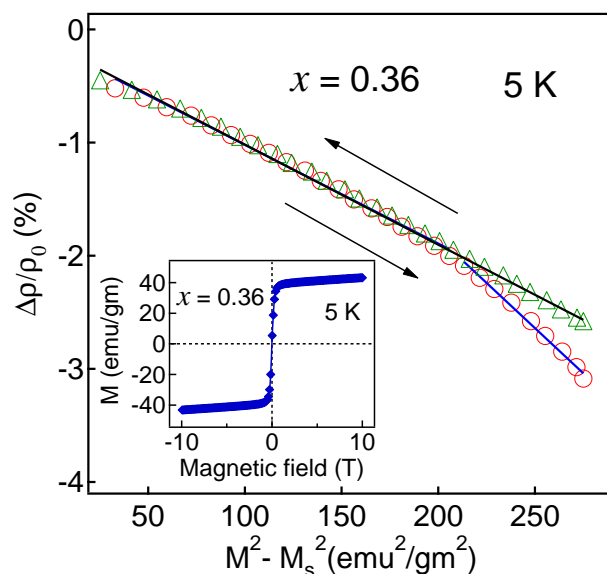


Figure 6.12 MR as a function of $M(H,T)^2 - M_s^2$ at 5 K in the martensitic phase. Solid line is linear fit to curve. Inset shows ZFC isothermal M vs H behavior at 5 K for $x = 0.36$.

disorder. The Mn at In site (Mn2) is anti-ferromagnetically coupled with the Mn at Mn site (Mn1) that have ferromagnetic ground state [35–37]. Thus the martensitic phase has mixed magnetic (ferro and anti-ferro) ground state with site disorder. The slight change in slope during increasing M^2 cycle shows that a possible glassy state with mixed magnetic phase exist at 5 K according to Eq. 6.2 and Eq. 6.3. Due to this, also, the MR with increasing (0 T \rightarrow 8 T) and decreasing (8 T \rightarrow 0 T) magnetic field does not follow the same path [Fig. 6.10 (b)]. Also the martensitic phase consists of twins oriented in different directions. This might give rise to magnetization in different directions. The Zeeman energy difference between two phases is much higher than magneto-crystalline anisotropy difference between two phases [5]. Thus the net effect of magnetic field is to rotate the magnetization within the unfavourable magnetically oriented twins. Also the twin boundary scattering is reduced. These mechanisms give rise to lower negative MR with ZFC at low temperature. The $x = 0.42$ and 0.48 are also in the martensitic phase at 5 K. The MR is -2.2% (8 T) and -1% (8 T) for $x = 0.42$ and 0.48 , respectively. Since these alloys are in mixed ferromagnetic and anti-ferromagnetic martensitic phase, with the increase in Mn2 the anti-ferromagnetic spins within the ferromagnetic domain of a twin is increasing. It might increase the twinning stress and

spin disorder scattering. Thus MR reduces with more Mn2.

6.2.3 Co doped Ni-Mn-In alloys

The FC MR as a function of temperature for NCMI1 ($\text{Ni}_{1.81}\text{Co}_{0.22}\text{Mn}_{1.46}\text{In}_{0.51}$) at 7 T is shown in Fig. 6.13. At 300 K MR is -0.4% (7 T). The MR increases with decreasing temperature. The MR variation with temperature is very much similar with $\text{Ni}_2\text{Mn}_{1.48}\text{In}_{0.52}$ alloy. At 300 K it is in the paramagnetic martensitic phase. The isothermal magnetization shows that short range magnetic correlations begin to develop below 150 K. The magnetic state of both NCMI1 and $\text{Ni}_2\text{Mn}_{1.48}\text{In}_{0.52}$ is similar. Thus the MR has same origin in both alloys.

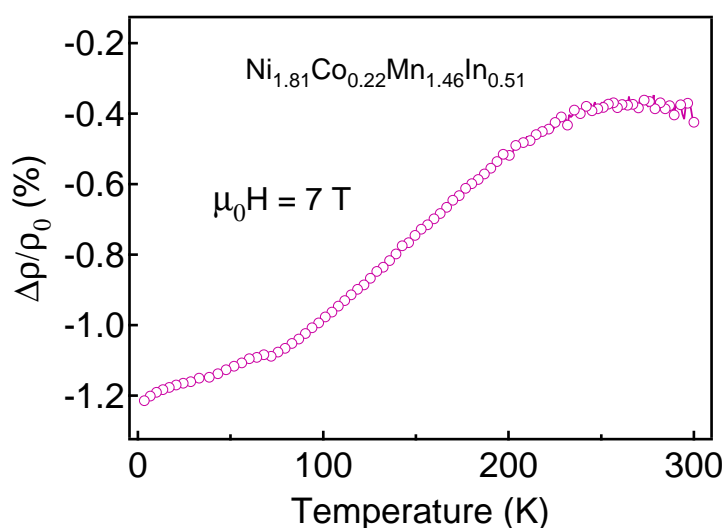


Figure 6.13 FC MR as a function of temperature for $\text{Ni}_{1.81}\text{Co}_{0.22}\text{Mn}_{1.46}\text{In}_{0.51}$ at 7 Tesla field.

The ZFC isothermal MR upto 8 Tesla is shown in Figs. 6.14 (a), (b) and (c). At 300 K MR is -0.48% (8 T) and shows parabolic variation. It is due to the presence of paramagnetic martensitic phase. At 150 K MR is -0.7% (8 T). It increases due to the presence of short range magnetic correlations in the paramagnetic martensitic phase. At 5 K MR is -1.2% (8 T). The ZFC isothermal MR has same magnitude as FC MR.

The temperature dependence of FC MR of NCMI2 ($\text{Ni}_{1.81}\text{Co}_{0.22}\text{Mn}_{1.45}\text{In}_{0.52}$) at different magnetic fields are shown in Fig.6.15. Although there is negligible difference in the composition of

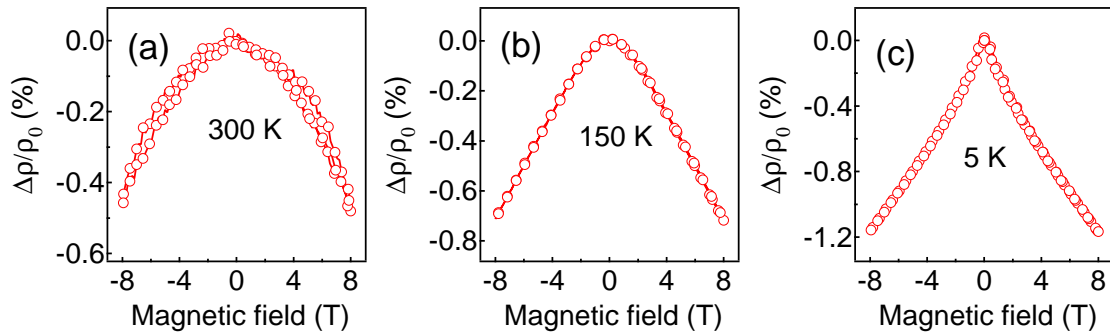


Figure 6.14 ZFC isothermal MR of $\text{Ni}_{1.81}\text{Co}_{0.22}\text{Mn}_{1.46}\text{In}_{0.51}$ at (a) 300 K, (b) 150 K, (c) 5 K.

both NCMI1 and NCMI2 alloys, their MR behaviour is completely different. The MR is -13% (1 T) at 300 K. It drastically increases with high magnetic field and is -70% at 7 T. A hysteresis in temperature dependent MR is obtained below 300 K and it increases with higher fields. At 300 K sample is in the mix state of austenitic and martensitic phase because M_F is 292 K. Application of 7 T magnetic field at 300 K induces the reverse phase transformation due to the decrease in martensitic transformation temperature. Thus large MR near 300 K is due to the magnetic field

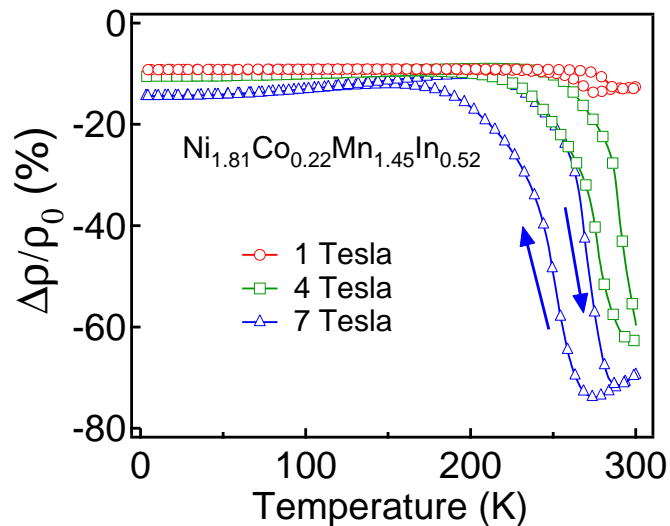


Figure 6.15 FC MR as a function of temperature for $\text{Ni}_{1.81}\text{Co}_{0.22}\text{Mn}_{1.45}\text{In}_{0.52}$.

induced reverse phase transformation (MFIRPT). This hysteresis in MR is related with the struc-

tural (martensitic) transformation. The maximum MR is -74% (7 T) at 276 K. Below the structural transformation MR is almost constant (-9%) upto 5 K at 1 T. At 7 T magnetic field MR slowly increases with decreasing temperature below the structural transformation. The MR of -14% (7 T) is obtained at 5 K. Further below the transformation temperature FC MR is mainly due to kinetic arrest of the austenitic phase fraction. The contribution from the other factors discussed later in the isothermal MR is very less. The isothermal MR at 300 K, 150 K, 5 K are shown in the Fig. 6.16. The MR of -52% is obtained at 8 T field. At 300 K, hysteresis clearly represent the MFIRPT. The isothermal MR at 300 K is measured just after the thermal cycling (300 K - 5 K - 300 K) at 4 T. Thermal cycling at 4 T increases the austenitic phase fraction at 300 K. Thus isothermal MR is less than the FC MR at 300 K.

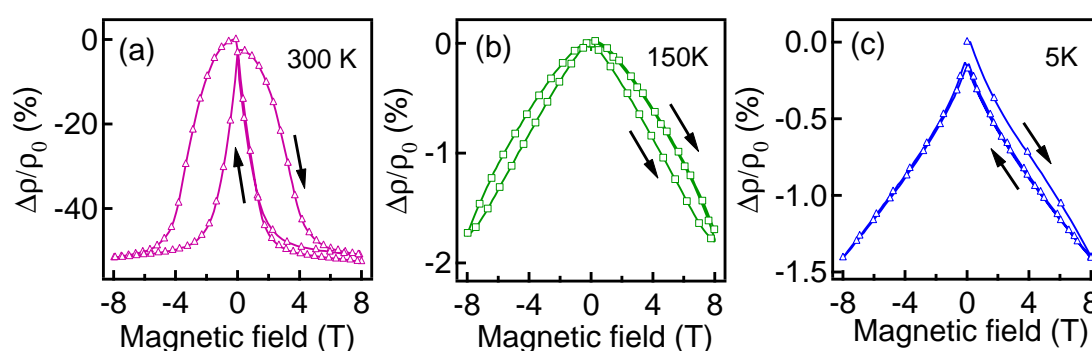


Figure 6.16 Isothermal MR of $\text{Ni}_{1.81}\text{Co}_{0.22}\text{Mn}_{1.45}\text{In}_{0.52}$ at (a) 300 K, (b) 150 K, (c) 5 K.

The isothermal MR at 150 K and 5 K are measured after ZFC from 300 K to desired temperature. The isothermal MR at 150 K is -2% at 8 T. At 150 K sample is in paramagnetic state with short range magnetic correlations. Thus MR is mainly due to the reduction in the magnetic scattering by alignment of magnetic spins along the field direction. Small hysteresis in the MR curves is due to the reverse phase transformation caused by the magnetic field. The MFIRPT is very less at 150 K because this temperature is much below the M_F temperature. At 4 K isothermal magnetization confirms the dominant ferromagnetic behaviour. At 5 K, MR is -1.4% at 8 T. At this temperature spin disorder induced scattering mechanisms has dominant contribution in origin of MR.

6.3 Conclusion

The longitudinal MR of Ni-Mn-Sn, Ni-Mn-In and Ni-Co-Mn-In alloys has been studied as functions of temperature and magnetic field. In the austenitic phase at 300 K maximum MR -4.6% (8 T) is observed in $\text{Ni}_2\text{Mn}_{1.4}\text{Sn}_{0.6}$. The maximum MR in austenitic phase of $\text{Ni}_2\text{Mn}_{1.36}\text{In}_{0.64}$ is -10% (8 T) at 300 K, which is higher than that of Ni-Mn-Sn alloys. In the austenitic phase, *s-d* scattering is responsible for negative MR. The large MR is observed across the martensitic transformation in these alloys. The large MR of -36% and -81% within the martensitic transition temperature range is observed in $\text{Ni}_2\text{Mn}_{1.4}\text{Sn}_{0.6}$ and $\text{Ni}_2\text{Mn}_{1.36}\text{In}_{0.64}$, respectively. The large MR is due to the magnetic field induced reverse phase transformation which is because of spin alignment in ferromagnetic state favoring $L2_1$ lattice of austenitic phase through spin lattice coupling. The large difference in the FC and ZFC MR is observed in the martensitic phase of $\text{Ni}_2\text{Mn}_{1.36}\text{In}_{0.64}$. With FC and ZFC at 5 K the maximum MR is -79% and -3.1%, respectively, at 7 T. The large MR with FC is due to presence of austenitic phase with structural and magnetic ordering. In contrast the small MR with ZFC is because of presence of martensitic phase where magnetization rotation within twin and reduction of twin boundary scattering occurs. This large difference in MR with FC and ZFC makes this system flexible for application, which is not possible with Ni-Mn-Sn. Although large MR -81% is obtained in Ni-Mn-In alloy but it is achieved much below room temperature (115 K). The Co doped Ni-Mn-In alloy show the large negative MR (-70%) at room temperature. Thus Ni-Co-Mn-In alloys are more promising candidate for the room temperature applications. The large MR value with FC than ZFC at low temperature is also achieved in Ni-Co-Mn-In alloys due to the kinetic arrest of austenitic phase fraction under FC condition.

Bibliography

- [1] C. Biswas, R. Rawat, and S. R. Barman, *Appl. Phys. Lett.* **86**, 202508 (2005).
- [2] Y. Sutou, Y. Imano, N. Koeda, T. Omori, R. Kainuma, K. Ishida, and K. Oikawa, *Appl. Phys. Lett.* **85**, 4358 (2004).
- [3] K. Koyama, K. Watanabe, T. Kanomata, R. Kainuma, K. Oikawa, and K. Ishida, *Appl. Phys. Lett.* **88**, 132505 (2006).
- [4] R. Kainuma, Y. Imano, W. Ito, Y. Sutou, H. Morito, S. Okamoto, O. Kitakami, K. Oikawa, A. Fujita, T. Kanomata, and K. Ishida, *Nature* **439**, 957 (2006).
- [5] H. E. Karaca, I. Karaman, B. Basaran, Y. Ren, Y. I. Chumlyakov, and H. J. Maier, *Adv. Funct. Mater.* **19**, 983 (2009).
- [6] K. Koyama, H. Okada, K. Watanabe, T. Kanomata, R. Kainuma, K. Oikawa, W. Ito, and K. Ishida, *Appl. Phys. Lett.* **89**, 182510 (2006).
- [7] M. Khan, A. K. Pathak, M. R. Paudel, I. Dubenko, S. Stadler, and N. Ali, *J. Magn. Magn. Mater.* **320**, L21-L25 (2008).
- [8] S. Chatterjee, S. Giri, S. Majumdar, and S. K. De, *J. Phys.D: Appl. Phys.* **42**, 065001 (2009).
- [9] I. Dincer, E. Yüzüak, Y. Elerman, *J. Alloys Comp.* **506**, 508 (2010).
- [10] S. Y. Yu, Z. H. Liu, G. D. Liu, J. L. Chen, Z. X. Cao, G. H. Wu, B. Zhang, and X. X. Zhang, *Appl. Phys. Lett.* **89**, 162503 (2006).

- [11] V. K. Sharma, M. K. Chattopadhyay, K. H. B. Shaeb, A. Chouhan, and S. B. Roy, *Appl. Phys. Lett.* **89**, 222509 (2006).
- [12] B. M. Wang, L. Wang, Y. Liu, B.C. Zhao, Y. Zhao, Y. Yang, and H. Zhang, *J. Appl. Phys.* **106**, 063909 (2009).
- [13] A. K. Pathak, B. R. Gautam, I. Dubenko, M. Khan, and S. Stadler, *J. Appl. Phys.* **103**, 07F315 (2008).
- [14] M. K. Chattopadhyay, M. A. Manekar, V. K. Sharma, P. Arora, P. Tiwari, M. K. Tiwari, and S. B. Roy, *J. Appl. Phys.* **108**, 073909 (2010).
- [15] W. Ito, K. Ito, R. Y. Umetsu, R. Kainumaa, K. Koyama, K. Watanabe, A. Fujita, K. Oikawa, K. Ishida, and T. Kanomata, *Appl. Phys. Lett.* **92**, 021908 (2008).
- [16] L. Chen, F. X. Hu, J. Wang, J. Shen, J. Zhang, J. R. Sun, B. G. Shen, J. H. Yin, and L. Q. Pan, *J. Appl. Phys.* **107**, 09A940 (2010).
- [17] A. K. Pathak, I. Dubenko, C. Pueblo, P. Basnyat, S. Stadler, and N. Ali, *IEEE Trans. Magn.* **46**, 6 (2010).
- [18] L. Chen, F. X. Hu, J. Wang, J. L. Zhao, J. R. Sun, B. G. Shen, J. H. Yin, and L. Q. Pan, *J. Phys.D: Appl. Phys.* **44**, 085002 (2011).
- [19] T. K. Nath and A. K. Majumdar, *Phys. Rev. B* **57**, 10655 (1998).
- [20] S. Banik, R. Rawat, P. K. Mukhopadhyay, B. L. Ahuja, A. Chakrabarti, P. L. Paulose, S. Singh, A. K. Singh, D. Pandey, and S. R. Barman, *Phys. Rev. B* **77**, 224417 (2008).
- [21] S. Banik, S. Singh, R. Rawat, P. K. Mukhopadhyay, B. L. Ahuja, A. M. Awasthi, S. R. Barman, and E. V. Sampathkumaran, *J. Appl. Phys.* **106**, 103919 (2009).
- [22] P. A. Lee and T. V. Ramakrishnan, *Rev. Mod. Phys.* **57**, 287 (1985).

- [23] T. Kanomata, T. Yasuda, S. Sasaki, H. Nishihara, R. Kainuma, W. Ito, K. Oikawa, K. Ishida, K.-U. Neumann, and K. R. A. Ziebeck, *J. Magn. Magn. Mater.* **321**,773 (2009).
- [24] X. Moya, L. Mañosa, A. Planes, S. Aksoy, M. Acet, E. F. Wassermann, and T. Krenke, *Phys. Rev. B* **75**, 184412 (2007).
- [25] S. Singh and C. Biswas, *Appl. Phys. Lett.* **98**, 212101 (2011).
- [26] M. Kataoka, *Phys. Rev. B* **63**, 134435 (2001).
- [27] V. K. Sharma, M. K. Chattopadhyay, and S. B. Roy, *Phys. Rev. B* **76**, 140401(R) (2007).
- [28] R. Y. Umetsu, W. Ito, K. Ito, K. Koyama, A. Fujita, K. Oikawa, T. Kanomata, R. Kainumaa, and K. Ishida, *Scripta Mater.* **60**, 25 (2009).
- [29] M. K. Chattopadhyay, S. B. Roy, and P. Chaddah, *Phys. Rev. B* **72**, 180401(R) (2005).
- [30] W. Wu, C. Israel, N. Hur, S. Park, S-W. Cheong, and A. D. Lozanne, *Nat. Mater.* **5**, 881 (2006).
- [31] A. Banerjee, K. Mukherjee, K. Kumar, and P. Chaddah, *Phys. Rev. B* **74**, 224445 (2006).
- [32] J. Dubowik, K. Załęski, I. Gościańska, H. Głowiński, and A. Ehresmann, *Appl. Phys. Lett.* **100**, 162403 (2012).
- [33] T. Kasuya, *Prog. Theor. Phys.* **16**, 58 (1956).
- [34] R. J. Elliot, in *Theory of Magnetism in the Rare Earth Metals*, Magnetism Vol. IIA, edited by G. T. Rado and H. Suhl (Academic, New York, 1965).
- [35] V. V. Khovaylo, T. Kanomata, T. Tanaka, M. Nakashima, Y. Amako, R. Kainuma, R. Y. Umetsu, H. Morito, and H. Miki, *Phys. Rev. B* **80**, 144409 (2009).
- [36] B. L. Ahuja, A. Dashora, N. L. Heda, K. R. Priolkar, L. Vadkhiya, M. Itou, N. Lobo, Y. Sakurai, A. Chakrabarti, S. Singh, and S R Barman, *J. Phys. : Condens. Matter.* **22**, 446001 (2010).

- [37] V. D. Buchelnikov, P. Entel, S. V. Taskaev, V. V. Sokolovskiy, A. Hucht, M. Ogura, H. Akai, M. E. Gruner, and S. K. Nayak, *Phys. Rev. B* **78**, 184427 (2008).

Chapter 7

Electronic structure

7.1 Introduction

The electronic structure studies on Ni-Mn-Sn are studied by very few [1–5]. The Ni₂MnSn does not exhibit martensitic transition whereas Ni₂Mn_{1+x}Sn_{1-x} alloys undergo martensitic transition. It is expected that the electronic structure plays the driving role in the martensitic transition. In 2001 A. Deb et al. [2] studied the spin-dependent electron momentum density in the Ni₂MnSn Heusler alloy. In the electronic density of states (DOS) of Ni₂MnSn the majority spin states are below the Fermi level. In the minority spin states, the two peaks [≈ -2 eV below and $\approx +1$ eV above the Fermi level (E_F)] are separated by the low density region in which the E_F is situated. This feature is characteristic of the stability of ferromagnetic ordered alloys and is interpreted as the energy separation between the bonding and anti-bonding orbitals. The partial density of states (PDOS) shows that the Ni 3*d* states and Mn 3*d* majority spin states are mainly confined to the 0 - 4 eV region of the valence band. The Mn 3*d* minority spin states dominate 0 - 3 eV region of the conduction band above the Fermi level. Therefore, the main carrier of the magnetic moment of Ni₂MnSn is Mn and the magnetic moment of the Ni atom is negligible. The Mn moment in Ni₂MnSn is almost equally contributed by 3*d* e_g and 3*d* t_{2g} subbands. The first principle ab-initio calculation of off-stoichiometric Ni₂Mn_{1+x}Sn_{1-x} ($x = 0.25, 0.50$) shows that the peak structure around -0.5 eV below E_F composed of the minority-spin 3*d* e_g states in the high temperature cubic phase has a systematic energy shift towards E_F with increasing Mn concentration (x). With increasing x the hybridization between Ni 3*d* and Mn2 (Mn at Sn site) 3*d* states causes the energy shift of Ni 3*d* e_g states towards E_F . Further the Jahn-Teller splitting of the Ni 3*d* e_g states plays an important role in driving the martensitic transition of the cubic phase for $x \geq 0.36$. Thus the martensitic transition for higher Mn concentrations is closely related to the electronic structure.

The photoelectron spectroscopy is a basic tool to probe the electronic structure experimentally. Very recently, High energy X-ray photoelectron spectroscopy (6 keV) study is performed by M. Ye et al. [3] on Ni₂Mn_{1+x}Sn_{1-x} ($0 \leq x \leq 0.42$) to find out the origin of martensitic phase transformation. A peak located around a binding energy (BE) of 1.5 eV was observed that did not change in all of the samples over the whole measured temperature range. In the vicinity of the E_F , a sharp

peak was observed at 0.3 - 0.4 eV BE at 300 K ($T \geq M_S$) in the austenite phase. A sudden reduction of the peak intensity near E_F is clearly observed for $x = 0.42$ when the temperature is decreased from 240 K to 220 K across the martensitic transition temperature (230 K). At lower concentrations ($x = 0.12$ and 0.00) there is no noticeable change near E_F with temperature. It shows that martensitic phase transformation is possible for $x \geq 0.36$. In this chapter, the X-ray photoelectron spectroscopy (XPS) and ultraviolet photoelectron spectroscopy (UPS) studies on $\text{Ni}_2\text{Mn}_{1+x}\text{Sn}_{1-x}$ and $\text{Ni}_2\text{Mn}_{1.32}\text{In}_{0.68}$ surface is reported.

7.2 Clean surface preparation under UHV

The surface sensitivity of photoelectron spectroscopy (PES) technique needs the surface of the solid to be free of contamination. Exposure to air contaminates the sample surface with atmospheric carbon, oxygen, etc. Hence, in-situ cleaning of any sample surface in ultra high vacuum (UHV) is very important. The cleanliness of the sample is monitored by recording O 1s and C 1s peak. Two methods widely used to prepare the clean surfaces in UHV are (a) mechanical scrapping using diamond file and (b) ion sputtering and annealing, [6] which are discussed below:

(a) The polycrystalline samples of $\text{Ni}_2\text{Mn}_{1+x}\text{Sn}_{1-x}$ alloys were mechanically scraped using diamond file in UHV to expose fresh intra-grain surfaces devoid of oxygen and carbon contamination. During scraping the base pressure was maintained at 1×10^{-9} mbar. Figure. 7.1 shows XPS spectra of contaminated surface with huge O 1s and C 1s before scrapping and clean surface after scrapping of $\text{Ni}_2\text{Mn}_{1.4}\text{Sn}_{0.6}$.

(b) The ions of rare gas, usually Ar, with energies between 500 eV to 3 keV are directed at the surface to be cleaned by a sputter gun. The collision of the incident ion with surface atoms give excess energy to the surface atoms. This excess energy displaces the atoms resulting in a cascade process that causes the ejection of atoms and clusters when it reaches the surface. The surface is therefore eroded by the loss of material. However, ion sputtering introduces defects on the surface. These defects can be removed by annealing at higher temperature. For the study of $\text{Ni}_2\text{Mn}_{1.32}\text{In}_{0.68}$ alloy, surface was sputtered with 1.5 keV Ar^+ ions for 1 hour and annealed above

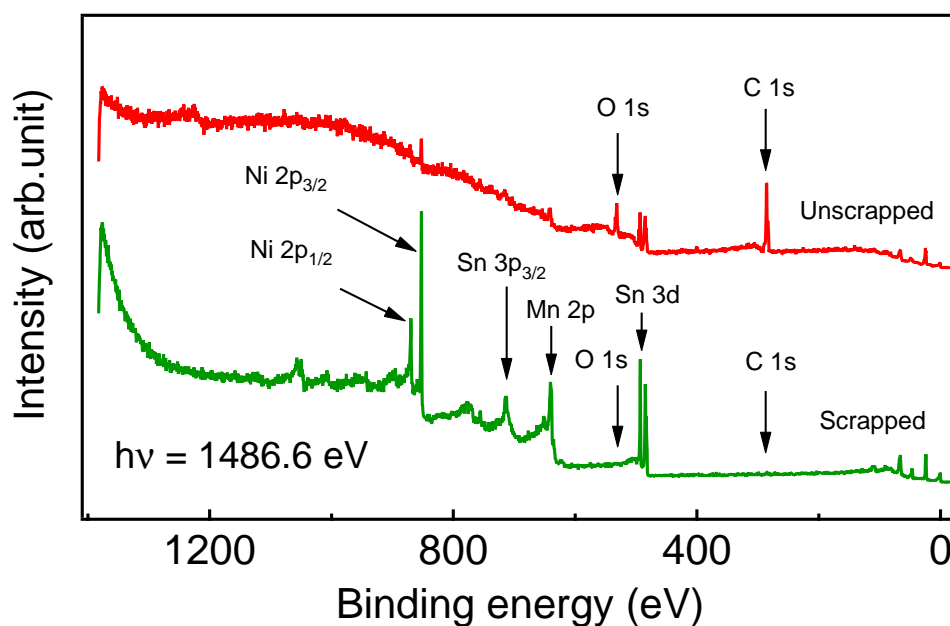


Figure 7.1 XPS spectra of contaminated surface before scraping and clean surface after scraping for $\text{Ni}_2\text{Mn}_{1.4}\text{Sn}_{0.6}$ recorded with $h\nu = 1486.6$ eV.

325°C for 2 hours. Results are discussed in section 7.4.1.

7.3 Data analysis procedure

All the data analysis was done using Igor Pro software [7]. From the core-levels, background due to inelastic scattering was subtracted using the Tougaard method. Figure. 7.2 shows the XPS spectrum before and after background subtraction. Tougaard and Sigmund [8] derived a rigorous formula to extract the primary spectrum from the measured spectrum taking into account the influence of elastic and inelastic electron scattering on the shape and intensity of the spectrum in the vicinity of the primary peak:

$$F(E) \cong j(E) - B_1 \int_E^\infty \frac{E' - E}{[C + (E' - E)^2]^2} j(E') dE' \quad (7.1)$$

where, $F(E)$ is the primary excitation spectrum, $j(E)$ is the measured flux of emitted electrons at energy E from a homogeneous solid, $C = 1643 \text{ eV}^2$, and B parameter is changed in order to match

the background of the spectrum on the higher and lower kinetic energy side. After background sub-

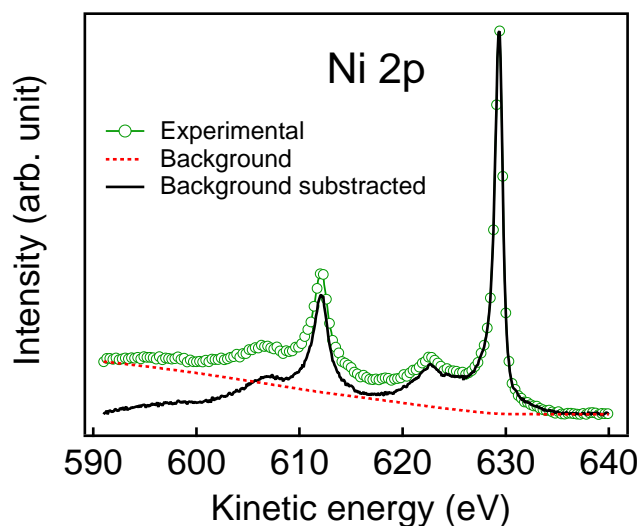


Figure 7.2 Comparison of XPS spectra with and without Tougaard background subtraction.

traction, the instrumental factors (i.e. the analyzer and the photon source related broadenings) have been determined. The main core-level peak has been fitted with Doniac-Sunjic (DS) line-shape, which is characteristic of metals. The DS line-shape is discussed in next paragraph. To account for the instrumental parameters, the DS line-shape has been convoluted with the Voigt function. The Voigt function is the convolution of a Lorentzian and a Gaussian function. The Lorentzian contribution arises from the line width of the X-ray source and intrinsic line width due to lifetime of the core hole in the photo-excited atom. The analyzer transmission function is assumed to be Gaussian. Thus, in the curve fitting the parameters that are freely varied are the Gaussian and Lorentzian widths, intensity, DS asymmetry parameter, core-level kinetic energy and lifetime broadening (2γ). A least square iterative fitting was performed to find the fitting coefficients such that they minimize the chi-square. Chi-square is a multidimensional error function, which is the measure of the goodness of fit and is defined as:

$$\sum_i \left(\frac{y - y_i}{\sigma_i} \right)^2$$

where, y is the fitted value for a given point, y_i is the original data value for the point and σ_i is the standard deviation for the point. The fitting procedure uses Levenberg-Marquardt (LM)

algorithm [9, 10] to minimize chi-square [7].

Doniach-Sunjic asymmetry: The Doniach-Sunjic (DS) asymmetry [11] of the core-level line-shape toward higher binding energy (BE) side is a final state effect that is observed in metals only. The screening of the core-hole produced in the photoemission final state gives rise to infinitesimal electron-hole excitations across the E_F [12]. The density-of-states (DOS) above the E_F provides a continuous range of allowed one-electron excitation energies. Thus, an asymmetric tailing on the low energy side of the elastic peak is observed. The line-shape associated with such process in XPS core-level emission is expressed by convoluting $1/E^{1-\alpha}$ singularity with the lifetime broadening 2γ [11]

$$Y(E) = \frac{\Gamma(1-\alpha) \cos[\pi\alpha/2 + (1-\alpha) \arctan(E/\gamma)]}{(E^2 + \gamma^2)^{(1-\alpha)/2}} \quad (7.2)$$

where, E is kinetic energy measured from the threshold of the unbroadened one-electron-transition peak, γ is the lifetime broadening of the core-hole. α is the DS asymmetry parameter given as

$$\alpha = \sum_l (2l+1) (\delta_l/\pi)^2$$

where, δ_l is the phase shift of the l^{th} partial wave for electrons at the Fermi energy scattering from the core-hole. If $\alpha = 0$, $Y(E)$ is reduced to a Lorentzian lifetime broadening and for $(E/\gamma) \gg 1$ i.e. for the infinite lifetime of hole state the $1/E^{1-\alpha}$ dependence is obtained. The spectral line-shape given by $1/E^{1-\alpha}$ is obtained by perturbation theory by considering the effect of sudden application of potential on a Fermi gas [13]. As $E \rightarrow 0$, a logarithmic divergence is obtained which is known as infrared catastrophe [14].

The data collected with non-monochromatic (MgK_α) X-ray source consists of K_β photon energy. Hence, satellite subtraction is also done for such spectra. The features due to the MgK_β satellite lines have been subtracted using a routine written in Igor programming language [7]. In the routine, it is assumed that the satellites produce a replica spectrum as the main line, but is shifted and reduced in intensity.

7.4 Result and Discussion

7.4.1 Surface characterization

The photoelectron spectroscopy is surface sensitive technique. The typical probing depth by XPS is around 20 Å. Thus the spectra is representative of both surface and bulk features. So, it is important to characterize the surface. For multicomponent alloys the surface properties like segregation, termination, relaxation and reconstruction are important in determining the electronic structure. The properties are also highly sensitive to surface preparation.

For Ni-Mn-Z(Sn and In) Heusler alloys with martensitic transition the understanding of surface properties is very much needed since the properties of thin films of these materials are intimately related to detailed understanding of electronic structure. Also the bulk properties are found to change significantly with slight change in composition. Thus it is important to make sure that whether the surface electronic structure also undergoes noteworthy changes with composition or not.

The surface composition of these alloys is determined by XPS. The area under the XPS core-level is determined by fitting the spectra with Doniac-Sunjic (DS) line-shape [11]. Tougaard method [15] is used for the background subtraction. The instrumental broadening is considered in fitting by convoluting the line shapes with a Voigt function. The instrumental parameters are kept fixed during the fitting. The instrumental parameters are obtained from the standard Ag sample. For determining composition, the atom density (N) of each constituent is calculated by normalizing the area under the corresponding core-level peak (I) by the respective photo-ionization cross-section σ [16], the mean free path (λ) of the photoelectron for an inorganic compound [17], and the analyzer étendue ($G(E)$). The analyzer étendue of Phoibos 100 is proportional to $E_{\text{kin}}^{0.5}$ [6], whereas that for Scienta R4000 is given by $G(E) = 1 - 0.041q + 9.4e^{-4}q^2 - 1.0e^{-5}q^3 + 3.9e^{-8}q^4$, where $q = E_{\text{kin}}/E_{\text{pass}}$, E_{kin} is the kinetic energy of the photoelectron, E_{pass} is the pass energy of the analyzer. Thus, N is given by the equation

$$N = \frac{I}{\sigma \cdot \lambda(E) \cdot G(E) \cdot C} \quad (7.3)$$

where C is a product of the detector efficiency, angular asymmetry photoelectron intensity, flux of the X-ray characteristic line per unit area, inverse cosine of incidence angle and cosine of emission angle.

The surface of $\text{Ni}_2\text{Mn}_{1+x}\text{Sn}_{1-x}$ is prepared clean by mechanical scrapping. The core-level spectra (Ni $3p$, Mn $3p$ and Sn $4d$) of clean surface for $x = 0.40 - 0.52$ is shown in Fig. 7.3. The Ni $3p$, Mn $3p$ and Sn $4d$ core-levels are chosen for determining the composition because their BE are close to each other such that the differences in analyzer étendue and λ are small. These core-levels appear at 66.1 ± 0.1 eV, 46.8 ± 0.1 eV, 23.8 ± 0.1 eV BE, respectively. There is no change in BE with composition.

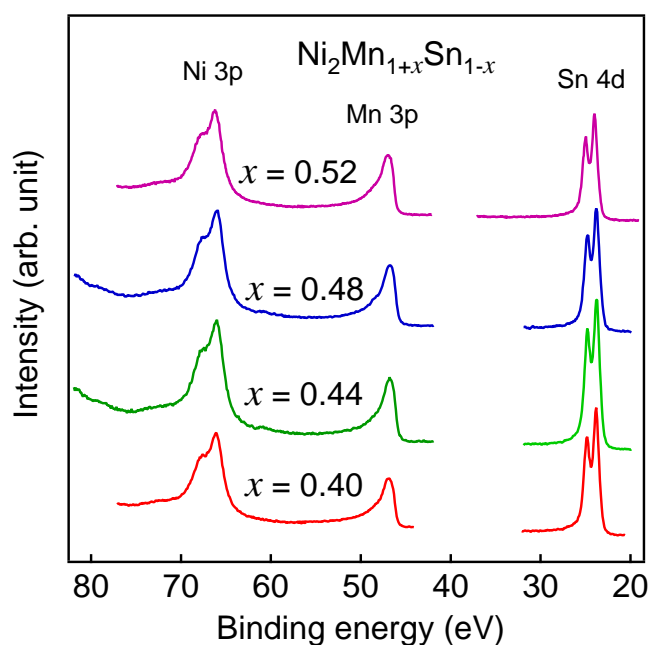


Figure 7.3 Ni $3p$, Mn $3p$ and Sn $4d$ core-level spectra of $\text{Ni}_2\text{Mn}_{1+x}\text{Sn}_{1-x}$ recorded with $h\nu = 1486.6$ eV.

The calculated surface composition is shown in Table 7.1. The surface composition is different than bulk composition. As compared to bulk the surface is Sn rich and Mn deficient. However,

the surface is still Mn excess and extra Mn occupies mostly the Sn site. The reduction in Mn concentration at the surface could be due to diffusion of Mn from surface to bulk. It is known that the diffusion rate of Mn is larger than other elements [18]. The vapour pressure of Mn is the highest of all constituents. The loss of Mn from surface could also occur during sample preparation due to evaporation of Mn when annealed in vacuum. Also, the different chemical potential for surface

Table 7.1 Surface composition of $\text{Ni}_2\text{Mn}_{1+x}\text{Sn}_{1-x}$ deduced from Ni 3*p*, Mn 3*p* and Sn 4*d* core-levels.

Bulk composition	Surface composition
$\text{Ni}_2\text{Mn}_{1.40}\text{Sn}_{0.60}$	$\text{Ni}_{1.97}\text{Mn}_{1.14}\text{Sn}_{0.89}$
$\text{Ni}_2\text{Mn}_{1.44}\text{Sn}_{0.56}$	$\text{Ni}_{1.91}\text{Mn}_{1.25}\text{Sn}_{0.84}$
$\text{Ni}_2\text{Mn}_{1.48}\text{Sn}_{0.52}$	$\text{Ni}_{1.92}\text{Mn}_{1.34}\text{Sn}_{0.74}$
$\text{Ni}_2\text{Mn}_{1.52}\text{Sn}_{0.48}$	$\text{Ni}_{1.85}\text{Mn}_{1.48}\text{Sn}_{0.67}$

and bulk could cause deviation from a constant concentration throughout the sample [18]. The Ni percentage is almost similar in both bulk and surface. This surface composition is obtained in normal emission geometry with maximum probing depth of 16 Å. To check the variation of surface composition with depth the emission angle was changed. The Fig. 7.4 presents the surface

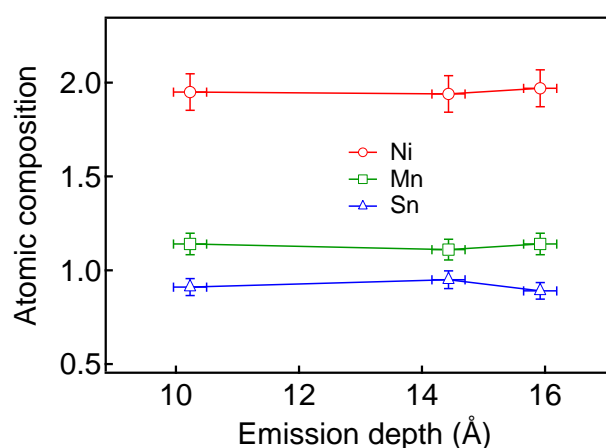


Figure 7.4 Surface composition of $\text{Ni}_2\text{Mn}_{1.4}\text{Sn}_{0.6}$ as a function of emission depth.

composition of $\text{Ni}_2\text{Mn}_{1.4}\text{Sn}_{0.6}$ as a function of depth. The concentration of Ni, Mn and Sn remains constant. Thus, the surface composition is same within the error till 16 Å depth.

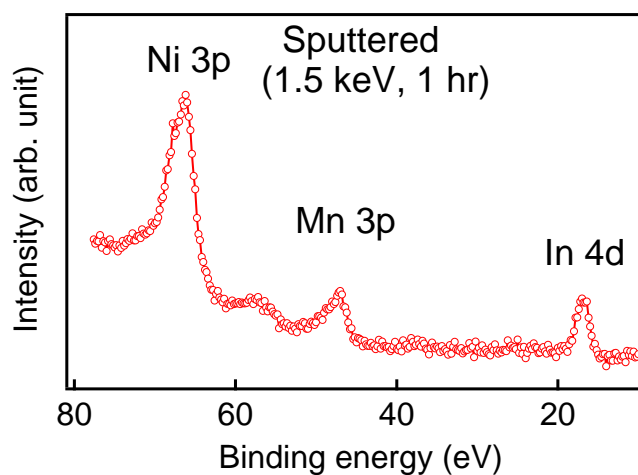


Figure 7.5 Ni 3*p*, Mn 3*p* and In 4*d* core-level spectra of sputtered $\text{Ni}_2\text{Mn}_{1.32}\text{In}_{0.68}$ recorded with $h\nu = 1253.6$ eV.

The surface composition could be made similar to bulk composition as shown for Ni-Mn-Ga system [19] by sputtering and annealing process. Thus, the clean surface of $\text{Ni}_2\text{Mn}_{1.32}\text{In}_{0.68}$ is prepared by Ar ion (1.5 keV) sputtering on the polycrystalline sample for 1 hour. The Fig. 7.5 represents the Ni 3*p*, Mn 3*p* and In 4*d* core-levels after sputtering. These core-levels appear at 66.2 ± 0.2 eV, 47 ± 0.2 eV, 16.8 ± 0.2 eV BE, respectively. The surface composition determined from above core-levels is $\text{Ni}_{2.9}\text{Mn}_{0.8}\text{In}_{0.3}$ in contrast to the bulk composition ($\text{Ni}_2\text{Mn}_{1.32}\text{In}_{0.68}$). Due to sputtering Ni content in the sample increases, while Mn and In content decreases. This is because the sputtering yield of Ni is less than Mn and In. Such Ni enrichment due to sputtering is also observed for $\text{Ni}_{2.1}\text{Mn}_{0.9}\text{Ga}$ [19].

To achieve the bulk composition on surface, $\text{Ni}_2\text{Mn}_{1.32}\text{In}_{0.68}$ is annealed at 325 °C and above after sputtering. The Ni 3*p*, Mn 3*p* and In 4*d* core-level spectra of sputtered surface and annealed at different temperatures are shown in Fig. 7.6 (a). The corresponding Ni, Mn and In content are plotted in Fig. 7.6 (b). Annealing at 325 °C increases the Mn 3*p* and In 4*d* peak intensity while Ni 3*p* peak intensity decreases. The composition after annealing at 325 °C is $\text{Ni}_{2.1}\text{Mn}_{0.9}\text{In}_{1.0}$. It

suggests that with annealing Mn and In segregates to the surface. The Mn segregation by annealing has also been observed in a similar half-metallic Heusler alloy NiMnSb [20,21]. Further increasing

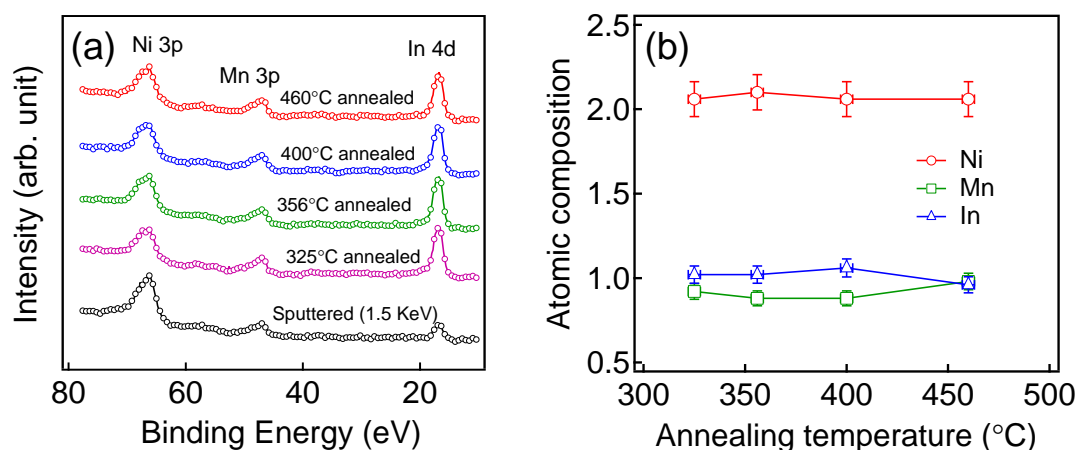


Figure 7.6 (a) Ni 3*p*, Mn 3*p* and In 4*d* core-level spectra of Ni₂Mn_{1.32}In_{0.68} (recorded with $h\nu = 1253.6$ eV) after sputtering (Ar ion) and annealed at different temperatures after sputtering. (b) Variation in the surface composition as a function of annealing temperature.

the annealing temperature upto 460°C brings the surface to stoichiometric composition. This indicates that the loss due to evaporation during annealing is compensated by segregation of Mn and In from bulk. At 460°C the surface tries to stabilize at the stoichiometric composition Ni₂MnIn. Similar behavior is also observed for Ni₂Mn_{1.4}Sn_{0.6} using sputtering and annealing technique [22].

The XPS VB spectra of Ni₂Mn_{1.32}In_{0.68} recorded with $h\nu = 1253.6$ eV after Ar ion sputtering (1.5 keV) and annealing at different temperatures is shown in Fig. 7.7. The VB of sputtered surface shows a peak around 0.8 eV BE while annealed surface exhibits a broad peak centered at 1.3 eV BE. The photoionization cross-section of Mn 3*d* (0.0026 mega barn) and In 5*s* (0.0013 mega barn) states for $h\nu = 1253.6$ eV radiation is very less than that of Ni 3*d* (0.01 mega barn) states [16]. Thus, the XPS VB peak is mainly dominated by Ni 3*d* states. As discussed above, the sputtered surface is Ni excess surface. The pure Ni metal VB shows a peak around 0.7 eV BE [23]. Thus the VB peak around 0.8 eV BE is due to excess Ni on the sputtered surface. The valence band width (W) of sputtered surface is determined to be 4.7 eV following Ref. [23] as shown in Fig. 7.7. It is same as the W of Ni metal (4.7 eV). The sputtered surface is highly Ni rich compared to bulk

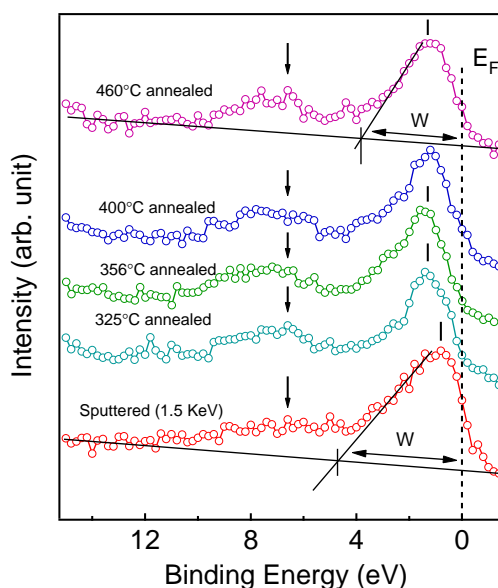


Figure 7.7 XPS valence band spectra of sputtered $\text{Ni}_2\text{Mn}_{1.32}\text{In}_{0.68}$ at different annealing temperatures recorded with $h\nu = 1253.6$ eV.

that is why the band width is matching with pure Ni metal. The VB of annealed surface has 3.8 eV band width. The VB width of annealed surface is less than that of sputtered surface and pure Ni metal (4.7 eV). A broad feature appears at around 6.6 eV (arrow in Fig. 7.7) in all the spectra. The calculated DOS of Ni_2MnIn does not show any feature at 6.6 eV BE [5]. The feature at 6.6 eV, might be due to the satellite feature as reported for Ni metal and Ni-Mn-Ga [24]. However, the satellite intensity is less for sputtered surface. One of the reasons for satellite appearance is narrow band width of Ni [24]. For sputtered surface the W is more than that for annealed surface. Thus, sputtered surface satellite has less intensity.

7.4.2 Core level

Ni 2p

Figures 7.8 (a) - (d) show the Ni 2p core-levels of $\text{Ni}_2\text{Mn}_{1+x}\text{Sn}_{1-x}$ as a function of temperature. From the fitting BE of Ni $2p_{3/2}$ and $2p_{1/2}$ peaks for $x = 0.40$ is found to be 852.7 ± 0.1 and 869.9 ± 0.1 eV, respectively, with a spin-orbit splitting of 17.2 eV. The $2p_{3/2}$ peak position of 852.7 eV

is within the literature value range of $852.7 \text{ eV} \pm 0.4 \text{ eV}$ for Ni metal [25]. No significant change in the BE is observed as a function temperature and Mn concentration within the experimental resolution. The concentration of Ni in alloys is 50%. It remains constant for all the compositions. Thus, Ni BE is similar to Ni metal and it does not vary with Mn concentration. Although the first nearest neighbor of Ni is Mn and there is significant hybridization between Ni and Mn [3] the core-level BE remains unchanged. The Ni $2p$ spectra shows two features at 6.7 and 5.7 eV higher

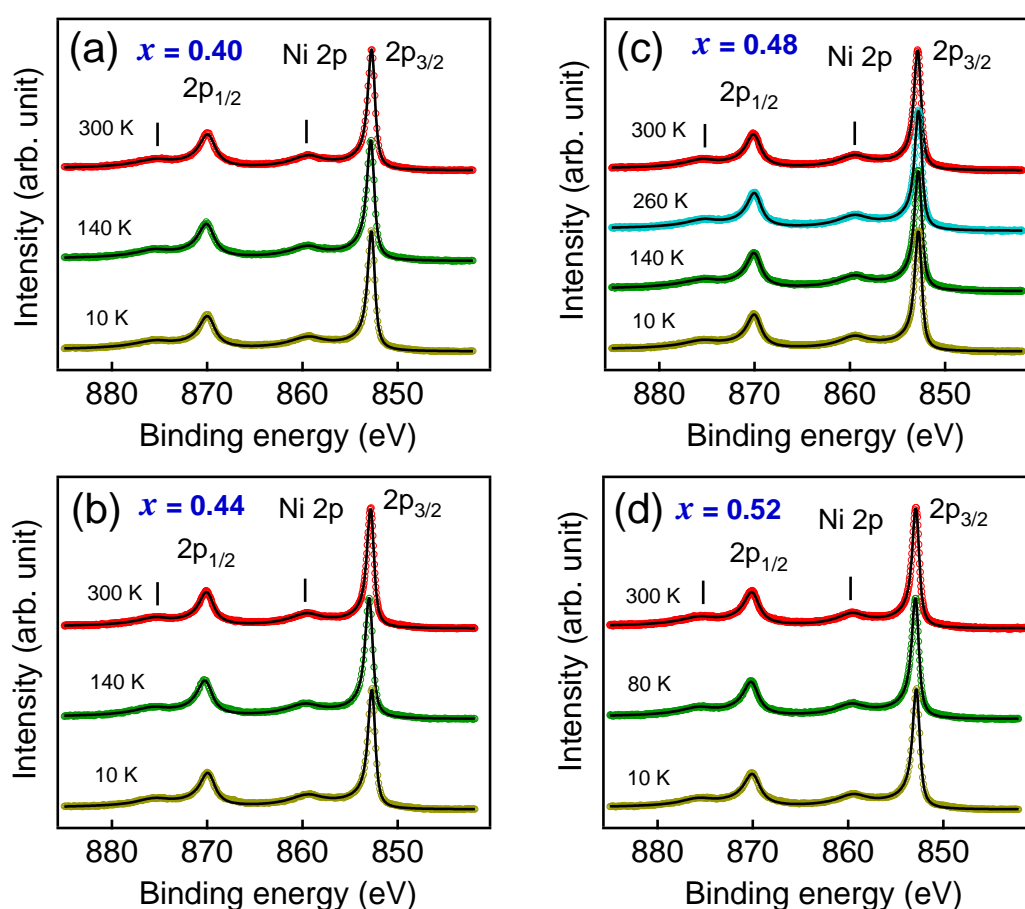


Figure 7.8 Ni $2p$ core-level spectra of $\text{Ni}_2\text{Mn}_{1+x}\text{Sn}_{1-x}$ recorded with $h\nu = 1486.6 \text{ eV}$. The solid line is fitting with DS line shape.

BE side of the $2p_{3/2}$ and $2p_{1/2}$ main peaks. The similar features has been observed in the Ni $2p$ spectra of Ni-Mn-Ga system also [24]. In the pure Ni metal, a satellite feature at 6 eV higher BE compared to Ni $2p_{3/2}$ peak is observed. The separation (ΔE) between the core-level and the

satellite peak position of Ni $2p_{3/2}$ (6.7 eV) and Ni $2p_{1/2}$ (5.7 eV) in $\text{Ni}_2\text{Mn}_{1.40}\text{Sn}_{0.60}$ is more than that of Ni metal (6 eV of Ni $2p_{3/2}$ and 4.5 eV of Ni $2p_{1/2}$).

The origin of 6 eV satellite in core-level photoemission spectra of Ni have been explained [26–29] by interaction of d states with s conduction states through s - d hybridization and with d states of other atoms through d - d transfer interaction. This initial mixing gives $3d^94s$ ground state of Ni. Upon creation of the core-hole, the $3d$ band is pulled down because of strong core-hole $3d$ coulomb interaction (U_{dc}) and this final state interaction gives rise to two possible final states. In one state, the core-hole is better screened as the $3d$ hole is filled by the transfer of an electron from $4s$ conduction band giving $3d^{10}$ configuration, while in other the $3d$ hole remains and the core-hole is poorly screened since $4s$ conduction electron transfer does not occur giving $3d^9$ configuration at higher BE in the final state. The later configuration is the excited state with one hole in the core-level and other in localized d state producing the satellite. The calculated XPS spectra [30–33] for Ni $2p$ assigns the $2p^53d^{10}$ final state to the main peak, the $2p^53d^9$ state to the 6 eV satellite.

The ΔE for alloy differs from ΔE for pure Ni metal because the first nearest neighbors of Ni are Mn and there is significant hybridization between Ni and Mn. Thus the d - d transfer interaction between Ni and Mn is different than that between two Ni atoms. Therefore, the effect of Ni-Mn hybridization is also visible through satellite peaks. No significant change in the BE of satellite peaks are observed as a function temperature. With small concentration of Mn substitution at Sn site there is no significant change in BE of satellite within the experimental resolution. The intensity of satellite also remains almost constant. However, the intensity of satellite is less than that in Ni metal.

The difference in ΔE between Ni $2p_{3/2}$ and $2p_{1/2}$ satellites is due to the difference in their multiplet splitting. For Ni metal the multiplet splitting of $2p_{3/2}$ satellite is different than the $2p_{1/2}$ satellite. The lower energy multiplets of $2p_{3/2}$ satellite are strongly decreased in intensity because U_{dc} is small and they do not form the bound states. Only high energy multiplets are visible for $2p_{3/2}$ satellite, whereas for $2p_{1/2}$ satellite, all of the multiplets form bound states. The multiplets are intense and are wide spread. Thus, the position of the $2p_{1/2}$ satellite structure is the configuration average position giving rise to different satellite position as compared to $2p_{3/2}$ satellite [26].

This is also the reason why the energy separation of the $2p_{1/2}$ satellite and main peak (4.5 eV for

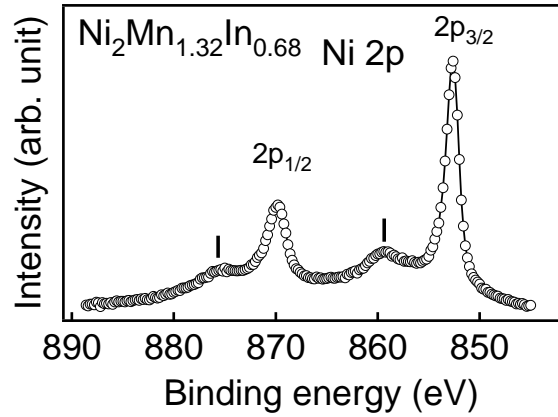


Figure 7.9 Ni $2p$ core-level spectra of $\text{Ni}_2\text{Mn}_{1.32}\text{In}_{0.68}$ in austenitic phase. The spectra is recorded with $h\nu = 1486.6$ eV.

Ni) corresponds to calculated U_{dc} (4.6 eV) [34]. Similarly, for $\text{Ni}_2\text{Mn}_{1+x}\text{Sn}_{1-x}$, U_{dc} is equal to ΔE for Ni $2p_{1/2}$ i.e. 5.7 eV. The theoretical electronic structure calculation till now have been reported using either generalized gradient approximation (GGA) [2, 3, 35] or GGA+U [36]. For GGA+U the U only on Mn is considered. The present thesis finding imply that electronic structure calculation with U on Ni from the experiment must also be checked.

The Ni $2p$ core-levels of $\text{Ni}_2\text{Mn}_{1.32}\text{In}_{0.68}$ after 1 hr Ar ion (1.5 keV) sputtering and annealing at 325°C for 2 hrs is shown in Fig. 7.9. The BE of Ni $2p_{3/2}$ and $2p_{1/2}$ peaks is found to be 852.6 ± 0.2 and 869.8 ± 0.2 eV, respectively, with a spin-orbit splitting of 17.2 eV. The $2p_{3/2}$ peak position of 852.6 eV is within the literature value range of $852.7 \text{ eV} \pm 0.4 \text{ eV}$ for Ni metal [25]. No significant difference in the BE from $\text{Ni}_2\text{Mn}_{1+x}\text{Sn}_{1-x}$ is observed. The Satellite appears at 6.6 ± 0.2 eV and 5.6 ± 0.2 higher BE of $2p_{3/2}$ and $2p_{1/2}$, respectively. The ΔE is similar to $\text{Ni}_2\text{Mn}_{1+x}\text{Sn}_{1-x}$.

Mn 3s

The Mn $3s$ core-level spectra of $\text{Ni}_2\text{Mn}_{1+x}\text{Sn}_{1-x}$ as a function of temperature are shown in Figs. 7.10 (a) - (d). The spectra show clearly two peaks that arise due to the exchange interaction between

the unpaired $3d$ electrons and the $3s$ photo-hole. When photo-hole is created in $3s$ level by photoemission, the $3s$ level is left with spin of $s = \pm 1/2$. This electron couples in either parallel or anti-parallel orientation with the total unpaired electron spin in the valence $3d$ orbital. This inter-

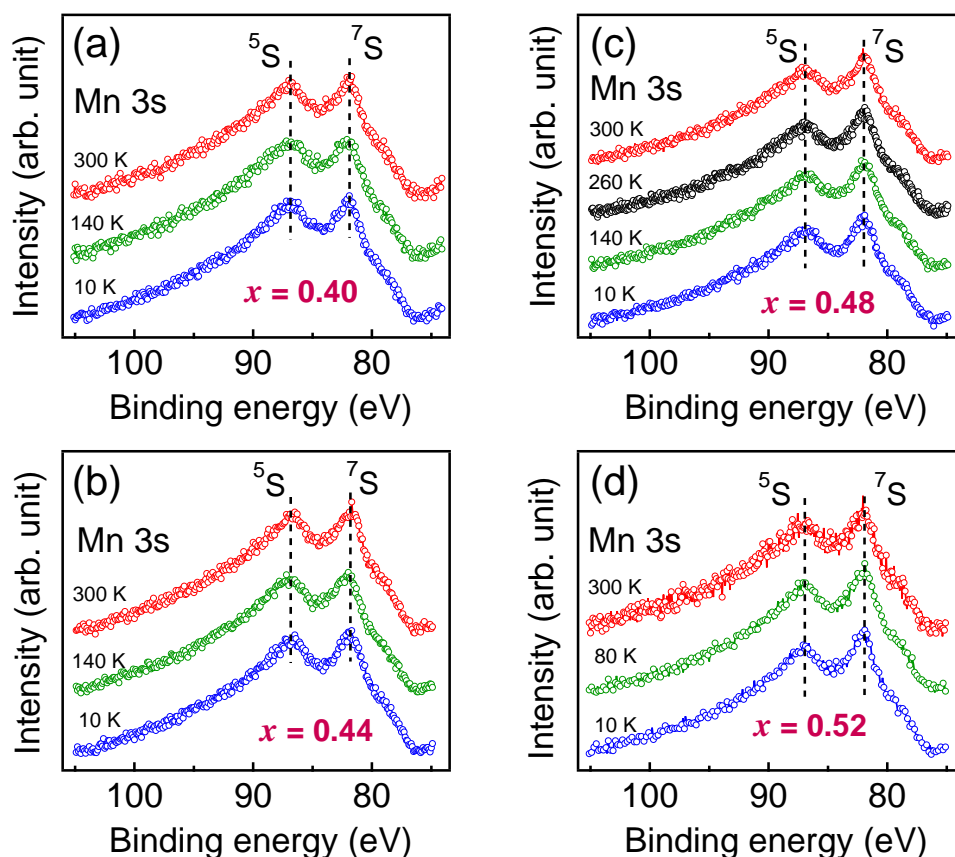


Figure 7.10 Mn $3s$ core-level spectra of $\text{Ni}_2\text{Mn}_{1+x}\text{Sn}_{1-x}$ recorded with $h\nu = 1486.6$ eV.

action gives rise to the exchange splitting and leads to two final states, referred as $7S$ and $5S$. The energy difference between these two states is the exchange splitting (ΔE_{ex}) and is good measure of the d band moment. Thus, the splitting of the Mn $3s$ peaks also provides a quantitative estimate of the average local magnetic moment of Mn atoms. For $x = 0.40$, $7S$ and $5S$ peak positions are 81.9 ± 0.1 eV and 86.9 ± 0.1 eV, respectively. The ΔE_{ex} is 5.0 ± 0.2 eV. The linear dependence of exchange splitting and magnetic moment (spin only) has been observed for Mn [37, 38]. From that relation, McFeely et al. [37] reported that the ΔE_{ex} of 4.08 eV corresponds to the local moment

of $2.5 \mu_B$ for α -Mn. From above relation magnetic moment of Mn atoms can be estimated for $\text{Ni}_2\text{Mn}_{1+x}\text{Sn}_{1-x}$. For $x = 0.40$, magnetic moment of Mn atoms is $\simeq 3.4 \mu_B$. From magnetization the maximum magnetic moment for $x = 0.40$ is $\simeq 2.55 \mu_B/f.u.$ at 200 K. The lower magnetic moment in the magnetization is due to the presence of anti-ferromagnetic coupling between Mn1 and Mn2. As a function of temperature, peak position and ΔE_{ex} remains same. Thus, in both martensitic and austenitic phase the Mn atomic moment remains same. As a function of Mn doping, no significant change in peak positions and ΔE_{ex} is observed. In $\text{Ni}_2\text{Mn}_{1+x}\text{Sn}_{1-x}$ the nearest neighbour of Mn is Ni [39], which is unchanged with temperature and Mn doping at Sn site. Thus, the localized Mn atomic moment remains unchanged with temperature and Mn doping at Sn site. These results also support that the decrease in the total magnetic moment upon the martensitic transition and Mn doping at Sn site is due to the enhanced anti-ferromagnetic coupling between Mn1 and Mn2.

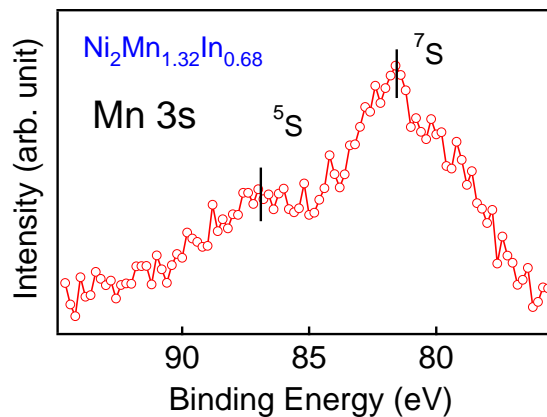


Figure 7.11 Mn 3s core-level spectra of $\text{Ni}_2\text{Mn}_{1.32}\text{In}_{0.68}$ in austenitic phase. The spectra is recorded with $h\nu = 1253.6$ eV.

The Mn 3s core-level of $\text{Ni}_2\text{Mn}_{1.32}\text{In}_{0.68}$ after 1 hr Ar ion (1.5 keV) sputtering and annealing at 325°C for 2 hrs is shown in Fig. 7.11. The ${}^7\text{S}$ and ${}^5\text{S}$ peak positions are 81.5 ± 0.2 eV and 86.9 ± 0.2 eV, respectively. The ΔE_{ex} is 5.4 ± 0.4 eV. The estimated magnetic moment per Mn atom is $\simeq 3.8 \mu_B$. The $\text{Ni}_2\text{Mn}_{1.32}\text{In}_{0.68}$ has higher ΔE_{ex} and higher magnetic moment as compared to $\text{Ni}_2\text{Mn}_{1+x}\text{Sn}_{1-x}$ which is very well matching with the magnetization results.

Sn 4d

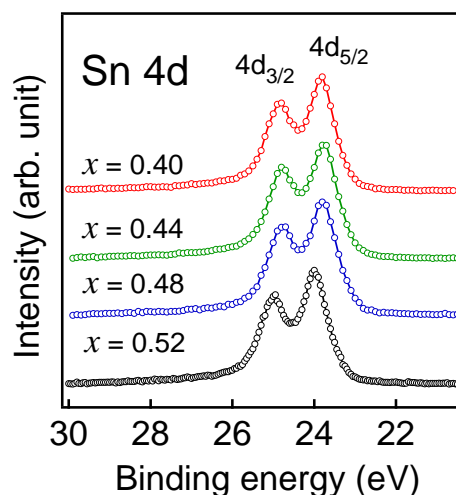


Figure 7.12 Sn 4d core-level spectra of $\text{Ni}_2\text{Mn}_{1+x}\text{Sn}_{1-x}$ in austenitic phase ($x = 0.40, 0.44$) and martensitic phase ($x = 0.48, 0.52$) at 300 K. The spectra are recorded with $h\nu = 1486.6$ eV.

Fig.7.12 shows the Sn 4d core-level as a function of Mn doping in $\text{Ni}_2\text{Mn}_{1+x}\text{Sn}_{1-x}$ at 300 K. The spin-orbit split Sn $4d_{3/2}$ and $4d_{5/2}$ core-levels are at 23.8 eV and 24.8 eV BE, respectively. The spin-orbit splitting is 1.0 eV. The BE is matching with the Sn metal [40]. There is no change in the Sn 4d core-level BE as a function of Mn concentration, in both phases, within the instrumental resolution.

7.4.3 Valence band

XPS valence band

The XPS valence band (VB) of $\text{Ni}_2\text{Mn}_{1+x}\text{Sn}_{1-x}$ at room temperature in austenitic phase is shown in Fig. 7.13 for clean surface. The VB spectral weight is, mainly, around 0.8 ± 0.05 eV with a shoulder around 1.6 ± 0.05 eV BE. The shape of the VB in the austenitic phase is similar for $x = 0.40$ and $x = 0.44$. Theoretical calculation shows that the VB of stoichiometric Ni_2MnSn is mainly dominated by the Ni 3d and Mn 3d states [2]. The feature at 0.8 eV is mainly contributed by Ni 3d states and 1.6 eV feature has contribution from hybridized Ni 3d - Mn 3d states [2]. Further, a

feature (shown by tick in Fig. 7.13) at 6.3 eV BE is also observed. The calculated DOS of Ni_2MnSn does not show any feature at 6.3 eV BE [2]. Also, the feature at 6.3 eV BE is asymmetric in shape. The feature at 6.3 eV, might be due to the satellite feature as reported for Ni metal and Ni-Mn-Ga [24]. The origin of this satellite is discussed in section 7.4.2 for Ni 2*p* core-level satellite. The band width (*W*) of VB is determined to be 3.7 eV following Ref. [23] as shown in Fig. 7.13. The VB width is less than that of Ni metal (4.7 eV).

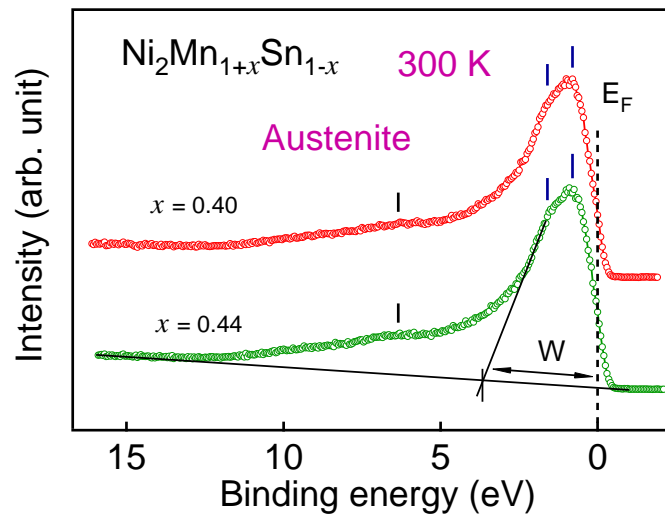


Figure 7.13 XPS VB spectra of $\text{Ni}_2\text{Mn}_{1+x}\text{Sn}_{1-x}$ in the austenitic phase at 300 K recorded with $h\nu = 1486.6$ eV.

The XPS valence band (VB) of $\text{Ni}_2\text{Mn}_{1+x}\text{Sn}_{1-x}$ at 10 K in martensitic phase is shown in Fig. 7.14. The VB shows two features at 0.8 eV and 1.6 eV BE similar to austenitic phase. The similar feature at 1.5 eV BE is reported for $\text{Ni}_2\text{Mn}_{1+x}\text{Sn}_{1-x}$ using high energy photoelectron spectroscopy [3]. This feature do not change with temperature because it has contribution from hybridized Ni 3*d* - Mn 3*d* states that remains essentially same upon transition. For similar reason, the 0.8 eV feature also remains same upon transition. The band width of VB for both $x = 0.40$ and 0.44 is 3.7 eV. It remains constant upon martensitic transition.

It is interesting to note that the 3*d* band width is narrow and is less than U_{dc} . The Ni satellite arises due to narrow band width of Ni metal. For $U_{dc} > W$, the satellite to main peak ratio can be

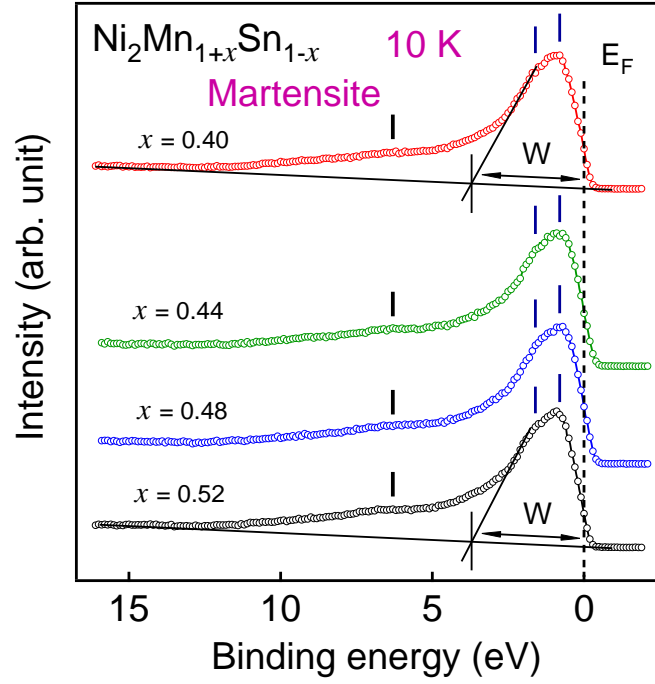


Figure 7.14 XPS VB spectra of $\text{Ni}_2\text{Mn}_{1+x}\text{Sn}_{1-x}$ in the martensitic phase at 10 K recorded with $h\nu = 1486.6$ eV.

related to the number of holes in the d band by [26]

$$\frac{I_{sat}}{I_{main}} = \frac{n_h}{1 - n_h} \quad (7.4)$$

Where I_{sat} and I_{main} are the area under the satellite and main peak, respectively. The I_{sat} and I_{main} have been calculated by the deconvolution of instrumental broadening from experimental data after the fitting. The DS line shape has been used for the fitting of main peaks. The calculated number of holes from the Eq. 7.4 at 300 K, 140 K and 10 K are 0.20, 0.18 and 0.20, respectively, for $x = 0.40$. The n_h is constant $\simeq 0.20$ as a function of Mn concentration in both austenitic and martensitic phases. The number of holes in the $3d$ band of Ni_2MnGa is also found to be 0.2 [24]. This is less than 0.6 holes estimated in Ni metal [41]. The decrease in number of holes in the d band of $\text{Ni}_2\text{Mn}_{1+x}\text{Sn}_{1-x}$ ensures better screening of the core-hole. Thus, the satellite intensity is less than Ni metal.

UPS valence band

In order to understand the electronic structure effect on martensitic phase the high resolution VB spectra of $\text{Ni}_2\text{Mn}_{1+x}\text{Sn}_{1-x}$ are recorded with $h\nu = 21.2$ eV. The Fig. 7.15 (a) shows the VB of $\text{Ni}_2\text{Mn}_{1.4}\text{Sn}_{0.6}$ as a function of temperature. In the austenitic phase (300 K), the spectral weight of VB is mainly at 1.0 eV (feature B) and 1.6 eV (feature A) in agreement with XPS VB (Fig. 7.13 and its discussion).

The most important and interesting observation is that the shape of VB changes with temperature. Upon martensitic transition (below M_F) the VB is mainly marked by one broad feature centred at 1.3 eV (feature C) BE. In between M_F and T^* the shape of VB remains almost similar. Within martensitic phase the shape of valence band is significantly modified below T^* temperature. The T^* (78 K for $x = 0.40$) is the temperature below which the magnetization drops further in zero field cooled (ZFC) state [Fig. 4.1 (a), chapter 4] [42]. At 10 K, the valence band is again dominated mainly by two features at 1.0 eV (feature E) and 1.6 eV (feature D). Although the features A & D and B & E appear at similar BE the nature of the feature might not be the same and for which detailed DOS calculation is required. Similar trends in the change of VB shape is also observed for $x = 0.44$ [Fig. 7.15 (b)], 0.48 [Fig. 7.15 (c)] and 0.52 [Fig. 7.15 (d)]. The change in VB shape within the martensitic phase as a function of temperature implies that the redistribution of DOS happen with temperature. The crystal structure analysis at room temperature [Table 3.6, chapter 3] shows that the martensitic phase consists of two co-existing crystal structures, orthorhombic 4L and 14L. Further analysis of crystal structure as a function of temperature [43] reveals that the phase fraction of 4L and 14L changes with temperature. In between M_F and T^* , $\approx 80\%$ 14L phase and 20% 4L phase co-exist ($x = 0.40$). Below T^* the 14L phase fraction starts reducing and 4L phase fraction increases. At 10 K, $\approx 45\%$ 4L and $\approx 55\%$ 14L phase co-exists ($x = 0.40$) [43]. Similar crystal structure changes are observed for other compositions also [43]. This implies that with the change in phase fraction the redistribution of DOS occurs. This DOS redistribution is manifested as the change in VB shape. Thus, the VB changes imply that the martensitic phase is unstable. The instability of martensitic phase is further explored near the Fermi edge, where change in electronic

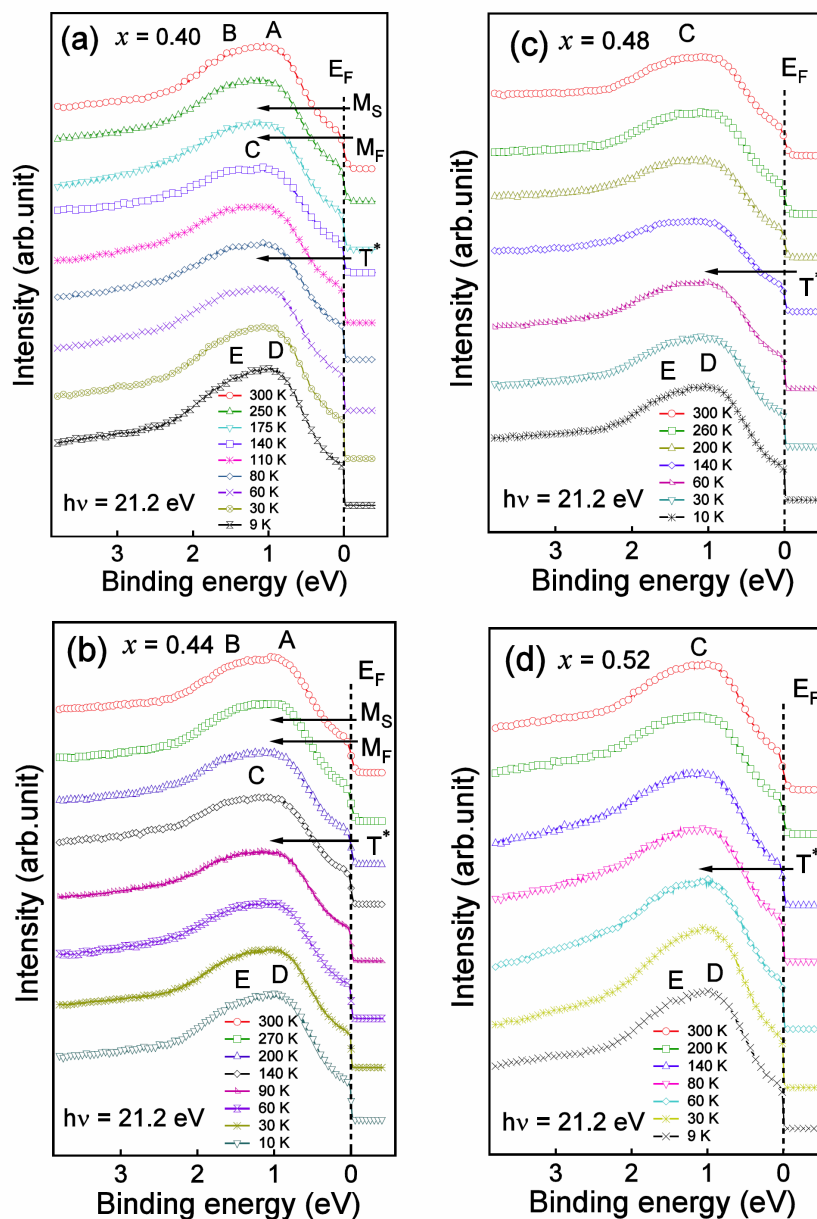


Figure 7.15 UPS VB spectra of $\text{Ni}_2\text{Mn}_{1+x}\text{Sn}_{1-x}$ as a function of temperature recorded with $h\nu = 21.2$ eV.

structure also causes the martensitic transition [3, 44].

The spectral density of states (SDOS) around E_F (-0.12 eV to 0.12 eV) is estimated by symmetrization of the experimental spectra $[I(E - E_F) + I(E_F - E)]$, where $I(E)$ is photoemission in-

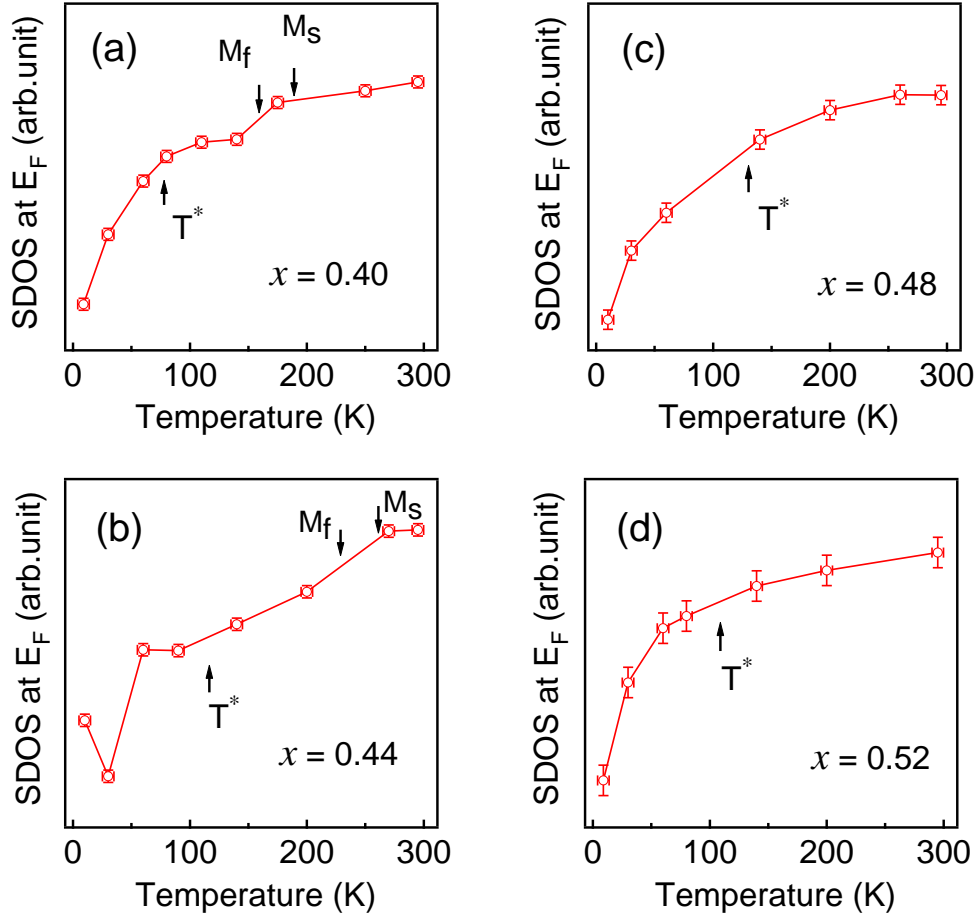


Figure 7.16 SDOS at E_F as a function of temperature for $\text{Ni}_2\text{Mn}_{1+x}\text{Sn}_{1-x}$ ($0.40 \leq x \leq 0.52$).

tensity [45]. The instrumental resolution broadening (FWHM = 1.5 meV) is small compared to thermal broadening at room temperature ($\simeq 25$ meV). Thus, in symmetrization method the temperature induced broadening is deconvoluted through Fermi-Dirac distribution function. In the metals, near E_F , the electron distribution is governed by Fermi-Dirac distribution. Thus photoelectron intensity can be given as $I(E - E_F) = \frac{DOS}{e^{(E-E_F)/k_B T} + 1}$, where T is absolute temperature. By taking the mirror image of function with respect to intensity axis through E_F , $I(E_F - E) = \frac{DOS}{e^{(E_F-E)/k_B T} + 1}$. Thus, the SDOS is equal to $I(E - E_F) + I(E_F - E)$.

The SDOS at E_F obtained after symmetrization procedure are shown as a function of temperature in Figs. 7.16 (a) - (d) for $x = 0.40 - 0.52$. The SDOS is almost constant in the austenitic phase

[Fig. 7.16 (a) for $x = 0.40$]. After martensitic transition (M_F) the SDOS decreases suddenly. In between M_F and T^* , the SDOS remains essentially constant [Fig. 7.16 (a) - (d)]. Below T^* SDOS rapidly decreases with decreasing temperature. Similar trend is also observed in all compositions.

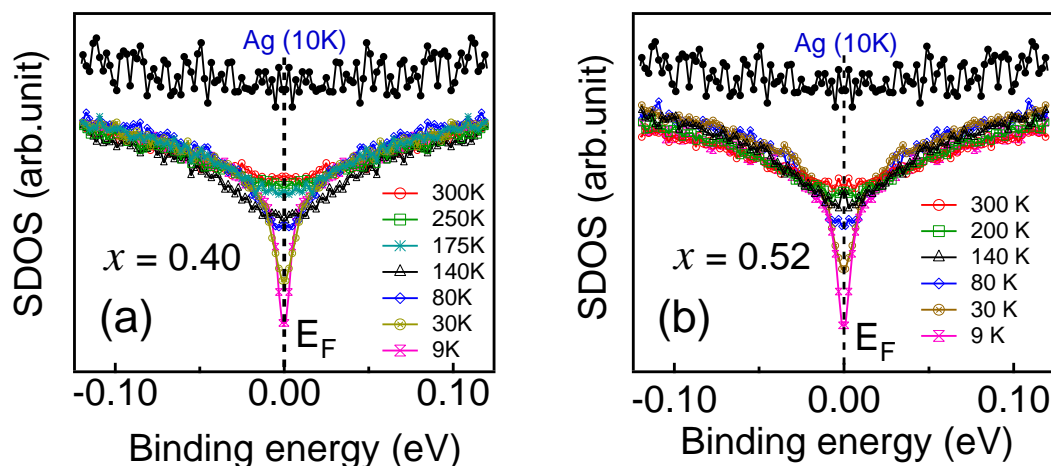


Figure 7.17 Appearance of pseudogap at E_F due to depletion of SDOS as a function of temperature for (a) $Ni_2Mn_{1.4}Sn_{0.6}$, (b) $Ni_2Mn_{1.52}Sn_{0.48}$. The flat band of Ag (10 K) SDOS is shown for clear identification of the pseudogap.

The structural analysis [43] shows that the phase fraction of 4L and 14L remains constant in the temperature range between M_F and T^* . The magnetization behaviour [Fig. 4.1 (a), chapter 4] is also constant in the temperature range M_F and T^* . The shape of VB is also approximately same between M_F and T^* . Thus, the SDOS at E_F also does not show significant change. Below T^* the phase fraction of 4L and 14L changes as discussed before. The magnetization exhibits a sudden drop in ZFC state. The VB shape also changes. Thus redistribution of DOS depletes the SDOS at E_F giving rise to pseudogap at E_F as shown in Fig. 7.17. As predicted in chapter 5, the existence of extended and localised states could give rise to pseudogap. The experimental observation of pseudogap calls for detailed spin-polarized DOS calculation using experimental lattice parameters. The existence of pseudogap at E_F in the martensitic phase makes the phase unstable.

Furthermore, it should be noted that a feature around 0.4 - 0.5 eV BE is present in polycrystalline $Ni_2Mn_{1+x}Sn_{1-x}$ as observed by high energy X-ray (6 keV) [3]. This feature is not observed in the present polycrystalline $Ni_2Mn_{1+x}Sn_{1-x}$ using He I (21.2 eV) source. However this feature

is recorded in single crystalline Ni_2MnGa using 21.2 eV photon energy [44], whereas the feature is absent in polycrystalline Ni_2MnGa taken using 21.2 eV photon energy [46]. This feature is mainly responsible for martensitic transition. At the surface the surface relaxation and anti-site defects could suppress the feature as shown by theoretical calculation [46]. Thus, in polycrystalline Ni_2MnGa surface the feature is not observed [46]. Similarly, the surface relaxation and anti-site defects could suppress the feature in polycrystalline $\text{Ni}_2\text{Mn}_{1+x}\text{Sn}_{1-x}$. The bulk is free of such constraints. Therefore using 6 keV photon energy (bulk sensitive) the feature is observable for polycrystalline $\text{Ni}_2\text{Mn}_{1+x}\text{Sn}_{1-x}$.

7.5 Conclusion

The natural surface of Ni-Mn-Sn equilibrates with less content of Mn and more content of Sn as compared to bulk. However, the surface still remains Mn excess with extra Mn occupying Sn site as found in the bulk. The sputtering and annealing process brings the natural surface of Ni-Mn-In to stoichiometric composition. Thus, using sputtering and annealing technique it is not possible to obtain surface composition same as bulk composition for Ni-Mn-Sn and Ni-Mn-In unlike Ni-Mn-Ga. Since natural surface prefers to be at different composition than bulk.

The experimental electronic structure, thus, obtained for $\text{Ni}_2\text{Mn}_{1+x}\text{Sn}_{1-x}$ is essentially for Mn excess concentration at Sn site near the surface. However, the changes in electronic structure could very well synchronize with the changes in bulk properties like crystal structure, magnetization and resistivity. Thus, these finding also indicate that thin films of $\text{Ni}_2\text{Mn}_{1+x}\text{Sn}_{1-x}$ could have similar bulk and functional properties with composition different than bulk.

Most important to note that the presence of pseudogap in the martensitic phase and the re-distribution of SDOS near E_F and upto 4 eV BE with respect to E_F within the martensitic phase induces instability in martensitic phase. Although the martensitic phase is energetically favourable than austenitic phase, the change in electronic structure below M_F indicates that martensitic phase still lacks stability. The field-cooled magnetization do not show drop in magnetization below T^* indicating that application of magnetic field could hinder the changes in SDOS through spin-lattice

coupling. This eventually brings stability to the system through shifting of martensitic transition towards lower temperature. The shifting of transition temperature in turn causes the attractive functional properties. Thus, electronic structure might be the basic driving mechanism behind magnetic field induced reverse phase transition. This calls for very detailed theoretical DOS calculation.

Bibliography

- [1] S. Plogmann, T. Schlatholter, J. Braun, M. Neumann, Yu. M. Yarmoshenko, M. V. Yablonskikh, E. I. Shreder, E. Z. Kurmaev, A. Wrona, and A. Slebarski, *Phys. Rev. B* **60**, 6428 (1999).
- [2] A. Deb, N. Hiraoka, M. Itou, Y. Sakurai, M. Onodera, and N. Sakai, *Phys. Rev. B* **63**, 205115 (2001).
- [3] M. Ye, A. Kimura, Y. Miura, M. Shirai, Y. T. Cui, K. Shimada, H. Namatame, M. Taniguchi, S. Ueda, K. Kobayashi, R. Kainuma, T. Shishido, K. Fukushima, and T. Kanomata, *Phys. Rev. Lett.* **104**, 176401 (2010).
- [4] S. Imada, A. Yamasaki, K. Kusuda, A. Higashiya, A. Irizawa, A. Sekiyama, T. Kanomata, and S. Suga, *J. Elec. Spec. Rel. Phen.* **156**, 433 (2007).
- [5] M. V. Yablonskikh, J. Braun, M. T. Kuchel, A. V. Postnikov, J. D. Denlinger, E. I. Shreder, Y. M. Yarmoshenko, M. Neumann, and A. Moewes, *Phys. Rev. B* **74**, 085103 (2006).
- [6] *Practical Surface Analysis Volume I: Auger and X-ray Photoelectron Spectroscopy* by D. Briggs and M. P. Seah, Second edition, John Wiley and Sons Ltd. (1990).
- [7] Igor Pro User's Manual, Wavemetrics Inc.
- [8] S. Tougaard and P. Sigmund, *Phys. Rev. B* **25**, 4452 (1982).
- [9] K. Levenberg, *Quart. Appl. Math.* **2**, 164 (1944).

- [10] D. Marquardt, *SIAM J. Appl. Math.* **11**, 431 (1963).
- [11] S. Doniach and M. Sunjic, *J. Phys. C* **3**, 285 (1970).
- [12] G. D. Mahan, *Phys. Rev.* **163**, 612 (1967).
- [13] J. J. Hopfield, *Comm. Solid State Phys.* **2**, 40 (1969).
- [14] *Photoemission in Solids I: General Principles* by M. Cardona and L. Ley, Springer-Verlag Berlin (1978).
- [15] S. Tougaard, *Surf. Sci.* **216**, 343 (1989).
- [16] J. J. Yeh and I. Lindau, *Atomic Data Nuclear Data Tables* **32**, 1 (1985).
- [17] M. P. Seah and W. A. Dench, *Surf. Interf. Anal.* **1**, 2 (1979).
- [18] P. Pörsch, M. Kallmayer, T. Eichhorn, G. Jakob, H. J. Elmers, C. A. Jenkins, C. Felser, R. Ramesh, and M. Huth, *Appl. Phys. Lett.* **93**, 022501 (2008).
- [19] C. Biswas and S. R. Barman, *Appl. Sur. Sci.* **252**, 3380 (2006).
- [20] D. Ristoiu, J. P. Nozières, C. N. Borca, B. Borca, and P. A. Dowben, *Appl. Phys. Lett.* **76**, 2349 (2000).
- [21] A. N. Caruso, C. N. Borca, D. Ristoiu, J. P. Nozières, and P. A. Dowben, *Surface Science* **525**, L109 (2003).
- [22] M. Maniraj, S. W. D'Souza, S. Singh, C. Biswas, S. Majumdar, and S. R. Barman, *J. Electron Spectrosc. Relat. Phenom.* Submitted.
- [23] J. C. Fuggle, F. U. Hillebrecht, R. Zeller, Z. Zolnierok, P. A. Bennett, and Ch. Frieburg, *Phys. Rev. B* **27**, 2145 (1982).
- [24] C. Biswas, S. Banik, A.K. Shukla, R.S. Dhaka, V. Ganesan, and S.R. Barman, *Surf. Sci.* **600**, 3749 (2006).

- [25] A. V. Naumkin, A. Kraut-Vass, S. W. Gaarenstroom, and C. J. Powell, NIST Standard Reference Database 20, Version 4.1 (Web Version), <http://srdata.nist.gov/xps/>.
- [26] A. Bosch, H. Feil, G.A. Sawatzky, and N. Mårtensson, *Solid State Commun.* **41**, 355 (1982).
- [27] A. Kotani and Y. Toyozawa, *J. Phys. Soc. Jpn.* **37**, 912 (1974).
- [28] L. A. Feldkamp and L. C. Davis, *Phys. Rev. B* **22**, 3644 (1980).
- [29] L. C. Davis and L. A. Feldkamp, *J. Appl. Phys.* **50**, 1944 (1979).
- [30] G. van der Laan and B. T. Thole, *J. Phys.: Condens. Matter* **4**, 4181 (1992).
- [31] G. van der Laan, B. T. Thole, H. Ogasawara, Y. Seino, and A. Kotani, *Phys. Rev. B* **46**, 7221 (1992).
- [32] G. van der Laan, M. Surman, M. A. Hoyland, C. F. J. Flipse, B. T. Thole, Y. Seino, H. Ogasawara, and A. Kotani, *Phys. Rev. B* **46**, 9336 (1992).
- [33] Y. Liu, Z. Xu, P. D. Johnson, and G. van der Laan, *Phys. Rev. B* **52**, R8593 (1995).
- [34] N. Mårtensson and B. Johansson, *Phys. Rev. Lett.* **45**, 482 (1980).
- [35] S. R. Barman, S. Banik, and Aparna Chakrabarti, *Phys. Rev. B* **72**, 184410 (2005).
- [36] B. Himmetoglu, V. M Katukuri, and M. Cococcioni, *J. Phys.: Condens. Matter* **24**, 185501 (2012).
- [37] F. R. McFeely, S. P. Kowalczyk, L. Ley, and D. Shirley, *Solid State Commun.* **15**, 1051 (1974).
- [38] P. Steiner, H. Höchst, W. Steffen, and S. Hüfner, *Z Physik B* **38**, 191 (1980).
- [39] P. A. Bhohe, K. R. Priolkar, and P. R. Sarode, *J. Phys.: Condens. Matter* **20**, 015219 (2008).
- [40] R. A. Pollak, S. Kowalczyk, L. Ley, and D. A. Shirley, *Phys. Rev. Lett.* **29**, 274 (1972).

- [41] F. U. Hillebrecht, J. C. Fuggle, P. A. Bennett, Z. Zolnierrek, and Ch. Frieberg, *Phys. Rev. B* **27**, 2179 (1983).
- [42] S. Singh and C. Biswas, *Appl. Phys. Lett.* **98**, 212101 (2011).
- [43] S. Pal, S. Singh, P. Mahadevan, and C. Biswas, unpublished.
- [44] C. P. Opeil, B. Mihaila, R. K. Schulze, L. Mañosa, A. Planes, W. L. Hults, R. A. Fisher, P. S. Riseborough, P. B. Littlewood, J. L. Smith, and J. C. Lashley, *Phys. Rev. Lett.* **100**, 165703 (2008).
- [45] G. Adhikary, R. Bindu, S. Patil, and K. Maiti, *Appl. Phys. Lett.* **100**, 042401 (2012).
- [46] A. Chakrabarti, C. Biswas, S. Banik, R. S. Dhaka, A. K. Shukla, and S. R. Barman, *Phys. Rev. B* **72**, 073103 (2005).